



HAL
open science

Ingénierie des défauts dans H et He implantés Si

Shay Reboh

► **To cite this version:**

Shay Reboh. Ingénierie des défauts dans H et He implantés Si. Matériaux. Université de Poitiers, 2008. Français. NNT: . tel-00459734

HAL Id: tel-00459734

<https://theses.hal.science/tel-00459734>

Submitted on 24 Feb 2010

HAL is a multi-disciplinary open access archive for the deposit and dissemination of scientific research documents, whether they are published or not. The documents may come from teaching and research institutions in France or abroad, or from public or private research centers.

L'archive ouverte pluridisciplinaire **HAL**, est destinée au dépôt et à la diffusion de documents scientifiques de niveau recherche, publiés ou non, émanant des établissements d'enseignement et de recherche français ou étrangers, des laboratoires publics ou privés.

THESIS

Submitted to:

Universidade Federal do Rio Grande do Sul - Brasil

Escola de Engenharia

Pos-Graduação em Ciência dos Materiais (PGCIMAT)

and

Université de Poitiers - France

Faculté des Sciences Fondamentales et Appliquées

Diplôme National-Arrêté du 7 août 2006

Ecole Doctorale : Sciences pour l'Ingénieur & Aéronautique

Secteur de Recherche : Milieux denses, matériaux et composants

in Fulfillment of the Requirements for the Degree of

Doctor of Philosophy

Defect engineering in H and He implanted Si

Presented by:

Shay Reboh

July 2008

P. F. P. Fichtner	Professor (Univ. Fed. do Rio Grande do Sul-BR)	Thesis director
J. F. Barbot	Professor (Univ. de Poitiers-FR)	Thesis director
M. F. Beaufort	Research Director CNRS (LMP, Poitiers-FR)	Thesis director
A. Claverie	Research Director CNRS (CEMES, Toulouse-FR)	Examining committee (Reporter)
A. Reguly	Professor (Univ. Fed. do Rio Grande do Sul-BR)	Examining committee
B. Pichaud	Professor (Université Paul Cézanne-FR)	Examining committee (Reporter)
J. Dupont	Professor (Univ. Fed. do Rio Grande do Sul-BR)	Examining committee
S. E. Donnelly	Professor (University of Salford-UK)	Examining committee

Abstract

The present work relates an investigation of H_2^+ and He^+ coimplanted (001)-Si substrates. The phenomena of blistering and exfoliation were studied by SEM as a function of the implantation parameters (energy, fluence, current and H/He ration) and annealing protocol. A window behavior as function of the implanted fluence was observed and two distinct fluence dependents mechanisms of exfoliation were indentified and discussed. The microstructure of the implanted samples was studied using TEM and related to ballistic effects and stress-strain dependent interactions. The strain was measured using DRX and a model to describe the stress-strain distribution into the implanted layer is developed. A new phenomenon of delamination of thin layer from implanted Si substrates was observed to emerge from particular implantation conditions. The behavior was studied and explained using fracture mechanics concepts and contrasted to blistering/exfoliation processes. Finally, the elastic interaction between He and H plate-like precipitates giving rise to arranged nanostructure was demonstrated and studied using TEM. An elasticity based model was developed to understand the behavior. The result set the basis for further developments of nanostructures within a crystalline matrix by manipulating preferential orientations of precipitates in nanometric scale.

Keywords: silicon, ion implantation, helium, hydrogen, DRX, MET, strain, SEM, elasticity.

Résumé

Ce travail porte sur l'étude des phénomènes induits par implantation d'hydrogène et/ou d'hélium dans le silicium monocristallin. Le cloquage et l'exfoliation dus à la coimplantation *d'hélium et d'hydrogène* ont été étudiés en fonction des paramètres d'implantation (énergie, fluence, courant, rapport H/He) et des conditions de recuit. Un comportement de type fenêtre a été observé dont le maximum de surface exfoliée dépend uniquement de la fluence. Deux mécanismes d'exfoliation liés aux régimes de fluence ont été identifiés et discutés. D'autre part, la microstructure des échantillons a été étudiée par MET, et les déformations ont été mesurées par diffraction des Rayons X. Un modèle décrivant la distribution des contraintes dans le substrat implanté a été proposé. Le phénomène de delamination des substrats qui apparaît pour des conditions particulières d'implantation a également été étudié, comparé aux phénomènes de cloquage et exfoliation, et expliqué en utilisant des concepts de la mécanique de la fracture. Enfin, l'interaction élastique entre précipités d'He et d'H a été étudiée pour des profils d'implantation superposés et décalés. Dans ce dernier cas, nous avons montré que le champ de contraintes générées par les plaquettes d'hélium en surpression pouvait être utilisé comme source locale de contraintes pour contrôler la formation et la croissance de plaquettes d'hydrogène. Afin d'interpréter nos résultats expérimentaux, nous avons développé un modèle basé sur l'interaction élastique pour la nucléation des précipités dans un solide semi-infini.

Mots clés : silicium, implantation ionique, hélium, hydrogène, DRX, MET, contrainte, SEM, élasticité.

Acknowledgements

Strangely, I may begin this acknowledgement with a conclusion, because my advisers have suppressed this conclusion from the Section "General Conclusion" even if it is the main conclusion of this thesis. It will be a confidence for very few people, because very few people will read this acknowledgement. I will be short. Here it goes: *I will never more do another thesis on the next months!!!!....* Ok... I said...

First of all, I want to express my *deep blue ocean* consideration and acknowledgements to my funny dear family, my father Franck *that gives me the best coffee of the world* among other less important things like love and etc..., my mother Suzanne *that gives me the best food of this world* among other less important things like care and etc...and my brother Yonathan more recognized by the codename of "*Tanga*" or "*Teta*" that simply gives me his *presence in this world* as something I could not live without. I am very proud of his new job of oil platform sinker. Superhighmegadoubletriplemasterhyper thanks to my wife Gabriela the "*Gabiruta*", who has being by my side...or on my back or on behind me or jumping on my head, making me happy, punching my stomach when I least expect it (I have now finally persuaded her to stop with this in exchange for authorizing her to punch my chest sometimes, it is less painful), thanks for telling me the beautiful stories of her magic world...and also for asking me strange questions about the stars, other planets and physics. Thanks also to my dear "*Vô Arão*" for encouraging me to do a thesis and also for the wonderful books that have significantly changed my mind. Thanks to my uncle *Tatio* for the strong friendship and partnership...and care...and for the "*second home*"... and for not being upset when I destroyed his wonderful new car's door on an "*invisible*" thing on that beach and thanks also for many other things. Thanks to my uncle Eric Reboh for the friendship, for the funny days and nights, for the *Pastis*, for the "*third home*", for teaching me impressive card tricks and for teaching me how important it is to "*walk fast*" in France, it really works!! "*walk very fast toward the "bureaus" just to go have some water or tea, if you have nothing to do all day long at least you should have some 4 or 5 rides to the bathroom crossing all bureaus doors very fast and serious*". Thanks also for finding that thing on wheels that was my car and home for a while.

The same level of acknowledgement as my family goes to Paulo F. P. Fichtner. Thank you for the true friendship and for trusting on me to do a thesis directly from "green" graduation. Thanks for all the support and motivation and for spending a lot of time and effort on this work. I can consider that if one of these days I become a good scientist the foundations were laid here. And thanks also for teaching those strange...bizarre things about science, materials personalities....electrons that

fly...that interfere...may talk and foolish with us...strange, very strange...It's still hard to believe those stories...but ok...it seems to work. Thank also for sometimes working till late at night and also on Saturdays and Sundays. Thanks to Monica, his wife, for understanding this absurd.

Thanks a *big big hugemaster lot* to Marie from the “*modest*” clan of the “*Beau*” and “*Fort*” family, for the true friendship, for the wonderful “*dinners*” where we were also gifted in appreciating the memorable Daniel's wines, for the pressure sometimes, for screaming behind me “*dépêche toi qu'es tu fait??!!...je suis partie!!*”...for being very present and interested on my work, for helping me to organize my disorder, and for some insights like “*tu est partie dans tout les sens...ça va pas ça!!*”, for listening to my foolish ideas and helping me to go ahead with my explanations “*avec les mains*”, and for the discussions, and for the nice conversations about anything or everything, and for having supporting me a lot for all this time, for the help with TEM and also for the tea...and of course...for the rides also. Two things, in particular, I will never forget...1) the first greeting of the day “*voila le Shay...bof!!*”, after lunch “*tu fait chier toiii!!!*”, at the end of the day “*ces't quand qui tu rentre au Bresil??...*”; 2) The international traffic of foie-gras, please Marie stop this, the customs are getting harder.

Thanks a lot to Jean “*c'est faux!*” François “*je ne suis pas d'accord!*” Barbot or *Bab*, for the discussions, for the sensitive judgment of my first essays to write in English: “*c'est la merde...incompréhensible il faut tout réécrire, allez...poubelle...c'est partie*”. Thanks for helping me to write the heart of this manuscript in a very few days, reading and correcting it very quickly when I was suddenly put into a lot of pressure to finish it. Thanks for the nice insights like “*une thèse n'est pas une catalogue*” or “*d'ou es q tu sors ça??!! Ta quand même de l'imagination...on vire*” and also for teaching me a lot of things and for promptly helping me with my worries. Thanks also for trying to teach me to write something “*simple et carré*”...I am not sure that I can do it but I am working very hard on this sense Bab.

Thanks to my great friend Augusto “*do Mato*” for the comradeship and essential help on this work. For the SEM teaching and the beautiful images that he did and helped me to do, for the “*buteco parceria*” and many other things. Thanks my friend.

Very special thanks to Jean Grilhé who played a crucial role in the development of the theoretical work in this study. Thanks a lot for teaching me many interesting things and making me appreciate the “*elasticité*”. It had opened a new door to me, I hope I can get in. And thanks also for the patient, careful listening and thinking about the *problems* we put forward and also for promptly answering my questions and for that smart “*insight*” on the fracture problem.

A very special thanks to Alain “speed” Declémy for the nice friendship, for those beers in the downtown and for the XRD measurements, and by introducing and teaching me many things, with a lot of patience, about the technique, interpretation and simulation. I appreciate it very very much.

Thanks to Borba, Miro, Augustinho and Manoel for carefully performing the sometimes “pain in the ass” implantations we asked for.

Thanks to my friend Francis Rossato for the help on the hard “*statistical*” work of great importance for this study.

Thanks to the Prof. Bergmann for the comprehension and support to the co-tutela regimen that I had the opportunity to get in. Thanks also for the trust, help and for teachings during the undergraduate period. Thanks a lot for helping and opening the doors with that “*first*” project with Petrobras Energia S.A. from where everything has begun. Be sure that we all have a great appreciation for this.

Thanks to Steve “Devil’s advocate” Donnelly, for the short but very valuable discussions where he always found a way to make me doubt my results and therefore evaluate them better, very useful I will say. It is a great challenge to try to convince him of something but I will find a way one day...don’t worry Steve.

Thanks to the Laboratorio de Implantação Iônica and Centro de Microscopia Eletrônica from the UFRGS for supporting this thesis. Thanks also to the Laboratoire de Métallurgie Physique from the Univ. of Poitiers for the nice “*accueil*”.

I would like also to thank my laboratory colleagues from both countries. Marcio Morschbacher, for some valuable discussions at the beginning of this work. Suzana “*Peripolenta*” for the “*punch in the mouth*” that she never gave me. Douglas “*Bukowski*” “*trash surf style*” da Silva, for the friendship and also for the “*motivation*” to do a thesis. Stephanie Leclerc “*la grosse*” for the friendship and funny company during many lunches and for explaining to me why in France we have less showers and why there the foot smells bad. The “*batman and robin*” Karim “*bijour*” and Cyril for the nice friendship. Azzam for the friendship and for taking care of the best “*vieux bagnole*” I will ever have. That “*redhead from the cold north*” Kerry that was a nice company all the times we met.

Thanks to my good friend Marco “*Kbça*” for the “*Heinekens*” and philosophical discussions.

Thanks to the “*gurias*” Aline, Me and Nanda for the “*all night long*” bar camaraderie during a nice few years of the beginning.

Thanks to Saulzinho "*el mexicano*" and Eric "*dedo de E.T.*" for the amity and help since the beginning in Poitiers.

Thanks to Alain Claverie for the short but motivating discussions.

Thanks to Ricardo Papaleo for the AFM measurements.

Thanks to Ludovic for the help with that "*strange defect*".

Thanks to Mark "*ça boom*" for the implantations in Poitiers.

Thanks to Dominique for the discussions and help with the TEM.

Thanks to the CAPES and CNPq for financial support in Brazil and France.

Many thanks to the French Embassy from Brasilia (in special for Jean-Pierre Courtiat) and "SPI&A Ecole doctorale" for the financial support during my second stay in France.

Thanks to Petrobras Energias S. A. for the partnership on the project and financial support for important laboratory facilities.

Cleber Lambert "*le philosophe*", for the friendship, philosophical-scientific discussions and the exchange and traffic of beer door-to-door.

Thanks to Joel "*good humor early in the morning*" Bonneville for the nice "*accueil*" in the LMP, and for the short but nice discussions.

Thanks to Pizzagalli the "*pizza de galinha*" for the funny "*accueil*" in the Lab.

Thanks Peco for the friendship and for repairing my *narguila*.

Thanks to Prof. Afonso Reguly for the memorable classes on the undergraduate course and also for the brief and valuable discussions about fracture.

Thanks to all the Professors that has been my teachers on the Materials Engineering course.

Thanks to the Prof. Pedro Grande for introducing me to the Ion Implantation group when I was in the under graduation.

Table of contents

Foreword	1
Introduction	2
CHAPTER 1 Background and state of the art	5
1.1 SOI technology and the ion induced splitting process	5
1.2 Blistering and exfoliation	8
1.3 Splitting mechanisms models	13
1.4 H and He coimplantation and blistering/exfoliation process	14
CHAPTER 2 Experimental techniques and methods	16
2.1 Ion implantation	16
2.2 Plasma immersion	18
2.3 Thermal annealing	18
2.4 Scanning electron microscopy (SEM)	18
2.5 Transmission electron microscopy (TEM)	18
2.6 X-ray diffraction	19
2.7 Glancing illumination optical microscopy (GIOM)	21
2.8 Atomic force microscopy (AFM)	21
2.9 Material	22
CHAPTER 3 Effects of the implantation fluence, implantation energy and thermal annealing protocol on the exfoliation phenomena: “Macro-mechanism of exfoliation”	23
3.1. Implantation parameters, thermal annealing protocols and data evaluation methodology	24
3.1.1. Implantation fluence (Φ)	24
3.1.2. Order of implantation and current density	24
3.1.3. Implantation energy	24
3.1.4. Thermal annealing protocols	25
3.1.5. Evaluation methods	26
3.2. Results for the 2H:1He fluence ratio	27
3.2.1. High energy case	27
3.2.2. Low energy case	30

3.2.3.	Summary of the results	33
3.3.	Discussions	35
3.3.1.	A_{ex} dependence on the implanted fluence.....	35
3.3.1.1.	The fluence window for exfoliation	35
3.3.1.2.	A_{ex} dependence on the implantation energy	37
3.3.1.3.	Mean size of individual exfoliation areas S_{ex} and exfoliation morphology	38
3.4.	Conclusion	50
CHAPTER 4 Fluence and current density effect on the exfoliation behavior of 1H:1He implanted Si.....		
4.1.	Experimental parameters	53
4.1.1.	Implantation fluence (Φ)	53
4.1.2.	Implantation energy	53
4.1.3.	Order of implantation and current density	53
4.1.4.	Thermal annealing protocols	53
4.2.	Results	54
4.3.	Discussions	61
4.3.1.	Effect of the H:He ratio on exfoliation efficiency	61
4.3.2.	Microstructure evolution as function of the implanted fluence and its consequence on A_{ex} and S_{ex}	61
4.3.3.	Strain evolution as a function of the implanted fluence.....	65
4.3.4.	Elasticity based expression and calculation of the same of the in-plane stress	67
4.3.5.	Stress distribution model and its correlation with preferential orientation of platelets along the Z-direction	70
4.4.	Thin films delamination via unstable crack propagation	76
4.4.1.	Results.....	76
4.4.2.	Discussions and model formulation for the delamination process drives by fast crack propagation.....	86
4.5.	Conclusions.....	89
CHAPTER 5 Multilayer exfoliation study and multilayer transfer concept		
5.1.	Experimental	93
5.2.	Results	94
5.3.	Discussions and conclusions.....	100

TABLE OF CONTENTS

5.3.1.	Group 1 samples	100
5.3.2.	Group 2 samples	100
5.3.3.	H implanted sample	101
5.3.4.	Engineering of exfoliation temperature	101
5.3.5.	Mechanical interactions between the implanted layers.....	102
5.4.	Conclusions.....	104
5.4.1.	Perspectives and potential applications	105
CHAPTER 6	Effects of H implantation in Si containing overpressurized He -plates.....	107
6.1.	Experimental	108
6.2.	Results and comments	109
6.2.1.	He-plates.....	109
6.2.2.	Overlapped H and He profile experiments.....	112
6.2.3.	Shifted H and He profile experiments	114
6.2.4.	Plasma hydrogenation experiments	123
6.2.5.	Final considerations	125
CHAPTER 7	Ordering of Nanostructures by Stress Engineering.....	126
7.1.	Experimental	127
7.2.	Results	127
7.3.	Model and Discussions	133
7.3.1.	Introduction to the model	133
7.3.2.	Calculation of the total stress tensor	134
7.3.3.	Energy minimization criteria.....	140
7.4.	Calculation results	141
7.4.1.	Verification of the experimental observations	141
7.4.2.	Predictions of the model	142
7.5.	Conclusions.....	146
General conclusion		148
Bibliography		151

Foreword

This thesis was born from the idea to study the “*hot*” subject of ion induced layer transfer of single crystalline materials onto host substrates, a new, generic and powerful technique for materials integration. However, as it naturally can happens during a long investigative journey as a thesis, ***peripheral*** findings may strongly hold our attention. So, while following the *main route*, I also attempted to explore its *landscape*. In accordance with my advisers, this manuscript also includes some of these *deviations*.

Introduction

Silicon is the basic material for the microelectronic industry, which represents a market of more than 150 billion dollars per year. In the present scenario, the demand for integrated circuits working at low voltage/low power (LVLP) conditions is strongly increasing and has reached an annual growth rate of more than 40% since 2004 [SOI 2008]. This demand is mostly stimulated by the portable electronics market which requires the reduction of power consumption in complex circuits to limit overheating troubles and extend battery operation times. The use of Silicon-on-Insulator (SOI) wafers is one of the most successful approaches, enabling integrated circuits to operate at LVLP. Among several methods proposed to produce SOI wafers, until the present date, the only one able to actually provide a practical and economical solution to the problem is the ion splitting method, uncovered in 1995 and commercially known as Smart-Cut® [Bru 1995].

In combination with direct bonding techniques, the ion splitting process expands the possibilities to produce high quality heterostructures, allowing the transfer of single crystalline layers sliced from bulk onto host substrates even of mismatched lattice structures [Asp 1997]. The basic idea for Smart-Cut® process arose from observations of blistering in gas implanted solids. Blistering, flaking and exfoliation are macroscopic results from the thermal evolution of microscopic lattice defects induced by high fluence inert gas or hydrogen ion implantation. Especially for *H*-implanted silicon, blistering (and ultimately the ion splitting process) is usually attributed to the formation of highly pressurized H₂ filled crack-like structures (nano and microcracks) within a specific depth location in the original bulk substrate. Upon subsequent thermal treatments the internal pressure increases and the crack-like structures tend to expand. For unbonded substrates, this expansion results on the lift of the material layer above the plate-like structures causing localized blistering or exfoliation within the implanted surface. When a host (“stiffener”) substrate is bonded onto the implanted surface, blistering and/or exfoliation is prevented by the mechanical strength of the stiffener and the lateral crack propagation process is favored.

Blistering strength is usually considered a figure of merit related to a successful ion induced splitting process, thus stimulating a large number of fundamental studies as

reviewed elsewhere [Ter 2007]. It is generally believed that thermally induced ion splitting results from the coalescence of the plate-like structures forming microcracks, which may individually expand and also coalesce with other similar structures, thus covering the complete wafer area [Bru 1995]. In comparison with single *H* implants, the coimplantation of *H* and *He* can significantly reduce the total blistering/exfoliation fluence [Aga 1998]. In addition, for energies from 30 to 50 keV were most studies were performed, the damage accumulation [Ngu 2005] and the proximity to the free surface may also affect the point defect fluxes and the retained gas content already during the implantation process [Mor 2004]. Blistering/exfoliation are multi-step phenomena evolving the combination of atomic mechanisms including diffusion, precipitation, coarsening and chemical interactions and macro mechanisms as bulk and local stress and strain effects with elastic and plastic deformation, microcleavage and crack propagation mechanisms. Hence, blistering /exfoliation processes render a quite complex situation, which so far has not been completely understood.

This thesis presents a systematic investigation on blistering/exfoliation phenomena in co-implanted H and He ions into Si (001) substrates. In comparison with previous studies from the literature, the present work innovates in exploring simultaneously both, “high” and “low” implantation energy ranges, using an expanded investigation methodology. Particularly for the high energy case, we show that crack propagation parallel to the sample surface may compete with the vertical lift of Si over layers that leads to localized blistering or exfoliation. As a consequence, both processes could be studied under the similar experimental conditions (i.e. avoiding the thermal treatments and the surface tension introduced by the pre-bonding procedures), thus providing new insights into the effects of the implantation and annealing parameters on both mechanisms. For both implantation energy cases, the exfoliation behavior is statistically investigated and the results are discussed in terms of the blistering precursors and their physical interactions, attempting to correlate the macro and the micro mechanisms behind blistering, exfoliation and ultimately the ion induced wafer splitting.

To substantiate the discussions, a brief summary of the state-of-the-art is presented in Chapter 1. Chapter 2 presents a short description of the experimental techniques. In Chapter 3, the experimental methodology is described. Then, based on scanning electron

microscopy (SEM) observations and their statistical analysis, possible exfoliation macro mechanisms are discussed and a phenomenological model is proposed to explain the results. Chapter 4 starts with a detailed transmission electron microscopy (TEM) investigation of the exfoliation precursors. Results from strain measurements via X-ray diffraction measurements (XRD) are presented and introduced into the discussions based on elasticity considerations. A model correlating the strain distribution to microstructure formation is then proposed. In the second part of Chapter 4, we report on a new thin film delamination phenomena taking place when the implantations are performed under higher fluence rates (i.e. beam current densities). This delamination phenomenon is discussed in terms of a catastrophic crack propagation process triggered at a single nucleation point, which is introduced as an alternative and probable concurrent process to the usual concept that layer splitting is governed by the growth and coalescence of individual nanocracks. An exfoliation engineering concept based in sequential multilayer splitting is introduced in Chapter 5. Chapter 6 explores the effects of *H* implantation into samples containing pre-existing pressurized *He*-plates, showing some examples of how defect interactions can be tailored to produce distinct cavity arrangements and geometries. In addition, Chapter 6 also reveals that strain fields can be used to tailor the local three dimensional arrangements of *H*-platelets. This phenomenon is more deeply studied in Chapter 7, where model calculations based on the minimization of the *H*-platelet formation energy with respect to their lattice orientation are introduced and successfully used to describe the experimental observations. Finally, main conclusions perspectives for further investigations are summarized in Chapter 7.

CHAPTER 1

Background and State of the Art

1.1 SOI technology and the Ion induced splitting process

Device performance and, more recently, energetic *ecosystem* [TSMC 2007] requirements from the semiconductor industry have been stimulating the progress of the silicon-on-insulator (SOI) technology for ultra-large-scale integrated (ULSI) devices. The use of SOI technology allows the fabrication of devices with considerable advantages over bulk Si [Col 1997], such as processing speed, high packing density, elimination of latch-up phenomena, low voltage/low power operation ($\approx 50\%$ less than bulk Si, LVLP) and high resistance to ionizing radiation [Cel 2003]. A typical SOI substrate consists of a thin layer of single-crystal silicon supported by an underlying insulator.

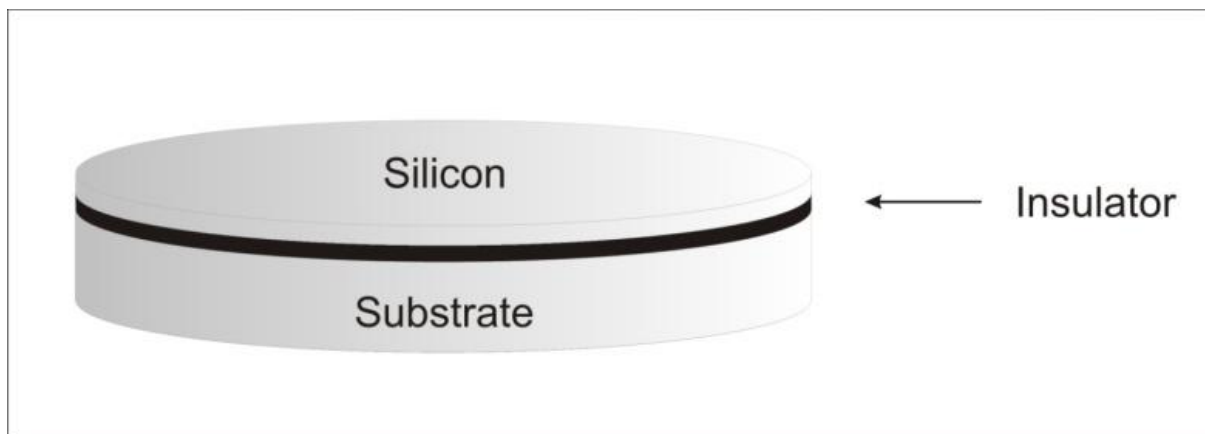


Figure 1.1- Diagram of Silicon-on-Insulator (SOI) substrates.

The fabrication of high-quality, defect-free, single-crystal silicon thin film supported by an insulating layer has been a great challenge. Several techniques have been proposed [Bea 1977, Izu 1978, Lea 1982, Cel 1983, Jas 1983, Gup 1983, Fan 1983, Ima 1984, Pri 1985, Cel 1985, Yam 1985, Phi 1985, Las 1986, Yon 1994, Jur 2000], but none of them provide the requirements of cost and quality needed for large scale production. Around 1995, however, a promising technique commercially known as Smart-Cut[®] [Bru 1995] appeared as an

alternative solution. This ion implantation based technique permits the production of high quality SOI substrates for a reasonable cost with the current technologies used in the microelectronic industry [Asp 2000]. Nowadays Smart-Cut® has boosted technology applications and overwhelmingly dominates the SOI market [SOI 2008]. Its importance and potential for novel applications have prompted the need for more basic and integrated knowledge comprehending several fields of science and technology, including ion beam modification of materials, surface physics, chemistry and tribology in connection to wafer bonding, ultra-precise etching and polishing techniques, as well as elasticity, mechanic of solids, materials science and even nuclear engineering concepts. The fabrication of SOI substrates was only the first (and most commercially successful until the present date) example of materials integration possibilities. The full potential of this new tool is still being realized. Several combinations of high quality single crystalline (polycrystalline were also possible [Yun 2003]) materials have been reported in the literature [Asp 2000, Asp 2001]. This includes silicon or other semiconductor (Ge, SiC, GaAs and InP) films transferred onto different types of substrates (e.g., glass, metals, polymers) [Bru 1995, 1996, 1999; Jal 1998 Asp 1996, 1997, 1999, 200, 2001; Ton 1997, 1998, 2000, Cio 1996, Rad 2003]. The transfer of structured and patterned thin silicon films has also been demonstrated [Asp 1996, 1999; Yun 1998, 1999]. The use of such ion induced layer transfer technology allows the fabrication of new functional materials [Gad, 2003] with increasing liberty of devices design, promoting significant device advance as often announced by manufacturers such as Toshiba Inc., AMD Inc., Sony Inc. and others.

The Smart-Cut® is an ion induced splitting process based on blistering/exfoliation phenomena [Bru 1995, Ter 2007]. It is known that Si implanted with hydrogen ions (H^+) at high fluences produces crack-like cavities with high internal pressure after annealing. The relaxation of this pressure results in the deformation surface and appearance of blisters [Lig 1976, Bru 1995, Wel 1997, Lu 1997, Hua 1999, Bed 2001, Zhe 2001, Ter 2007]. If, before the annealing treatment, the implanted surface is bonded to a rigid substrate (stiffener), the formation of surface blisters is mechanically impeded [Bru 1995, 1998, Fen 2004]. Once mechanical relaxation via blistering is avoided, the stress (due to the internal pressure) developed into the cracks relaxes via lateral growth [Bru 1995, Wel 1997]. Crack coalescence over the whole wafer area is regarded as the basic mechanism leading to the split of the

implanted layer from the substrate [Bru 1995, Wel 1997, Fre 1997, Hoc 2001, Yan 2003, Fen 2004]. The ion induced SOI fabrication process is schematically illustrated in Fig. 1.2. It starts from two thermally oxidized Si wafers A and B. The wafer A is implanted with H^+ ions (or $H+He$), defining the depth of the layer to be transferred. The depth localization of H^+ ions is defined by the ion acceleration energy. After implantation, the wafers A and B are face to face bonded. The assembly is thermally annealed (usually at temperatures ranging from 400°C to 600°C) to promote the splitting process. The remaining substrate surfaces are polished to reduce roughness. The wafer B now constitutes a SOI substrate and the wafer A is submitted to a new cycle. The as obtained SOI substrate is often annealed at a high temperature ($\approx 1100^\circ\text{C}$) to strengthen the bonding of the transferred layer on the substrate [Asp 1997, Bru 1999].

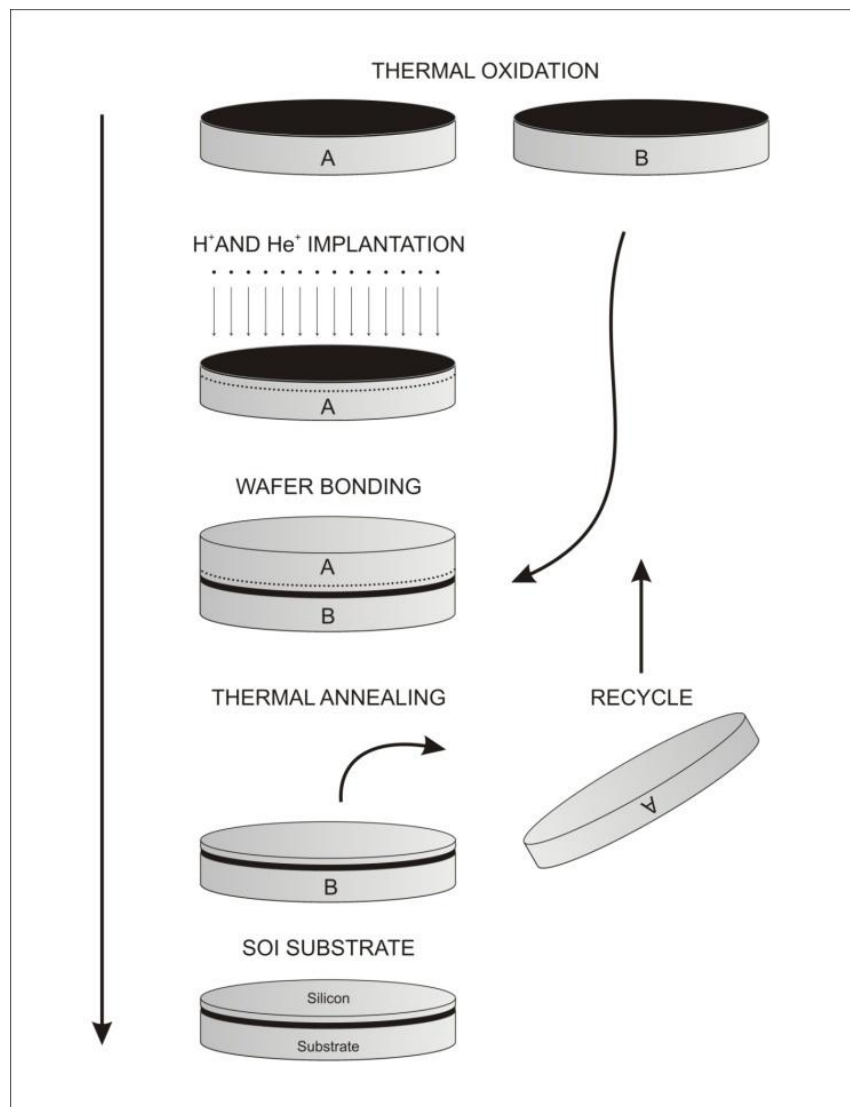


Figure 1.2- Basic processing flow of the ion cut technique.

In spite of the several successful applications already demonstrated and of the intensive attentions received since its first publication [Bru 1995], a complete understanding of the underlying physical mechanisms of the process is still missing.

Blistering/exfoliation strength is considered a figure of merit related to a successful splitting. This phenomenon is systematically investigated in the present work, and therefore the most important literature concepts will be briefly reviewed in the next sections.

1.2 Blistering and exfoliation

Blistering, swelling and exfoliation of metals and ceramics, due to the incorporation of inert gases, have been first studied in an attempt to avoid its deleterious effects in nuclear materials [Das 1980]. Blistering has been observed as well in semiconductors, such as Ge [Gös 1998, Gig 2007, Des 2008], SiC [Gig 2007, Cio 1996], GaAs [Gig 2007, Rad 2003, Jal 1998], InP [Asp 2001], as well as in insulators such as diamond [Gös 1998], Si₃N₄ [Asp 2001], SrTiO₃ [Gig 2007, Kub 1999], LaAlO₃ [Hua 1999b], LiNbO₃ [Asp 2001]. Surface blistering of single crystalline Si samples induced by implantation of *H* was firstly reported in 1976 [Lig 1976]. *He* implantation can also induce blistering in Si, but at very high fluences ($\Phi > 2 \times 10^{17}$ cm⁻²) [Aga 1998]. For lower *H* or *H+He* fluences ($\Phi \approx 4 \times 10^{16}$ cm⁻²), blistering or exfoliation occurs only upon subsequent thermal annealing (generally between T=400°C-550°C) and appears as illustrated in Fig.1.3.

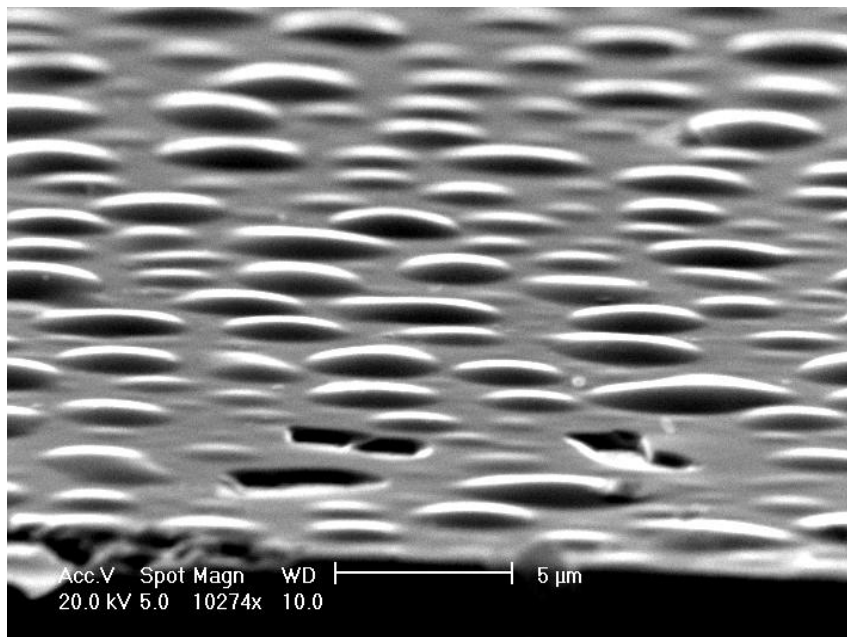


Figure.1.3- SEM image of an *H+He* coimplanted Si (30keV *H*⁺ ions at 5×10^{16} ion/cm² + 33keV *He*⁺ ions at 5×10^{16} ion/cm²) after annealing (500°C 1800s). Dome shaped blisters and exfoliated areas (craters) are observed (data from this work).

Light ion (H and He) induced blistering is generally understood in the following terms. Inert gases (He) are practically insoluble in solids, and tend to segregate forming gas-vacancy complexes which develop into pressurized cavities. To a certain extent, H presents a similar behavior. However, their chemical properties strongly differentiate their behavior. H atoms can easily react with Si dangling bonds in contrast to the inert gas character of He . During annealing, the formed cavities coarsen [Gri 2000, Don 1991]. If a characteristic size is reached, the high internal pressure developed into the cavities cause the deformation of the surface; i.e. blistering [Fen 2004].

The blistering behavior in H implanted Si is a multistep phenomenon, that results from a combination of several and complex atomic mechanisms. This includes radiation damage, diffusion and segregation of atoms, nucleation, growth and coalescence of H -vacancy clusters or small cavities, as well as physical and chemical interactions between the matrix and the gas atoms. Stress and strain induced effects, crack propagation and elastic or plastic deformations can also play an important role in this phenomenon.

In this scenario, two basic main causes for blistering of light ion irradiated materials have been discussed in the literature, the internal gas pressure [Eva 1977] and the integrated lateral stress-induced buckling of the surface [Eer 1977]. The gas pressure blistering is predominantly assumed in most works considering semiconductors. However, an attempt to include the lateral stress-induced factor in the recent discussions has been made [Bed 2000] and blistering/exfoliation may be considered a combined result from both mechanisms. So far, a conclusive concept has not been established.

However, due to economical and technological reasons, considerable progress into the fundamental understanding of H induced blistering of implanted Si is now available and some relevant concepts are summarized in the following sections.

1.2.1 BLISTERING PRECURSORS

After implantation (generally at room temperature) H induced platelet cavities with diameters around 10 nm and ≈ 1 nm thick is readily observed. These, are considered as the blistering precursors [Bru 1995, Cer 2000, Gri 2000]. H -platelets are believed to be filled with hydrogen molecules (H_2) and coated with hydrogen atoms captured by dangling Si bonds at

the cavity internal surface or at the crack tip [Wel 1997; Koz 2000]. The schema shown in Fig. 1.4 exemplifies the structure concept.

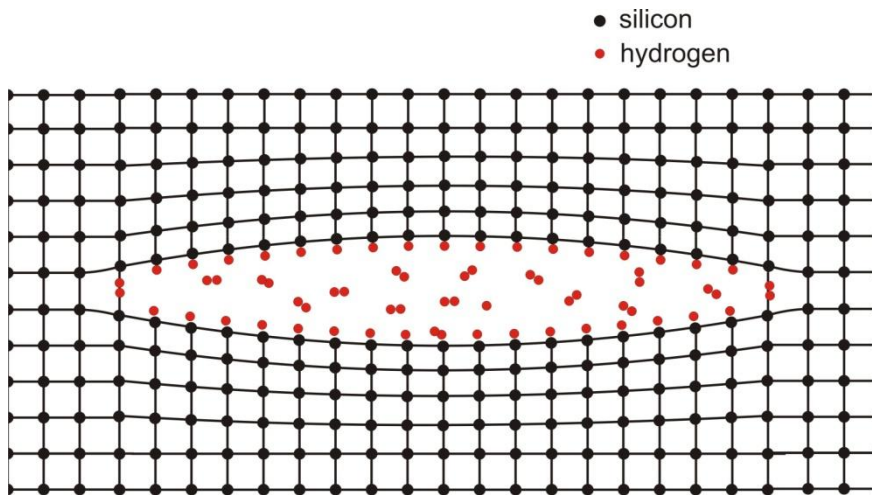


Figure 1.4- Schematic concept of *H*-platelet structures. The cavity is filled with H_2 molecules and the internal walls are decorated with *H* atoms captured by dangling bonds.

In Si, the *H*-platelets usually form oriented along two lattice planes (111) and (001). Figure 1.5 shows HRTEM images of *H*-platelets in their most common habit planes.

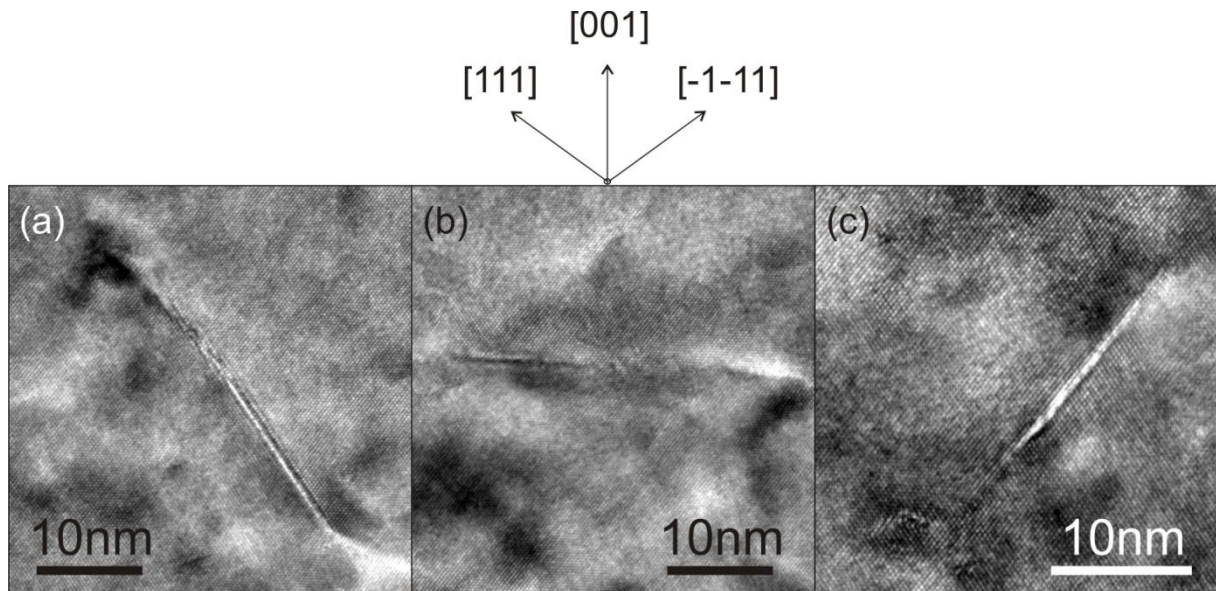


Figure 1.5- A cross sectional TEM images of (a) (-1-11) *H*-platelet, (b) (001) *H*-platelet and (c) (111) *H*-platelet. The images were obtained after implantation of 30keV $0.5 \times 10^{16} H_2/cm^2$ and annealing at 400°C-900s (data from this work).

The {111} oriented *H*-platelets have in principle the lower formation energy [Nic 2000] but the subject is controversial [Mar 2005, Nas 2005]. Surprisingly, when *H* is introduced by implantation, the dominant orientation of platelets is **parallel to the surface** regardless of the wafer orientation (001) or (111) [Asp 1997, Zhe 2001, Hoc 2002, Fra 2002]

(i.e. in (111) wafers H -platelets are preferentially alignment to the (111) plane parallel to the surface and, in (001) wafers, H -platelets are preferentially alignment to the (001) plane parallel to the surface). This preferential alignment is resultant from stress and strain effects. H implanted wafers tend to develop an in-plane compressive stress on the implanted layer [Höc 2002]. As a consequence, an out-of-plane strain also occurs as shown in Fig. 1.6. The out-of-plane strain tends to produce a localized stretch of the Si lattice on the direction perpendicular to the surface.

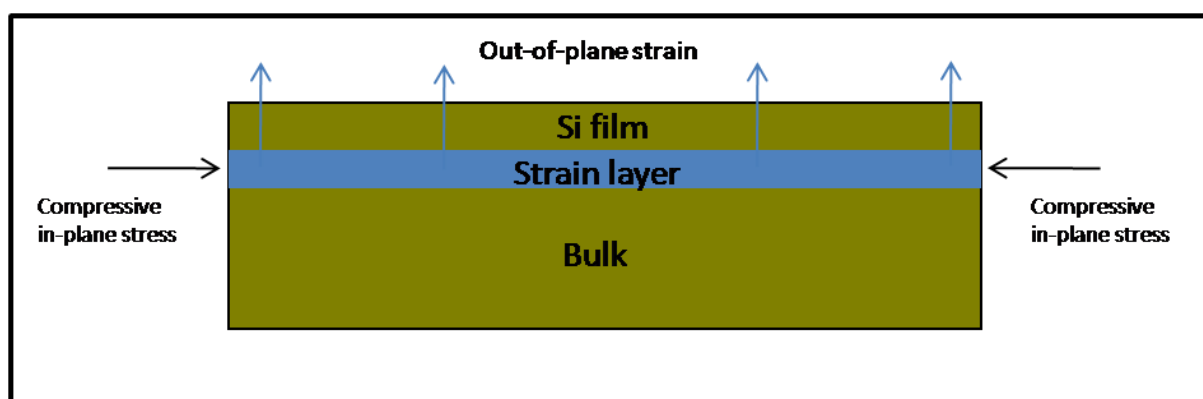


Figure 1.6- Schema of the stress-strain conditions of the material after implantations. It develops an in-plane compressive stress that leads to the appearance of an out-of-plane strain.

The alignment of H -platelets was then attributed to the preference of hydrogen to establish Si–H bonds with the stretched Si–Si bonds that are perpendicular to the surface, thus, producing internal surfaces that are parallel to the surface [Höc 2002]. Later, the alignment effect was attributed to a favorable H -platelet nucleation parallel to the plane of stress [Nas 2005]. Moreover, a mechanism for the formation and concentration of platelets into a narrow layer has been proposed in the following terms. The out-of-plane strain induced by the in-plane stress [Höc 2002] generates a flux of vacancies into a narrow layer coincident with the maximum of strain [Lee 2006]. This high concentration of vacancies will tend to form *aligned vacancy dislocations loops*. These loops are expected to be easily decorated by the implanted H , since hydrogenation reaction of vacancies is highly exothermic, thus, causing the formation of the H -platelets also into a narrow layer and parallel to the surface.

Under annealing, platelets grow while their number density decreases [Cer 1992, Asp 1997, Asp 1998, Gri 2000]. This occurs by random exchange of atoms and vacancies characterizing an Ostwald ripening mechanism [Gri 2000]. Further H -platelet development

may lead to a coalescence process giving rise to nanocracks. Figure 1.7a shows a TEM image of nanocracks formed in H implanted Si. Figure 1.7b shows a HRTEM detail of a nanocrack.

Nanocracks have often a zigzagged configuration because they result from coalescent platelets were not necessarily in the same atomic plane. Further *nanocrack* growth or coalescence produce larger defects referred as *microcracks* [Wel 1997, Asp 2001, Hóc 2002]. Interestingly, typical *microcrack* diameters are one order of magnitude larger than H -platelets and one order of magnitude smaller than blisters. It is then natural to consider microcracks as an intermediate step of the blistering process. Nevertheless, it is the combination of internal pressure, critical crack size and depth location that controls the blistering formation.

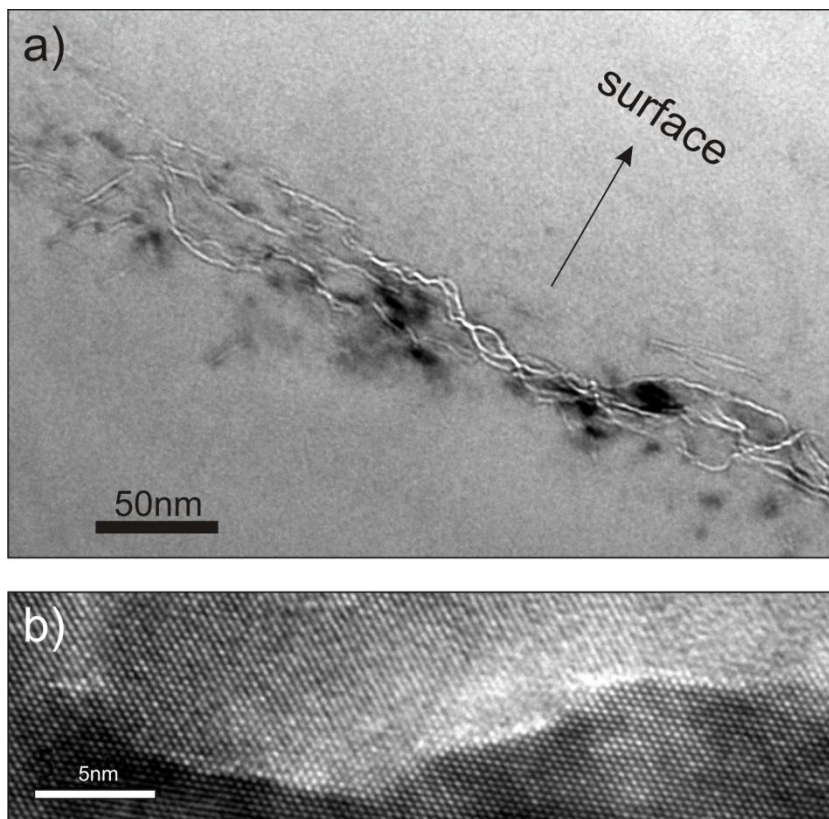


Figure 1.7- (a) Cross sectional TEM image of a coimplanted ($H^+ 1.10^{16} \text{cm}^{-2} + He^+ 1.10^{16} \text{cm}^{-2}$) Si sample annealed at 400°C 900s. (b) HRTEM image of a nanocrack (data from this work).

1.2.2 BLISTERING ONSET AND FLUENCE WINDOW

A minimum of H concentration seems to be one of the fundamental parameters for blistering. Roughly, ≈ 5 at % of H is the threshold concentration for blistering [Ter 2007]. Maximum fluences for blistering have been also observed [Lu 1997, Mou 2004, Mou 2005]. Hence, there are characteristic fluence windows for blistering. The width of the window

increases with the implanted energy [Ter 2007]. The suppression of blistering for very high fluences has been less explored, and tentatively attributed to a modest expansion of spherical cavities, resulting in surface swelling to relieve the stresses. Amorphization effects have also been suggested to explain the inhibition of blistering at high fluence [Ngu 2005, Ngu 2007, Ter 2007].

The onset of blister formation seems to be a critical phenomenon [Hua 1999]. The implanted surface remains unmodified until blisters suddenly pop-up with well-defined diameters after an incubation period. Hydrogen-induced blisters are roughly circular and dome-like shaped as if produced by elastic deformation of pressurized thin plates. A general condition for blister to occurs has been proposed as $h/r \ll 1$, being h depth of the crack (thickness of the over-layer) and r its radius [Feng 2004]. It implies that the crack length must exceed many times its characteristic depth to produce a deformation of the surface. As a trend, it is also expected that blister diameters increase with the crack depth location.

1.3 Splitting mechanisms models

Ion induced splitting, observed along damaged layers is generally attributed to the growth and coalescence of crack-like cavities until the whole layer separates from the substrate [Fre 1997, Var 1997]. This occurs over typical areas about 10^2cm^2 , which are approximately 10^{10} times larger than the size of a single blister (10^{-8}cm^2). The splitting phenomenon requires long annealing times, about 10 times more than those for blistering formation [Ton 1997, Asp 1998]. The activation energies for both phenomena in H implanted Si are similar [Ton 1997], indicating that their micromechanisms are also similar. This result supports the assumption made by several authors, that basic studies on the blistering behavior observed in unbonded wafers can be used to explore or optimize the ion splitting process [Wel 1997, Hoc 2002, Ter 2007].

It seems also interesting to point out that wafer splitting generates an audible sound [Asp 1998, Bru 1999]. This somehow contrasts with the splitting concept driven by slow cavity growth and coalescence.

The splitting process has been also examined on the basis of fracture mechanics concepts [Fre 1997, Yan 2003, Fen 2004]. These authors have used the Stress Intensity Factor (SIF) criterion to calculate conditions of crack propagation sustained by the internal

gas pressure of the cavities [Sih 1973, Kan 1985, Tad 2000]. They have indeed, considered that, once the critical stress at the crack tip (K_{Ic} value) is achieved, the cracks grow in order to relieve the internal pressure, and a continuous supply of gas is required to sustain this process. This characterizes a “**stable**” crack propagation regime. However, the SIF criterion is used to calculate or estimate the stress condition of a crack that once overcome K_{Ic} , leads to “**unstable**” crack propagation (i.e. fast and catastrophic fracture). The misleading occurs because the existent theoretical approaches neglect the effect of **sub-critical growth** or **stress corrosion cracking** (SCC) [Cre 1967, Wie 1970, Gib 1984, Jon 1992, Ard 1999]. Considering the SCC phenomenon, the growth of a crack can easily takes place at sub-critical stress conditions ($K_I < K_{Ic}$), what seems to be the case of H implanted Si. Hence, SCC not necessarily leads to a catastrophic failure, but rather to a slow (stable) growth of the crack. SCC occurs in particular combinations of material and environment and is very sensitive to temperature, chemical species and concentration involved in the process. The chemical role of H in the process is somewhat evident. Even more, when contrasting the following facts:

- H pressurized plate-like cavities easily evolve onto long crack structures.
- He pressurized plate-like cavities (possibly even higher pressurized than the H cavities) instead of evolve into cracks forms smaller spherical bubbles [Fic 1997].

The first effect is clearly related to the chemical action of H on the crack tip, opening the cracks and stabilizing the as formed internal surfaces. Mechanisms of SCC are generally complex and dependent on chemical reactions. Classic examples of SCC can be taken from austenitic stainless steels, aluminum alloys, some ceramics, glasses and polymers in moist air, and also steels in hydrogen containing environments.

1.4 H and He coimplantation and blistering/exfoliation process

In a pioneer study, it was shown that H and He coimplantation produces blistering at a much smaller total fluence than any of the individual elements alone [Aga 1998]. Best results were obtained by implanting first H and then He [Aga 1998]. However, there are controversial reports about the benefits of the implantation order. For very low implantation energies (i.e. below 10 keV), best results are obtained when He is implanted first [Mou 2005b]. The accumulation of implantation damage seems to play an important role which cannot be explained only in terms of ballistic effects. For energies from 30 to 50 keV were

most studies were performed, the accumulated damage seems to be significantly larger (even leading to the formation of amorphous pockets) in samples implanted first with H as compared to the reverse case [Ngu 2005]. In this case, it is argued that, if H is implanted first, the post implantation of He destroys clusters needed to form the blistering/exfoliation precursors. However, the situation is more complex. Experiments considering non-coincident H and He depth profiles report better results when the element to be placed deeper is implanted first [Ngu 2005, Ngu 2007].

In a first approach it is usually considered that, during the implantation, He diffuses and becomes trapped in the hydrogen filled structures, causing the increase of their internal gas pressure and reconverts H_2 molecules into Si-H bonds [Wel 1998]. Figure 1.8 provides a schematic illustration of a plate-like structure formed by the coimplantation of H and He . The role of each gas species can be summarized as: i) the H atoms readily nucleate H -platelets during implantation where individual atoms tend to passivate dangling bonds at the internal surfaces and break Si bonds at the platelet tips. During annealing, H_2 molecules are formed inside the cavity volume and act as pressurizing elements. ii) He atoms tend to segregate into the H -platelets where they are claimed to produce a much more effective pressure by atom [Wel 1998, Duo 2001, Ton 2002].

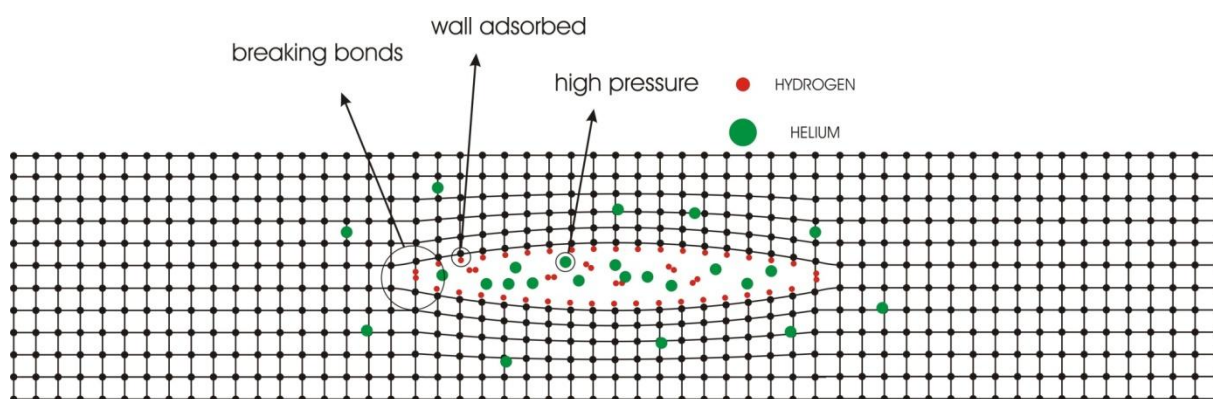


Figure 1.8- Schematic representation of the synergetic effect of $H+He$ implantation.

CHAPTER 2

Experimental Techniques and Methods

2.1 Ion implantation

Ion implantation [Dea 1973] equipments usually consist of an ion source (where ions of a desired element are produced and extracted), an accelerator line (where the ions are electrostatically accelerated to a high energy) and electrostatic and magnetic lenses to guide, focus and scan the ion beam towards the target material placed in a target chamber. Usually, an ion beams consists of a selected ionized atom or molecule specie. The actual amount of material impinging the target is the time integral of the ion current. This is called fluence (Φ) and is expressed in terms of number of ions per square centimeter (ions/cm²). The fluence rate (i.e. current density) $\left(\frac{d\Phi}{dt}\right)$ corresponds to the number of implanted ions per unit area and time and it is expressed in units of microamperes per square centimeter ($\mu A cm^{-2}$). The current densities supplied by ion implanters are typically small (from 0.05 to 5 $\mu A cm^{-2}$). Thus, ion implantation generally finds application in cases where the amount of chemical or physical change required can be performed very effectively by a small amount of implanted atoms. Typical ion energies are in the range from 0.5 keV to several MeV. Energies lower than 0.5 keV generally cause only surface erosion or result in very little implantation or target damage. Smaller energies may fall under the designation of ion beam deposition. The concentration-depth distribution of the implanted ions mostly depends on the ion specie, energy and target composition. The average ion penetration depth is called projected range (R_p) while the ion dispersion around R_p is referred as range straggling (ΔR_p). Under typical circumstances, ion ranges will be between a few nanometers to several micrometers. Therefore, ion implantation is especially useful in cases where the desired chemical or structural changes are near the target surface. Ions gradually lose their energy as they travel through the solid, both from occasional collisions with target atoms (which cause abrupt

energy transfers), and from a mild drag from overlap of electron orbital, which can be regarded as a continuous process. Nowadays, ion trajectories, energy losses or concentration-depth distributions can be quite accurately calculated using simulating software codes such as SRIM (Stopping and Range of Ion in Matter) [SRIM 2008].

Elastic collisions between ion and target atoms can generate a high density of *Frenkel* defects (auto-interstitial - vacancy pairs). The overall damage produced by implantation can be eventually minimized by in situ recombination of vacancies and interstitials (dynamic annealing), basically depending on the mobility of the point defects (e.g. by increasing the target temperature). The remaining point defects and the extra host atoms originate a wide range of extended defects including dislocation loops, stacking faults, point defect clusters or even cavities or precipitates either in as-implanted or after thermal annealing.

Semiconductor doping is perhaps the most common application of ion implantation. However, the technique is also applied for several other purposes including the production of silicon on insulator (SOI) substrates from conventional silicon substrates, as described in Chapter 1. The pictographic schema in Fig. 2.1 illustrates a target material being implanted with accelerated ions. The formation of a localized damaged layer occurs within a depth layer at $R_p \pm \Delta R_p$ determined by the implantation energy E .

The implantations performed in the present work were done in a HVEE 500 kV ion implanter from the Institute of Physics, UFRGS. All the implantations were performed in 7° off the sample surface to minimize ion channeling effects.

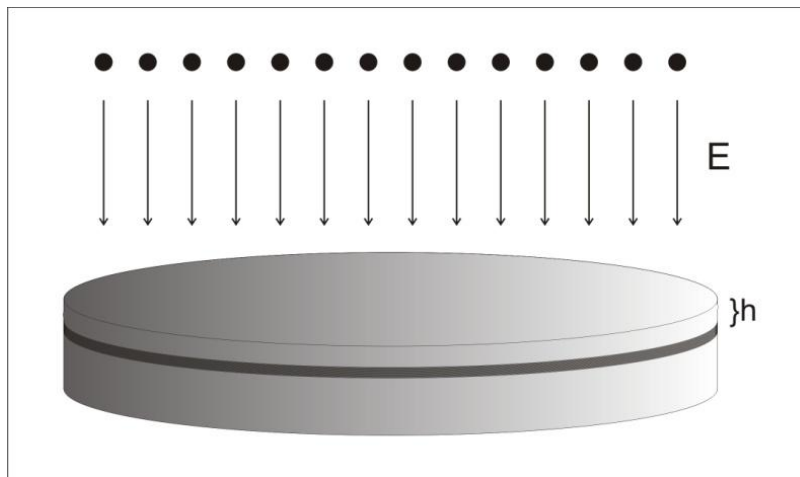


Figure 2.1- Illustration of the implantation process. A buried damaged layer containing the implanted species is formed on the target at a depth h defined by the implantation energy E .

2.2 Plasma immersion

Plasma immersion technique consists basically of a substrate (or “target”) immersed in a plasma atmosphere. Plasma can be generated in a suitably designed vacuum chamber with the help of various plasma sources such as DC glow discharge [Ros 1990]. Since it has not been extensively used in this work, it will not be further described here.

2.3 Thermal annealing

All thermal annealing performed in this work were done using a standard furnace with a temperature stability of $\pm 2^{\circ}\text{C}$, and with samples kept in a quartz tube continuously pumped (turbo molecular pump) under high vacuum conditions.

2.4 Scanning Electron Microscopy (SEM)

Scanning electron microscopes (SEM) [Gol 1992] create images by scanning a focuses a high energy electron beam onto the sample surface. Signals from backscattered, secondary electrons or even x-rays resulting from interactions between the incident electrons and sample atoms are detected and processed to produce the images. Detailed images from the surface topology can be obtained from secondary electrons. SEM images have great depth of field yielding a characteristic three-dimensional appearance useful for understanding surface structures. Most of the SEM images used in this work were obtained in a JSM 5800 microscope from the Electron Microscopy Center (UFRGS).

2.5 Transmission electron microscopy (TEM)

Transmission electron microscopy (TEM) [Ful 2002] is a technique whereby an uniform and coherent beam of energetic electrons are transmitted through a rather thin specimen, interacting with the specimen atoms. These interactions modulate the intensity distribution of the transmitted beam, thus providing information of the sample microstructure which can be recorded as electron diffraction patterns or magnified images. The intensity of the diffraction spots depend on how close the orientation of the crystal planes with respect to

the electron beam satisfies the dynamic or kinematic Bragg conditions. Specimen holders allow specimen tilting in order to obtain specific diffraction conditions, which leads to diffraction or phase contrast imaging processes. High-contrast images are formed when deflected electrons are blocked by placing an aperture that allows only unscattered electrons through. This technique (known as *Bright Field diffraction contrast*) is particularly useful to observe extended lattice defects in an otherwise ordered crystal. Reversely, it is also possible to produce an image using only a specific diffraction reflection by letting this reflection pass through the aperture, thus rendering *Dark Field* images. High resolution (HRTEM) lattice images are obtained by phase contrast conditions, as the interference of several diffraction reflections can be tailored by an appropriate focus of the objective lens. A second type of phase contrast related to the formation of Fresnel fringes is also applied to allow the observation of cavities or small particles.

In the present work, the TEM observations were performed at 200 kV using the JEM 2010 microscope from the Electron Microscopy Center (UFRGS) or the JEM 200 CX from the Physical Metallurgy Laboratory of the University of Poitiers. All TEM specimens characterized were prepared by mechanical polishing and ion milling.

2.6 X-ray diffraction

X-rays are electromagnetic radiation with typical wavelength from 0.01 to 10 nm. For diffraction applications, only short wavelength x-rays (hard x-rays) in the range $0.01 < \lambda < 0.5$ nm are used. Because the wavelength of x-rays is comparable to the interatomic distances, they are ideally suited for probing the structural arrangement of atoms and molecules in a wide range of materials [Cul 1978]. X-rays can penetrate deep into the materials and provide information about the bulk structure, as well as localized defects.

The x-ray scattering follow the Bragg diffraction principles and leads not only to distinct structural information such as crystal structure and phase determination, but also information comprising, e.g., stress distribution, interface roughness or dispersed second phase nano particle mean sizes. Bragg's law can be expressed as

$$2d \sin \theta = n\lambda$$

where λ is the x-ray wavelength, 2θ the scattering angle, and n an integer representing the order of the diffraction peak.

In the present work, strain measurements are of particular interest. In single crystalline implanted (001) Si samples, strain information is accessible by measuring in the direction perpendicular to the sample surface using the 004 reflection. Thus, the recorder signal is characteristic of the lattice strain in the direction normal to the sample surface. A typical diffraction patterns of a single crystalline pristine sample exhibit only a single strong peak. Interplanar strain produces an angular shift of diffracted intensity from that of unperturbed crystal. **Dilatation** of the crystal lattice introduces shifts towards $\theta < \theta_{B004}$ (i.e. left side from the peak). Conversely, **compression** of the crystal lattice introduces shifts towards $\theta > \theta_{B004}$ (right side from the peak). Figure 2.2 shows a typical diffraction pattern obtained for *H*-implanted Si together with an unperturbed (non-implanted) crystal. The figure is expressed in terms of the diffracted intensity as function of the relative strain ($\Delta d/d$), as easily obtained using the Bragg's Law. The scattered intensity resulting from an implanted region exhibits a fringe pattern with varying fringe spacing. This behavior reveals a normal dilatation strain gradient in the implanted region. The fringes result from the coherent interference between two zones of same strain on either side of the damaged zone. Therefore, the periodicity of the fringes depends on the width of the strain profile, being the fringe space inversely proportional to the width between zones with the same strain. The width between two zones of same low strain (near to 004 reflection peak) is clearly higher than for the region of maximum strain (far from 004 reflection peak). For *H*-implanted Si, the strain profile is likely to be roughly proportional to the host atoms concentration and could be approximated by a Gaussian shaped profile [Sou 2006].

More than variations in the interspacing of lattice planes, the evolution of localized implantation related defects may cause strong displacements of individual atoms from their sites on the diffractive planes. This displacement lowers the diffraction intensity of the referred planes. This phenomenon is described by the static Debye-Waller factor which presents a strong dependence on the type and size of defects [Ded 1973]. In the present work, the X-ray measurements were performed in the Physical Metallurgy Laboratory of the University of Poitiers using a 5 kW Rigaku RU 200 generator with a copper rotating anode with the principal characteristic ray $\lambda_{CuK\alpha 1} = 1.5405 \text{ \AA}$.

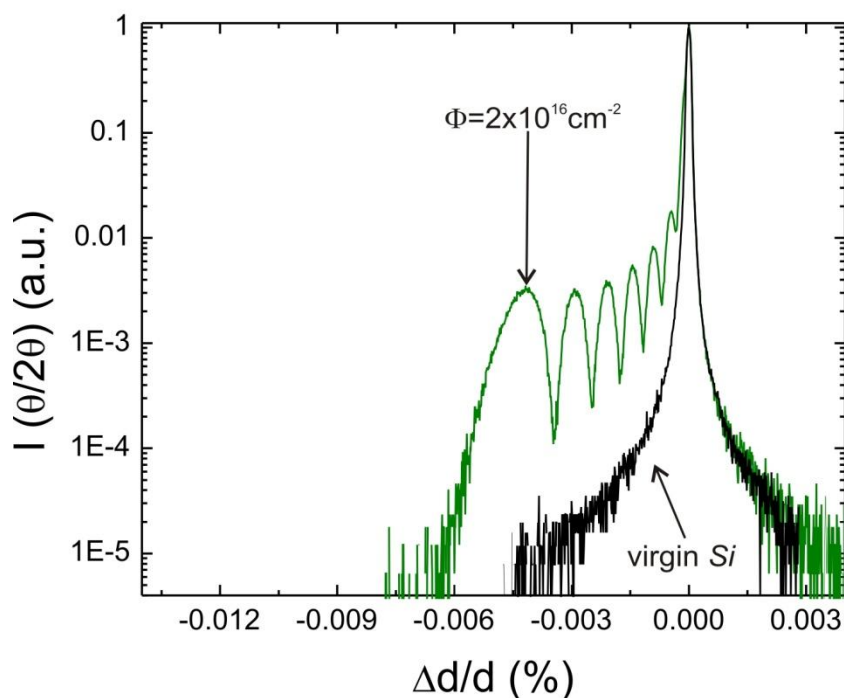


Figure 2.2- XRD scattering of an H-implanted Si ($2 \times 10^{16} \text{ cm}^{-2}$) together with a virgin sample.

2.7 Glancing Illumination Optical Microscopy (GIOM)

Glancing angle illumination [Chr 2006] in optical microscopy observations is a common metallographic technique. It is generally employed to observe beach marks and ratchet marks in fatigue fractures, chevron marks and radiating lines in brittle fractures, corrosion pits on smooth surfaces, and other topographic features. In this work, GIOM observations were performed by rotating the specimens with respect to the light source, using a standard optical microscope equipped with a CCD camera.

2.8 Atomic Force Microscopy (AFM)

Atomic force microscopy (AFM) is a method of measuring surface topography on a scale from angstroms to 100 microns. The technique involves imaging a sample through the

use of a probe, or tip, with a radius of 20 nm. The tip is held several nanometers above the surface using a feedback mechanism that measures surface–tip interactions. Variations in tip height are recorded while the tip is scanned repeatedly across the sample, producing a topographic image of the surface. In addition, the AFM instruments are generally able of producing images in a number of other modes, including tapping, magnetic force, electrical force, and pulsed force. In this work the images were obtained in the tapping mode using the AFM DI SPM IIIa equipment from the Physics Institute (UFRGS).

2.9 Material

All the samples used in the present study were p-type 1-20 Ω (001) CZ-Si wafers, chemically cleaned by RCA method.

CHAPTER 3

Effects of the Implantation Fluence, Implantation Energy and Thermal Annealing Protocol on the Exfoliation Phenomena:

“Macro-mechanism of Exfoliation”

This chapter presents a systematical investigation relating the influence of implantation fluence, implantation energy and thermal annealing protocol on the exfoliation macro-mechanisms for a $2H:1He$ implanted ratio. The experimental parameters and statistical methods are first described and then the results are presented and discussed. A careful characterization of exfoliated areas was performed by SEM. This data was used to conduct statistical analysis of exfoliated structures, comprising their mean sizes and number concentration. Distinct exfoliation macro-mechanisms are proposed for low and high implantation fluences and discussed in terms of a phenomenological model.

3.1. Implantation parameters, thermal annealing protocols and data evaluation methodology

3.1.1. Implantation fluence (Φ)

The implanted fluences were adjusted to provide a ratio of $2H:1He$. The fluence range was experimentally defined within a lower limit (smaller implanted fluence), characterized by the complete absence of exfoliation, and an upper limit, characterized by a reduction of more than 60% from the maximum exfoliation efficiency, as defined in section 3.1.5. Two energy cases are considered (see section 3.1.3). For both, the fluence range extends approximately from 1 to $7.5 \times 10^{16} \text{ cm}^{-2}$.

3.1.2. Order of implantation and current density

All the implantations were performed with targets kept at room temperature. H_2^+ ions were implanted first, followed by He^+ ones. Both ion species were implanted at low current density (I_c), comprised between 0.25 and $0.5 \mu\text{A cm}^{-2}$.

3.1.3. Implantation energy

The implantation energies were designed to define "**high energy**" (H_E) and "**low energy**" (L_E) cases. The H_E corresponds to 336 keV for H_2^+ and 345 keV for He^+ , providing coincident projected range values at $\approx 1.5 \mu\text{m}$. The L_E corresponds to 60 keV for H_2^+ and 33 keV for He^+ , and was calculated to provide projected ranges of $\approx 300 \text{ nm}$. The simulated profiles for both energies were calculated using the SRIM code [Zie 1985], as shown in Fig. 3.1.

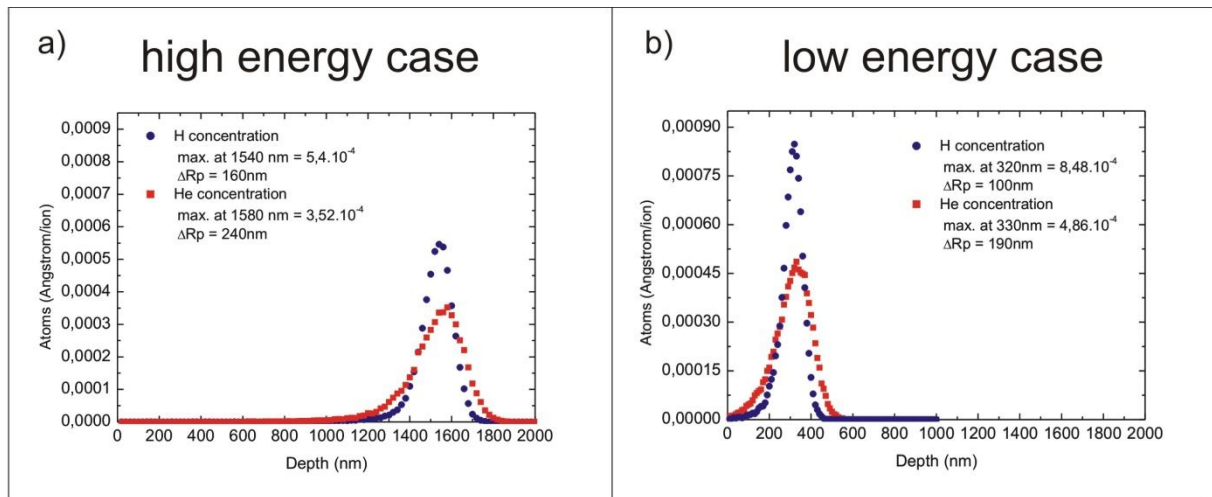


Figure 3.1- Simulated profiles of concentrations versus depth for (a) 168keV H^+ and 345keV He^+ and (b) 30 keV H^+ and 33keV He^+ obtained using SRIM simulation code.

3.1.4. Thermal Annealing Protocols

Two protocols were chosen to study the influence of the annealing conditions on the exfoliation behavior.

Protocol 1 (annealing at 700°C 1800s)

The annealing protocol 1 conducts the samples directly to blistering/exfoliation temperatures ($T \geq 400^\circ\text{C}$). Its duration of 1800s is sufficient to allow maximum blister/exfoliation efficiencies within each situation. This was verified by evaluating the exfoliation efficiency of controlled samples submitted to longer annealing times (3600s and 5400s), where no significant differences were found.

Protocol 2 (annealing at 350°C 1800s + 700°C 1800s)

The annealing protocol 2 consists of two steps. The first step, at 350°C for 1800s, is referred as "pre-annealing", since samples are annealed at a temperature below the exfoliation appearance. The samples are then brought to room temperature and submitted to the second annealing step at 700°C for 1800s. The objective of protocol 2 is to provide a higher thermal budget on the sample.

3.1.5. Evaluation methods

The exfoliation behavior was evaluated as a function of the total implanted fluence and annealing protocol for each energy case. Three parameters were introduced to quantify the exfoliation: i) the exfoliation efficiency A_{ex} ; ii) the mean exfoliation area S_{ex} (also referred as exfoliation size) and; iii) the exfoliation density D_{ex} .

The exfoliation efficiency is defined as

$$A_{ex} \% = \frac{A_{ex}^{total}}{A_{sample}^{total}} \cdot 100 \quad (3.1)$$

where A_{ex}^{total} is the total exfoliated area obtained by the sum of the individual exfoliated areas and A_{sample}^{total} is the total area of the image.

The mean individual exfoliation area S_{ex} is determined by the relation

$$S_{ex} = \frac{A_{ex}^{total}}{N_{ex}} \quad (3.2)$$

where N_{ex} is the total number of individual exfoliations measured in the image.

The exfoliation density D_{ex} is defined as the number of individual exfoliations per area and calculated as:

$$D_{ex} = \frac{N_{ex}}{A_{sample}^{total}} \quad (3.3)$$

These parameters were evaluated from SEM images. The process was conducted considering several hundred particles for each sample. The measurements of exfoliation areas were performed using the "Image Tool" code [Wil 2002] and the data were statistically evaluated using the "Origin 6" code.

3.2. Results for the 2H:1He fluence ratio

3.2.1. High energy case

Figure 3.2 presents SEM observations of blistering/exfoliation regions for samples implanted at high energy (H_E). Figures 3.2a, b, c and d, were obtained from samples submitted to the annealing protocol 1 (700°C). Figures 3.2e, f, g and h, were obtained from samples submitted to the annealing protocol 2 (350°C + 700°C). Modifications in exfoliation sizes and densities are evident (as function of fluence but not of protocol). Figure 3.3 shows the exfoliation efficiency A_{ex} behavior as a function of fluence for both annealing protocols. The dotted lines provide a guideline for the eyes.

The curves show the same trend for both protocols. At low fluences ($\Phi \leq 1.5 \times 10^{16} \text{cm}^{-2}$) no exfoliation is observed. Exfoliation can be detected within a threshold range of $\Phi = 1.5 - 2.25 \times 10^{16} \text{cm}^{-2}$. The values of A_{ex} abruptly increase from the threshold fluence up to a maximum around 22% A_{ex} for $\Phi = 3 \times 10^{16} \text{cm}^{-2}$, and then gradually decrease.

Figure 3.4 presents the variation of the individual exfoliation mean size, S_{ex} , as a function of the fluence for both annealing protocols. Similarly to A_{ex} , S_{ex} seems roughly independent of the annealing protocol. At $\Phi = 2.25 \times 10^{16} \text{cm}^{-2}$, large exfoliation mean sizes S_{ex} of $\approx 950 \mu\text{m}^2$ arise. With increasing fluence, S_{ex} increases and reaches values of $\approx 1500 \mu\text{m}^2$ at $\Phi = 3 \times 10^{16} \text{cm}^{-2}$. For higher fluences, S_{ex} decreases. A reduction of $\approx 90\%$ from the maximum value, S_{Max} , is observed for $\Phi = 7.5 \times 10^{16} \text{cm}^{-2}$.

Figure 3.5 shows the exfoliation density D_{ex} behavior for both annealing protocols. Starting from the threshold fluence, D_{ex} first slightly decreases and then increases again. The minimum D_{ex} value occurs at the fluence where maximum A_{ex} and S_{ex} values are observed.

High energy

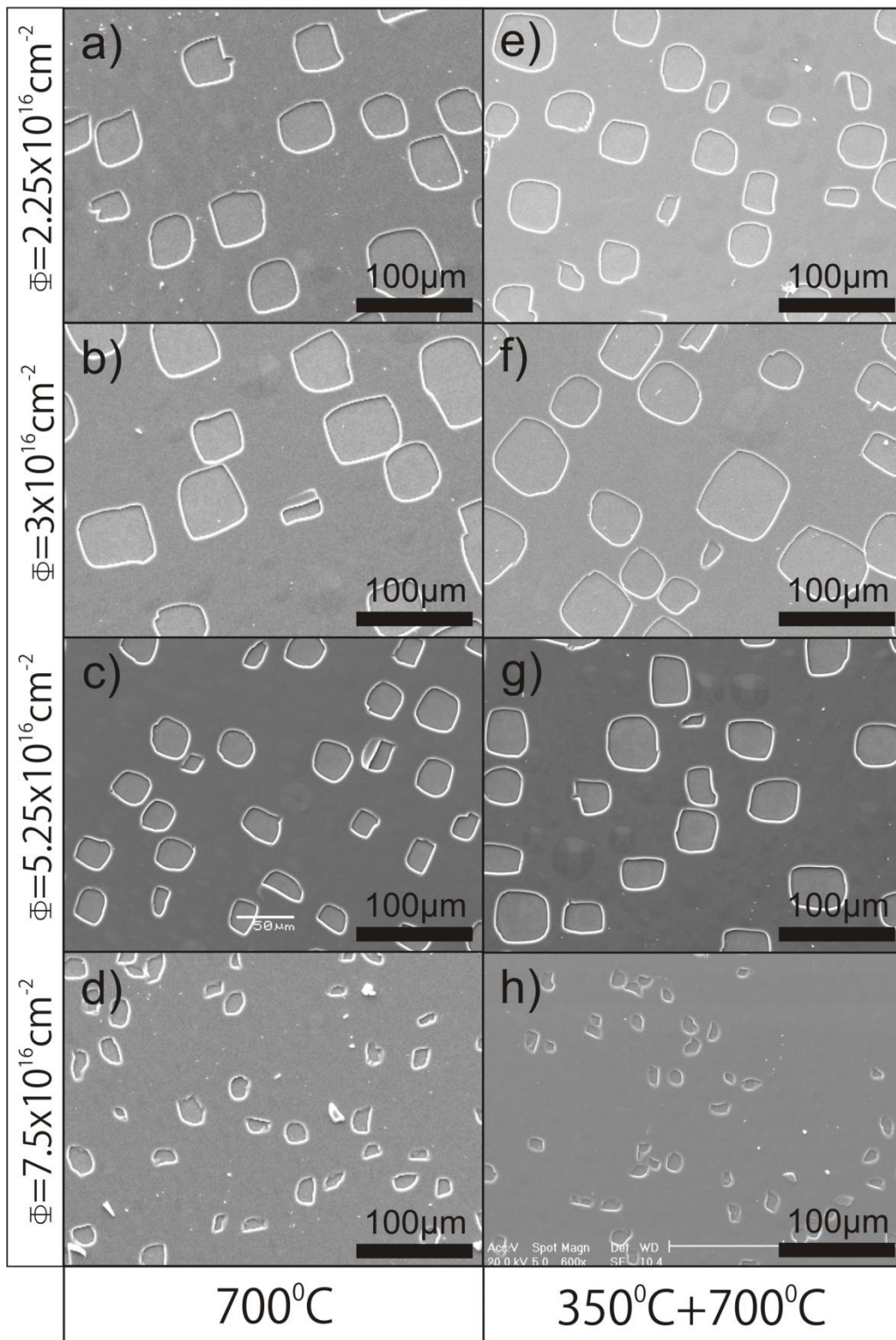


Figure 3.2- SEM images of the sample surface showing general views of the exfoliation in the H_E case as function of the fluence and for the two annealing protocols. Protocol 1: (a), (b),(c) and (d). Protocol 2: (e), (f),(g) and (h).

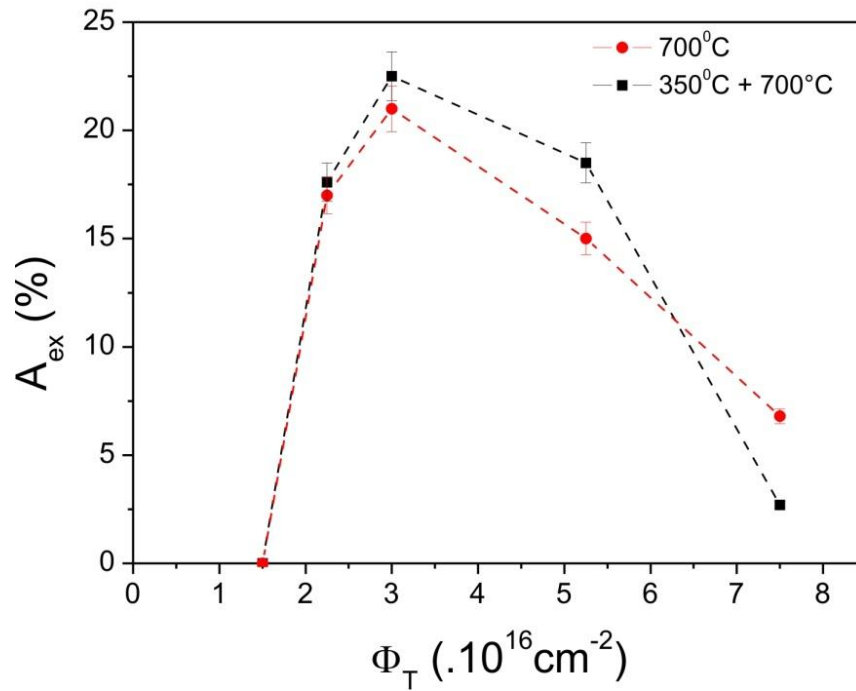


Figure 3.3- Exfoliation efficiency A_{ex} plotted as a function of the fluence in the H_E cases for both annealing protocols. The dotted lines provide a guideline for the eyes.

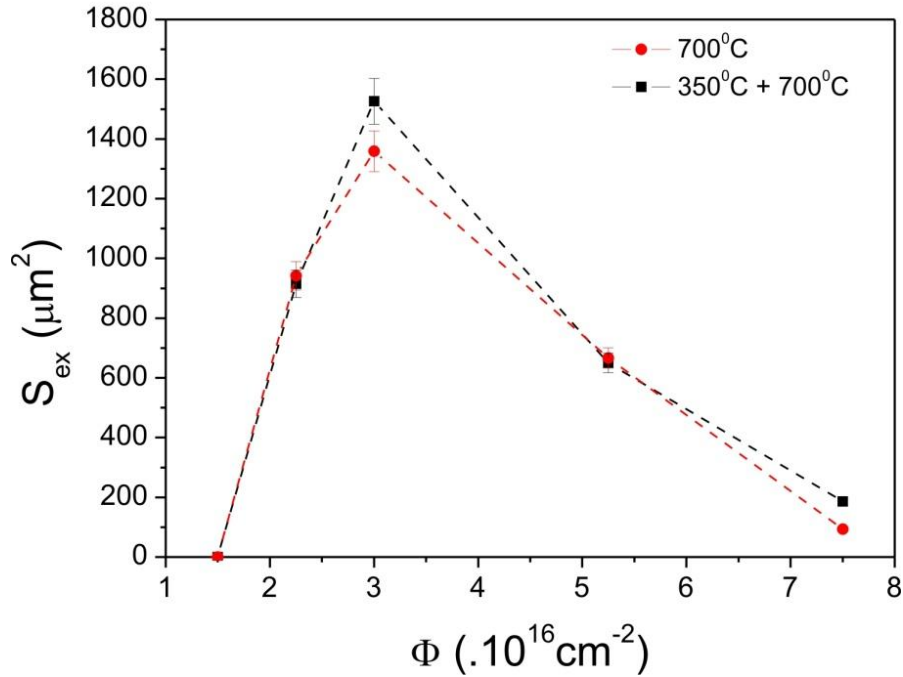


Figure 3.4- The exfoliation mean size S_{ex} plotted as function of the fluence Φ for the L_E case and both annealing protocols. The dotted lines provide a guideline for the eyes.

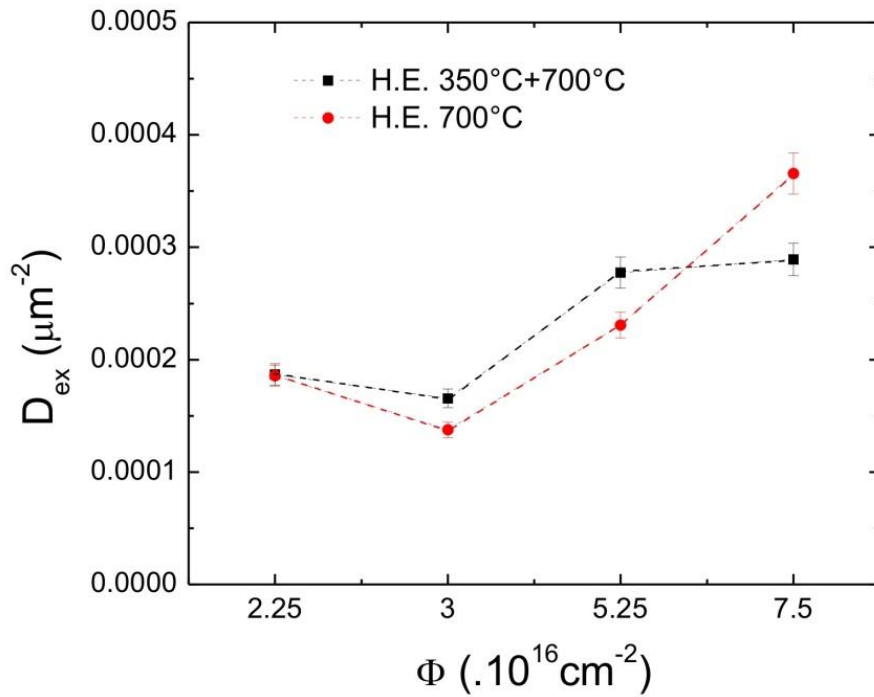


Figure 3.5- The density of exfoliation D_{ex} plotted as function of the fluence Φ for the H_E case and both annealing protocols.

3.2.2. Low energy case

Figure 3.6 shows characteristic blistering/exfoliation morphologies for samples implanted at low energy (L_E) and submitted to both annealing protocols. Only three fluences were studied for the annealing protocol 1 (700°C). Similarly to the H_E case, the images clearly show modifications on exfoliation sizes and density as a function of both the fluence and the protocol used (compare Fig. 3.6b and Fig. 3.6e).

In Fig. 3.7, the exfoliation efficiency A_{ex} values are plotted as function of the fluence for both annealing protocols. Independently of the annealing protocol, exfoliation starts abruptly for fluences in the range $\Phi=1-1.5 \cdot 10^{16} \text{ cm}^{-2}$. The two curves show a different behavior. For the annealing protocol 1, the A_{ex} values are about twice lower than for protocol 2 and tend to saturate. For the annealing protocol 2, the A_{ex} values rapidly increase to a maximum at $\Phi=2.25 \cdot 10^{16} \text{ cm}^{-2}$ and then gradually decrease attaining the same level of the samples annealed using protocol 1 at $\Phi=7.5 \cdot 10^{16} \text{ cm}^{-2}$. In this latter case, the trend of the curve is similar to those reported for the H_E case, but the efficiency values are considerably smaller.

Low energy

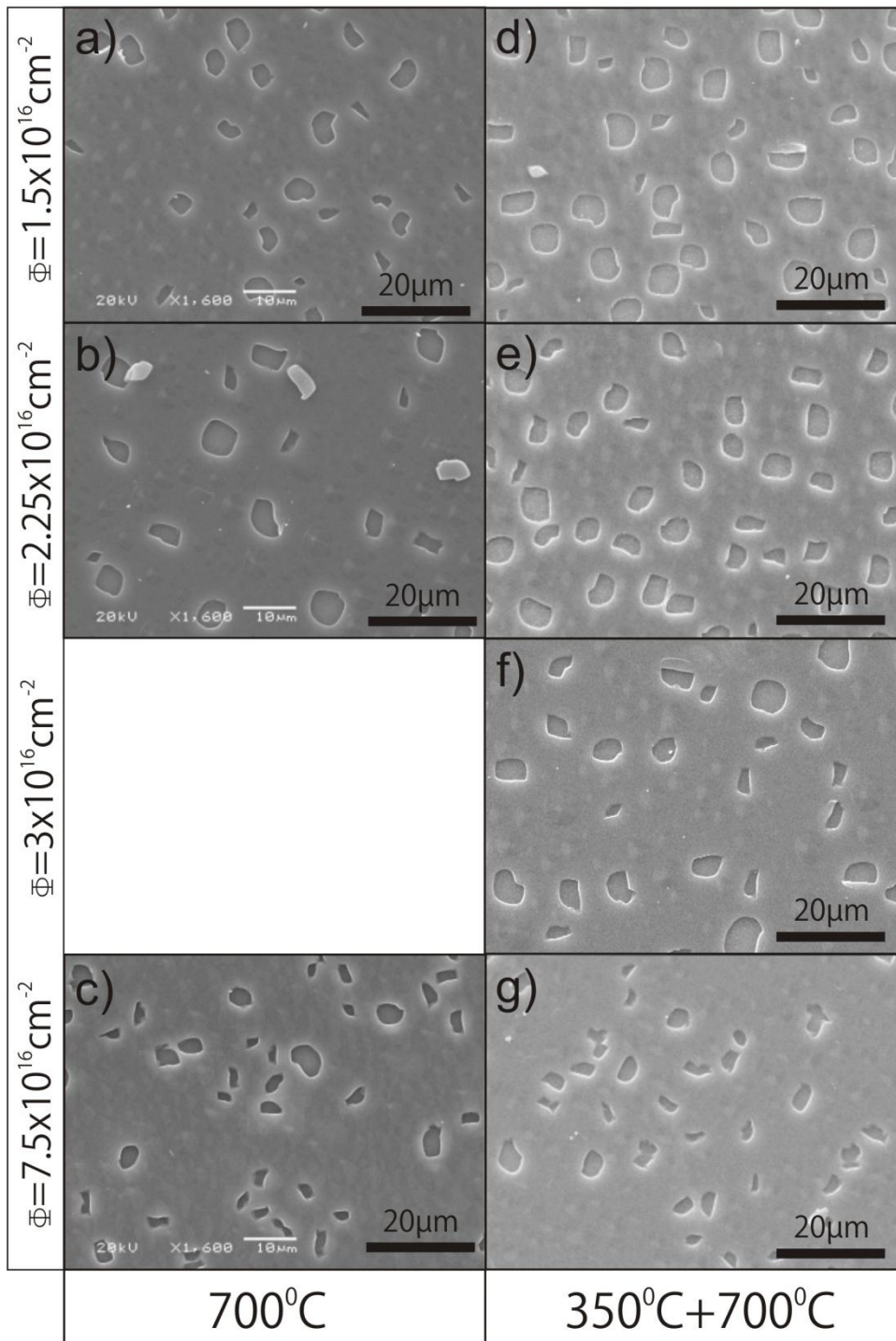


Figure 3.6- SEM images of the sample surface showing general views of the exfoliation in the L_E case as function of the fluence and for the two annealing protocols. Protocol 1: (a), (b) and (c). Protocol 2: (d), (e),(f) and (g).

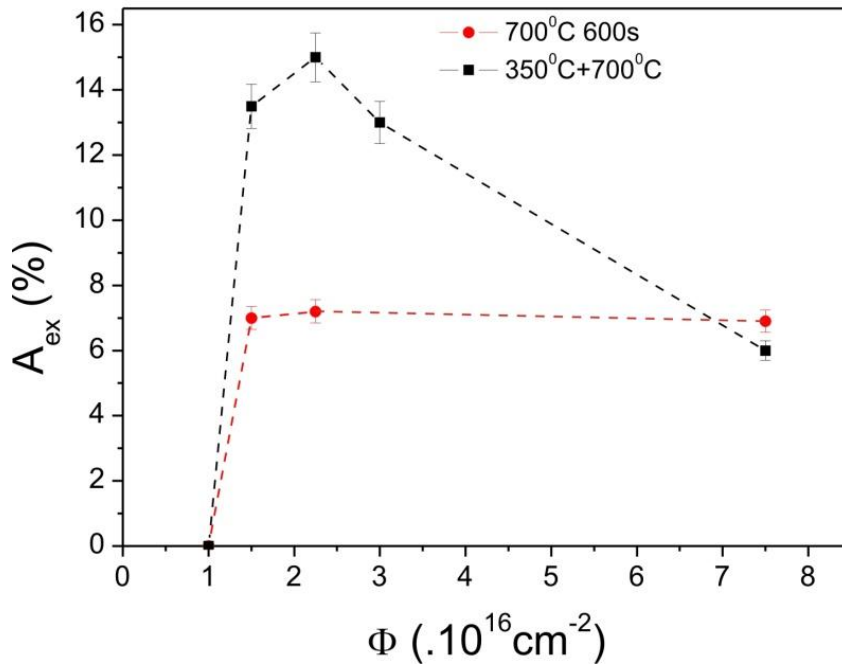


Figure 3.7- Exfoliation efficiency plotted as function of the implanted fluence Φ for the L_E case and both annealing protocols.

The annealing protocol does not affect the S_{ex} behavior as a function of fluence, as shown in Fig. 3.8. For both protocols, the maximum S_{ex} value corresponds to $\approx 15 \mu\text{m}^2$ and occurs for $\Phi=2.25 \times 10^{16} \text{ cm}^{-2}$, and then the values gradually decrease.

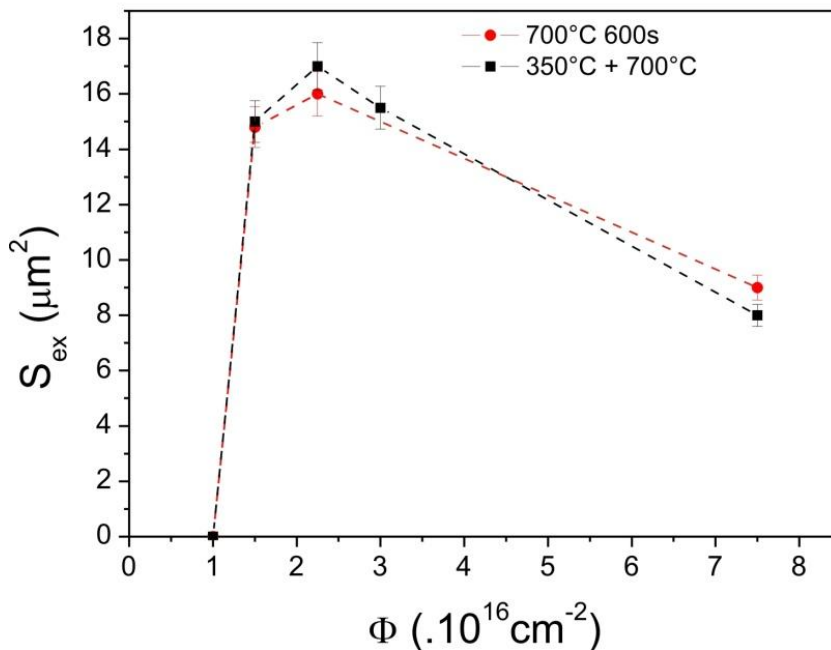


Figure 3.8- Mean size S_{ex} as a function of the implanted fluence Φ for the L_E case and both annealing protocols.

Figure 3.9 shows the D_{ex} versus fluence behavior for both annealing protocols. The curves show a different tendency. For the protocol 2, D_{ex} slightly decreases with increasing fluence, whereas the opposite behavior occurs for the annealing protocol 1. Both curves converge toward the same value for high fluences.

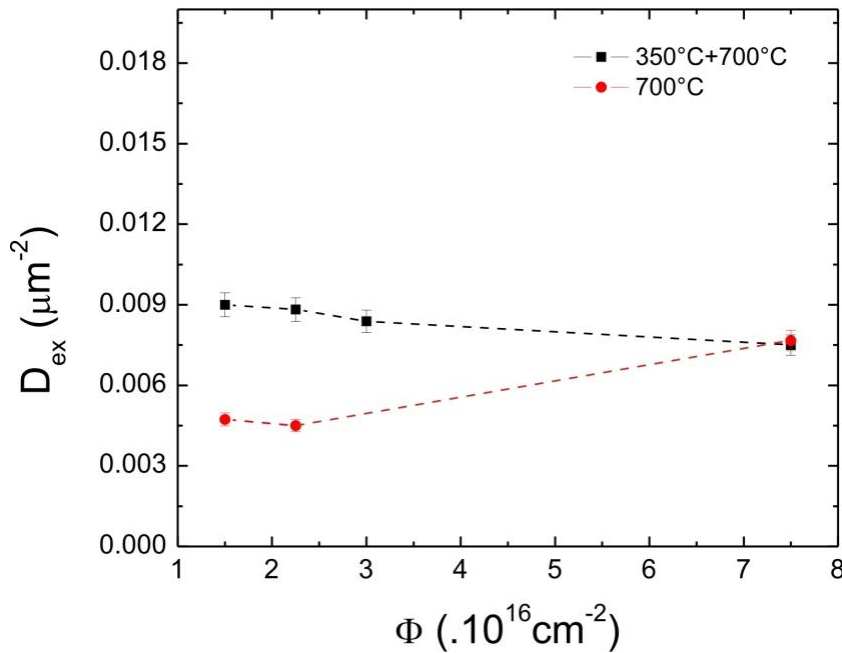


Figure 3.9- Exfoliation density D_{ex} plotted as a function of the implanted fluence Φ for the L_E case and both annealing protocols.

3.2.3. Summary of the results

The overall results can be summarized as follows:

i) S_{ex} behavior is independent of the annealing protocol, but strongly depends on the implantation energy and fluence. It increases with energy and present large values for low and medium fluences and small values for high fluences.

ii) A_{ex} strongly depends on the implanted fluence and energy. For the H_E case, it presents slight variations with the annealing protocol. In contrast, for the L_E case, a significant dependence on the annealing protocol is observed.

iii) Exfoliation is a threshold phenomenon with a minimum characteristic exfoliation S_{ex} and A_{ex} , both dependent on the incident energy. An abrupt increase of exfoliation S_{ex} and A_{ex} is observed after the threshold limit.

iv) The exfoliation also presents an upper fluence limit for S_{ex} and A_{ex} . However, this limit is not as well defined (abrupt) as the lower threshold limit.

After a maximum, S_{ex} and A_{ex} decrease slowly as illustrated schematically in Fig. 3.10.

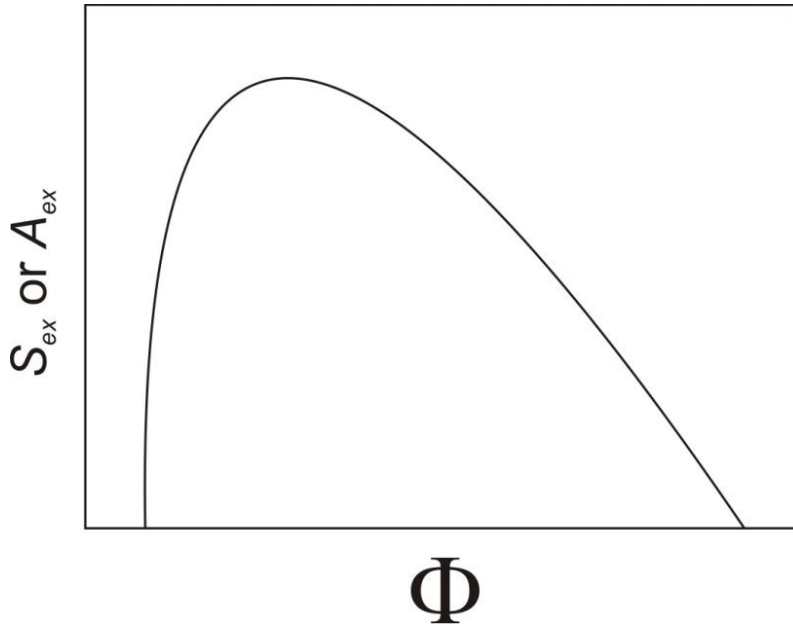


Figure 3.10- Schematic representation of the general trend found for the exfoliation behavior. A sharp increase at the threshold fluence and, after a maximum, it gradually decreases to reach very low values.

- v) The D_{ex} values do not depend on the annealing protocols for the H_E case. The fluence at which the minimum density value is observed corresponds to the fluence where the maximum A_{ex} and S_{ex} values occur. The D_{ex} values for the L_E case are about a factor of 10 larger than for the H_E case. Their behavior in terms of Φ and annealing protocol are quite distinct.

3.3. Discussions

In the following, the exfoliation results are analyzed and discussed in order to provide a general insight into their behavior.

3.3.1. A_{ex} dependence on the implanted fluence

3.3.1.1. The fluence window for exfoliation

Figure 3.11 shows the A_{ex} data obtained after the annealing protocol 2 for both energy cases. The curves clearly characterize fluence intervals where exfoliation is rather efficient (see arrows). The appearance of such "window behavior" seems independent from both the annealing protocol and energy. The observed efficiency window enlarges with increasing energy.

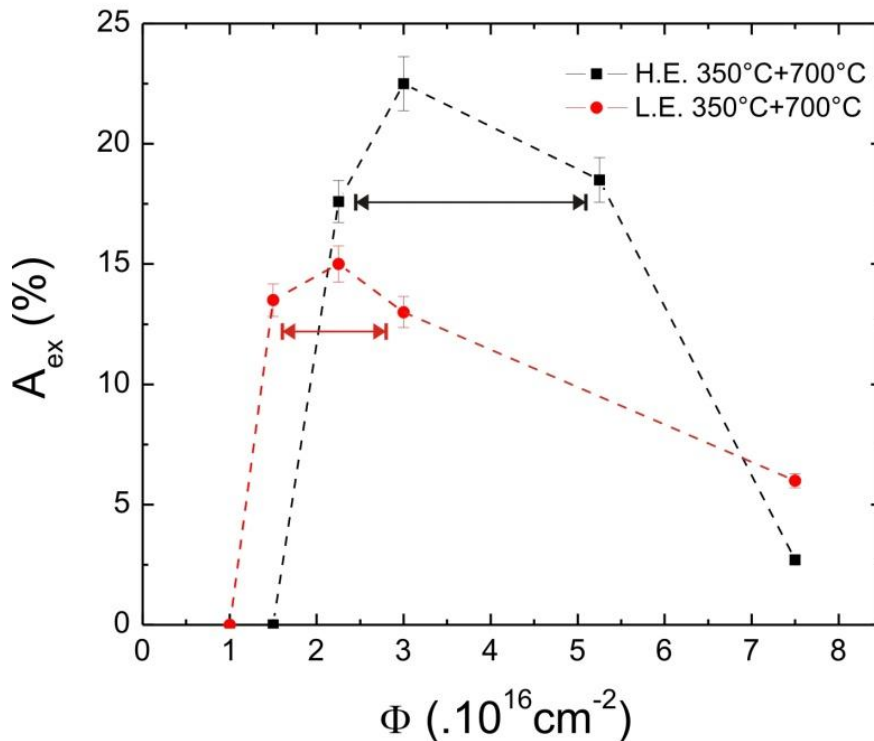


Figure 3.11- Exfoliation efficiency A_{ex} plotted as function of the implanted fluence Φ for both energy cases and annealing protocol 2.

The process of exfoliation suddenly starts at a given fluence. This represents a threshold phenomenon. The curves in Fig. 3.11 exhibit rather sharp threshold fluence intervals and indicate that higher implantation energies require higher fluences to trigger

the process. The threshold fluence for the H_E case is $\approx 50\%$ higher than the one for the L_E case. This behavior seems to be related with the implanted ion distribution. In particular, the straggling of the concentration-depth distribution increases with the implantation energy. Figure 3.12 shows the simulated profiles of the total implanted species ($H+He$) for both energy cases. The curves were obtained adding the individual simulated profiles calculated by the SRIM code [Zie 1985].

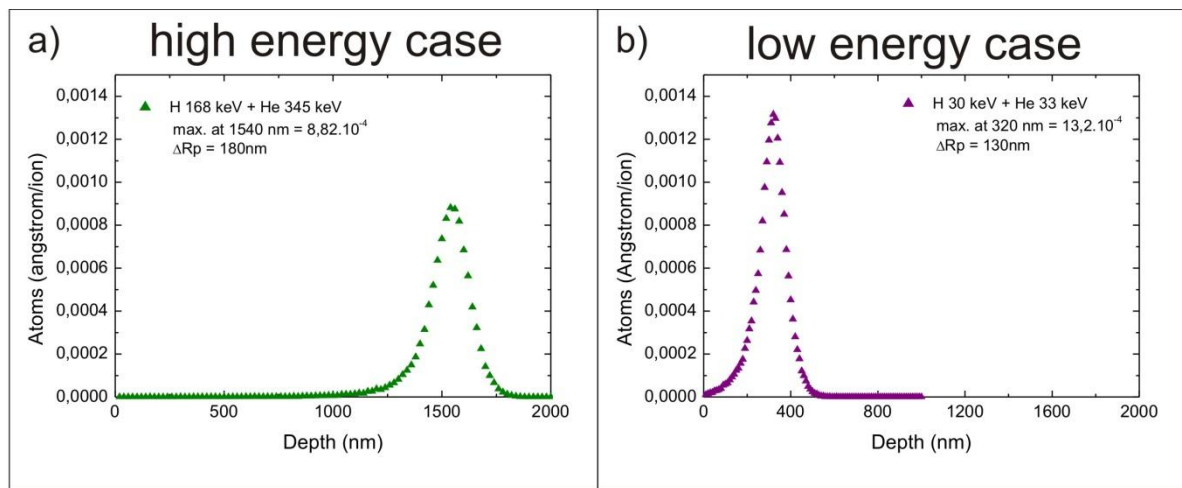


Figure 3.12- The simulated concentration profiles of the total implanted species ($H+He$) for (a) H_E and (b) L_E case.

The simulated profile for H_E has a peak concentration value $\approx 30\%$ smaller and a $\approx 40\%$ wider straggling than the corresponding one for L_E .

Considering the threshold fluences $\Phi = 2.25 \times 10^{16} \text{ cm}^{-2}$ for H_E and $\Phi = 1.5 \times 10^{16} \text{ cm}^{-2}$ for L_E , the calculated peak concentrations render very close values (2,14at.% for H_E and 2,16at.% for L_E). This result suggests that the exfoliation threshold is somehow correlated to a minimum peak concentration of gas atoms. It is probably related to the required concentration to form the precursor defects leading to *exfoliation efficient* cavities. The higher A_{ex} value observed for H_E can be obviously attributed to the higher amount of implant gas. For comparison, the threshold blistering fluence for only H implanted Si samples renders a peak concentration about 3,5at.% for implantation energies of 30keV. This value increases with energy reaching $\approx 5\text{at.}\%$ for $\approx 100\text{keV}$ [Ter 2007]. The same tendency is not observed for the exfoliation behavior observed from co-implanted samples. In our work, the peak

concentration at the threshold exfoliation fluence stays approximately constant around 2% as observed for rather broad energy limits (≈ 30 and 350 keV). This result corroborates and quantifies the reduction in total implantation fluence observed for the co-implantation process as compared to the single H implantation [Aga 1998]. We remark that we have compared our values from exfoliation experiments with literature results from blistering observations. Hence, the total fluence reduction effect quoted here is certainly underestimated, since the concentration of gas to produce exfoliation is certainly higher than that for blistering [Ter 2007].

The A_{ex} curves clearly present a maximum value from where an increase of fluence brings a detrimental result in exfoliation efficiency. Differently to the “**sharp increase**” observed right after the threshold limit, the upper fluence limit of the efficiency window is not so well defined, and microstructure modification effects may explain the “**gradual decrease**” of the curve. Such microstructure modifications will be discussed in more detail in Chapter 4.

Finally, comparing A_{ex} , S_{ex} and D_{ex} values (see Figs. 3.3, 3.4 and 3.5 for H_E and Figs. 3.7, 3.8 and 3.9 for L_E) we observe that, for H_E curves, A_{ex} is directly proportional to S_{ex} and inversely proportional to D_{ex} . On the other hand, D_{ex} is roughly constant for L_E . This indicates that the S_{ex} values determines the A_{ex} ones, leading to the conclusion that the considerably reduction of the exfoliation efficiency for high fluence is ultimately related to the reduction of the S_{ex} values.

3.3.1.2. A_{ex} dependence on the implantation energy

Figure 3.11 shows that, for a given fluence, the H_E case presents higher A_{ex} values. However, the calculated concentration of $H+He$ atoms for $\Phi=2.25 \times 10^{16} \text{ cm}^{-2}$ renders a peak concentration of 2.14 at% for the H_E case, and 3.25 at% for the L_E case. Moreover, the L_E sample has not only a higher peak concentration but also a narrower range straggling (roughly 60% narrower). Peak concentration arguments were already invoked to explain the threshold fluence and its displacement with the energy. However, at this point, we cannot provide a consistent explanation for the observed A_{ex} dependence on implantation energy. Several features may play an important role in this phenomenon. For example, the retained

He concentration may depend on the distance from the surface, particularly for energies smaller than 40 keV [Mor 2004]. In addition, specific defect formation features may also influence the A_{ex} behavior and will be considered in more detailed in Chapter 4.

3.3.1.3. Mean size of individual exfoliation areas S_{ex} and exfoliation morphology

S_{ex} is rather independent of the annealing protocol, varies within a factor of ≈ 2 for the L_E case and ≈ 10 for the H_E one, and significantly with the implantation energy or depth h ($h=300\text{ nm}$ for L_E and $h=1500\text{ nm}$ for H_E). Figure 3.13 shows the S_{ex} behavior as a function of fluence for both energy cases (notice the different vertical scale for each case). Differences up to a factor of 10^2 can be observed for fluences close to the maximum peak values of the curves.

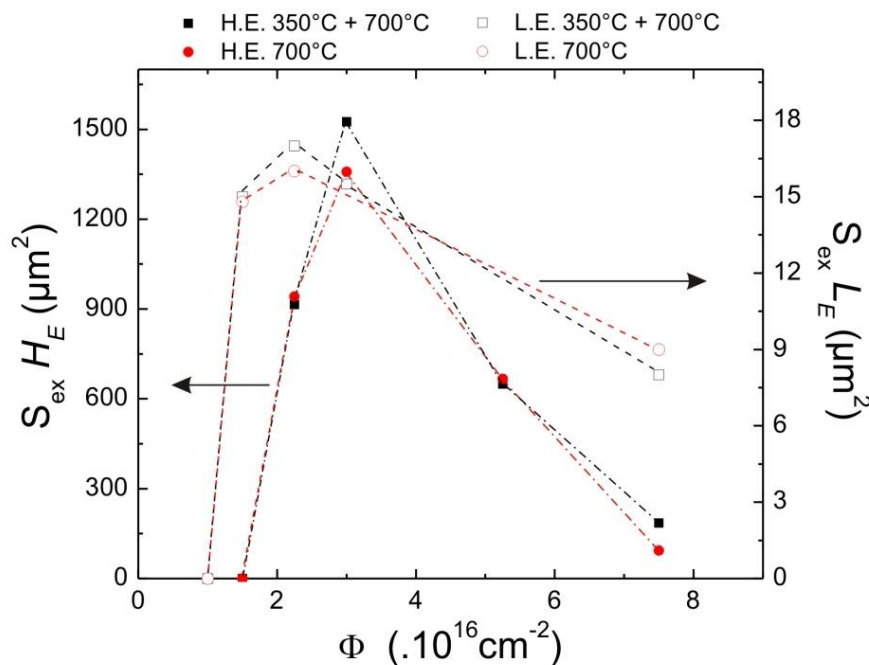


Figure 3.13- (a) Mean exfoliation area S_{ex} plotted as function of the fluence Φ for both implantation energies and annealing protocols.

A detailed SEM investigation was carried out and revealed some interesting aspects. Figures 3.14a and c show low magnified images of the H_E implanted samples for medium and high fluences respectively. Figure 3.14b reveals morphological details such as circular features contrast at the bottom of the exfoliated area. The typical radius of these circular marks ranges from ≈ 3 to $10\ \mu\text{m}$ and cover typically 40% of the local exfoliated area. The

circular form is probably related to pressurized plate-like cavity structures. With increasing fluence, Fig. 3.14d shows exfoliated regions with smaller sizes without distinguished features inside. It seems also important to remark that the circular areas observed for the medium fluence case have similar dimensions as a single exfoliated area observed from the high fluence case. The same behavior is observed for the L_E cases, as shown in the Fig. 3.15. These observations suggest that the circular marks observed for medium fluences are reminiscent features of the same kind of defect that originates a single exfoliation in the high fluence samples.

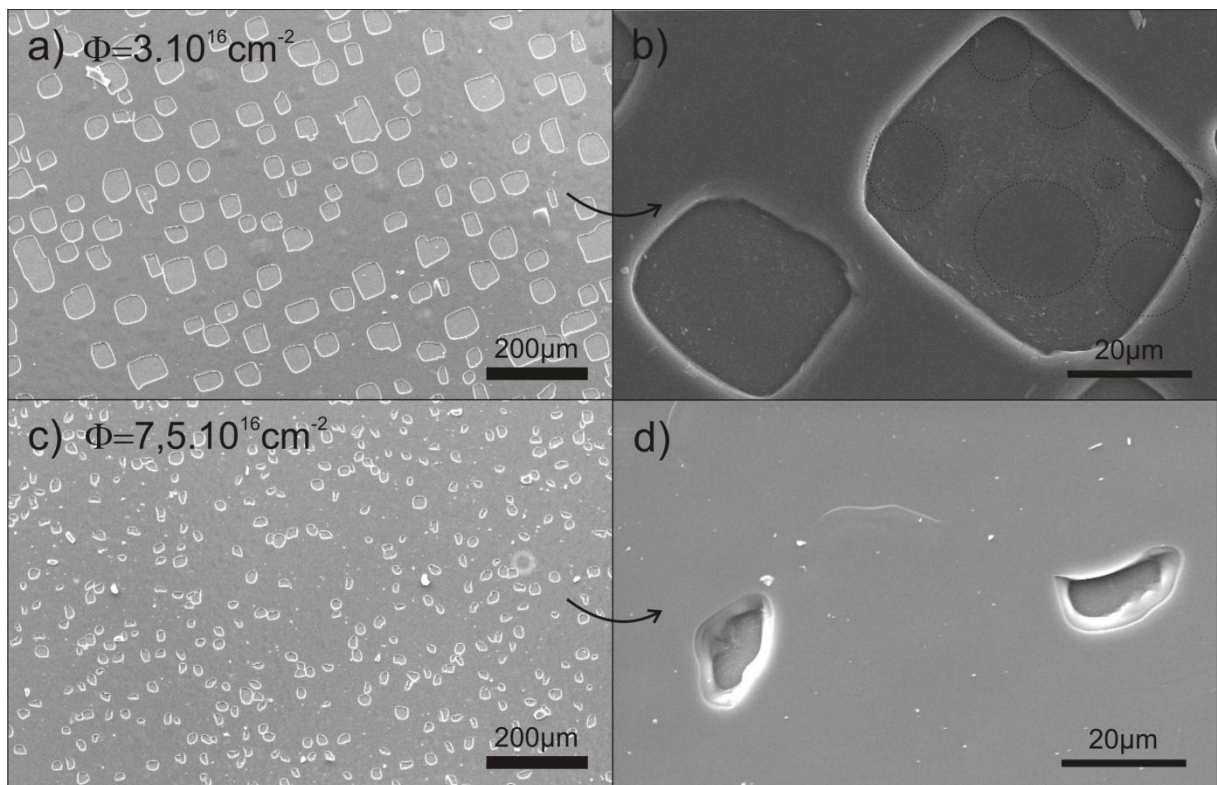


Figure 3.14- (a) and (c) are SEM images showing typical exfoliated areas of the H_E implanted samples at medium and high fluences respectively. Figures (b) and (d) reveal the detailed morphology of the individual areas for each fluence case. The samples are referent to the annealing protocol 1, but the same features are observed also for samples annealed using the protocol 2.

The exfoliation morphology also changes with the fluence (compare, e.g., Fig. 3.14b with d). At low and medium fluences, the lateral walls of the exfoliated areas are rather straight and follow the usual cleavage plans of the silicon lattice; square-like exfoliation

morphology is observed. The high fluence implanted samples shown in Figs. 3.14d and 3.15d display rather irregular lateral walls.

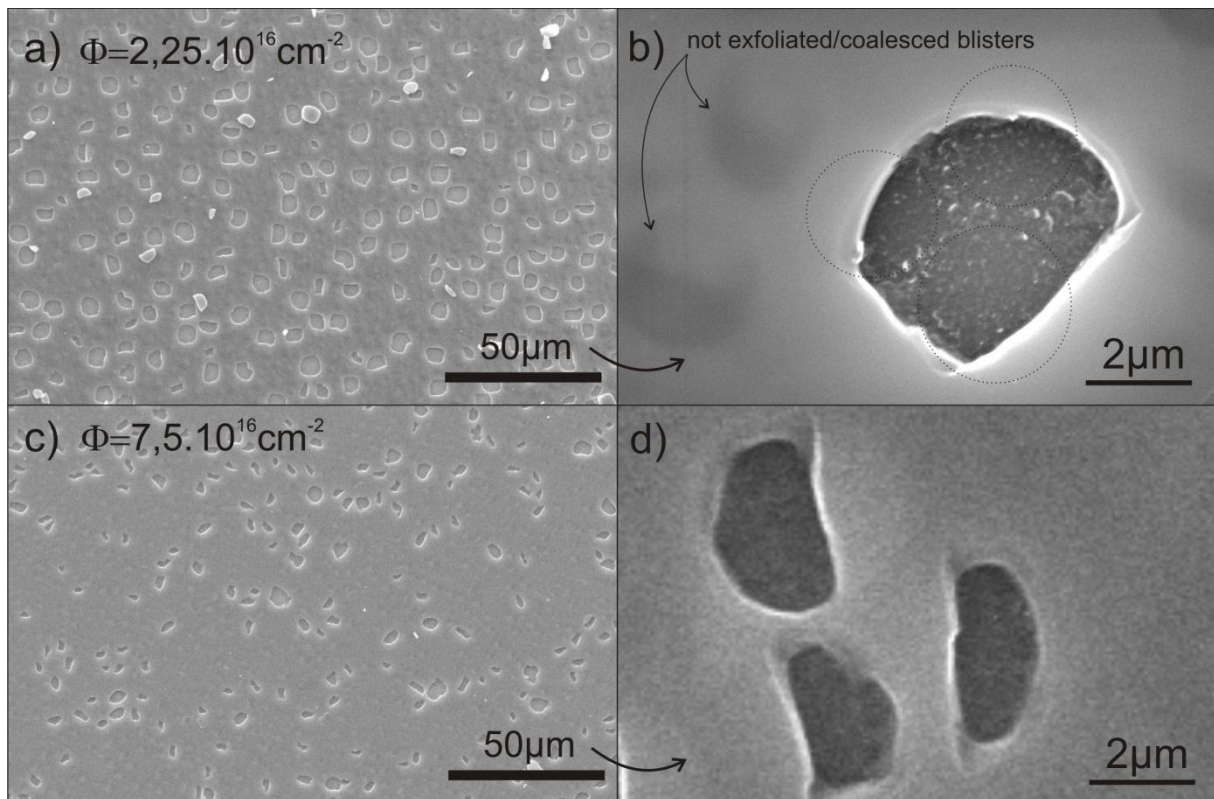


Figure 3.15- (a) and (c) are SEM images showing typical exfoliated areas of the L_E implanted samples at medium and high fluences respectively. Figures (b) and (d) reveal the detailed morphology of the individual areas for each fluence case. The samples are referent to the annealing protocol 1, but the same features are also observed also for samples annealed using the protocol 2.

The whole scenario described above suggests that high internal gas pressure has literally “exploded” the blister caps for the high fluence cases. For the low and medium fluence cases, however, the situation is different. The gas pressure in the individual circular blisters was not sufficient to “explode” their cap. Hence, a secondary relaxation mechanism must take place. This new mechanism can be defined as ***cleavage assisted coalescence of macro-defects (CAC)***.

In order to fundament the following discussions and explain the proposed CAC mechanism, it is worthwhile first to understand the different characteristic exfoliation sizes observed for distinct energies and fluences. Therefore, we delineate the following scenarios grounded on the experimental results and mechanics of exfoliation. The analysis is based on

an internal pressure model for exfoliation [Fen 2004]; the results will be then compared and contrasted with the model.

In the initial nanocrack formation stage, when $h/r \gg 1$ (being r the radius of the crack and h its distance to the surface), the structure is seen as a classical Griffith crack [Gri 1920] embedded in an infinite elastic medium. Figure 3.16 exemplifies the situation. Mainly driven by its internal pressure and assisted by the hydrogen action in breaking the strained bonds at the crack tip, the crack follows a sub-critical planar growth governed by a mode-I stress intensity factor (k_I).

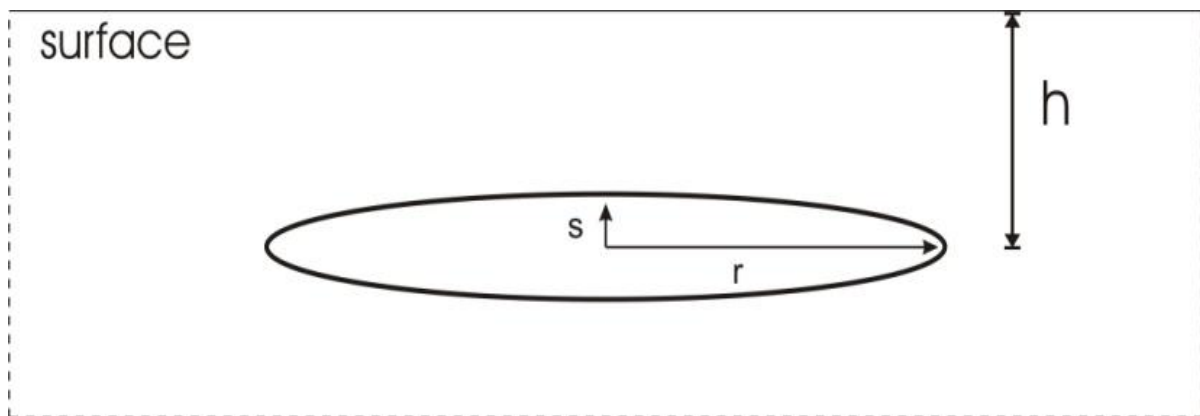


Figure 3.16- Griffith crack of major radius r and minor axis s embedded in an infinite elastic medium at a distance h from the surface.

When such a crack extends to a length r comparable to its distance from the surface h , the assumption that the crack is embedded in an infinite elastic medium becomes inappropriate. In this case, we shall regard the Si over-layer above a crack as a circular plate clamped along its edge with a uniform and constant pressure p [Fen 2004]. As the ratio h/r decreases, the mode-II stress intensity factor increases and the system must be treated as a mixed mode having both nonzero, mode-I (k_I) and mode-II (k_{II}) values. In the initial stage of crack growth, mode-II stress intensity factor is negligible ($K_{II} \approx 0$), resulting in a small deformation of the surface. Now, if the crack grows until $h/r \ll 1$, K_{II} increases and the thin plate above the crack experiences a larger deformation, leading to the appearance of blisters and/or exfoliation at the surface [Fen 2004]. Figure 3.17a shows a SEM image of blisters and exfoliations. Their distinct evolution stages are illustrated by the diagram in Fig. 3.17 and indicated on the SEM.

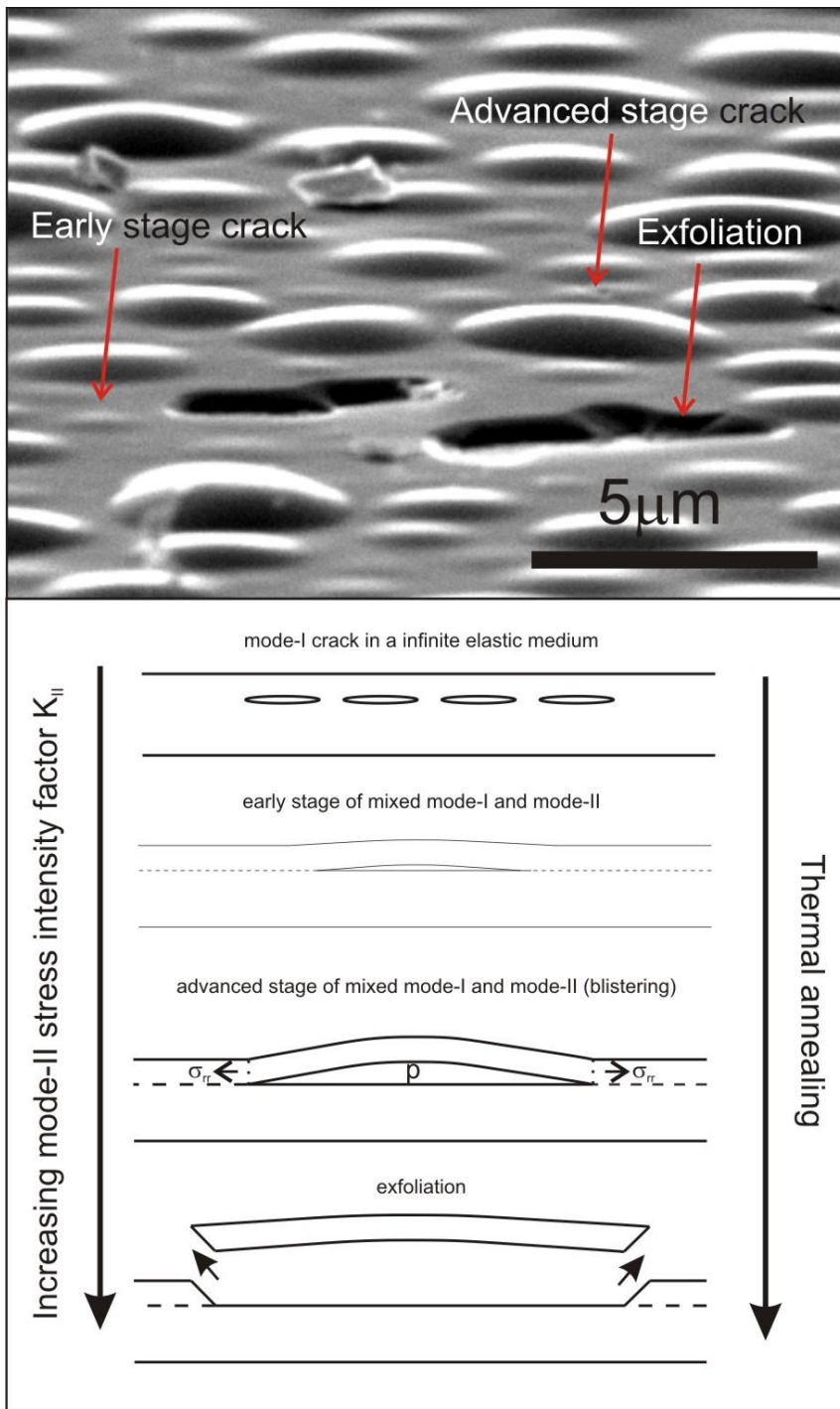


Figure 3.17-

Blistering/exfoliation in distinct stages of evolution are shown and indicated on the SEM at the top of the figure (30keV H^+ ions at 5×10^{16} ion/cm² + 33keV He^+ ions at 5×10^{16} ion/cm²) after annealing (500°C 1800s) and a diagram relating their evolution and correlation with stress intensity factors contribution and thermal annealing is schematically presented.

Following the thin-plate assumption [Hut 1992], the maximum tensile stress of the plate occurs along the circumferential edge (see Fig. 3.17), and is given by [Fen 2004]

$$\sigma_{rr}^{MAX} = \frac{3p}{4} \left(\frac{r}{h} \right)^2 \quad (3.4)$$

Since Si is a brittle material, it is reasonable to consider the maximum principal stress as failure criterion for exfoliation. Hence, exfoliation may take place when

$$\sigma_{rr}^{MAX} = \sigma_C, \quad (3.5)$$

where σ_C is the fracture stress of the material.

The measured individual exfoliated sizes S_{ex} allows the estimation of an **effective mean radius** r as

$$S_{ex} = \pi \cdot r_{eff}^2. \quad (3.6)$$

r_{eff} values versus fluence are plotted in Figs. 3.18 and 3.19 for the H_E and L_E case, respectively.

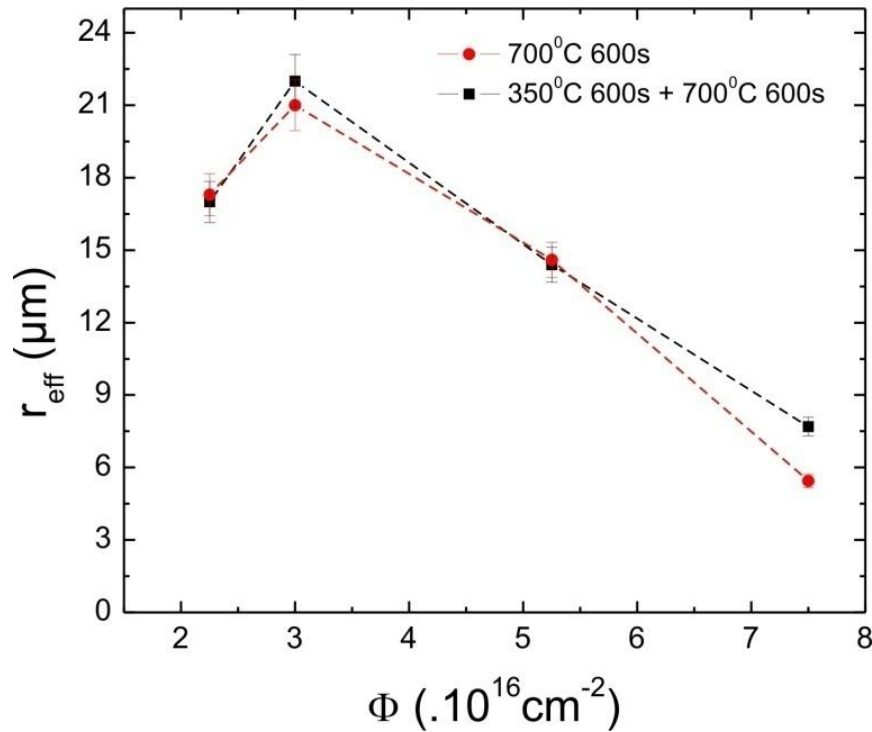


Figure 3.18- r_{eff} plotted as function of the fluence for the H_E samples and both annealing protocols.

Based on the internal pressure model for exfoliation [Fen 2004], the theoretical pressure P immediately before exfoliation can be estimated as

$$P_C = \frac{4\sigma_c}{3} \left(\frac{h}{r} \right)^2. \quad (3.7)$$

where $h=1500\text{nm}$ for H_E and $h=300\text{nm}$ for L_E . The h/r ratio and the calculated pressure P_c are presented in Fig. 3.20. The annealing conditions are not specified since S_{ex} does not vary with the annealing protocol.

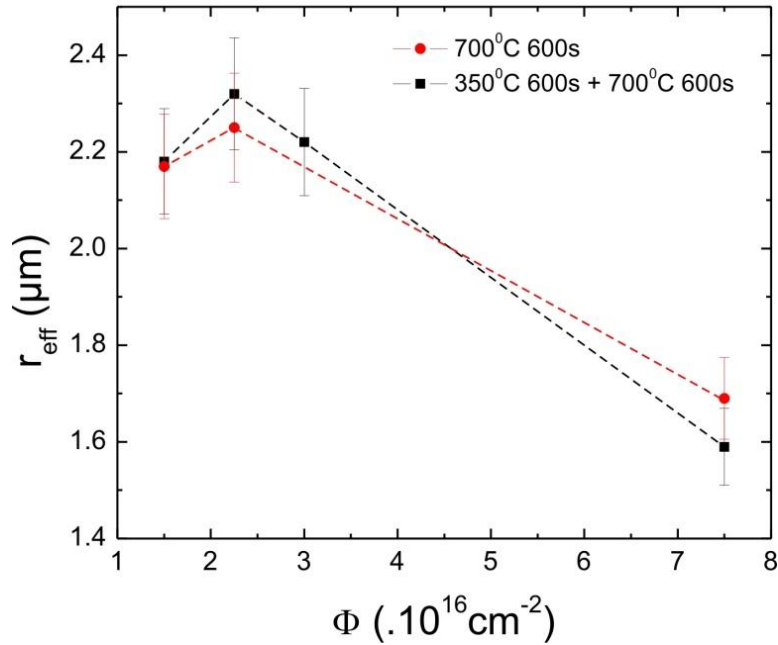


Figure 3.19- r_{eff} plotted as function of the fluence for the L_E samples and both annealing protocols.

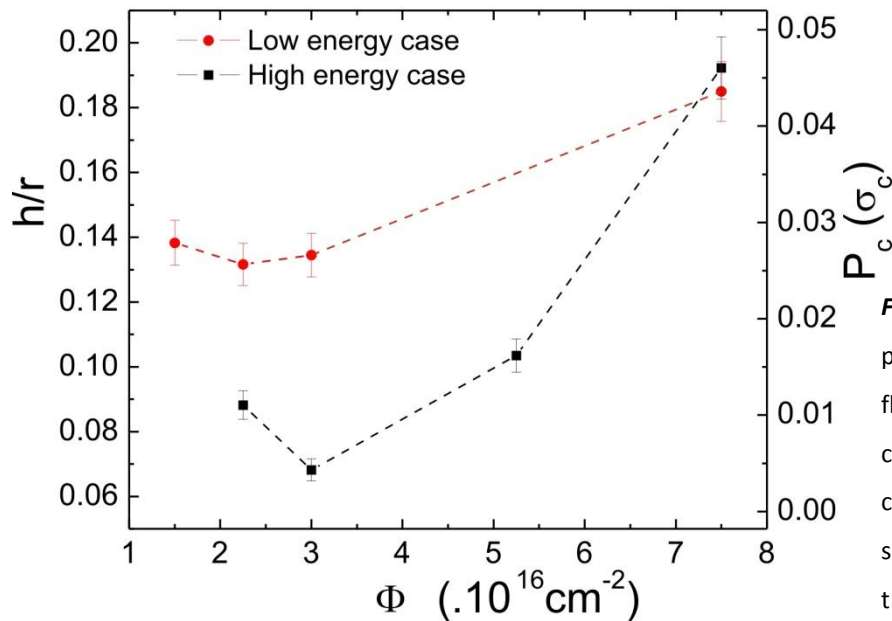


Figure 3.20- h/r ratio and P_c plotted a function of the fluence Φ for both energy cases. The annealing conditions are not indicated since S_{ex} does not vary with the protocols.

Considering the hypothesis that the internal pressure of blister-like cavities is correlated to the implanted fluence [Fre 1997, Yan 2003, Par 2007] as

$$P \propto \phi, \quad (3.8)$$

similar h/r factor values are expected for each fluence case regardless of the implanted energy. This means that, in order to produce exfoliation, a crack located at the depth h and with a gas pressure P should grow to a characteristic radius given by eq. 1.4. This is indeed verified for the high fluence regime, where the exfoliation h/r curves for H_E and L_E converge practically to the same value. On the other hand, a reduction of the fluence should decrease the pressure P and, therefore, render smaller h/r values. This is actually observed for both energy cases (Fig. 3.20), except for the threshold fluence point. However, assuming the hypothesis in Eq. 3.8, we should find similar values for h/r , independently of the depth location h and consequently, the implantation energy. This is clearly not observed in Fig. 3.20. In fact, for low and medium fluence cases the h/r values are quite distinct for each energy case. Curiously, the h/r factor obtained for the high energy case (larger h) suggests that exfoliation has occurred in a condition of lower pressure than for the low energy case. These discrepancies can be attributed to the existence of distinct exfoliation mechanisms operating at low and medium fluences as compared to the high fluence case. This is also supported by the distinct exfoliation structures shown in Figs. 3.14 and 3.15. In this way, we can differentiate the exfoliation mechanism as a function of the implanted fluence and delineate the following situations.

For low and medium fluences, the gas pressure inside the blisters is not high enough to overcome σ_c at its circumferential edge. Hence, their lateral growth may continue until a second relaxation mechanism takes place. At a given moment of the microstructure evolution, a cleavage assisted coalescence (CAC) process occurs between neighbor macro-defects (blisters or microcracks). The CAC process probably happens due to the high stress induced in the area between neighboring blisters [Use 2003, Hon 2007]. This process leads to the exfoliation of large areas since it includes the regions between blisters. Blister coalescence is also supported by the SEM observations. An example is shown in Fig. 3.21, obtained from the same L_E sample implanted to $\Phi=2.25 \times 10^{16} \text{ cm}^{-2}$ and annealed at 400°C (temperature just before exfoliation). Several blisters were observed in distinct coalescence stages. Figure 3.21a shows two uncoalesced individual blisters. Figure 3.21b and c show two

coalescing blisters where a neck between them appears. Figure 3.21d shows a large blister resulting from the coalescence of smaller ones.

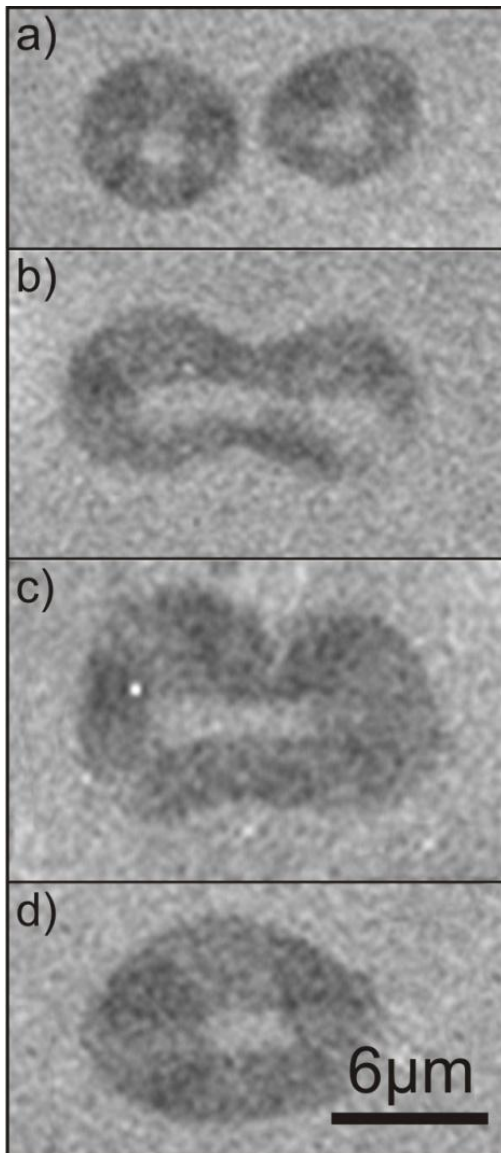


Figure 3.21- SEM images of L_E blisters at distinct stages of coalescence obtained from observations of the same sample implanted at $\Phi=2.25 \times 10^{16} \text{cm}^{-2}$ and annealed at 400°C for 1800s.

Finally, Figure 3.22 presents a schema illustrating the CAC process. It can explain how very large S_{ex} sizes are attained on the case of low and medium fluences, as well as the characteristic traits found on the remaining surface (i.e. the residual circular marks remaining from the pressurized blisters and/or large microcracks surrounded by apparently roughness areas). The rough areas (see Fig. 3.14b) seem to result from the cleavage along the disrupted layer, defined by H and He related defects as platelets, nano or microcracks.

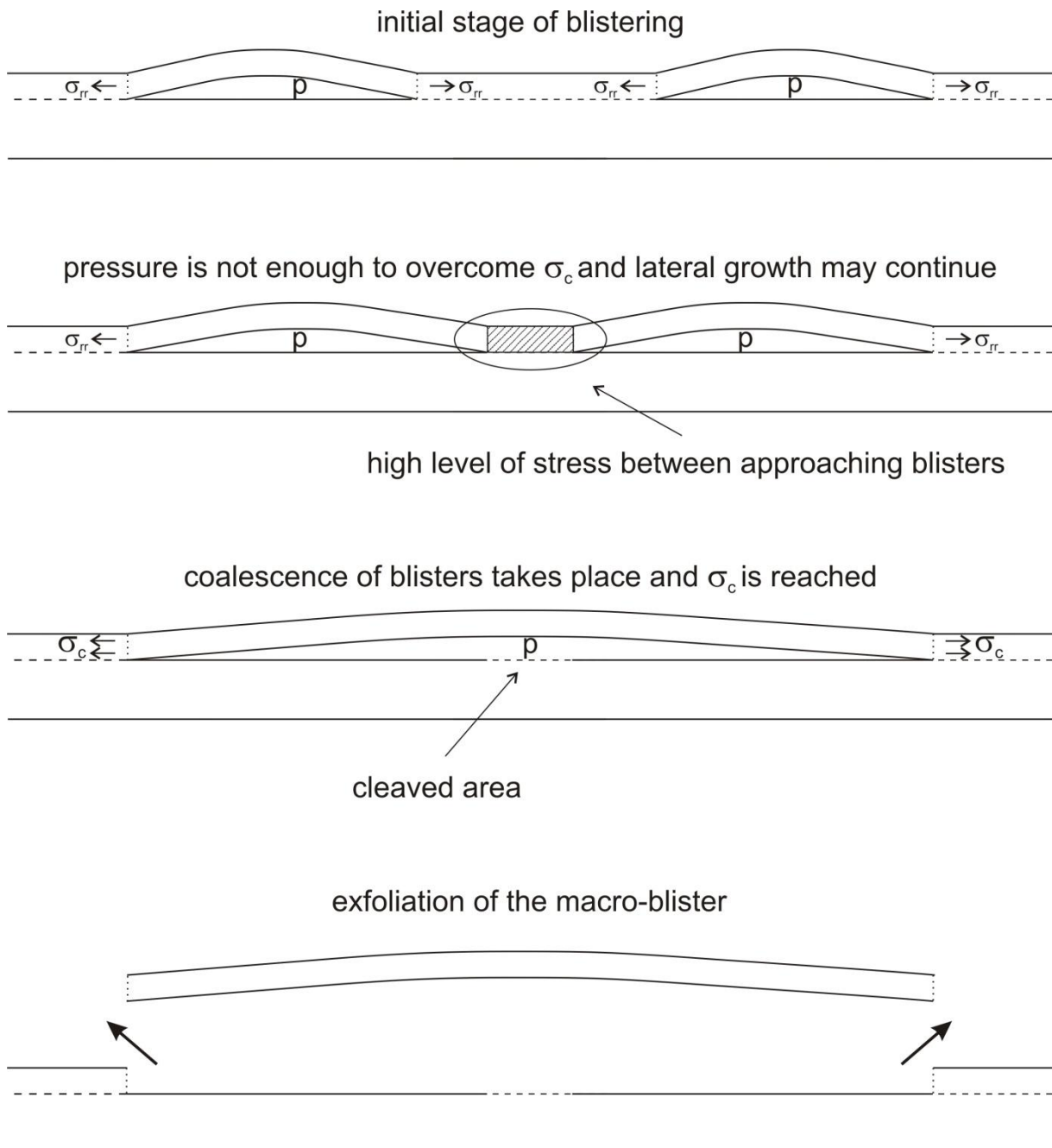


Figure 3.22- Schematic representation of the structures evolution distinct stages, resulting in the coalescence driven exfoliation model proposed to explain our experimental observations. This mechanism was commonly found for low and medium implanted fluences.

Another important observation is that the CAC process produces characteristic distributions of size for each fluence case. In the opinion of the author, this is somehow correlated to the stress distribution in the layer.

For high fluences, the concentration of implanted atoms in the matrix is sufficiently high to provide the necessary driving force to supply elevated pressures in the blister cavities, thus overcoming σ_c . In such conditions, exfoliation occurs at a given characteristic r which depends only on the h and P values (h =depth and P =internal pressure, eq. 1.6). Since P roughly increases with the implanted fluence, r should decrease as indeed observed experimentally (see Fig. 3.13). Hence, exfoliation becomes independent of any blisters coalescence process for high fluences ($h/r=cte$ for a given fluence). The exfoliation of individual blisters, preventing their coalescence, explains the observed increase of D_{ex} values and the decrease of the A_{ex} ones for high fluences. A schema of the pressure induced exfoliation process is shown in Fig. 3.23.

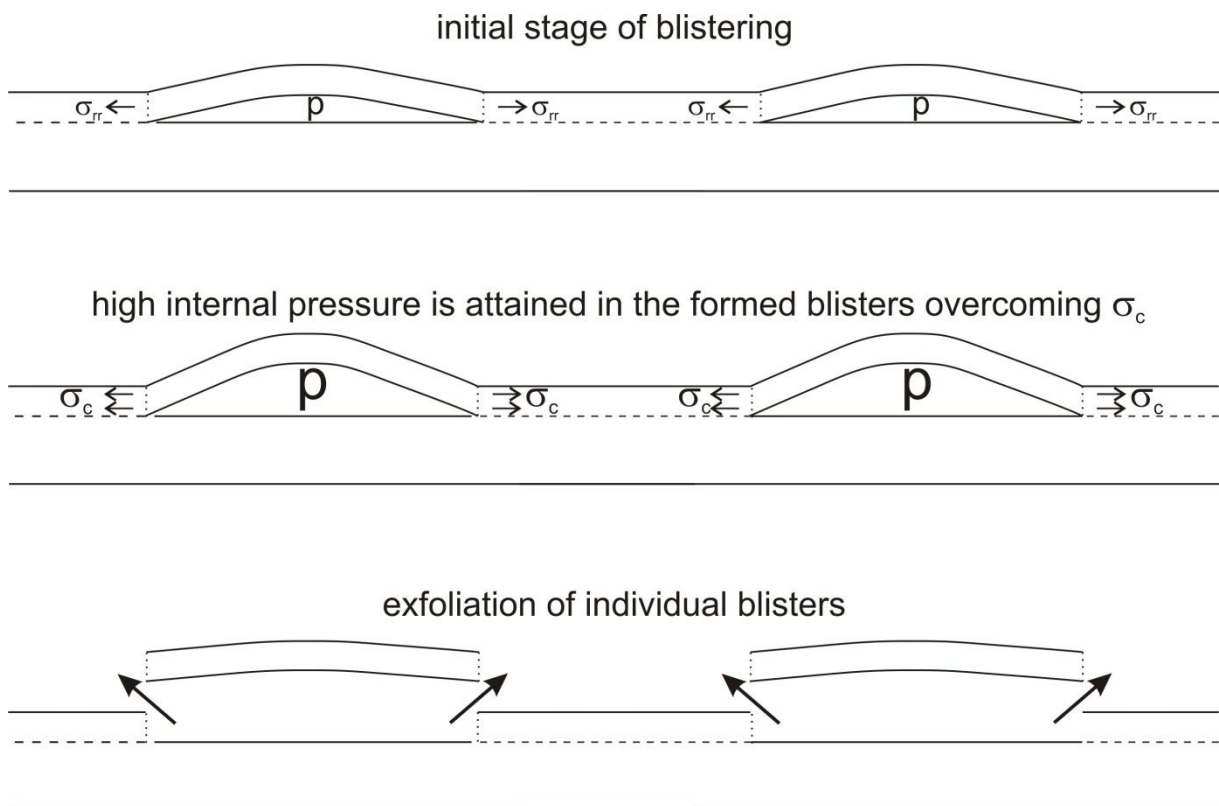


Figure 3.23- Schematic representation of the structures evolution distinct stages, resulting in the **pressure driven** exfoliation model operative in the restrict conditions of high implanted fluences.

Taking the value of fracture stress for Si ($\sigma_c=7000MPa$ [Caltech]) eq. 1.6 gives an internal pressure of $\approx 300MPa$ on the blisters prior to exfoliation for $\Phi=7.5 \times 10^{16} cm^{-2}$. The result is in good agreement with other estimations of internal gas pressure inside **blisters**,

for materials with similar Young's modulus and Poisson's ratio, to be around 200MPa [Par 2007]. However, the pressure for exfoliation is certainly higher than the one for blistering, thus corroborating the higher value of pressure estimated on the present work.

Figure 3.24 presents a schematic summary of the operative exfoliation mechanisms. In summary, the exfoliation mechanism is related to the regime of fluence, being the internal pressure model the dominant for high fluences and the cleavage assisted coalescence CAC the dominant for low fluences. Between both regimes, mixed contributions may take place. Indeed, it is possible to infer that after a minimum h/r value, the internal pressure of the cavities starts to increase.

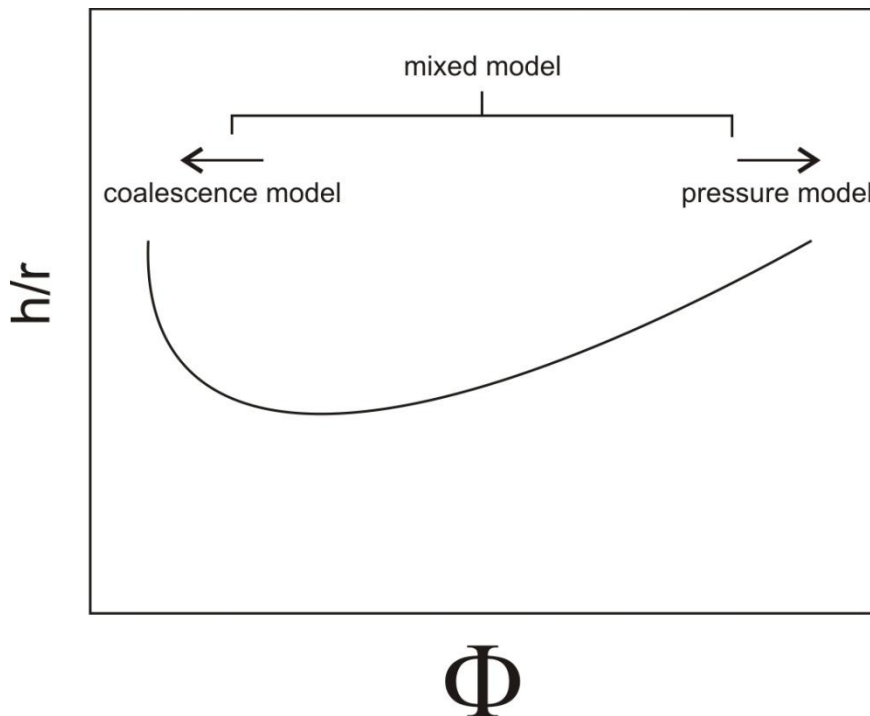


Figure 3.24- Schematic representation showing the exfoliation mechanisms as function of the implanted fluence. The coalescence model is dominant for the regime of low fluences and the internal pressure dominates for high fluences. A mixed contribution of both is observed between both limits cases.

3.4. Conclusions

In this chapter we have studied the exfoliation behavior of H and He co-implanted Si samples as a function of the implantation energy, fluence and annealing protocol. The methodology includes the statistical evaluation of exfoliation areas in order to deduce the exfoliation mean sizes S_{ex} , exfoliation efficiency parameter A_{ex} and exfoliation density D_{ex} .

The exfoliation behavior was characterized as a threshold phenomenon. An abrupt increase of A_{ex} and S_{ex} values is detected right after the threshold value. This behavior is connected with a minimum peak concentration of gas atoms, and explains why the threshold fluence increases with the implantation energy. After their abrupt increase, S_{ex} and A_{ex} reach a maximum and then slowly decrease with the fluence. This behavior is apparently caused by microstructure modifications that will be discussed in the next chapter. A_{ex} values do not vary with the energy as significantly as the factor 100 observed for S_{ex} . This behavior is correlated with the implantation depth h and the results are discussed in terms of gas pressure relations derived from elasticity concepts.

Blistering mechanisms for irradiated material have been widely discussed in the literature. Exfoliation is systematically considered a burst blister and has been less investigated. In this work, we show that exfoliation can be the result of an individual busted blister under high fluence conditions, where the gas concentration is sufficiently large to supply the necessary pressure to overcome the fracture stress σ_c of the material. A distinct exfoliation mechanism (i.e. the cleavage assisted coalescence (CAC) of blisters) has been proposed in order to explain the experimental results for low and medium implanted fluences. Its phenomenological description is supported by detailed investigation of exfoliation features obtained by SEM observations.

To explain the results we propose a phenomenological model where exfoliation evolves two macro-steps; i) formation of blistering, where the high internal pressure needed to overcome σ_c is not attained and ii) cleavage occurs between growing blisters leading to their coalescence, and then, resulting in exfoliation of large areas.

The major conclusions can be summarized as:

- For each depth location (i.e. implantation energy), there is a distinct fluence window where the exfoliation efficiency can be optimized (or manipulated in other sense).
- The lower limit of the window seems to be related to a minimum concentration of gas atoms, independently of the implanted energy, which implies that the threshold fluence increases with the implanted energy.
- The reduction of exfoliation efficiency for high fluences is related to the reduction of S_{ex} .
- For the same fluence, the reduction of the exfoliation efficiency A_{ex} for lower implantation energy is interpreted as a gas desorption enhancement due to the proximity of the free surface.
- Pre-annealing enhancement of the exfoliation efficiency A_{ex} occurs due to an increase of exfoliation density D_{ex} .
- The mechanisms of exfoliation were shown to be fluence dependent where:
 - A model internal gas pressure can be applied for the high fluence cases.
 - A blistering coalescence mechanism is observed for low and medium fluences.

CHAPTER 4

Fluence and Current Density Effects on the Exfoliation Behavior of 1H:1He Implanted Si

This chapter presents a more detailed microstructure investigation of high energy (H_E) implanted samples with a 1H:1He fluence ratio. The effects of fluence and current density on the exfoliation precursors are investigated by TEM and XRD.

The chapter also demonstrates that complete delamination of large areas can be attained when the samples are implanted with high fluence rates. This phenomenon is discussed in terms of a distinct mechanism, concurrent to the coalescence processes leading to blistering/exfoliation. A fracture mechanics based model is proposed to explain the results.

4.1. Experimental parameters

4.1.1. Implantation fluence (Φ)

The implantation fluences were adjusted to provide a 1H:1He ratio. The samples were implanted to total fluences ($H^+ + He^+$) of $\Phi = 2 \times 10^{16} \text{ cm}^{-2}$, $\Phi = 6 \times 10^{16} \text{ cm}^{-2}$, and $\Phi = 10 \times 10^{16} \text{ cm}^{-2}$, hereby denominated low, intermediate and high fluence cases. Control samples implanted only with H^+ at low and high fluences were also investigated.

4.1.2. Implantation energy

The implantations were performed at energies of 168 keV for H^+ or 336 keV for H_2^+ calculated using SRIM code [SRIM 2008] to provide coincident mean depth values about $1.5 \mu\text{m}$, corresponding to the “*high energy*” (H_E) case.

4.1.3. Order of implantation and current density

All the samples were first implanted with H^+ ions and then with He^+ ions under current densities from 0.25 to $0.5 \mu\text{A cm}^{-2}$, hereby denominated “low current” (L_c) mode. Samples were also implanted using current densities of $\approx 1.5 \mu\text{A cm}^{-2}$, denominated “high current” (H_c) mode. The current density effect was studied considering a fixed fluence $\Phi = 4 \times 10^{16} \text{ cm}^{-2}$.

4.1.4. Thermal Annealing Protocols

All implantations were performed with the target kept at room temperature. The implanted samples were then furnace annealed in a high vacuum ambient, using the same annealing protocol 1 (700°C for 1800s) defined in Chapter 3. An intermediate annealing temperature of 350°C for 1800s was used to perform TEM investigations of the sample microstructure.

4.2. Results

Figure 4.1 shows SEM images of the exfoliated surfaces for the three fluence cases after annealing using protocol 1 (700°C for 1800s).

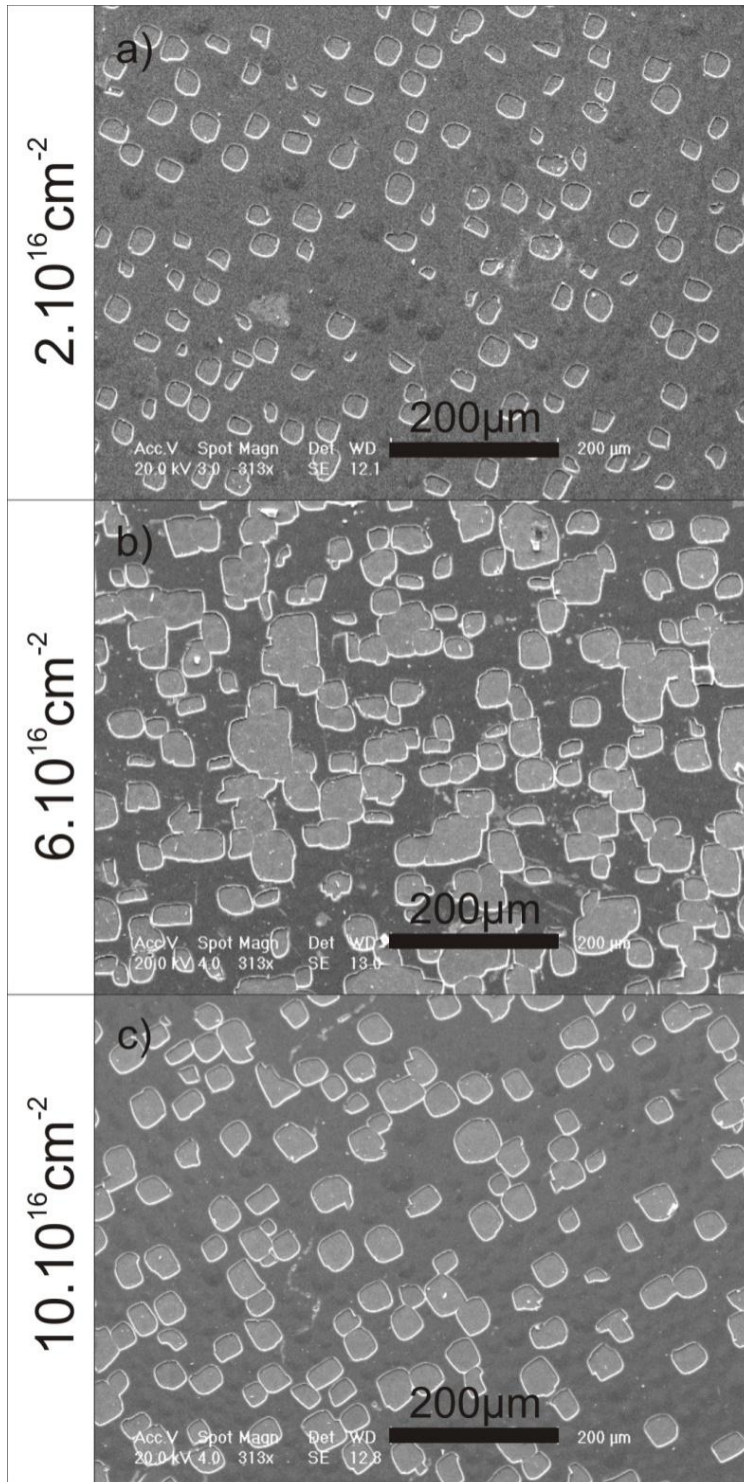


Figure 4.1- SEM images of the samples surface showing a general view of the exfoliation sizes and densities for (a) $\Phi=2 \times 10^{16} \text{cm}^{-2}$, (b) $\Phi=6 \times 10^{16} \text{cm}^{-2}$, and (c) $\Phi=10 \times 10^{16} \text{cm}^{-2}$, after annealing using protocol 1.

The samples were analyzed using the same methodology described in Chapter 3. The dependence of A_{ex} versus Φ (Fig. 4.2) reproduces the general window trend observed for the samples implanted with the 2H:1He ratio (see Chapter 3, Fig. 3.2). For the only H^+ implanted samples, no exfoliation is observed for $\Phi=2 \times 10^{16} \text{ cm}^{-2}$, and A_{ex} approaches 17% for $\Phi=10 \times 10^{16} \text{ cm}^{-2}$ (Fig. 4.2). The S_{ex} values were not evaluated because the exfoliated regions are highly overlapped (Fig. 4.1b), rendering unrealistic results.

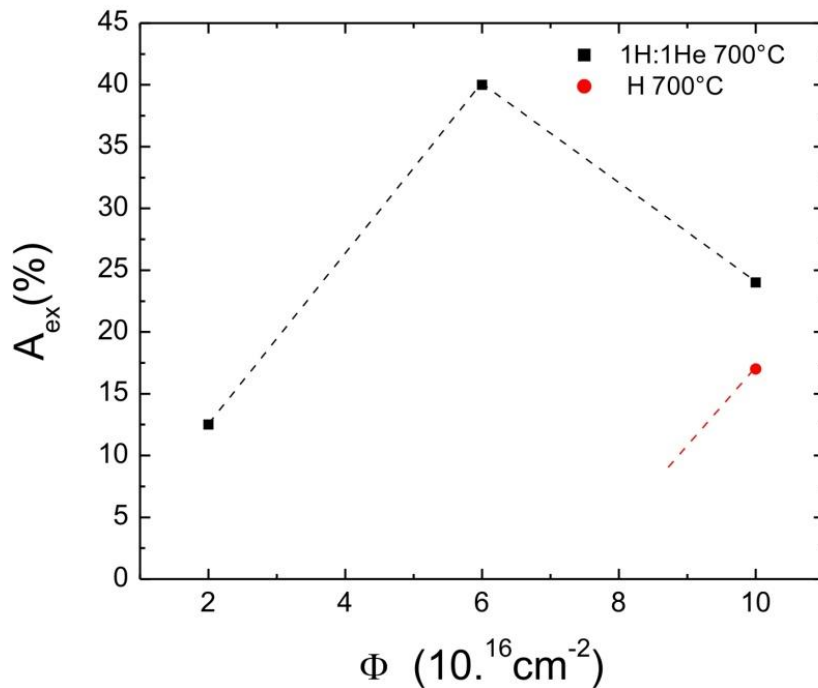


Figure 4.2- Exfoliation efficiency A_{ex} plotted as function of the implanted fluence Φ for the coimplanted samples, as well as the sample implanted only with H^+ at $\Phi=10 \times 10^{16} \text{ cm}^{-2}$.

Detailed SEM images of exfoliated regions reveal similar remaining circular marks as described in Chapter 3 (Fig. 3.14). The estimated areal ratio of circular features per exfoliated area is $\approx 65\%$ for the sample implanted at $\Phi=6 \times 10^{16}$ (Fig. 4.3). Figure 4.3b exemplifies the method used to determine the areal ratio. Figure 4.3c shows SEM images in high magnification providing details of the circular features.

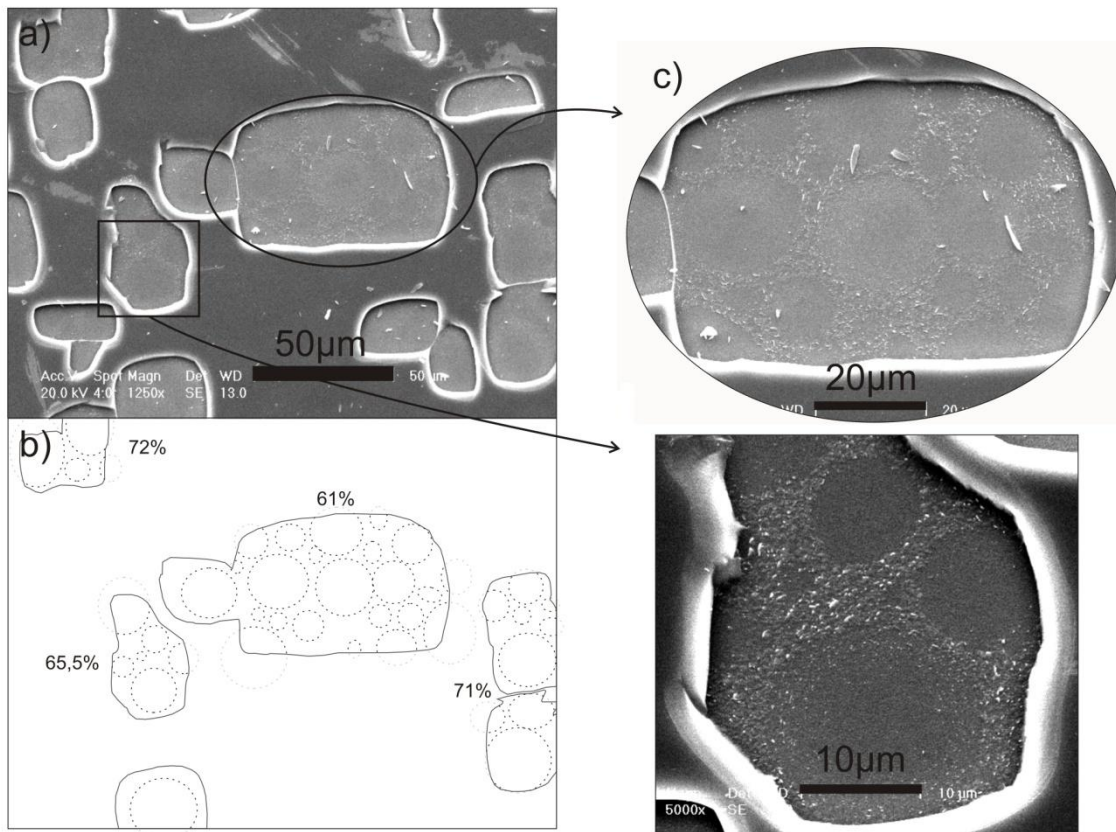


Figure 4.3- (a) SEM image revealing the circular marks at the bottom of the exfoliated areas. (b) The ratio of circular features by the area of exfoliation was estimated to be $\approx 65\%$ for the sample implanted at $\Phi=6 \times 10^{16}$. (c) Inserts of higher magnifications showing the circular features.

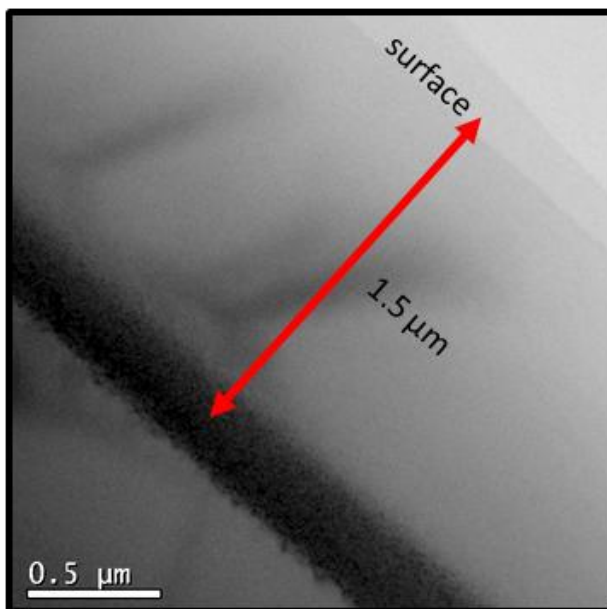


Figure 4.4- Shows a low magnification cross section TEM image of a sample implanted at $\Phi=10 \times 10^{16} \text{ cm}^{-2}$ and annealed at 350°C for 1800s. The formation of a buried damage layer at $\approx 1.5 \mu\text{m}$ depth from the surface is observed.

Figure 4.4 shows a cross-sectional TEM view of a H_E implanted sample ($\Phi=10 \times 10^{16} \text{ cm}^{-2}$) annealed at 350°C for 1800s. It reveals the formation of a damaged layer at the depth of $\approx 1.5 \mu\text{m}$, which is quite accurately reproduced by SRIM [SRIM 2008] calculations.

Figures 4.5a, b and c show TEM observations of the damaged layer for the three fluence cases (low, medium and high). The distance ℓ depicted on the images represents the characteristic width of the damaged layers. Figures 4.5d, e and f provide magnified views from these regions. They clearly show the formation of (001) nanocracks appearing as elongated white rods preferentially aligned parallel to the surface. The distance p indicated in the pictures refers to the width of the region within the damaged layer which effectively contains nanocracks. The values for ℓ and p are summarized in Table 4.1. The low fluence case (Fig. 4.5d) presents (001) oriented nanocrack structures about 100 nm long, distributed in a narrow depth layer centred on the damaged region. With increasing fluence, the nanocracks become smaller (typical lengths between $\approx 20\text{-}60\text{nm}$) and their depth distribution become slightly larger. For the three fluence cases, the depth distribution is centred at $\approx 1530\text{nm}$. It means that the damaged zone extends towards the surface as the fluence increases. A careful examination of this damage “tail” reveals the formation of a high density of small spherical cavities presenting diameters of $\approx 2\text{-}3\text{nm}$ (see Figs. 4.5e and f). Similar mean values of nanocrack length and cavity diameter are also observed for medium and high fluences. Hence, with increasing fluence, cavity concentration and/or their gas pressure must increase to accommodate larger gas contents. Independently of the implantation condition, preferential formation of {111} oriented platelets is observed at the deeper side of the implanted layer. Figure 4.6 illustrates schematically the observations above.

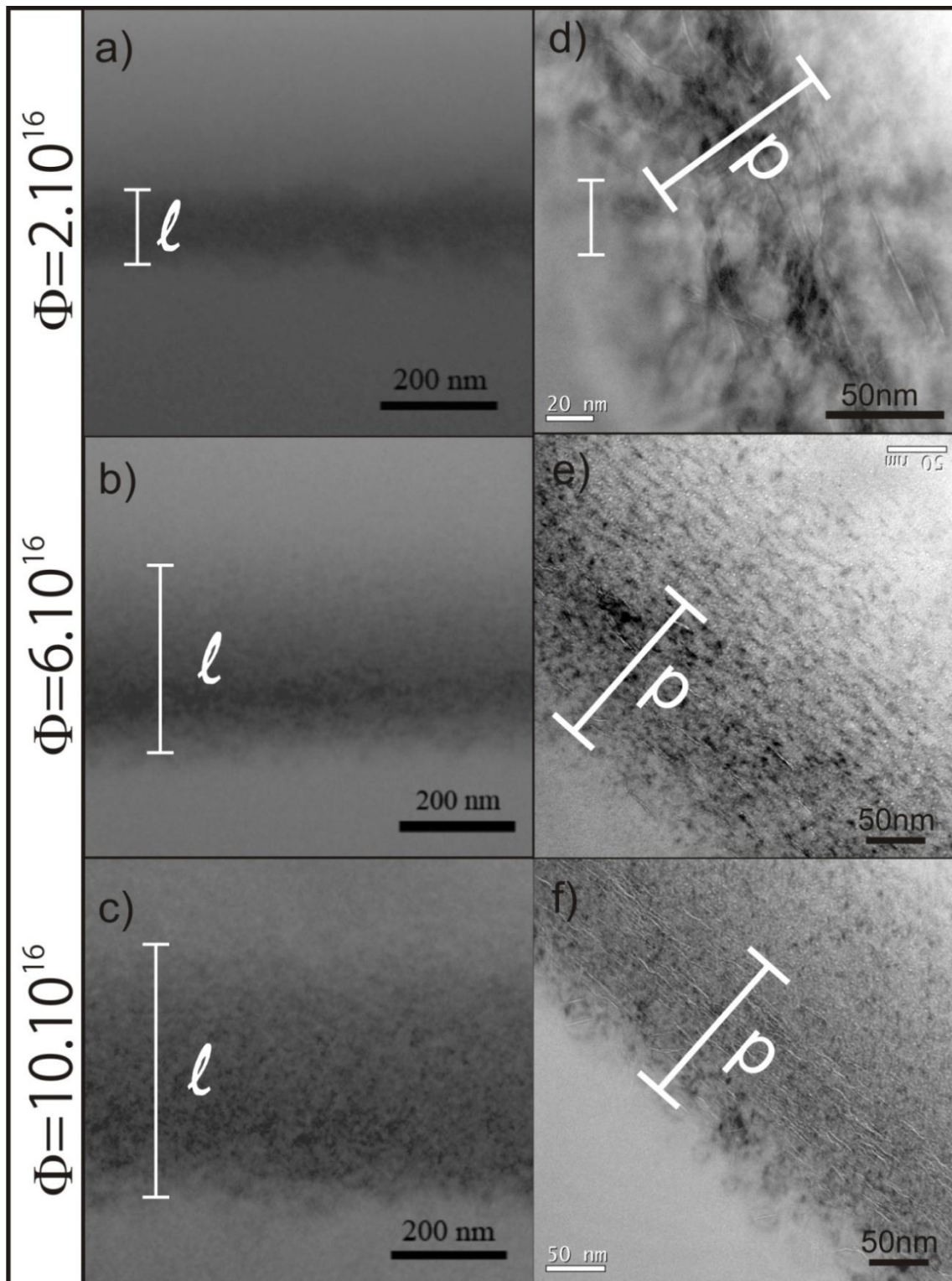


Figure 4.5- TEM images from samples annealed at 350°C for 1800s at low magnification (a), (b) and (c) and high magnification (d), (e) and (f). Their correspondent implanted fluence is indicated at the left of the figure. The parameters l and p are the characteristic width of the damaged layer and the length of the region which effectively contains nanocracks. It shows that microstructure evolves as fluence increase. The mean size of nanocracks reduces but their depth distribution slightly enlarges.

Table 4.1			
Implanted Fluence	$2.10^{16} \text{ cm}^{-2}$	$6.10^{16} \text{ cm}^{-2}$	$10.10^{16} \text{ cm}^{-2}$
Central depth localization of the nanocracks	1534nm	1531nm	1535nm
Width (ℓ) of the damage layer	170nm	320nm	375nm
Width (P) of the layer containing the nanocracks	85nm	110nm	112nm

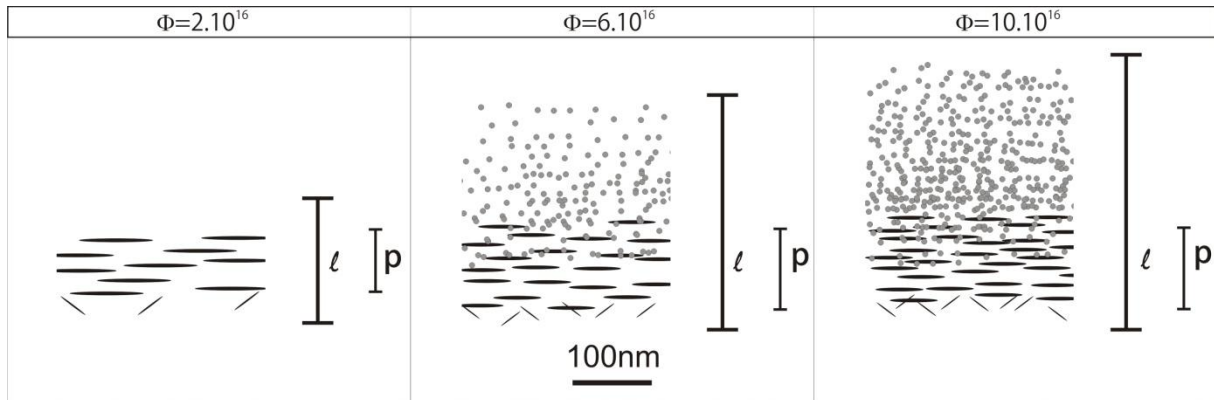


Figure 4.6- Schematic illustration of the microstructure for samples implanted at low, medium and high fluences.

Longitudinal ($\theta/2\theta$) x-ray scattering measurements in the vicinity of the (004) reflection were carried out on the as-implanted samples. The obtained data corresponds to scans along the surface normal, where information about planes parallel to the surface can be extracted. The XRD measurements are displayed in Fig. 4.7 (intensity versus relative strain $\Delta d/d$). Figure 4.7 also shows the measurement of a pristine sample (non-implanted Si). For all implanted cases fringe patterns are observed. The fringe spacing shortens and the intensity of the curves drops as fluence increases. This indicates that the strain profile widens with increasing fluence. The decrease of scattered intensity is related to strong local displacements of atoms from the diffractive planes [Ded 1973]. In the case of H implanted Si, this has been attributed to the formation of large defects (nano and microcracks) [Sou 2006,

Mic 2003], but could also result from the increase of pressure inside the defects. The maximum strain increases from 0.6% at $\Phi=2 \times 10^{16} \text{ cm}^{-2}$ to values larger than 1.2% for $\Phi=6 \times 10^{16} \text{ cm}^{-2}$ and $\Phi=10 \times 10^{16} \text{ cm}^{-2}$ (the curves are resolved until the ϵ_{MAX} of $\approx 1,2\%$, from where the intensity approaches the noise level limit associated to the technique and the characteristics of Si). In summary, as the fluence increases the maximum strain increases, the profile enlarges and the defects present at the as-implanted state are more and more able to produce stronger localized displacements of atoms from the diffractive planes.

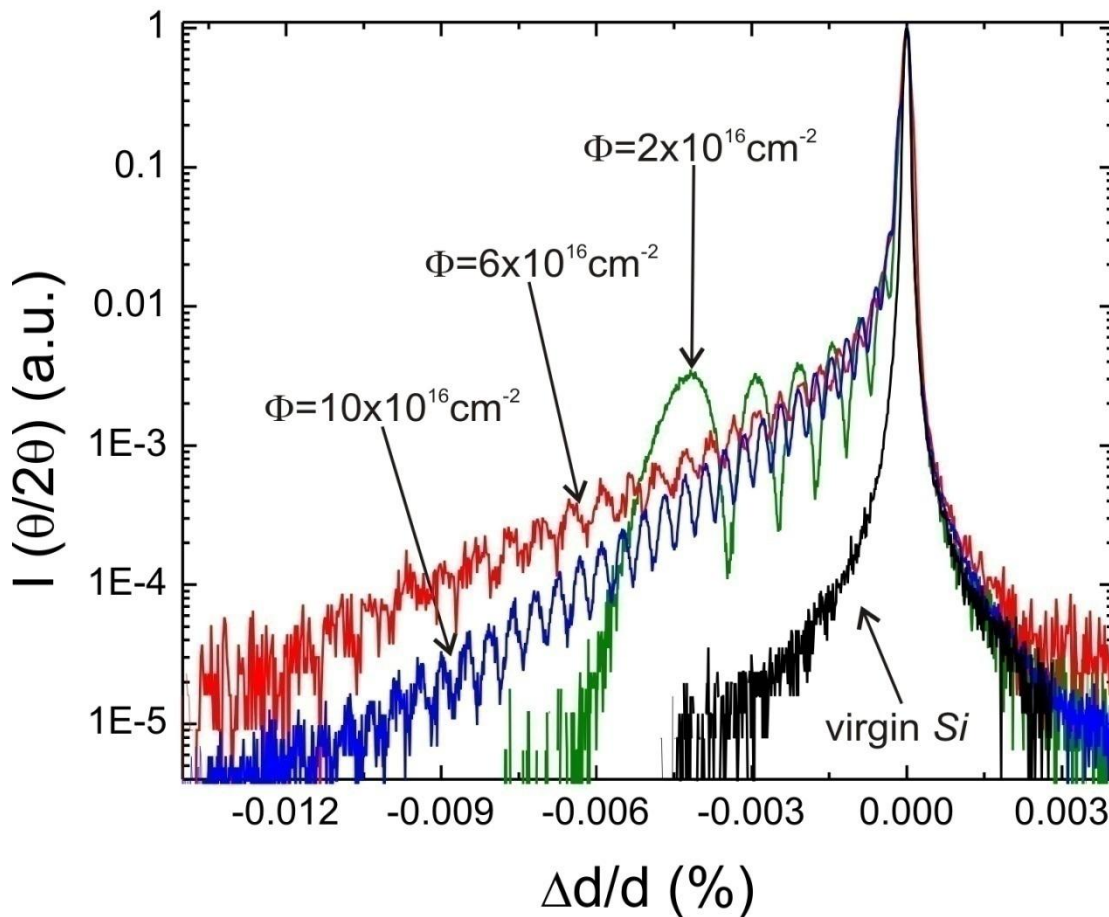


Figure 4.7- Present XRD (004) scattering intensity plotted against the relative strain for the three fluence cases and at the as-implanted state, as well as a reference sample (virgin Si).

4.3. Discussions

4.3.1. Effect of the H:He ratio on exfoliation efficiency

Figure 4.8 compares the A_{ex} behavior as a function of fluence for the 2H:1He and 1H:1He fluence ratios. Both curves show the same trend. However, for the 1H:1He case the efficiency window is wider and the maximum A_{ex} value is considerably higher ($\approx 100\%$) and shifted toward higher fluences. This enhancement of the exfoliation efficiency is consistent with the concept in the literature (see Chapter 1) that He atoms causes a more efficient pressurizing effect.

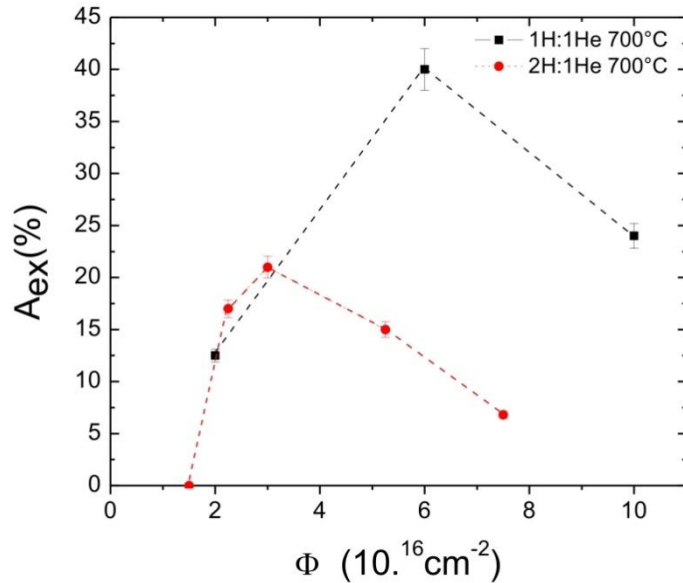


Figure 4.8- Exfoliation efficiency (A_{ex}) as a function of the implanted fluence (Φ) for both H:He implanted ratios.

4.3.2. Microstructure evolution as function of the implanted fluence and its consequence on A_{ex} and S_{ex}

The TEM observations presented in Fig. 4.5 and summarized in Fig. 4.6 show that the samples implanted to low fluence display rather long nanocrack structures concentrated within a narrow layer, in contrast to a larger distribution of smaller nanocracks observed for medium and high fluence cases. The fact that for a higher fluence of implantation we have observed a higher density of “smaller” cavities can be explained by the increase and broadening of the damaged layer (confirmed by both TEM and XRD results). Previous studies

have shown that if abundant traps sites for gas atoms are created at a broader depth, a more homogeneous distribution of nucleation centers is formed. In this case, a deceleration of the Oswald Ripening growth process of the cavities could be expected and one will find smaller cavities after a given time t of annealing [Del 2003].

It seems interesting to discuss why the damage layer shows spherical cavities mostly concentrated at shallower depths and nanocracks at deeper regions as schematically shown in Fig. 4.6. For high fluence He implanted Si, spherical cavities readily form during the implantation process because of the high availability of as-created vacancies [Fic 1997]. In this sense, the very small 2-3nm spherical-like cavities in the high fluence H+He coimplanted samples can be understood in terms of concentration and depth distributions of vacancies. Figure 4.9 shows SRIM [SRIM 2008] simulated concentration profiles of vacancies and atoms obtained for the combined H+He implantation. The peak concentration of vacancies is located at a shallower depth (1480nm) compared to the one for the implanted species (1540nm). The peak location of the gas concentration profiles at the depth of 1540nm is in good agreement with the observed location of the nanocracks (see Table 4.1). This observation suggests that the nanocracks form closer to the maximum concentration of the implanted species. As the fluence increases from $\Phi=2 \times 10^{16} \text{ cm}^{-2}$ to $\Phi=6 \times 10^{16} \text{ cm}^{-2}$, nanocracks are still formed at the same depth, but the excess of implanted atoms seems to agglomerate at the region where a high concentration of vacancies is available, and forming spherical bubbles.

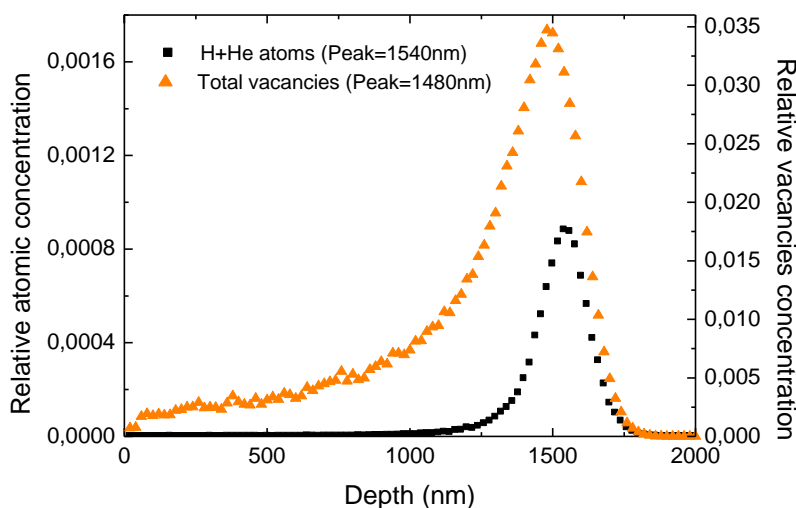


Figure 4.9- Shows the simulated profiles of vacancies and atoms concentration obtained for H+He implantations ($\text{H}^+168\text{keV} + \text{He}^+345\text{keV}$). Their peak depth concentration is indicated.

Our observations indicate that the concentration of spherical cavities is larger in the region close to the estimated vacancy concentration peak (1480nm), i.e. just beside the region where the nanocracks have formed (Figs. 4.5e and f, and Fig. 4.6). It is not possible to determine whether the spherical bubbles contain preferentially *H* or *He* atoms or a mixture of both, but it was verified that when *He* is implanted to $\Phi=2\times 10^{16} \text{cm}^{-2}$, it will form only spherical bubbles and *H* implanted to $\Phi=2\times 10^{16} \text{cm}^{-2}$ will form platelets and microcracks both after annealing 350°C 1800s as shown in Fig. 4.10. Since *H* was always implanted first, it seems plausible to assume that *H* platelets were already formed by *H*, as observed in previous works [Gri 2000]. Hence, when the *He* implantation started, the *He* atoms would already find a sample containing *H*-platelets and a tail of vacancy rich point defect clusters extending towards the surface. For low fluences, the concentration of the *H* induced point defect clusters may be quite small and ineffective to trap the *He* atoms, which would then preferentially be incorporated by the *H*-platelets, causing their growth. On the other hand, for larger fluences, preferential trap of *He* atoms at the *H* induced vacancy clusters leads to the formation of a high density of spherical like bubbles, thus not contributing to a significant platelet growth. In this sense, it could result in a deleterious effect on S_{ex} and A_{ex} .

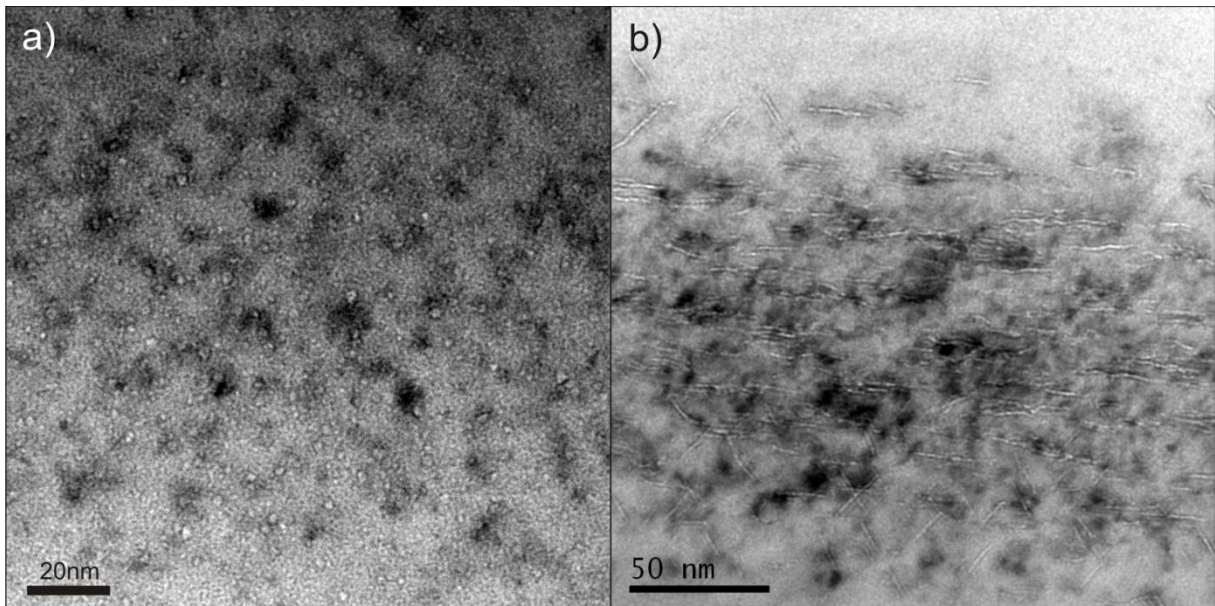


Figure 4.10- Shows cross section TEM images of (a) spherical bubbles formed on *He* implanted Si at $\Phi=2\times 10^{16} \text{cm}^{-2}$ (345keV) and (b) platelets and microcracks formation on *H* implanted Si at $\Phi=2\times 10^{16} \text{cm}^{-2}$ (168keV). Both samples were imaged after 350°C 1800s annealing.

Exfoliation is a threshold phenomenon and seems natural to attribute its emergence to the accumulation of minimum gas content able to give rise to the process as discussed in Chapter 3. However, the reduction of exfoliation efficiency for high fluences (ultimately defining the higher limit of the exfoliation window) is not obvious and several factors may play a role in this case. A similar window feature (for blistering, not exfoliation) was described in previous work [Mou 2005] where the reduction of blistering for high fluences is attributed to the widening of the damage profile as the implanted fluence increases. As a consequence, the spreading of depth distribution of nanocracks occurs, probably reducing their coalescence and ultimately inhibiting blistering. For the present case of *H+He* co-implanted samples, the correlation of the exfoliation efficiency with the widening of the damage profile is not so clear. We observed that, from $\Phi=2 \times 10^{16} \text{ cm}^{-2}$ to $\Phi=6 \times 10^{16} \text{ cm}^{-2}$, the damage profile widens in $\approx 90\%$, while the exfoliation area increases in $\approx 210\%$. On the other hand, from $\Phi=6 \times 10^{16} \text{ cm}^{-2}$ to $\Phi=10 \times 10^{16} \text{ cm}^{-2}$ there is a slight widening of $\approx 17\%$ accompanied by a reduction of 40% in the exfoliated area (see Table 4.1). The width of the region containing the nanocracks (length ρ) shows approximately the same behaviour. Thus, the inhibition of blistering/exfoliation for very high fluences is more probably related to other microstructure modifications.

This section shows that the nanocracks are observed within the region close to the peak concentration of implanted gas atoms. The accumulation of lattice defects with increase of fluence causes the formation of spherical bubbles (instead of nanocracks) close to the maximum concentration of vacancies, which may contribute to the reduction of the exfoliation efficiency.

Indeed, blistering and exfoliation is the result from a number of complex mechanisms including irradiation and thermally induced defects, diffusion and segregation of gas atoms and point defects, nucleation and growth of cavities [Gri 2000], gas pressure effects [Wel 1998], chemical interactions [Aga 1998, Wel 1998], stress and strain induced effects [Nas 2005, Lee 2006] and elastic or even plastic deformation [Fra 2004]. Additional factors such as localized relief of strain, localized amorphization of the implanted layer (amorphous Si do not blister [Ter 2007]) or even homogeneous swelling [Lec 2005] need to be studied for a better understand of the upper limit behavior.

4.3.3. Strain evolution as a function of the implanted fluence:

The XRD measurement (Fig. 4.7) from the $\Phi=2 \times 10^{16} \text{ cm}^{-2}$ implanted sample is characteristic of a normal type distribution of strain, where $\varepsilon_{MAX} \approx 0,6\%$ is achieved at the center of the profile. The simulation of the experimental x-ray scattering curve for $\Phi=2 \times 10^{16} \text{ cm}^{-2}$ sample was done using implantation [Zie 1985] and XRD [Ste 2007] simulation codes. Figure 4.11 shows the simulation results superposed with the experimental curve. The simulations were performed considering the combined (H+He) vacancy profile (Fig. 4.11a), the H+He concentration profile (Fig. 4.11b), only the He concentration profile (Fig. 4.11c) and only the H concentration profile (Fig. 4.11d).

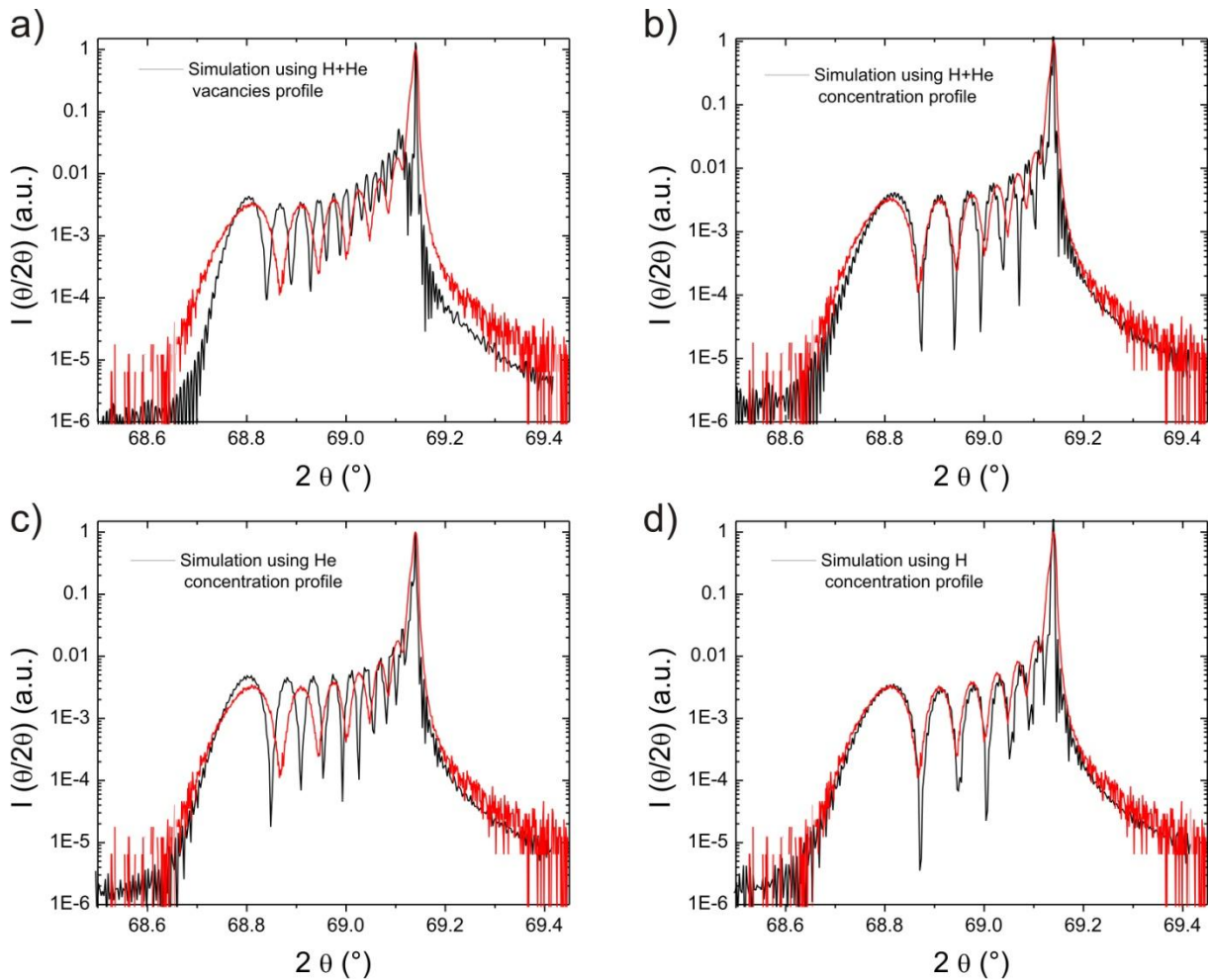


Figure 4.11- Shows the results of the simulation of x-ray scattering curves using (a) the H+He vacancies profile, (b) H+He atoms concentration profile, (c) only He atoms concentration profile and (d) only H atoms concentration profile respectively.

The results clearly show that the best fit of the experimental data is obtained by using the H concentration profile to simulate the strain distribution. A static Debye-Waller factor $DWF=1$ was used in all simulations (i.e. no effect of local atoms displacements has been accounted for), suggesting that only very small clusters are present in the as-implanted sample. The strain profile of the $\Phi=2 \times 10^{16} \text{ cm}^{-2}$ implanted sample was then reconstructed from the simulations and the result is presented in Fig. 4.12.

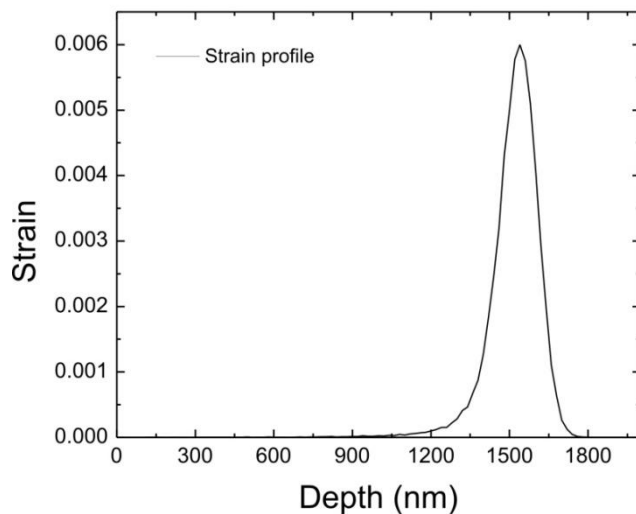


Figure 4.12- Strain profile of the $\Phi=2 \times 10^{16} \text{ cm}^{-2}$ sample reconstructed from the simulation of XRD curve using the H atoms profile.

The simulations of the strain profiles for the higher fluences could not be done with accuracy since there is a lack of data for the high strained zone of the samples ($\epsilon > 1.2\%$), but interestingly, the H simulated SRIM profile does not provide a good fitting of the XRD simulation as it provides for low fluence regime. Nevertheless, the general result is qualitatively summarized in Fig. 4.13, illustrating that the strain profile tends to widen and increase with the increase of the fluence.

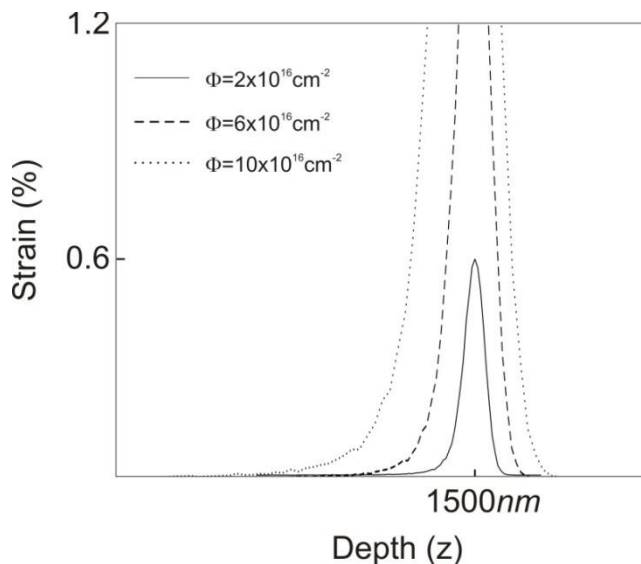


Figure 4.13- Summary of the strain distribution found for the three fluence cases. For the fluences of $\Phi=4 \times 10^{16} \text{ cm}^{-2}$ and $\Phi=10 \times 10^{16} \text{ cm}^{-2}$ the profile could be measured until $\epsilon \approx 1.2\%$ from where it gets in the noise level. Nevertheless, the profiles are observed to widen as fluence increases.

4.3.4. Elasticity based expression and calculation of in-plane stress

An implanted layer is considered a thin buried layer close to the surface, containing extra atoms and damage. It is reasonable to assume that the damage is homogeneously distributed within the x and y directions parallel to the surface and confined within a narrow z distribution (perpendicular to the surface). The z dimension is very small compared to the others and the stresses at the free surface of the substrate are null, thus characterizing a **plane stress state**. In this case, compressive in-plane stresses $\sigma_{yy}^{in-plane} = \sigma_{xx}^{in-plane}$ develop within the xy planes and, as consequence, an out-of-plane strain $\left(\frac{\delta d}{d}\right)_z$ occurs in the z direction. This situation is schematically illustrated in Fig. 4.14.

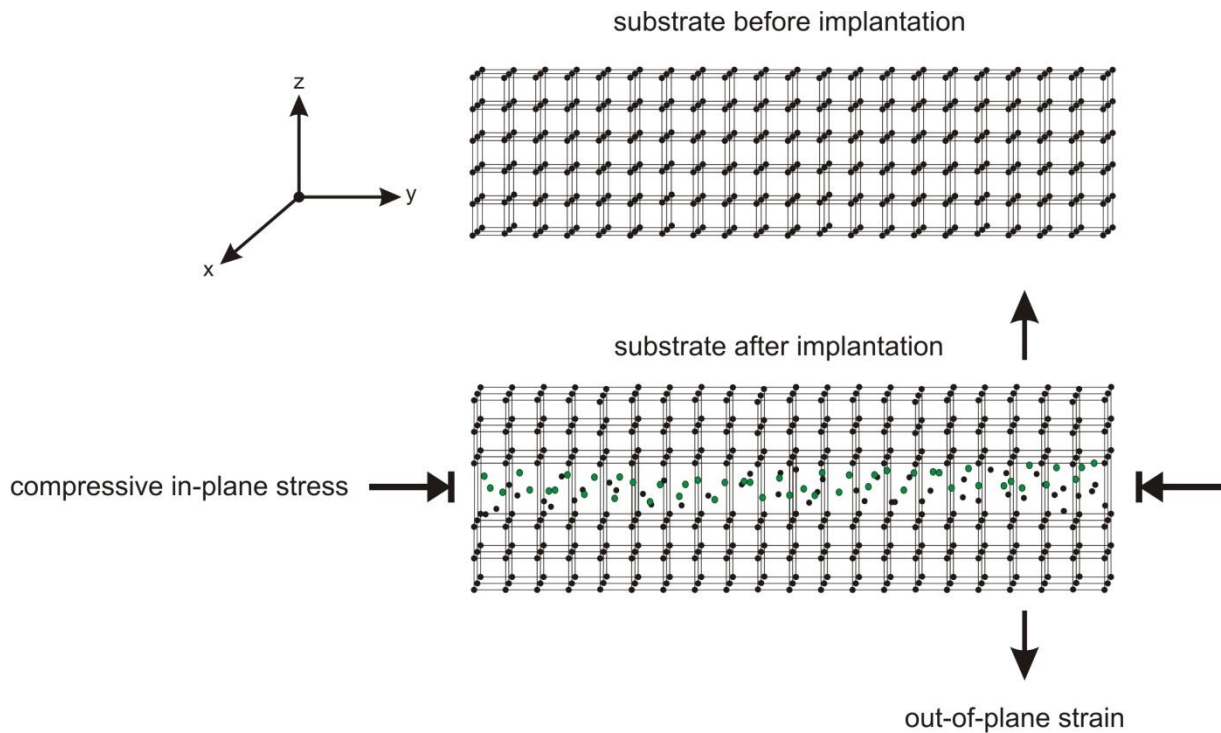


Figure 4.14- Representation of the compressive in-plane stress on the xy plane parallel to the surface and the out-of-plane strain on the z direction.

In the plane stress state, σ_{iz} is assumed to vanish and the remaining strain and stresses are independent of z ($\sigma_{zi} \vec{r} = 0$). Based on these considerations we can express the strain of an implanted layer as

$$\epsilon_{ij}^T = 0 \rightarrow i = x, y, j = x, y$$

$$\varepsilon_{ij}^T = \varepsilon_{ij}^* + e_{ij} \rightarrow i = z, j = z,$$

where ε_{ij}^* are the intrinsic deformations and e_{ij} are the elastic reaction of the material.

Then, the following relations are obtained

$$\varepsilon_{xx}^T = \varepsilon_{yy}^T = 0 \rightarrow \begin{cases} \varepsilon_{xx}^* + e_{xx} = 0 \rightarrow \varepsilon_{xx}^* = -e_{xx} \\ \varepsilon_{yy}^* + e_{yy} = 0 \rightarrow \varepsilon_{yy}^* = -e_{yy} \end{cases} \rightarrow \varepsilon_{xx}^* = \varepsilon_{yy}^* = \varepsilon^*$$

$$\varepsilon_{zz}^T = \varepsilon_{zz}^* + e_{zz} = \left(\frac{\delta d}{d} \right)_z.$$

The general elasticity relations of state are then simplified as

$$\begin{aligned} e_{xx} &= \frac{1}{E} [\sigma_{xx} - \nu \sigma_{yy}] \\ e_{yy} &= \frac{1}{E} [\sigma_{yy} - \nu \sigma_{xx}] \\ e_{zz} &= -\frac{\nu}{E} [\sigma_{xx} - \sigma_{yy}] = -\frac{\nu}{1-\nu} e_{xx} + e_{yy} \\ e_{xy} &= \frac{1+\nu}{E} \sigma_{xy} \\ e_{xz} &= \varepsilon_{yz} = 0 \end{aligned},$$

from which we can consider the following relations:

$$\begin{aligned} \varepsilon_{xx} + \varepsilon_{yy} &= \frac{1-\nu}{E} \sigma_{xx} + \sigma_{yy} \\ \varepsilon_{yy} &= \frac{-\nu}{E} \varepsilon_{xx} + \varepsilon_{zz}, \end{aligned}$$

and

$$\begin{aligned} \sigma_{xx} &= \frac{E}{1+\nu} \left[\varepsilon_{xx} + \frac{\nu}{1-\nu} \varepsilon_{xx} + \varepsilon_{yy} \right] = \frac{E}{1-\nu^2} \varepsilon_{xx} + \nu \varepsilon_{zz} \\ \sigma_{zz} &= \frac{E}{1+\nu} \left[\varepsilon_{zz} + \frac{\nu}{1-\nu} \varepsilon_{xx} + \varepsilon_{zz} \right] = \frac{E}{1-\nu^2} \varepsilon_{zz} + \nu \varepsilon_{xx} \end{aligned}$$

Moreover, we know that $e_{xx} = e_{yy} = -\varepsilon^*$ implying that

$$e_{zz} = -\frac{\nu}{1-\nu} -2\varepsilon^* ,$$

and

$$\sigma_{ij} = \frac{E}{1+\nu} \left[e_{ij} + \frac{\nu}{1-\nu} e_{xx} + e_{yy} \right]$$

$$\sigma_{yy} = \frac{E}{1-\nu^2} [e_{yy} + \nu e_{xx}]$$

$$\sigma_{xx} = \frac{E}{1-\nu^2} [e_{xx} + \nu e_{yy}]$$

$$\sigma_{zz} = 0$$

The in-plane stress and the out-of-plane strain in implanted layers are then correlated by the following expression:

$$\sigma_{yy}^{in-plane} = -2\mu \left(\frac{\delta d}{d} \right)_z .$$

The strains of the implanted layer can be extracted from the XRD curves. The maximum of the compressive stress have been thus estimated for the three studied fluences and are given in Table 4.2. The in-plane stress is observed to increase with the fluence.

Table 4.2

Fluence	$\Delta d/d$ (%)	compressive stress (GPa)
$2.10^{16} \text{ cm}^{-2}$	0.6	0.816
$6.10^{16} \text{ cm}^{-2}$	>1.2	>1.632
$10.10^{16} \text{ cm}^{-2}$	>1.2	>1.632

4.3.5. Stress distribution model and its correlation with the preferential orientation of platelets along the Z-direction

In the previous sections we have started to describe and discuss the depth distribution of platelet and spherical-like cavities. In what follows, the description of the cavity distribution is completed by relating and discussing the distinct preferential orientation of platelets along z-direction (depth). The observations are rationalized using a stress and strain dependent model.

As discussed in section 4.2.2, the damaged layer of co-implanted samples is characterized by:

- *Low fluence*: Preferential formation of (001) platelets (i.e. parallel to the surface) in the center of the layer and {111} platelets at deeper and shallower depths.
- *Medium and high fluence*: Preferential formation of spherical bubbles in the surface side, (001) platelets and nanocracks in the middle and {111} platelets at the end of the damaged layer.

Figures 4.15a and b illustrate details of the cavity arrangements observed for the co-implanted samples. Figure 4.15c illustrates the situation for a sample implanted only with H. The predominant (001) platelets observed at the core of the damaged layer and the preferential orientation of {111} platelets at its edges agree well with previous reports [Bru 1999].

Our results demonstrate that the platelet distributions coincide with the simulated concentration profile of the gas atoms (see Section 4.3.2) and, therefore, also coincide with the strain distribution (see Section 4.3.3).

Since the compressive in-plane stress $\sigma_{yy}^{in-plane} = \sigma_{xx}^{in-plane}$ is related to the depth distribution of implanted atoms, it is reasonable to consider the z-strain profile as a Gaussian distribution [Sou 2006]. In this case, the in-plane stress can be defined as:

$$\sigma_{ij}^{in-plane} = -2\mu \left(\frac{\delta d}{d} \right)_Z^{MAX} e^{\left(-\frac{x-Rp^2}{2\Delta Rp^2} \right)} \rightarrow i = (x, y), j = (x, y)$$

where $\left(\frac{\delta d}{d}\right)_z^{MAX}$ is the maximum of out-of-plane strain along z , R_p is the projected range of the implanted ion and ΔR_p is the FWHM (full width at half maximum) of the implanted profile.

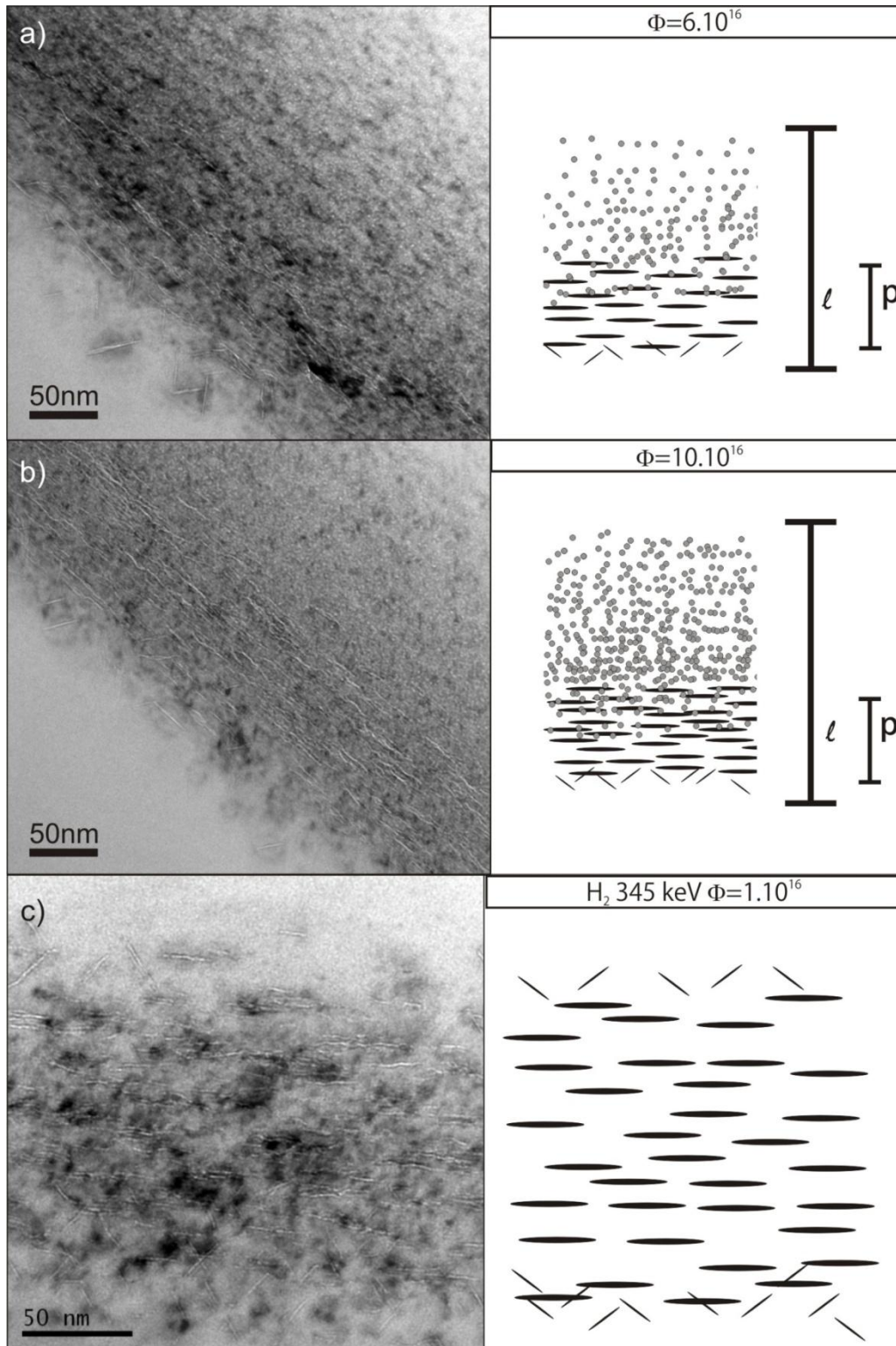


Figure 4.15- Detailed TEM images showing the distribution of cavities found on the co-implanted samples (a) medium fluence, (b) high fluence and only on H implanted samples (c).

H-platelets can be represented by dislocation loops of interstitial nature with an equivalent burgers vector \vec{b}_H ($\vec{b}_H = -\vec{b}_H \vec{n}$ for interstitial loops) characterizing its strain-field [Nee 1988, Gri 2000, Nas 2005]. In this case, the total energy of formation E^T will be given by:

$$E^T = E_f + \int \vec{b}_H \Sigma \vec{dS} \quad (4.1)$$

where E_f is the self-energy of the platelet, $\vec{dS} = dS \vec{n}$ is a surface element and Σ is the total external stress tensor, in this case, the in-plane stress. The following expression is then derived from eq. 0.1:

$$\Delta E = \frac{de}{dv} = - \int \vec{n} \Sigma \vec{n}$$

The interest now is to calculate the energy variation of distinct platelets orientations along the depth z. For this, the calculations were done in 2-D in the (y,z) planes with z parallel to the [001] direction and y corresponding to the [-110] direction (i.e. typical cross section image). In this case, each platelet is reduced to a dipole of edge dislocations with a normal and unitary burger's vector \vec{n} . The energy density variation ΔE of the platelets is then given by:

$$\Delta E = - \begin{pmatrix} n_z \\ n_y \end{pmatrix} \begin{pmatrix} \sigma_{zz} & \sigma_{zy} \\ \sigma_{yz} & \sigma_{yy} \end{pmatrix} \begin{pmatrix} n_z \\ n_y \end{pmatrix} \quad (4.2)$$

$$\Delta E = - n_y^2 \sigma_{yy} + 2n_y n_z \sigma_{zy} + n_z^2 \sigma_{zz} .$$

The (n_y, n_z) values are the projections of the \vec{n} vector on the y and z axis, geometrically determined as follows. The vector $\vec{v} = (y, z)$ parallel to the platelets planes (shown on Fig.

4.16) is given as $\vec{v}_{(111)} = (\frac{\sqrt{2}}{2}, 1)$, $\vec{v}_{(001)} = (1, 0)$ and $\vec{v}_{(100)} = (0, 1)$ from where the unit vectors

$\vec{v}' = y, z$ can be reduced from the relation $y^2 + z^2 = 1$. The unit vectors are then

$\vec{v}'_{(111)} = (\frac{1}{\sqrt{3}}, \frac{\sqrt{2}}{\sqrt{3}})$, $\vec{v}'_{(001)} = 1, 0$ and $\vec{v}'_{(100)} = (0, 1)$, from where the normal vector $\|\vec{v}'\| = \vec{n}$ is

obtained as:

$$\vec{v}' = \begin{bmatrix} y \\ z \end{bmatrix}$$

$$\vec{n} = \begin{bmatrix} 0 & -1 \\ 1 & 0 \end{bmatrix} \vec{v}' = \begin{bmatrix} -z \\ y \end{bmatrix}$$

The values of $\vec{n}_{(111)} = \left(-\frac{\sqrt{2}}{\sqrt{3}}, \frac{1}{\sqrt{3}}\right)$, $\vec{n}_{(001)} = 0,1$ and $\vec{n}_{(100)} = (1,0)$ are then deduced. Once obtained the \vec{n} vectors, the energy variation can be calculated.

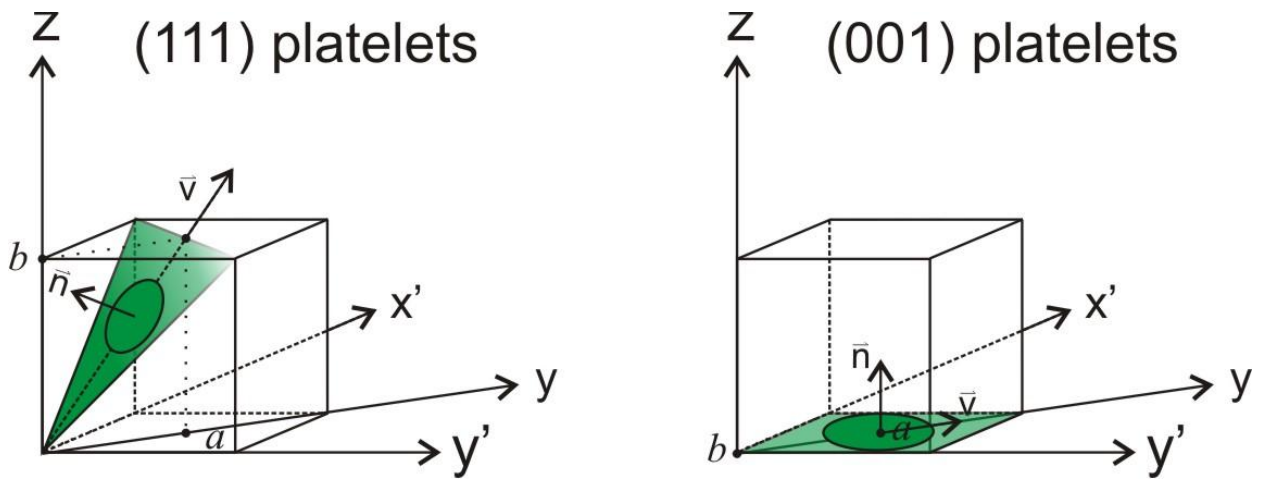


Figure 4.16- Schematic representation of the (111) and (001) platelets from where the \vec{n} vectors are obtained.

In the case of a plane stress ($\sigma_{zi} = 0$) the energy variation equation (Eq. 4.2) is simplified as

$$\Delta E = -n_y^2 \sigma_{yy}$$

where $n_y = -\sqrt{2}/3$ for the (111) platelets, $n_y = 0$ for (001) platelets parallel to the surface and $n_y = -1$ for (100) platelets perpendicular to the surface. For the (001) platelets the energy density variation induced by the in-plane stress is null

$$\Delta E_{(001)} = 0$$

Hence, the in-plane stress does not impose an energetic barrier for platelet nucleation on the planes xy parallel to the stress direction. On the other hand, the (111) platelets energy variation is expressed by:

$$\Delta E_{(111)} = -n_y^2 \left(-2\mu \left(\frac{\delta d}{d} \right)_Z^{MAX} e^{\left(-\frac{z-Rp^2}{2\Delta Rp^2} \right)} \right)$$

$$= \frac{4}{9} \mu \left(\frac{\delta d}{d} \right)_Z^{MAX} e^{\left(-\frac{z-Rp^2}{2\Delta Rp^2} \right)}$$

and the (100) platelets energy variation is given by

$$\Delta E_{(100)} = 2\mu \left(\frac{\delta d}{d} \right)_Z^{MAX} e^{\left(-\frac{z-Rp^2}{2\Delta Rp^2} \right)}$$

where $\left(\frac{\delta d}{d} \right)_Z^{MAX} = f(\Phi)$ is mainly function of the implanted fluence (for given implantation parameters such as temperature, energy among others). Rp is function of the ion energy and ΔRp a function of the implanted energy and fluence. Nevertheless, $\Delta E_{(111)}$ and $\Delta E_{(100)}$ are Gaussian functions of positive values, meaning that the in-plane stress impose an energetic barrier for platelet nucleation and growth into {111} and (100) planes. Considering E_f of both orientations {111} and {001} similar [Mar 2005], the predictions of the model for ΔE variation along the z axis are presented in Fig. 4.17.

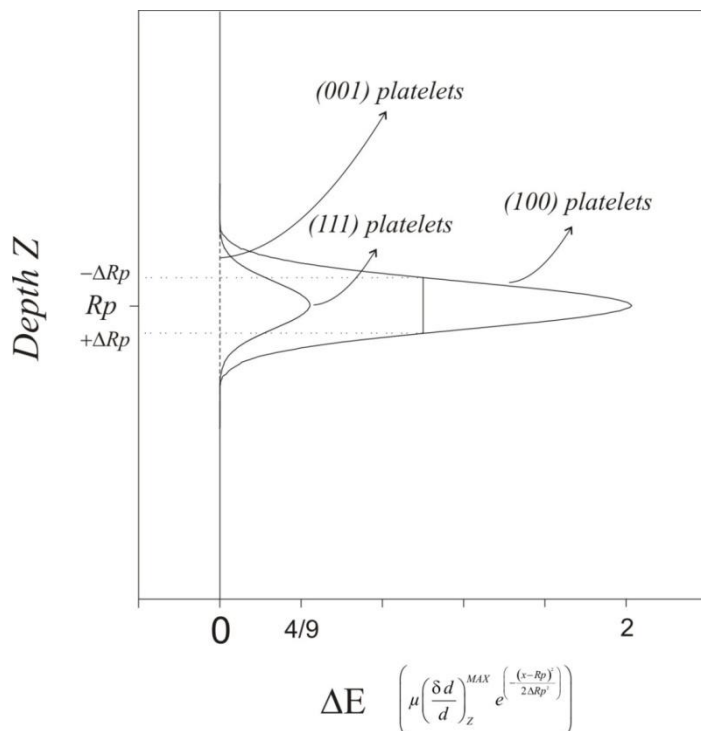


Figure 4.17- Predictions of ΔE variation along the z -axis for the (001), (100) and (111) platelets considering similar E_f .

The {111} and (100) platelets are seen to be strongly unfavorable within the central region of the implanted layer, explaining the predominance of (001) type. However, based on the hypothesis that both platelets orientation {111} and {001} have a similar self-energy E_f , one should expect an equal distribution of both orientations at the edges of the strain profile. Instead, **only platelets of {111} type are observed**. This result, linked with the experimental observation that only {111} platelets are observed when H is introduced by diffusion through plasma hydrogenation regardless of the Si wafer orientation [Nic 2000] (no stress is expected to be associated with the technique), suggests a distinct self-energy at the form as $E_f^{\{001\}} > E_f^{\{111\}}$. This energy difference may be small and probably only becomes evident when no external strain is acting on the system. Assuming $\Delta E_f^{\{001\}} = E_f^{\{001\}} - E_f^{\{111\}} > 0$ renders $\Delta E^{\{001\}} = \Delta E_f^{\{001\}} + \Delta E_{strain}$. According to this assumption, the predictions of the model are given in Fig. 4.18.

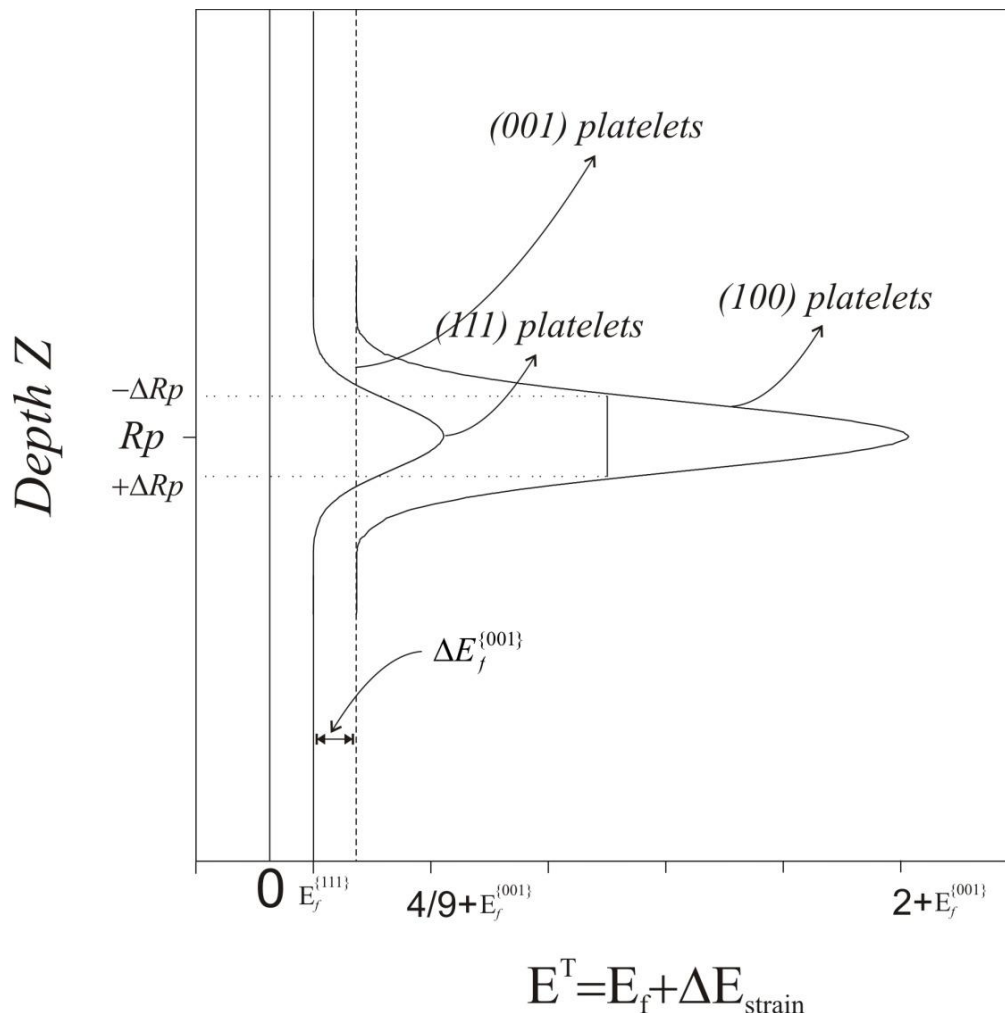


Figure 4.18- Predictions of the model for the ΔE variation along the z -axis for the (001), (100) and (111) platelets considering different self energies $E_f^{\{001\}} > E_f^{\{111\}}$.

With the above considerations, the general distribution of cavities observed for samples implanted only with H and for the low fluence coimplanted ones can be understood. Now, for medium and high fluence co-implanted samples, the absence of {111} type platelets at the shallow edge of the implanted layer can be attributed to the fact that a high concentration of vacancy-clusters favors the formation of spherical bubbles, instead of platelets.

4.4. *Thin film delamination via unstable crack propagation*

In this section we demonstrate that localized blistering/exfoliation may be replaced by a complete thin film delamination process leading to the formation of self-standing films. This phenomenon is triggered at a single nucleation point and is discussed in terms of an unstable crack propagation mechanism. We propose the unstable crack propagation process as a concurrent possibility for layer splitting, which is usually described in the literature in terms of nanocrack coalescence.

4.4.1. **Results**

The experiments were performed in samples implanted at the fluence $\Phi=4\times 10^{16} \text{ cm}^{-2}$, corresponding to the interval of maximum exfoliation efficiency (Fig. 4.2), using either a high current density mode Hc ($1.5 \mu\text{A}\cdot\text{cm}^{-2}$) and a low current density mode Lc ($0.5 \mu\text{A}\cdot\text{cm}^{-2}$). The Lc samples behaved as previously reported, i.e., presenting localized blistering and exfoliation after annealing for $T\geq 400^\circ\text{C}$. For the Hc samples, no localized exfoliation or blistering is observed after annealing at $T=400^\circ\text{C}$. Instead, fascinatingly, centimeter wide samples systematically show a complete delamination of the implanted surface after thermal annealing at $T\geq 450^\circ\text{C}$. The remaining surfaces of the samples also show a polished and bright appearance.

Approximately 10% of the H_c tested samples have failed to produce complete delamination. Instead, these samples presented some localized blistering/exfoliation zones in addition to complete delaminated ones. Figure 4.19a exemplifies this situation. It shows a blistered/exfoliated area at the upper left corner and a rather uniform contrast characterizing the delaminated zone. Figure 19b shows a glancing angle optical microscopy observation (GIOM) revealing a radial-like texture morphology on the remaining surface (i.e. the delaminated area). This feature is characteristic from rapid crack propagation in brittle materials and the marks on the surface point out the location from which the process originates. These marks are usually referred to as "chevron" or "herringbone" marks [Hen 2007].

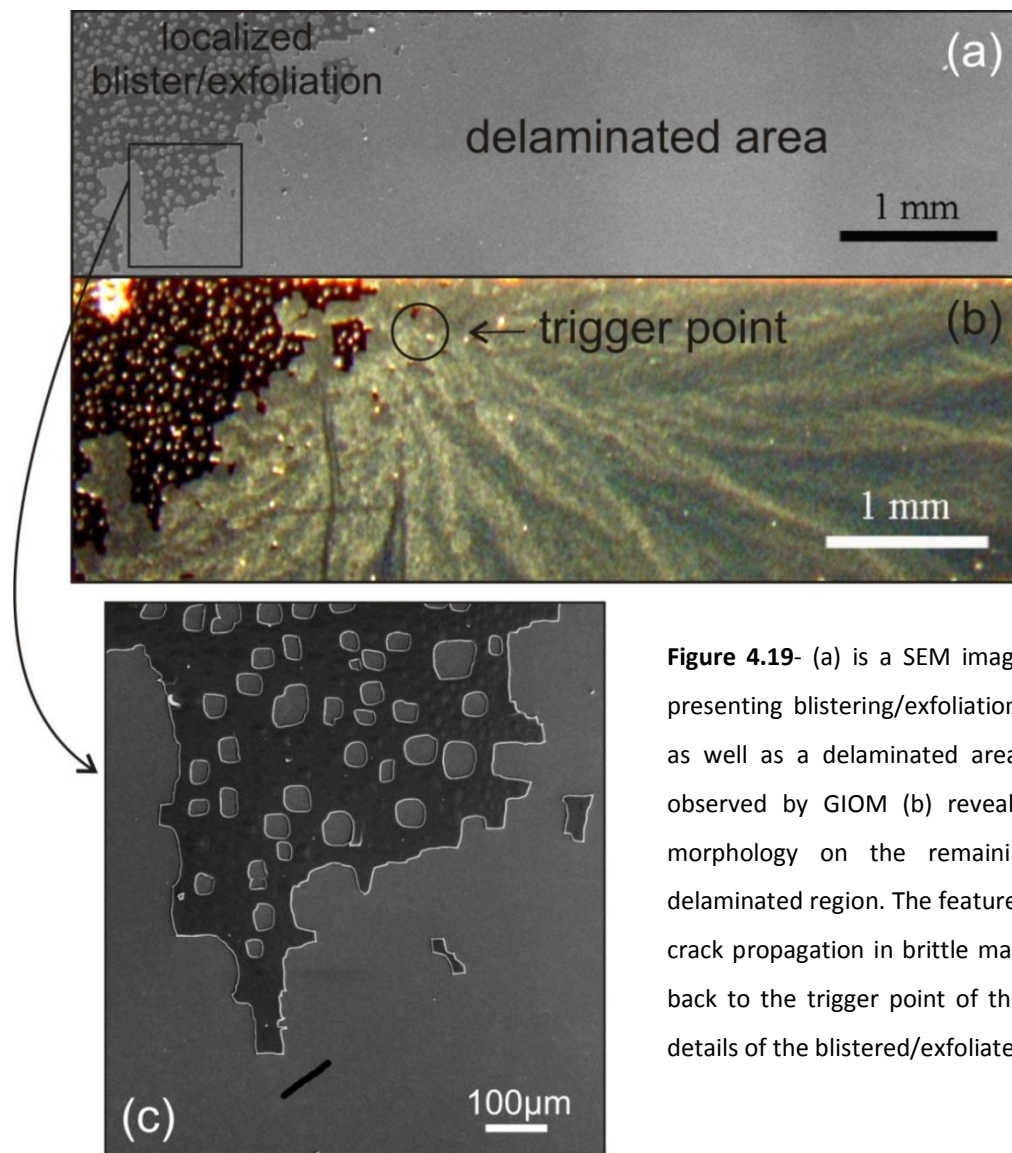


Figure 4.19- (a) is a SEM image showing a sample presenting blistering/exfoliation (upper left corner) as well as a delaminated area. The same sample observed by GIOM (b) reveals radial-like texture morphology on the remaining surface of the delaminated region. The feature is typical from rapid crack propagation in brittle materials and the point back to the trigger point of the process. (c) shows details of the blistered/exfoliated area.

Several implantation/annealing runs were carried out to check the reproducibility of the process. Figures 4.20a, b, c, d and e show GIOM images from some cases. All images present similar radial textures. Figure 4.20f shows in detail the morphology of the surface at the trigger point of the process.

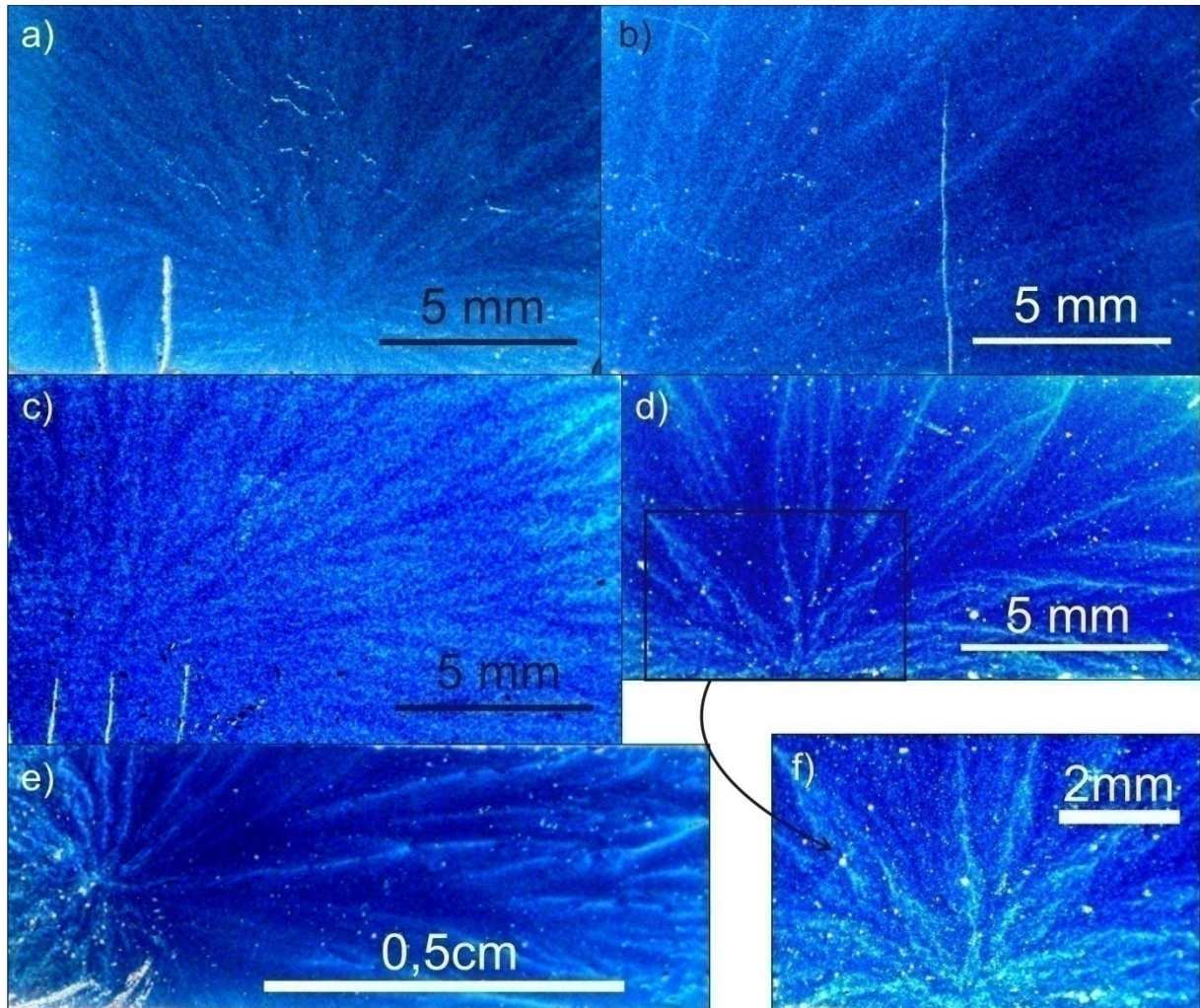


Figure 4.20- (a), (b), (c), (d) and (e) are GIOM images obtained from the remaining surfaces of samples submitted to five distinct implantation/annealing (450°C 1800s) runs respectively. It supports the reproducibility of the process. Fig. 4.17f shows the morphology of the surface at the trigger point of the process.

Figure 4.21 shows a GIOM image from a sample that failed complete delamination, where an interesting aspect is observed (see arrow mark). At this marked region the sample was protected by a mask and, therefore, was not implanted. This region was entirely contoured by the crack front of the delamination process, leaving back straight edges (Fig.

4.21a). Finally, Figure 4.21b shows a non-delaminated implanted region from the same sample, which presents localized blistering and exfoliation.

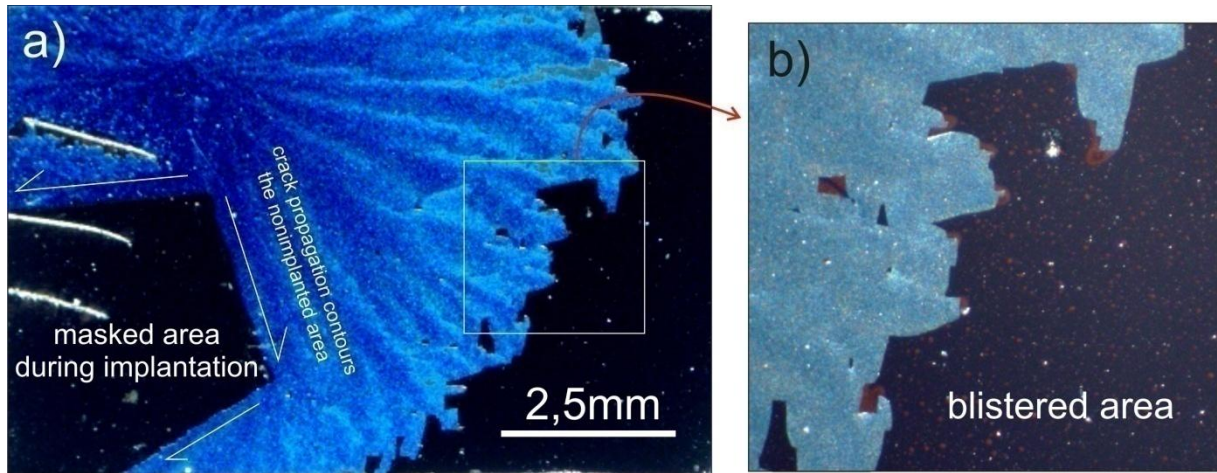


Figure 4.21- (a) shows one of the samples that failed to complete delamination, where an interesting aspect is observed, the masked area of the sample (non-implanted at the sample holding) was perfectly contoured by the crack front, leaving straight edges. (b) the non-delaminated area presented blistering/exfoliation.

Typical free-standing Si thin foils of $1,5\mu\text{m}$ thickness obtained from the crack propagation delamination process are shown in Fig. 4.22.

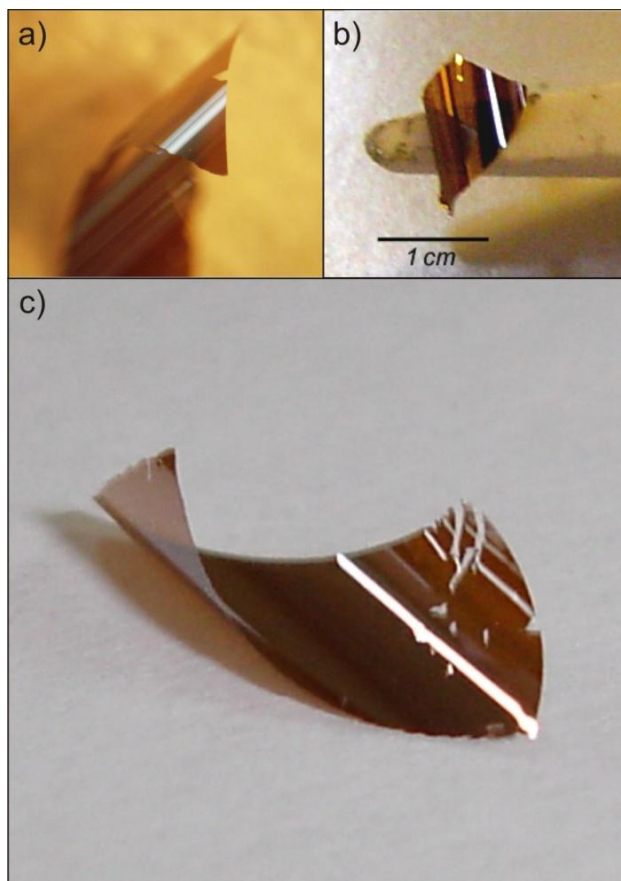


Figure 4.22- (a), (b) and (c) show typical free-standing Si thin foils of $1,5\mu\text{m}$ thickness obtained from Si samples by using the crack propagation delamination process.

The delaminated thin films are often bended in the convex sense. This fact can be understood considering that, when film separation occurs, the in-plane stress from the implanted region (localized at the bottom of the thin film) is free to relax. This creates a differential expansion on the film. The effect is explained schematically in Fig. 4.23.

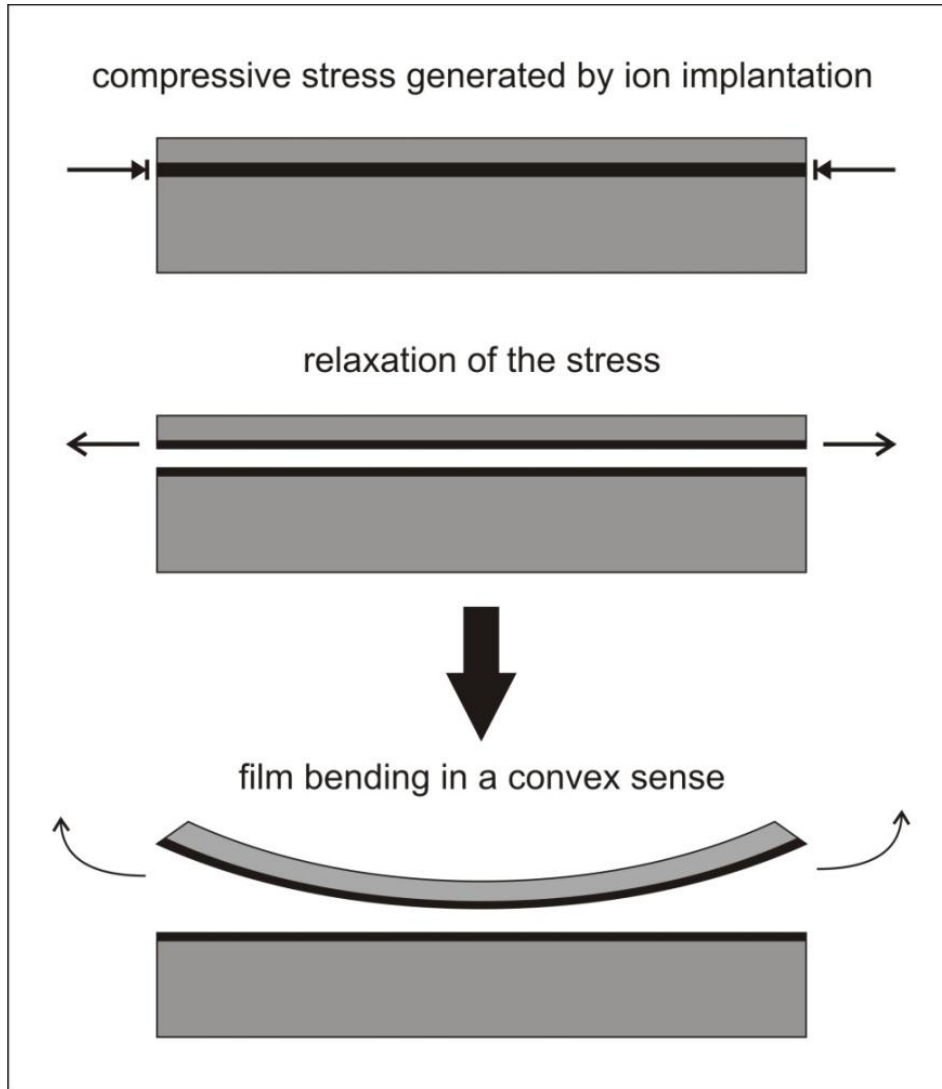


Figure 4.23- Schematic explanation of the convex bending observed on the delaminated thin foils.

Figure 4.24 shows a typical AFM measurement of the substrate delaminated surface. The measured roughness (RMS values) amounts $\approx 13\text{nm}$. This value is in the same order of the roughness obtained by the Smart-Cut[®] method [Cha 1999]. For comparison, the measured RMS roughness of a pristine surface from the same wafer is 0.15 nm.

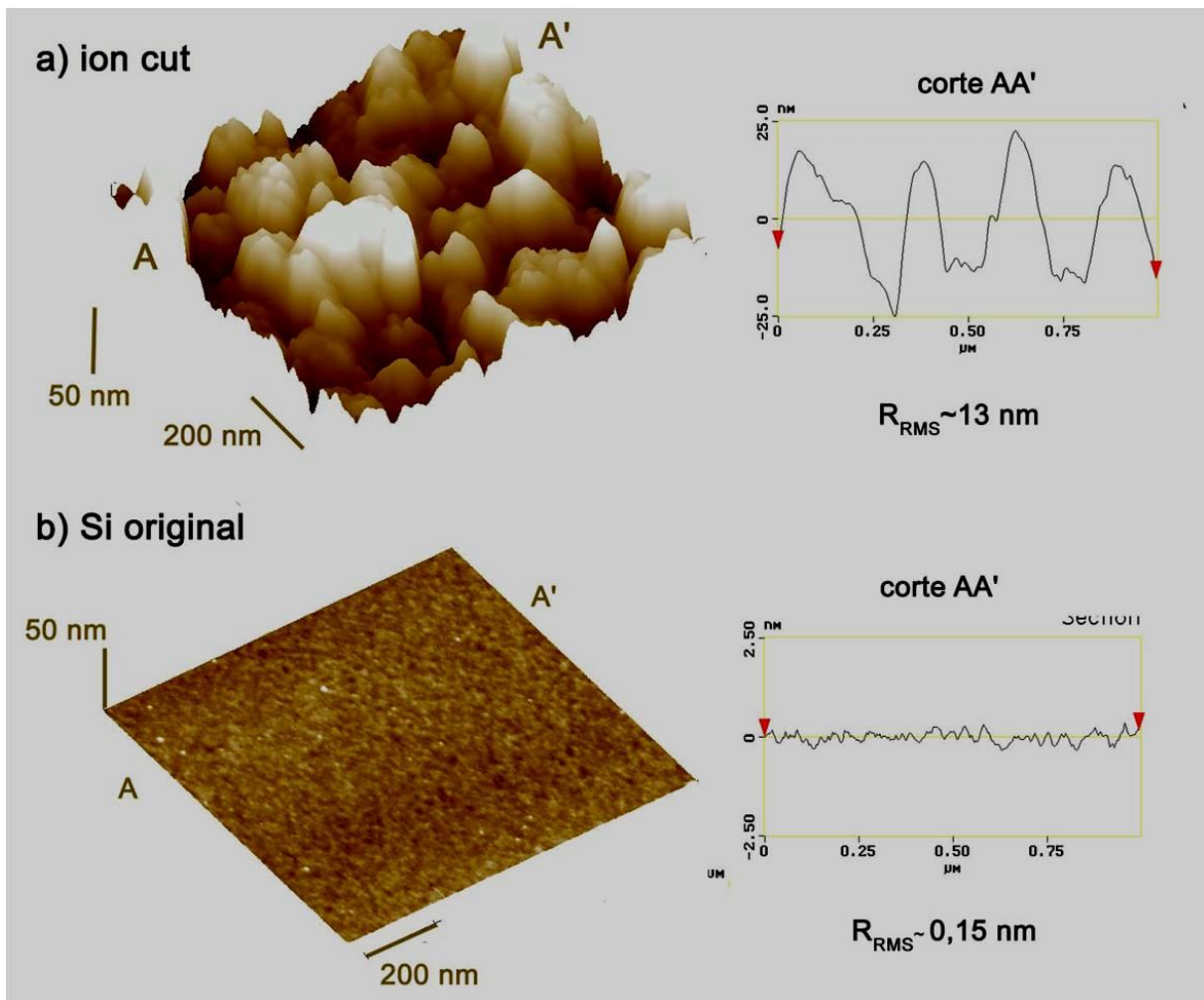


Figure 4.24- AFM measurements of the substrates surfaces after delamination presenting a RMS of $\approx 13\text{nm}$

TEM investigations of *Lc* and *Hc* samples after annealing of 350°C for 1800s were performed. Figures 4.22a and b show images from *Lc* implanted samples and Figs. 4.22c and d from *Hc* implanted ones. Apparently, a higher concentration of nanocracks form in the *Lc* samples, while the *Hc* ones are characterized by a scattered distribution of nanocracks and a high density of small spherical cavities.

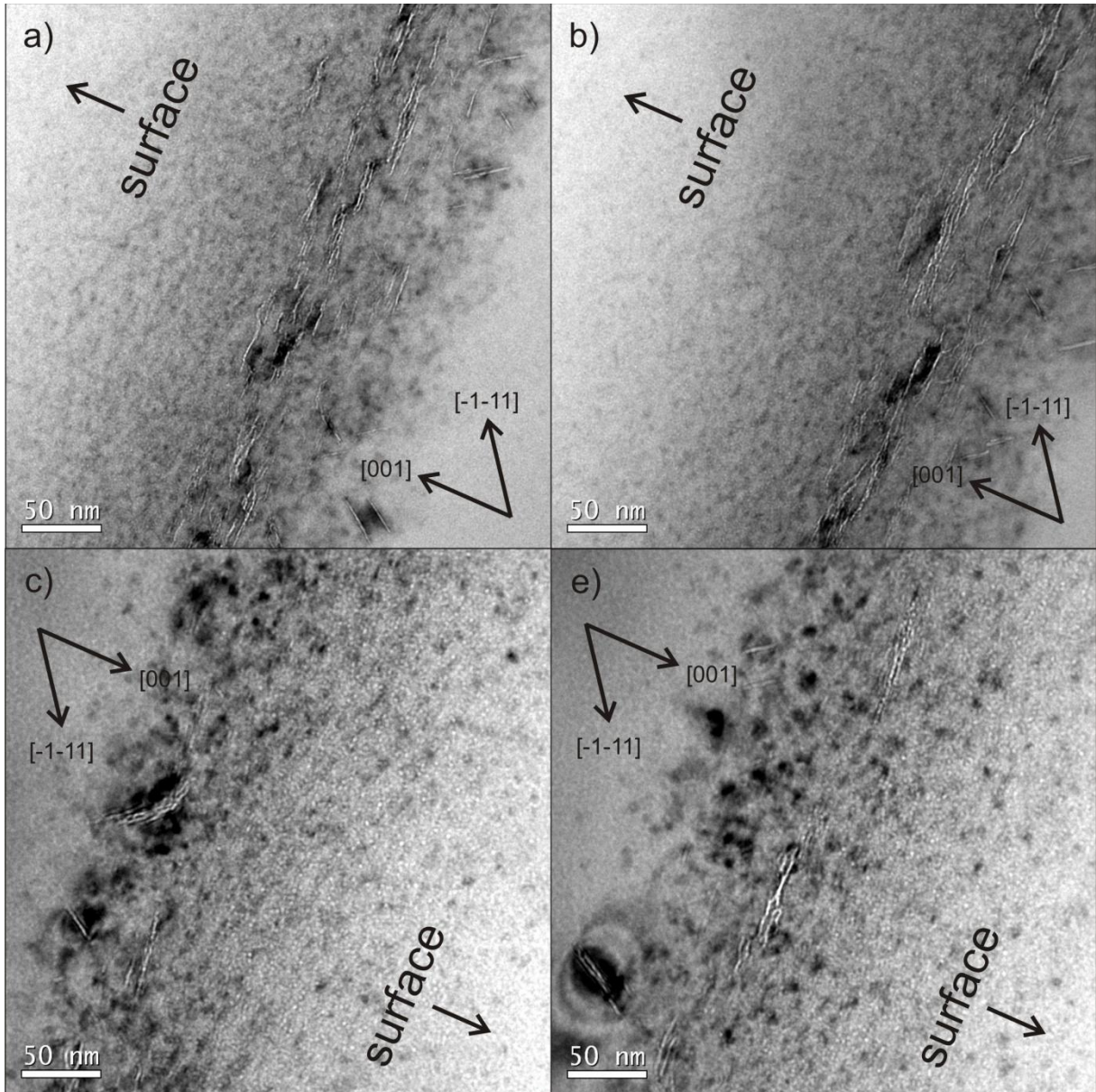


Figure 4.25- (a) and (b) show cross-section TEM images of the *Lc* sample and (c) and (d) refer to *Hc* mode.

Longitudinal ($\theta/2\theta$) x-ray scattering measurements in the vicinity of the (004) reflection were used to evaluate the strain content in both sample types, either at the as-implanted state and after 350°C (1800s) annealing. The results for the as-implanted samples are presented in Fig. 4.26. The interference fringes seem to arise a little earlier for the *Hc* sample, indicating that the strain profile is slightly wider. Both samples present quite similar fringe spacing up to the high strained zone, where differences appear. The *Lc* sample holds a $\epsilon^{\text{Max}} \approx 1.3\%$ and the *Hc* one $\epsilon^{\text{Max}} \approx 1.6\%$. Figure 4.27 presents the simulation of the strain profiles obtained using the method described in section 4.3.3.

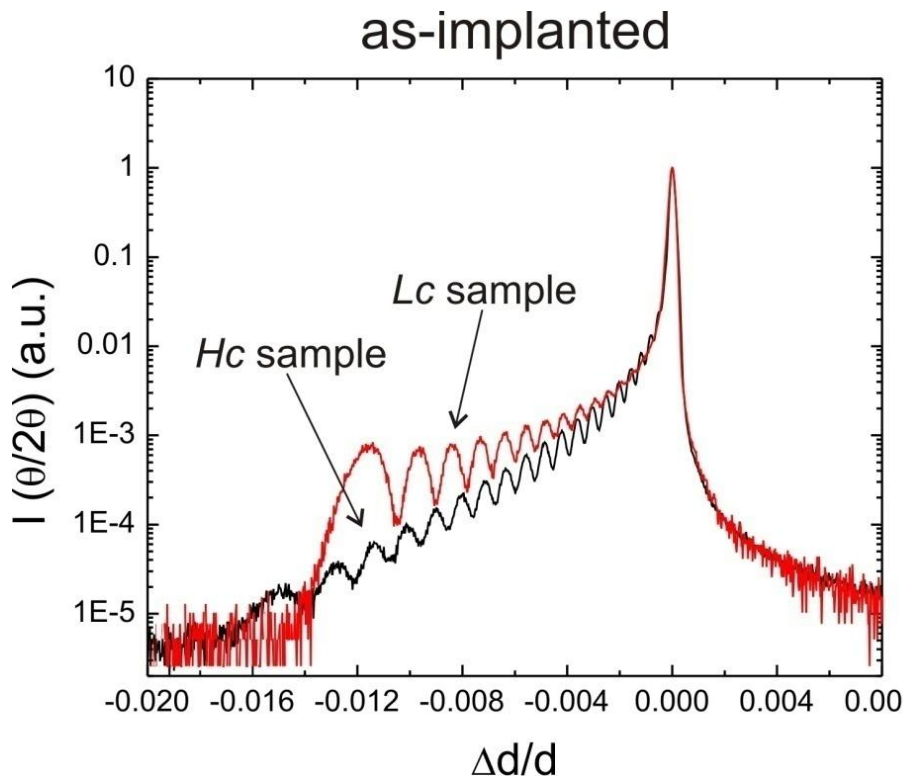


Figure 4.26- X-ray scattering profile of the (004) reflection obtained for the Hc and Lc samples in the as-implanted state.

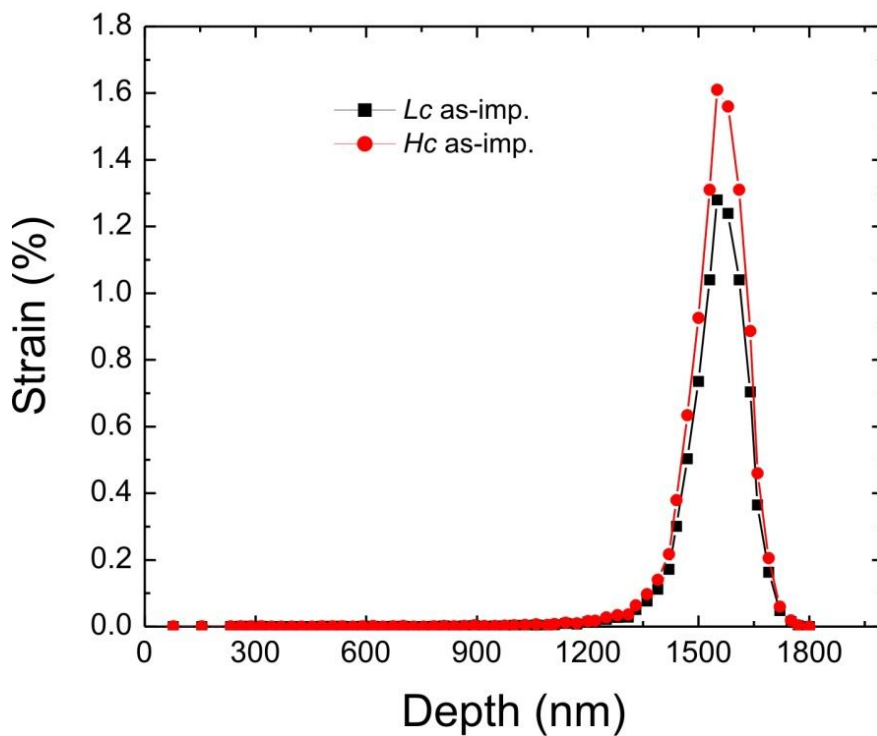


Figure 4.27- Simulation of strain profiles for the Hc and Lc as-implanted samples using the x-ray scattering data and SRIM simulated H atoms profile as reference.

The static Debye-Waller attenuation (Wh) factor has been extracted from the simulations and the result is presented (Fig. 4.28) in terms of Lh , defined as $Lh = -\ln(Wh)$ [Ded 1973]. It

clearly shows that a higher mean atomic displacement from the diffractive planes occurs for the H_C sample. A similar effect was previously attributed to the presence of larger clusters [Mil 1995]. In our case, the Wh factor behaviour seems to indicate that larger plate-like defects were already formed after the H_C mode implantation [Sou 2006].

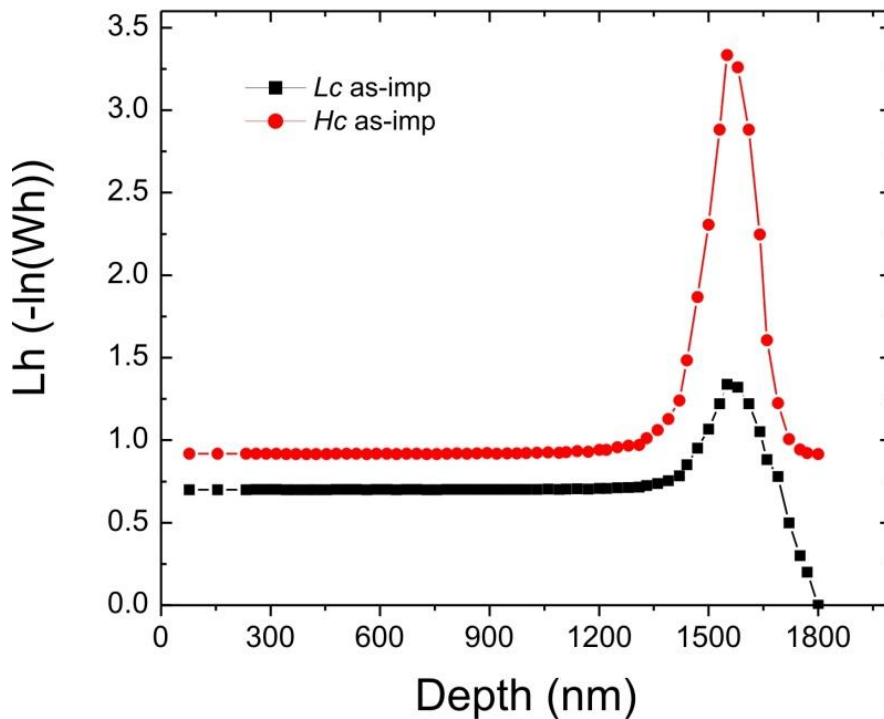


Figure 4.28- Debye-Waller attenuation Wh factor extracted from the simulations (presented in terms of L_h , defined as $L_h = -\ln(Wh)$) plotted against depth.

The scattering profiles obtained after annealing are presented in Fig. 4.29. It shows that the strain evolution of the samples is very different. After 350°C 1800s, a temperature not far below the exfoliation temperature ($\approx 400^\circ\text{C}$), the loss of interference fringes and a considerable decrease of the scattering intensity are observed for the L_C sample. Strain is still present at comparable level to the as-implanted state, although, the coherent interference originated from the highly strained crystalline planes is completely lost. This effect can be attributed to the formation of a high density of large defects, e.g. nano or microcracks, which cause strong and localized tilting of the crystalline planes [Sou 2006], as exemplified in Fig. 4.30.

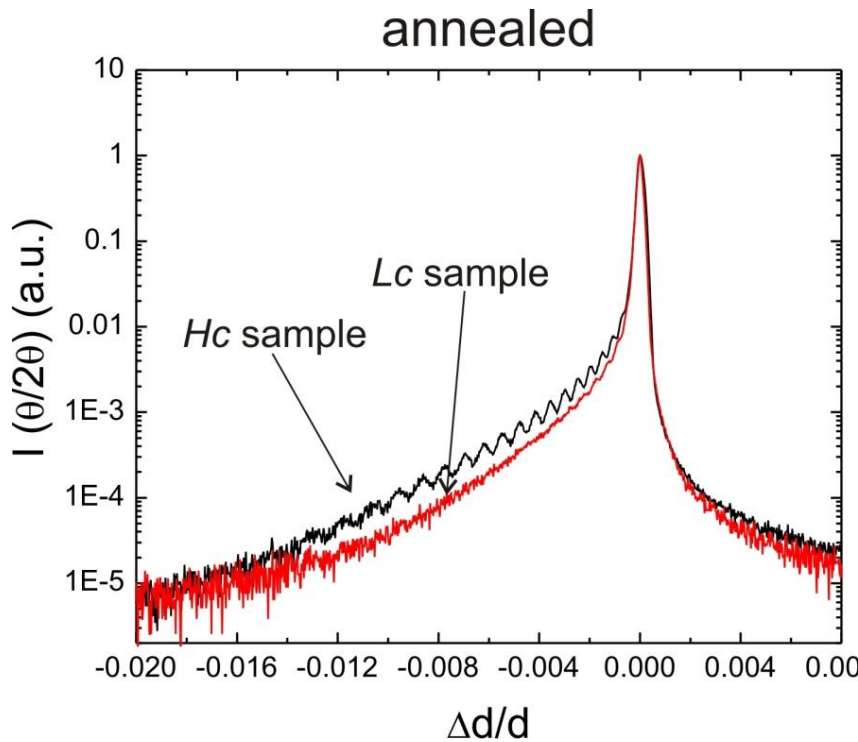


Figure 4.29- X-ray scattering profiles of the (004) reflection obtained for the *Hc* and *Lc* samples after annealing of 350°C for 1800s.

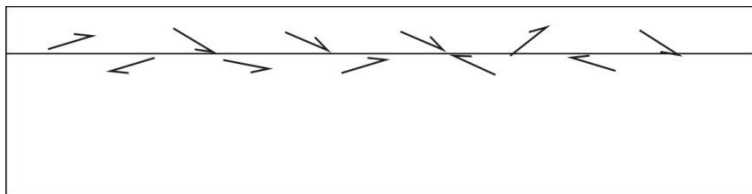


Figure 4.30- Schema of the localized tilting deformation of the crystalline planes after annealing of the *Lc* sample.

Differently, the *Hc* sample presented only a modest change of the strain profile after annealing. The fringes were still observed, similarly to the as-implanted state, but with slightly reduced intensity. This implies that a restricted evolution of the crack-like defects took place. Cracks may have formed but were not able to strongly deform the crystalline planes. It means that: i) even after quite high annealing temperature, the in-plane stress is still present in the implanted layer, basically acting parallel to the samples surface as a shear stress between the substrate and the thin film (above the implanted layer); ii) crack-like cavities did not grow considerably. This situation is schematically represented in Fig. 4.31. (compare with Fig. 4.30).

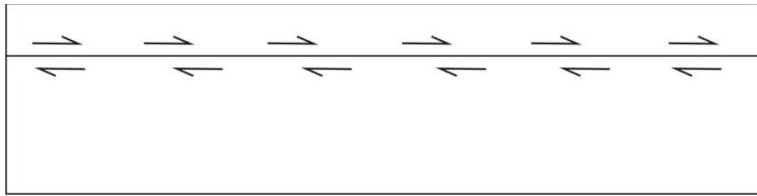


Figure 4.31- Schema showing that, even after annealing at 350°C, the H_c sample still presents the in-plane stress confined to a narrow layer.

4.4.2. Discussions and model formulation for the delamination process drives by fast crack propagation

TEM investigation (Fig. 4.25) suggests that, after annealing, a higher concentration of larger platelets and nanocracks are present in the L_c sample. The x-ray diffraction patterns confirm these observations and also indicate that the H_c samples present very limited evolution of crack-like cavities from the as-implanted to the low temperature annealed state.

The whole scenario could be explained as follows. The high ratio of energy transfer to the wafer impinged by the H_c mode, result in the increase of the substrate temperature during implantation. The thermal energy can promote the cavity formation during implantation, which explains the presence of larger clusters detected in the as-implanted state (x-ray measurements, Fig. 4.26). The implantation at high temperature also favours the formation of spherical bubbles [Sil 2004]. In our case, this occurs in detriment of the formation of platelets and nanocracks. During further annealing, the fewer nanocracks formed have less chance to grow, since a large amount of gas is trapped inside spherical cavities. They also have less chance to coalesce, since their density is reduced. Differently, the L_c sample will follow the usual route of nanocrack growth and coalescence until blistering/exfoliation occurs at $T \approx 400^\circ\text{C}$.

Blistering and exfoliation will occur when a crack grows until it achieves a characteristic size, as discussed in Chapter 3, as well as in H induced blistering studies from the literature [Hua 1999, Fen 2004, Ter 2007]. As a general rule, blistering/exfoliation only occurs under appropriate conditions represented by $h/r \ll 1$, being h the depth at where the crack is located and r its radius [Fen 2004].

In contrast, for H_c implanted samples, it is observed that blistering/exfoliation is inhibited (until 450°C). In addition, TEM and XRD results also indicate that cracks had

experienced sufficiently restricted growth to keep the condition $h/r \gg 1$, avoiding relaxation via blistering. Furthermore, GIOM observations indicate that delamination occurs by crack propagation triggered from a single nucleation point, thus suggesting that only very few cracks can achieve instability conditions. In order to explain these general observations, a model based on the fracture mechanics theory was developed. The model is grounded on the follow assumptions: i) the cracks experience a restricted growth ($h/r \gg 1$) thus avoiding blistering; ii) the process occurs by unstable crack propagation triggered from a single crack;

According to linear elastic fracture mechanics, and based on the stress intensity factor criteria, the failure mode resulting in the unstable propagation of a crack takes place when the stress intensity factor at the crack tip (K_I) reaches the fracture toughness of the material (K_{IC}). Assuming that $h \gg r$, the crack can be regarded as a Griffith's crack of radius r and short axis s ($s \ll r$) embedded in an infinite elastic body. Thus, driven by its internal pressure, the crack will experience a mode-I crack opening, and unstable propagation of the defect will occur if the following condition is achieved:

$$K_{Inanocrack} = K_{IP} \geq K_{ICSi} , \quad (4.3)$$

where $K_{Inanocrack}$ is the stress intensity factor at the crack tip of a given nanocrack expressed by K_{IP} , denoting that the stress intensity factor is related to the internal pressure, and K_{ICSi} is the fracture toughness of *Si*. The mode-I stress intensity factor of a crack embedded in an infinite elastic body containing an internal pressure p is given by [Tad 2000]

$$K_{IP} = 2p \sqrt{\frac{r}{\pi}} . \quad (4.4)$$

From the elasticity theory, the equilibrium pressure of a crack is obtained as [Har 2002]

$$p_{eq} = \sqrt{\frac{\pi\mu\gamma}{(1-\nu)r_{eq}}} . \quad (4.5)$$

The stress intensity factor at the crack tip can then be expressed by

$$K_{IP} = 2 \sqrt{\frac{\mu\gamma}{(1-\nu)}} . \quad (4.6)$$

Equation 4.6 states K_{IP} as a constant value for equilibrium conditions of a gas filled crack in a solid. Taking typical values for Si ($\mu=68\text{GPa}$, $\nu=0,22$ and $\gamma=1,38 \text{ j/m}^2$ [Hue 2006]) it renders

$$K_{IP} = 0,69 \text{ MPa} / \text{m}^2 ,$$

which is $\approx 60\%$ of $K_{ICSi} = 1,19 \text{ MPa} / \text{m}^2$ [Eri 1988] at room temperature and equilibrium conditions.

Equation 4.5 suggests that equilibrium crack growth outcomes in a pressure decrease. However, if the growth of the crack is limited ($h/r \gg 1$), assuming that the Griffith's crack geometry is preserved and using the ideal gas law as an approximation ($PV=nkT$), the pressure will be strictly a function of the temperature $P = f(T)$. The temperature at where delamination is observed to take place (450°C or $\approx 723\text{K}$) is $\approx 140\%$ higher than room temperature ($\approx 300\text{K}$), leading to an increase of $\approx 140\%$ in the pressure and eq. 2 will be expressed as

$$K_{IP723} = 4,8 \sqrt{\frac{\mu\gamma}{(1-\nu)}} . \quad (4.7)$$

rendering to $K_{IP723} = 1,65 \text{ MPa.m}^{-\frac{1}{2}}$. The result shows that, with the imposed conditions ($h/r \gg 1$, experimentally observed), the stress level at the crack tip could easily overcome K_{ICSi} and provide catastrophic propagation. Once triggered, the crack will propagate following the most energetically favourable pathway. The combination of the in-plane stress and a highly damaged layer seems to provide such energetic path. The result is the propagation of the crack front, without deviation, for long distances under the surface. All the approximations considered in the model may lead to an overestimation of the absolute value of K_{IP} at 723K. Nevertheless, the model provides a coherent and reasonable explanation for the experimental observations.

Interestingly, previous study has proposed an expression for the minimal thickness of the over-layer above the implanted layer to produce separation of the substrate without a stiffener [Hua 1998], and $t_{crit}=40\mu\text{m}$ is obtained for Si. It strongly contrasts with the $1.5 \mu\text{m}$ thickness obtained in the present work.

In summary, in this section we have shown that distinct macro-mechanisms of strain relief can develop into H/He implanted Si. One occurs when a high density of platelets and

nanocracks conduct to its coalescence, resulting in localized blistering/exfoliation of the surface. A second mechanism, opposed to the concept of growth and coalescence of individual cracks, occurs when a single defect achieves instability. The process produces the delamination of entire thin films by crack propagation without the presence of an external stiffener. The separation of thin films from a substrate by an ion induced method was believed to be only possible with the previous stiffening of the surface by wafer bonding or deposition methods, this, may holds true for a coalescence based mechanism of splitting.

4.5 Conclusions

The present chapter introduces several considerations on the effects of implantation fluence, and $H:He$ ratio and current density on the exfoliation phenomena. The major conclusions can be summarized as:

- Exfoliation efficiency can be optimized (or manipulated in other sense) with respect to $H:He$ ratio parameters. The 1H:1He implanted ratio presents larger exfoliation efficiency than the 2H:1He one.
- High-fluence co-implantation regimen produces a deleterious effect in exfoliation efficiency; the microstructure evolution has been investigated and discussed in terms of the formation of spherical bubbles instead of platelets and nanocracks. The formation of spherical cavities was correlated to the high availability and depth distribution of vacancies.
- The strain in the samples increase with the fluence. Moreover, for low fluence, the strain profile seems to be closely related to the H concentration depth profile.
- An elasticity based relation between the in-plane stress and the out-of-plane strain in the implanted layers was deduced. Associated to the XRD results, the value of stress in the implanted was estimated for the studied fluences.

- Stress distribution was modeled using a Gaussian distribution. The results were correlated with the depth distribution of platelets cavities distinct orientations.
- Distinct and concurrent mechanisms of localized blistering/exfoliation and delamination were discussed.
- The effect of the current density was investigated. A new phenomenon was uncovered: *the delamination of unbonded Si thin films by unstable crack propagation*. The phenomenon was investigated in details and a model based on the fracture mechanics theory and elasticity was introduced in order to explain the results qualitatively.

CHAPTER 5

Multilayer Exfoliation Study and Multilayer Transfer Concept

According to the concept of layer transfer, one implantation/wafer-bonding/annealing cycle results in a single engineered substrate. For a subsequent slicing of the wafer, a new cycle should be carried out [Bru 1995, Asp 1997]. In this chapter a concept to optimize the exfoliation process flow for layer transfer process is presented. Multiple energy implantations are performed within the same implantation run in order to produce several “ready to slice” splitting layers on the donor substrate. The key scientific concept explored in this chapter is the tailoring of the exfoliation temperature, since it would be worthless if all the layers would exfoliate at the same temperature.

Figure 5.1 (left) shows a process flow scheme of the usual layer transfer concept which results in a rate of

$$1 \text{ transfer} / \text{implantation}$$

In contrast, the multilayer transfer concept schematically presented in Fig. 5.1 (right) provides a process rate of

$$N \text{ transfer} / \text{implantation}$$

where the N value depends on the engineering ability of establishing N distinct temperatures of splitting according to a sequence of $T_i < T_{i+1}$ with $i = \{1, \dots, N-1\}$.

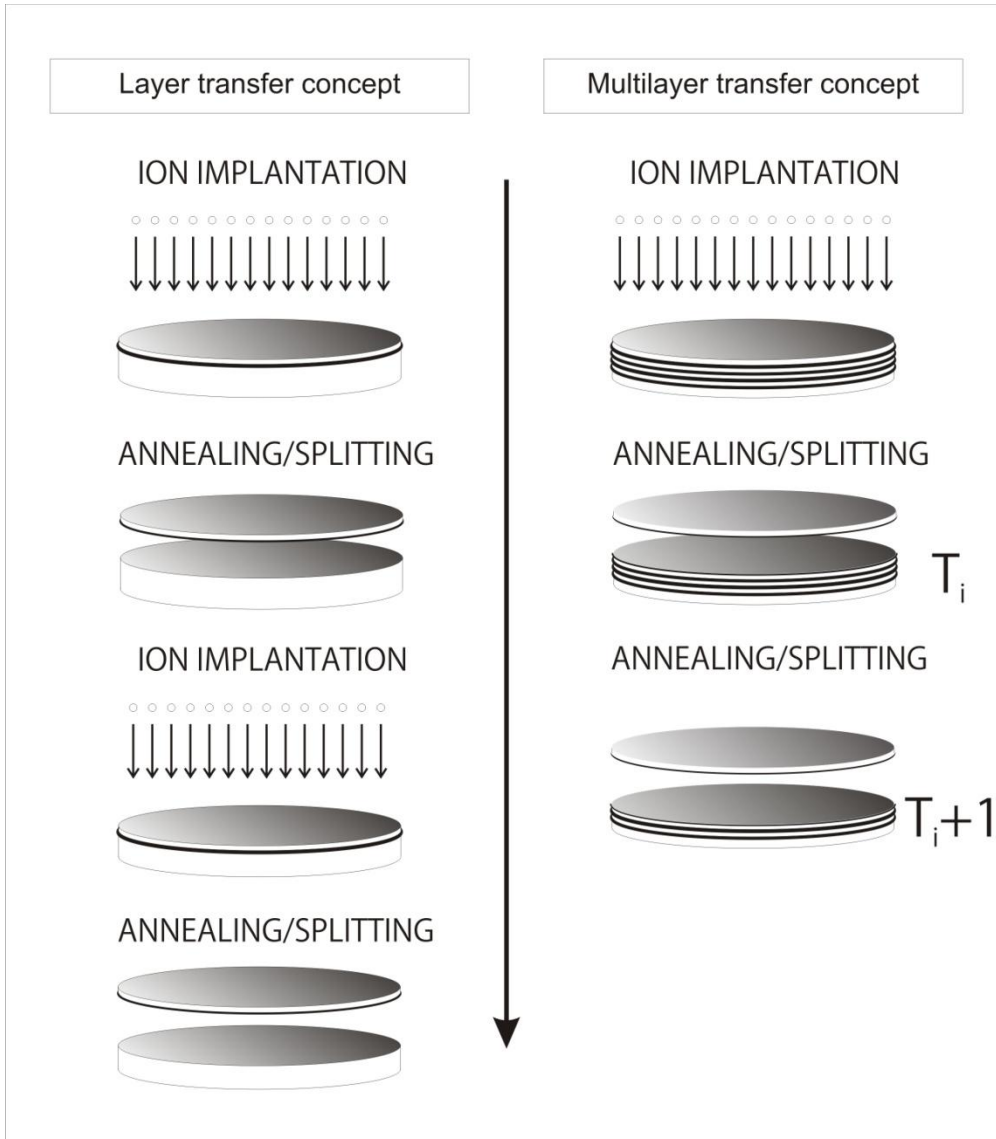


Figure 5.1- Process flow diagrams of the *traditional* single layer transfer (left) and the multilayer transfer process (right).

5.1. Experimental

All the samples were implanted with H_2^+ and He^+ ions, respectively according to 1H:1He ratio. The implantations were calculated to produce two implanted layers ($N=2$) referred as low energy (L_E) and high energy (H_E) layers. The H_E layer was always implanted first. Two groups of multilayer samples were prepared. The implantation parameters of group 1 (samples 1 and 2) are presented in Table 5.1. These samples present the peculiarity of having a 200 nm shift between the H and He profiles in the L_E layer (R_p for H is ≈ 185 nm and for He is ≈ 385 nm). The effects of profile shifting will be explored in more detail in Chapter 6. The H_E layer is located at a depth of approximately 1500 nm and its fluence is higher for sample 2 as compared with sample 1. For the L_E case, the same fluence is adopted for both samples.

Sample number	Implanted species	Energy (keV)	Fluence (cm ⁻²)
Sample 1	H ₂	336 } H_E	0,5X10 ¹⁶
	He	345 }	1,0X10 ¹⁶
	H ₂	30 } L_E	0,5X10 ¹⁶
	He	45 }	1,0X10 ¹⁶
Sample 2	H ₂	336 } H_E	1,0X10 ¹⁶
	He	345 }	2,0X10 ¹⁶
	H ₂	30 } L_E	0,5X10 ¹⁶
	He	45 }	1,0X10 ¹⁶

Group 2 of samples (samples 3 and 4) presents the L_E layer located at ≈ 300 nm and the H_E one at 1500 nm. The implanted fluence of the H_E case also increases from sample 3 to 4, while it is kept constant for the L_E case. A summary of the implantation parameters from group 2 samples is presented in Table 5.2.

Two control samples were also prepared. The first one (sample 5) was done to verify the multilayer concept in only H containing samples, where two layers were implanted only with H_2^+ ions at the depths of 300nm and 1500nm. The second control sample (sample 6) was implanted only at L_E to verify the influence of the H_E on the exfoliation behaviour of the shallow layer using Group 2 L_E parameters. The implantation parameters of these samples are listed in Table 5.3.

Table 5.2 GROUP 2 (overlapped L_E profile)			
Sample number	Implanted species	Energy (keV)	Fluence (cm ⁻²)
Sample 3	H ₂	336 } H_E	1,0X10 ¹⁶
	He	345 }	2,0X10 ¹⁶
	H ₂	60 } L_E	0,5X10 ¹⁶
	He	33 }	1,0X10 ¹⁶
Sample 4	H ₂	336 } H_E	1,5X10 ¹⁶
	He	345 }	3,0X10 ¹⁶
	H ₂	60 } L_E	0,5X10 ¹⁶
	He	33 }	1,0X10 ¹⁶

Table 5.3 Control samples			
Sample number	Implanted species	Energy (keV)	Fluence (cm ⁻²)
Sample 5	H ₂	336	4,0X10 ¹⁶
	H ₂	60	3,0X10 ¹⁶
Sample 6	H ₂	60	0,5X10 ¹⁶
	He	33	1,0X10 ¹⁶

After the implantations, all samples were annealed at temperatures ranging from 350°C to 550°C for 1800s to identify the starting exfoliation temperatures of each layer/sample. The samples were then studied by Optical Microscopy (OM), Scanning Electron Microscopy (SEM) and Transmission Electron Microscopy (TEM).

5.2. Results

To examine the general microstructure aspect of the double layer implantations, sample 3 annealed at 350°C for 1800s was observed by TEM (see Fig. 5.2). Both implanted layers are clearly located at the predicted depths of $\approx 300\text{nm}$ and $\approx 1500\text{nm}$. Inserts of higher magnification images are also shown. The microstructure of the L_E layer mainly shows crack-like cavities, in good agreement with previous works [Höc 2000]. The H_E layer presents nanocracks at the deeper part of the damaged layer (depth close to the $H Rp$) and spherical bubbles at a shallower depth towards the surface. The same kind of microstructure presenting distinct types of defects at distinct characteristic depths has been already

discussed in Chapter 4. The larger distribution of damage observed for H_E results from the increase of the implantation energy and fluence.

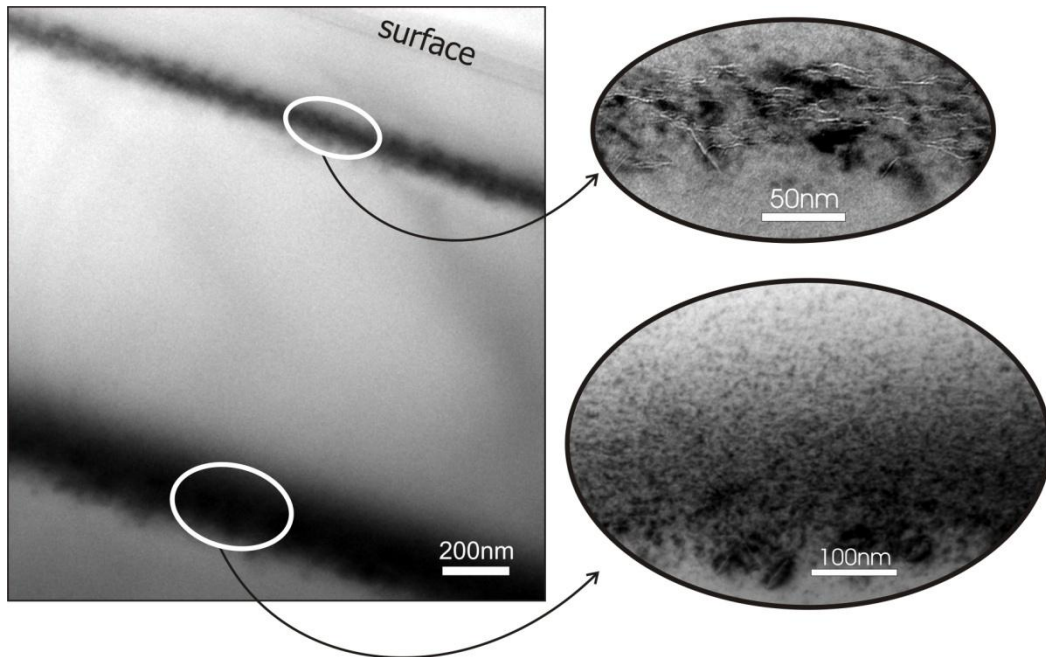


Figure 5.2- Cross-section TEM image of sample 3 after 350°C for 1800s. Both L_E and H_E implanted layer are seen to be formed at depths close to their projected range. The inserts show higher magnifications of the damaged layers.

The SEM images in Fig. 5.3 show the thermal evolution of the multilayer exfoliation from sample 1. The images were obtained with the sample tilted in relation to the electron beam. When annealed at 350°C, sample 1 did not present any exfoliation. After annealing at 400°C, it presented a high density of L_E exfoliations (Fig. 5.3a). The depth at where the L_E exfoliation occurs refers to the H implanted profile ($\approx 185\text{nm}$), indicating that He atoms have migrated to the H -rich region. This aspect will be further explored in Chapter 6. After annealing at 450°C (Fig. 5.3b) scattered H_E exfoliations start to appear in the sample. Figure 5.3d shows a highly magnified view of the surface where the H_E exfoliated areas are easily distinguished from the L_E related ones. After annealing at 500°C, sample 1 produces a very high density of both H_E and L_E exfoliations. As expected, the exfoliation mean size does not change for distinct annealing temperatures. According to the discussions in Chapter 3, it depends basically on the implanted energy and fluence for a given $H:He$ ratio.

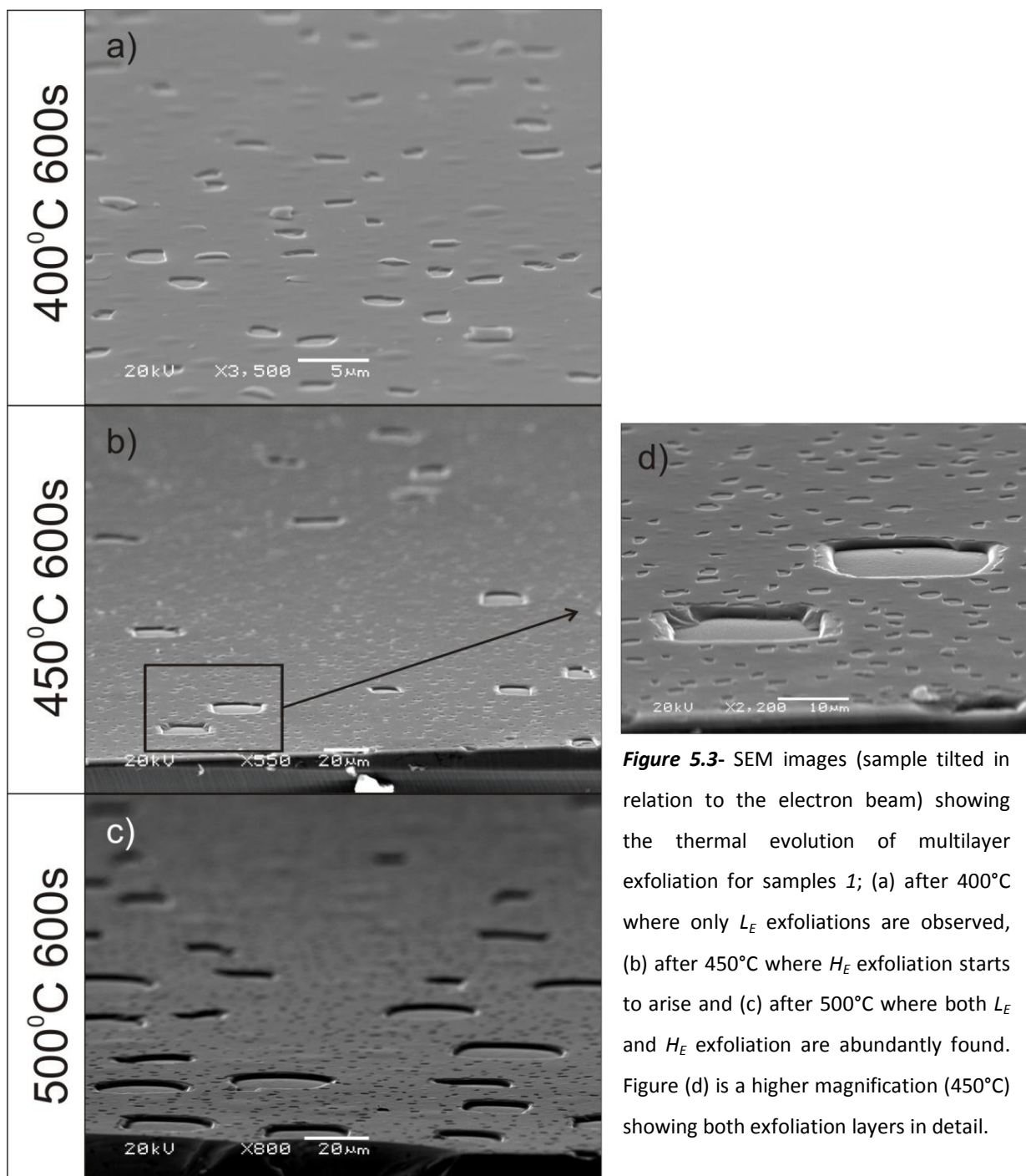


Figure 5.3- SEM images (sample tilted in relation to the electron beam) showing the thermal evolution of multilayer exfoliation for samples 1; (a) after 400°C where only L_E exfoliations are observed, (b) after 450°C where H_E exfoliation starts to arise and (c) after 500°C where both L_E and H_E exfoliation are abundantly found. Figure (d) is a higher magnification (450°C) showing both exfoliation layers in detail.

The SEM images shown in Fig. 5.4 present the thermal evolution of exfoliation for sample 4. Very few L_E exfoliated areas are observed after annealing at 400°C (Fig. 5.4a). This characterizes the lower limit of exfoliation temperature for L_E . In the high magnification insert image a single exfoliation with its cap material nearby is shown. After annealing at 450°C (Fig. 5.4b), the sample presents a significant increase of L_E exfoliation amount. At

500°C, the sample still presents exfoliation related only to the L_E layer. Finally, after annealing at 550°C, the H_E related exfoliation arises (Figs. 5.4c and d).

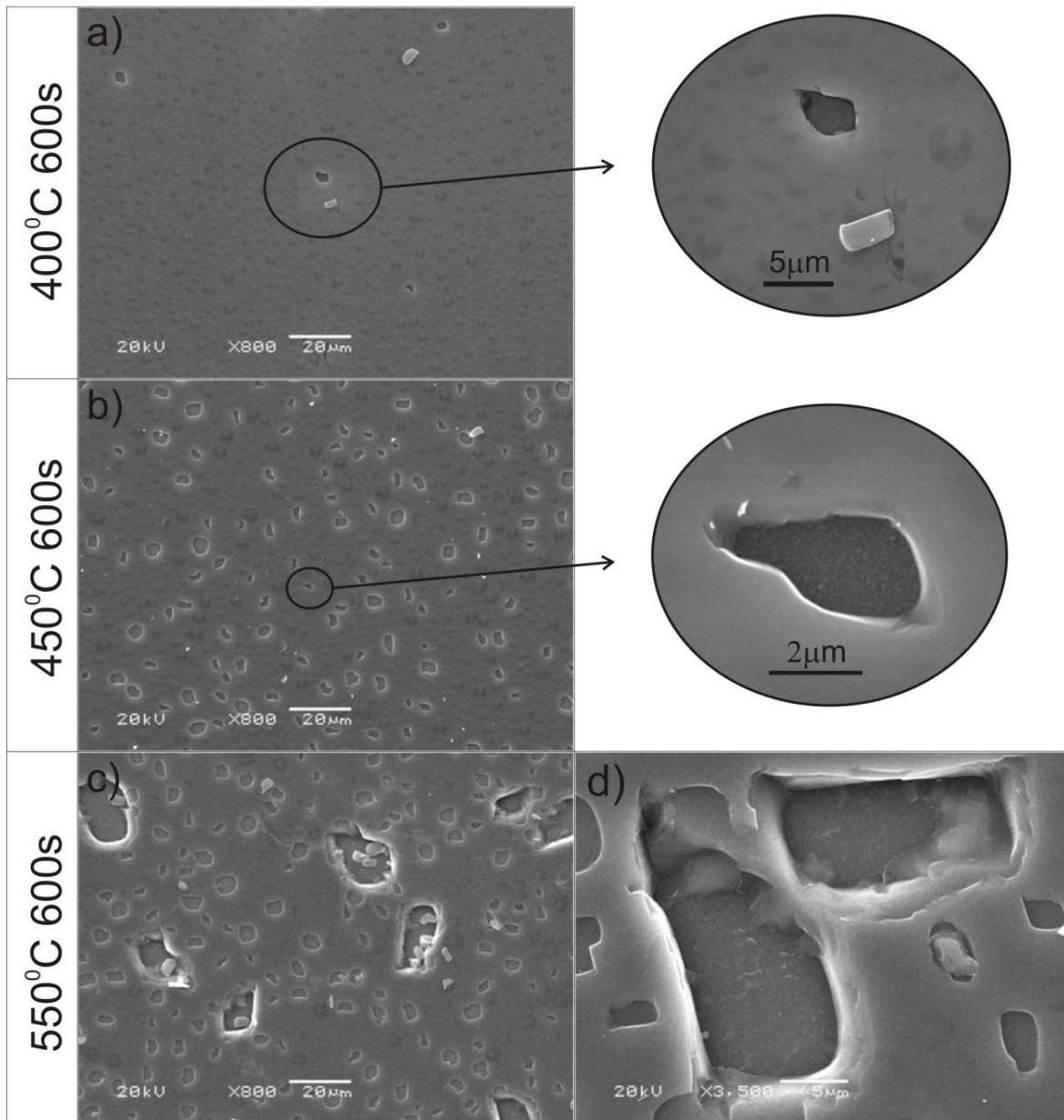


Figure 5.4- SEM images showing the thermal evolution of multilayer exfoliation for sample 4; (a) after 400°C where very few L_E exfoliations are observed, (b) after 450°C where L_E exfoliations are abundant and (c) after 550°C where both L_E and H_E exfoliation are observed. Figure (d) provides a higher magnification of the 550°C annealed sample showing both exfoliation layers in detail.

Optical microscopy (OM) observations reveal interesting aspects that could not be detected by SEM. Figures 5.5a and b were obtained from sample 1 annealed at 400°C and 450°C respectively. The exfoliated areas are easily discernible. In addition, the OM image

also reveals non-exfoliated cavities remaining under the surface, appearing as bright disks. The contrast results from the relatively higher penetration of the visible light compared to the electron beam (SEM). Figure 5.5a and b clearly show a high density of non-exfoliated cavities in the L_E implanted layer.

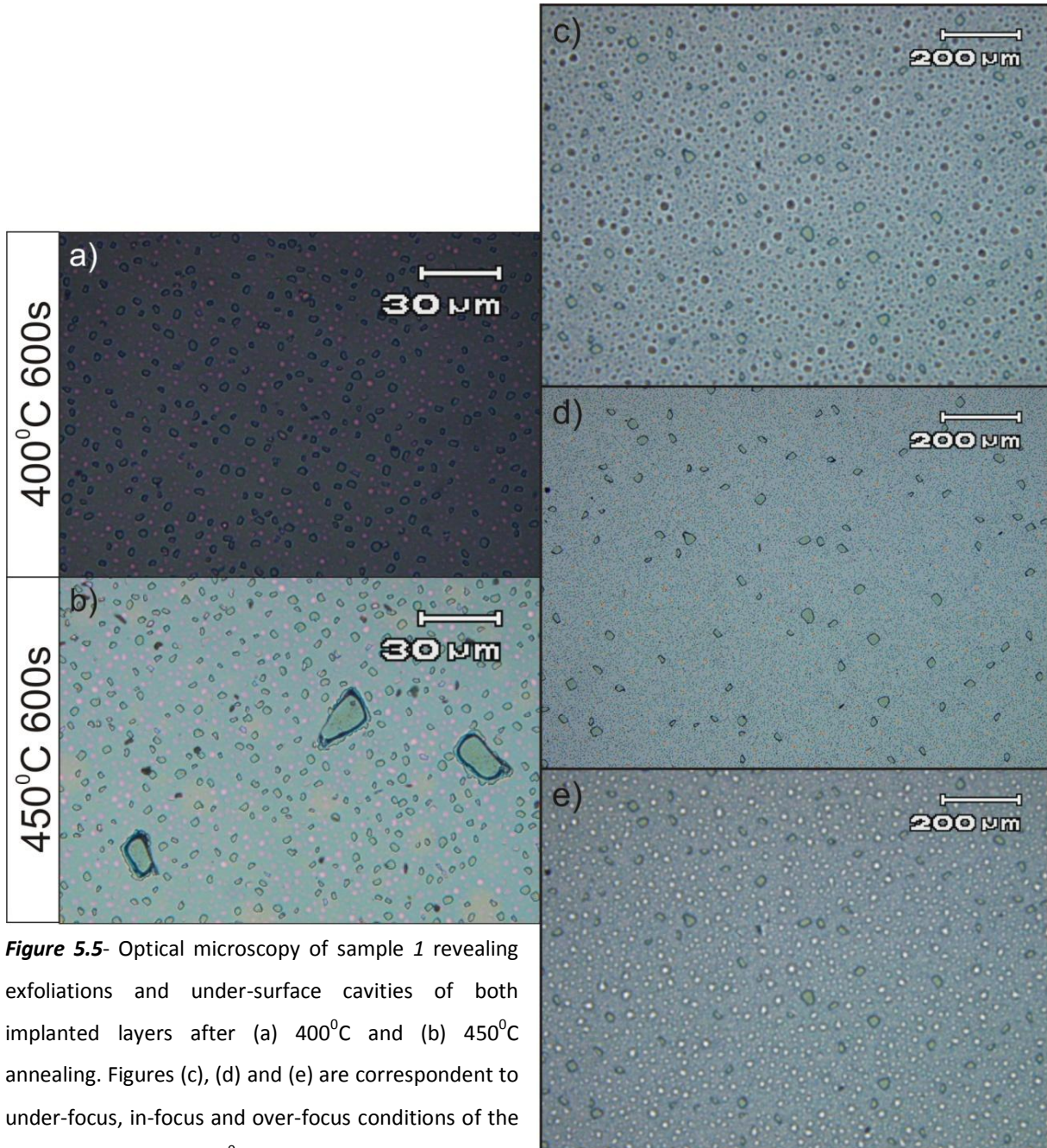


Figure 5.5- Optical microscopy of sample 1 revealing exfoliations and under-surface cavities of both implanted layers after (a) 400°C and (b) 450°C annealing. Figures (c), (d) and (e) are correspondent to under-focus, in-focus and over-focus conditions of the sample annealed at 450°C.

Figures 5.5c, d and e show that the lower magnification enhances the contrast of the under-surface cavities of the H_E layer. It also reveals an interesting focus effect. Image 5.5d obtained in focus conditions presents a weak contrast of the under-surface H_E cavities.

Varying from the in-focus position to over-focus or under-focus, Fig. 5.5c and Fig. 5.5e respectively, the non exfoliated cavities are revealed as dark or bright disks.

After annealing at different temperatures, the exfoliation appearance was verified by OM observations. The results are summarized qualitatively in terms of the appearance of exfoliation in Table 5.4.

Table 5.4. Summary of the results obtained by optical microscopy observations of exfoliation.				
Sample	Element	Energy (keV)	Fluence (at./cm ⁻²)	Annealing temperature (1800s) and results from the exfoliation observations
1	H ₂ He H ₂ He	336 345 30 45	0,5.10 ¹⁶ 1,0.10 ¹⁶ 0,5.10 ¹⁶ 1,0.10 ¹⁶	350°C = no 400°C = abundant L_E 450°C = abundant L_E and few of H_E 500°C = abundant L_E and H_E
2	H ₂ He H ₂ He	336 345 30 45	1,0.10 ¹⁶ 2,0.10 ¹⁶ 0,5.10 ¹⁶ 1,0.10 ¹⁶	350°C = no 375°C = L_E 400°C = abundant L_E and few of H_E 500°C = abundant L_E and H_E
3	H ₂ He H ₂ He	336 345 60 33	1,0.10 ¹⁶ 2,0.10 ¹⁶ 0,5.10 ¹⁶ 1,0.10 ¹⁶	350°C = no exfoliation 400°C = abundant L_E and few of H_E 450°C = abundant L_E and H_E 500°C = abundant L_E and H_E
4	H ₂ He H ₂ He	336 345 60 33	1,5.10 ¹⁶ 3,0.10 ¹⁶ 0,5.10 ¹⁶ 1,0.10 ¹⁶	400°C = no exfoliation 450°C = L_E 500°C = abundant L_E 550°C = abundant L_E and H_E
5	H ₂ H ₂	336 60	4,0.10 ¹⁶ 3,0.10 ¹⁶	350°C = no exfoliation 400°C = L_E 450°C = abundant L_E and H_E
6	H ₂ He	60 33	0,5.10 ¹⁶ 1,0.10 ¹⁶	400°C = no exfoliation 450°C = L_E

5.3. Discussions and conclusions

5.3.1. Group 1 samples

The confirmation of the multilayer exfoliation concept is observed in sample 1. When annealed at 400°C, it only presents L_E related exfoliation. With increasing temperature ($T=450^\circ\text{C}$), H_E related exfoliation starts and develops considerably at 500°C (see, Fig. 5.3). The temperature range for L_E related exfoliation is $350^\circ\text{C} > T \leq 450^\circ\text{C}$. The H_E fluence is higher in sample 2 and after 400°C it presents both H_E and L_E exfoliation. At 375°C, only the L_E exfoliation is observed. The distinct temperatures of exfoliation obtained for the H_E layers of the sample 1 and 2 are certainly related to microstructure modifications induced by the different fluences, as already discussed in Chapter 4.

Therefore, by an appropriate choice of fluences, the temperature of exfoliation can be tailored (exfoliation temperature engineering), thus clearly demonstrating the feasibility of the multilayer transfer concept.

5.3.2. Group 2 samples

Sample 3 annealed at 350°C did not present exfoliation. At 400°C, however, exfoliation from both implanted layers appears. The concentration of exfoliated areas increases for higher annealing temperatures. With the increase of the H_E layer fluence from sample 3 to sample 4 (Fig. 5.4), exfoliation is not observed at temperatures $T \leq 400^\circ\text{C}$. At 450°C, L_E exfoliation occurs abundantly while H_E exfoliation is only detected at $T \geq 550^\circ\text{C}$.

In summary, the remarkable observations obtained for group 2 samples are: i) sample 3 presents L_E exfoliation at $T=400^\circ\text{C}$, in contrast to the $T=450^\circ\text{C}$ value found for sample 4, in spite of the fact that both samples were implanted with the same fluence; ii) a higher annealing temperature is necessary to produce H_E layer exfoliation for sample 4 (higher fluence case). This behaviour seems to be related to mechanical interactions between both implanted layers and will be discussed in the following sections.

5.3.3. H-implanted sample

In the sample implanted only with H atoms (sample 6), the L_E and H_E exfoliation took place at 400°C and 450°C, respectively. Hence, the experiment demonstrates the feasibility of the method in substrates containing only the H specie.

5.3.4. Engineering of exfoliation temperature

Figure 5.6 shows the minimum exfoliation temperature found for the H_E layers as a function of implanted fluence for the multilayer samples.

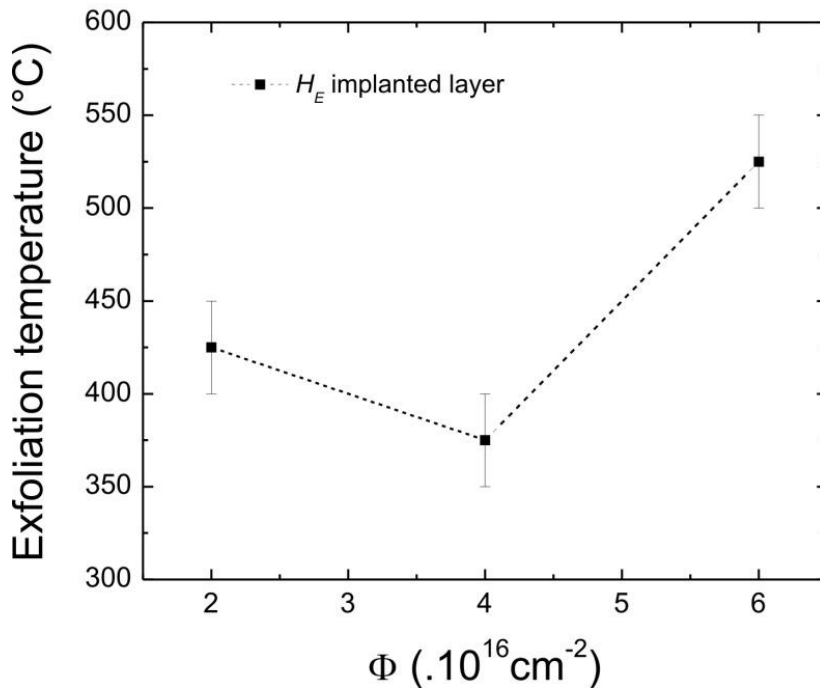


Figure 5.6- Plots the minimum exfoliation temperature of H_E layers as a function of implanted fluence observed for the multilayer samples.

The curve shows that a minimum temperature of exfoliation is obtained for intermediary fluence. This result is in agreement with those presented and discussed in Chapters 3 and 4, where the modifications of microstructure and its consequences on the exfoliation mechanisms and efficiency were indentified. In the present case, the first reduction of the exfoliation temperature could be attributed to the increase of gas content in the system enhancing the pressure of the cavities. The temperature increase for the high fluence point is probably related to microstructure modifications as, for example, the formation of spherical bubbles instead of platelets.

5.3.5. Mechanical interactions between the implanted layers

The SEM pictures in Fig. 5.7 show that the H_E related exfoliations are surrounded by a ring, characterizing a stair-like ring structure. This feature results from a *mechanically induced delamination* of the L_E layer during the uprising of the H_E blistering dome. A schema of the process is illustrated in Fig. 5.8. First, the mechanical interaction between both layers can be considered negligible (Fig. 5.8a). When blisters from the H_E layer arise, the bending efforts at the edges of the blister induce a mode-I crack opening on the upper thin film defined by the L_E implanted layer (Fig. 5.8b), as suggested by the schema in Fig. 5.8d. The crack advance will cause the film delamination following the disrupted layer defined by the L_E implantation induced defects. When the deflection becomes sufficiently large, the film failure occurs by cleavage or by the deflection of the crack propagation direction [Hut 1992].

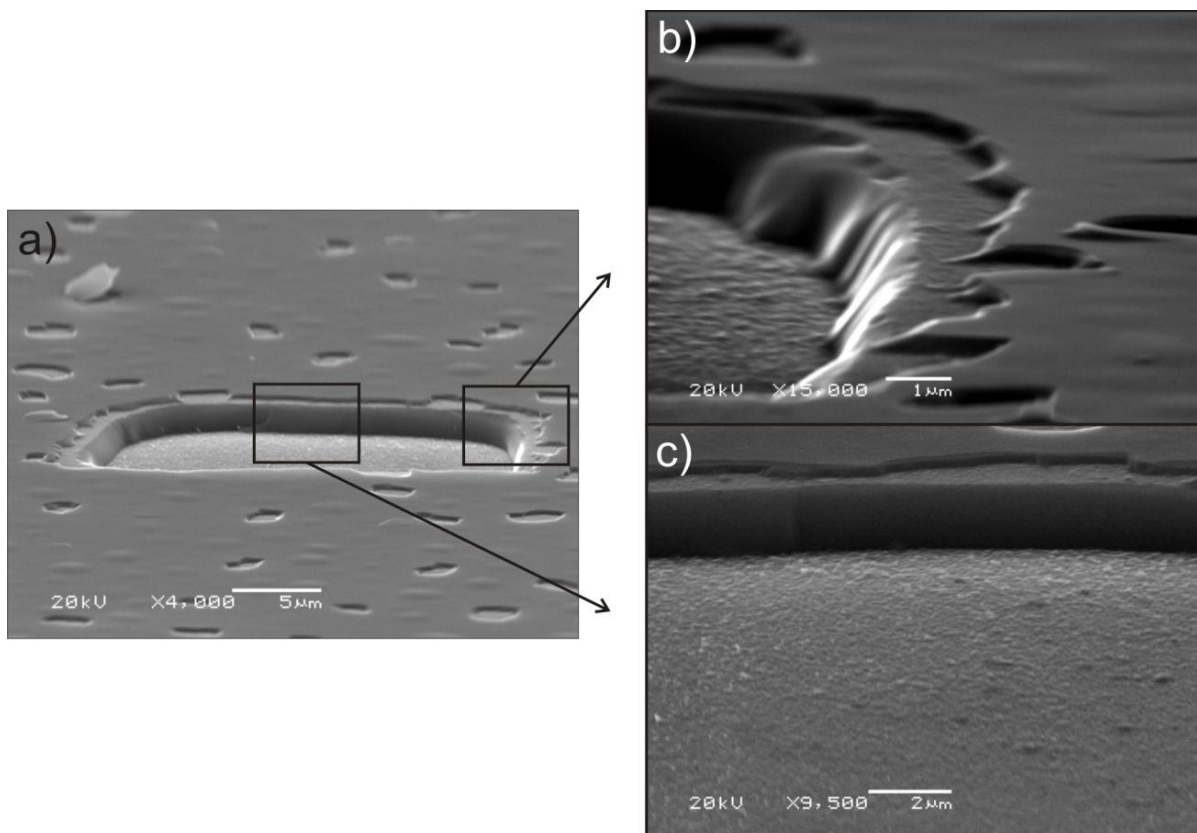


Figure 5.7- (a) SEM image obtained from sample 1 showing a H_E exfoliation surrounded by a delaminated ring. (b) detailed view of the step ring and (c) details of the roughness of the bottom and the straight walls formed at the faceted sides of the exfoliated area.

The result of the process is the observed step ring encircling all the H_E exfoliations (Fig. 5.8c). The observation of this phenomenon suggests that mechanical interactions between both layers affect their development, and some consequences of this effect are clearly perceptible in the exfoliation behavior of the L_E layer even before H_E exfoliation occurs.

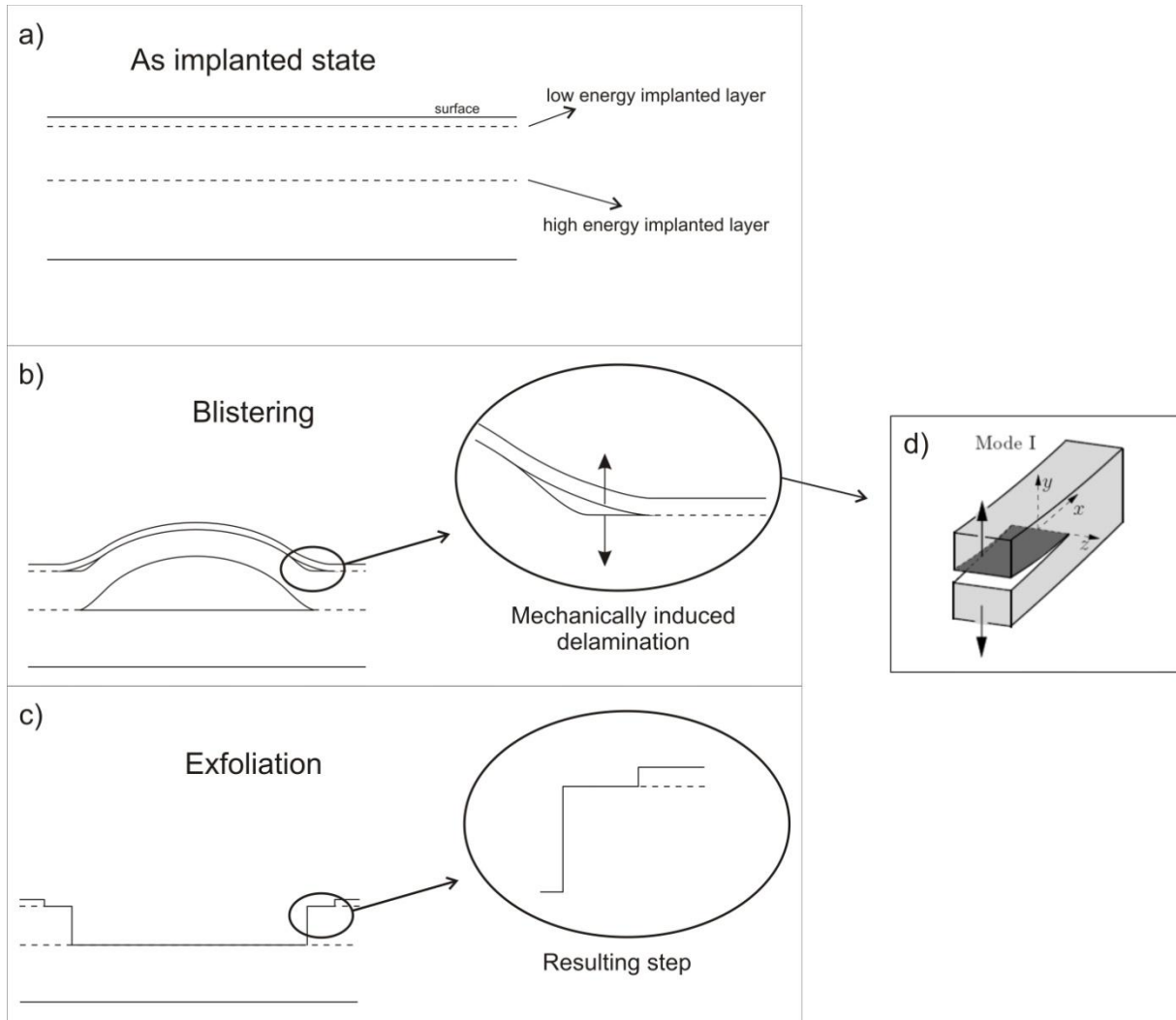


Figure 5.8- Schematic illustration of the mechanically induced delamination of the L_E layer during the H_E blister uprising. (a) at the as-implanted state, (b) the delamination taking place and (c) the resulting stair-like structure surrounding the H_E exfoliation.

Distinct exfoliation temperatures are observed: for the L_E layer in sample 3, it occurs at $T=400^\circ\text{C}$, and for sample 4 at $T=450^\circ\text{C}$. These samples were implanted to the same fluence (see Table 5.4). The reason for this distinct behaviour resides in the H_E layer development. The H_E layer of sample 4 was implanted to a higher fluence ($\Phi_T = 6 \times 10^{16} \text{ cm}^{-2}$) and presents an exfoliation temperature of $T=550^\circ\text{C}$ (see Fig. 5.6). The H_E layer of sample 3 was implanted to

a medium fluence ($\Phi_T=4 \times 10^{16} \text{ cm}^{-2}$) and produces exfoliation at $T=450^\circ\text{C}$. Therefore, we may state that the earlier development of the H_E layer in sample 3 is inducing (mechanically) the L_E layer to exfoliate in advance, as suggested schematically in Fig. 5.9. As counterproof, sample 6 was submitted only to a L_E implant, under the same conditions of samples 3 and 4. In this case, the exfoliation starts at $T=450^\circ\text{C}$, corroborating the idea that it was the thermal evolution of the H_E layer that affected the exfoliation behaviour of the L_E layer. For sample 4, where the development of the H_E layer is slower, the L_E layer exfoliates at the expected temperature of 450°C . These observations suggest that the mechanical interaction between both layers occurs even before macroscopic blistering as suggested in Fig. 5.9.

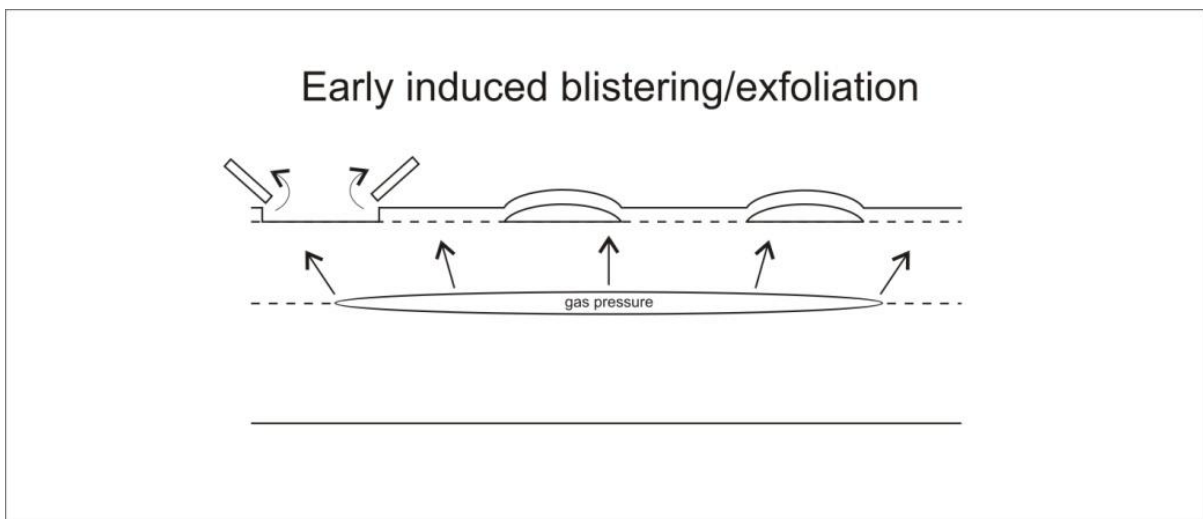


Figure 5.9- Schematic representation of the mechanical interaction between both implanted layers.

5.4. Conclusions

The possibility of performing one implantation run to produce the splitting precursors for several layers was presented. The study also introduces an innovative physical concept, relating the dependence of the exfoliation temperature with respect to the implanted fluence. Evidences connecting mechanical interactions between two distinct buried layers were also introduced. The manipulation of the temperature by means of the fluence, as demonstrated here, may not be the only possibility. Other parameters such as the implantation temperature, current density or $H:He$ ratio may also affect the process temperature, thus opening the possibility to expand the engineering of exfoliation related

processes. This concept was investigated using conventional ion implantation technique and can be further explored by using other techniques as it will be briefly commented on the next section.

5.4.1. Perspectives and potential applications

Plasma-based techniques for layer transfer process have been intensely studied in the last few years [Use 2002, Job 2005, Che 2005, Ghi 2007, Sha 20065, Sha 2006]. The main advantage of such techniques is their low operational cost.

In order to obtain a layer transfer by plasma methods, in general, the first step is to produce a buried trapping site layer to trap atoms introduced by diffusion-based techniques. This may be attempted, for example, by conventional ion implantation using very low fluence implantation of B^+ (at the order of 10^{12} - 10^{15} at/cm²) [Ton 1998, Che 2005] or by epitaxial growth of a buried strained layer [Sha 2005, Sha 2006]. The advantage of performing a conventional implantation followed by a plasma technique is the low implantation fluence required to produce the trapping layer, which reflects directly on the production cost. In this scenario, the multilayer concept could be very attractive and should be further investigated. A single implantation run could be used to introduce several trapping layers in the substrate. The substrate then could be submitted to the plasma techniques in order to introduce H atoms required for delamination of the distinct layers without the requirement of a conventional implantation step after each delamination. The diagram of the concept is presented in Fig. 5.11a. Any gas atom not trapped in the first layer has a potential to be trapped in a second layer enhancing the efficiency of the technique as exemplified in Fig. 5.11b

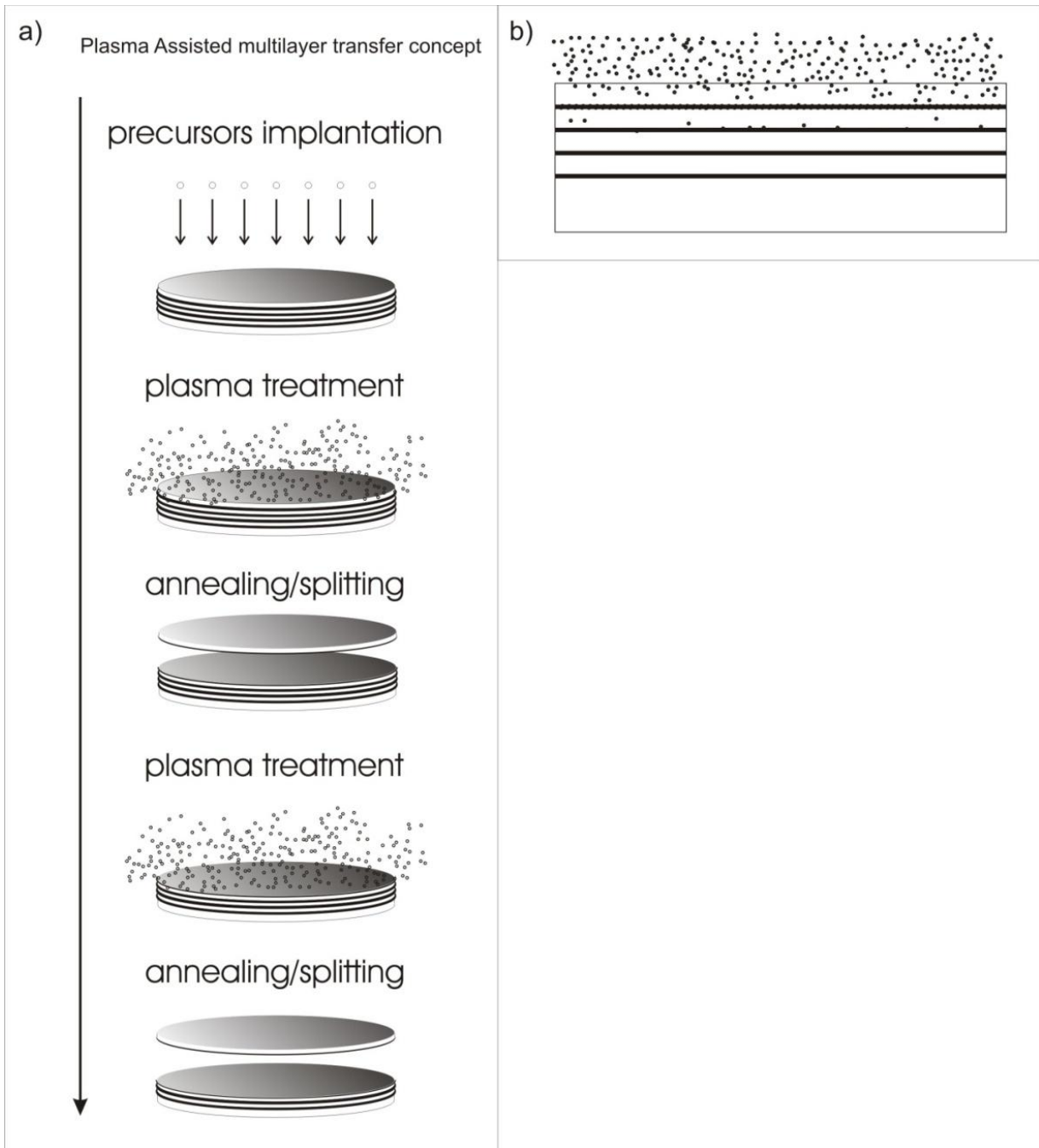


Figure 5.11- (a) Plasma-assisted multilayer transfer concept and (b) optimization of the process by multiple layer trapping.

CHAPTER 6

Effects of H Implantation in Si Containing Overpressurized He-plates

This chapter reports on rather exploratory experiments, which have not been more extensively investigated. The chapter starts with the characterization of overpressurized *He*-plates. Then two *H* implantation conditions are explored: i) *H* is implanted at the same depth location of the *He*-plates, and ii) *H* is implanted at half of the distance between the surface and the position of the *He*-plates. The microstructure evolution reveals attractive aspects of crack engineering and elastic interactions between *H*-platelets and *He*-plates. Some aspects of crack interaction behavior are also shown and briefly discussed.

6.1. Experimental

Two types of samples were prepared: i) samples containing **overlapped H and He profiles** and ii) samples containing **shifted H and He profiles**. Figure 6.1 characterizes the H and He concentration-depth profiles for both kinds of samples and Table 6.1 summarizes the implantation conditions.

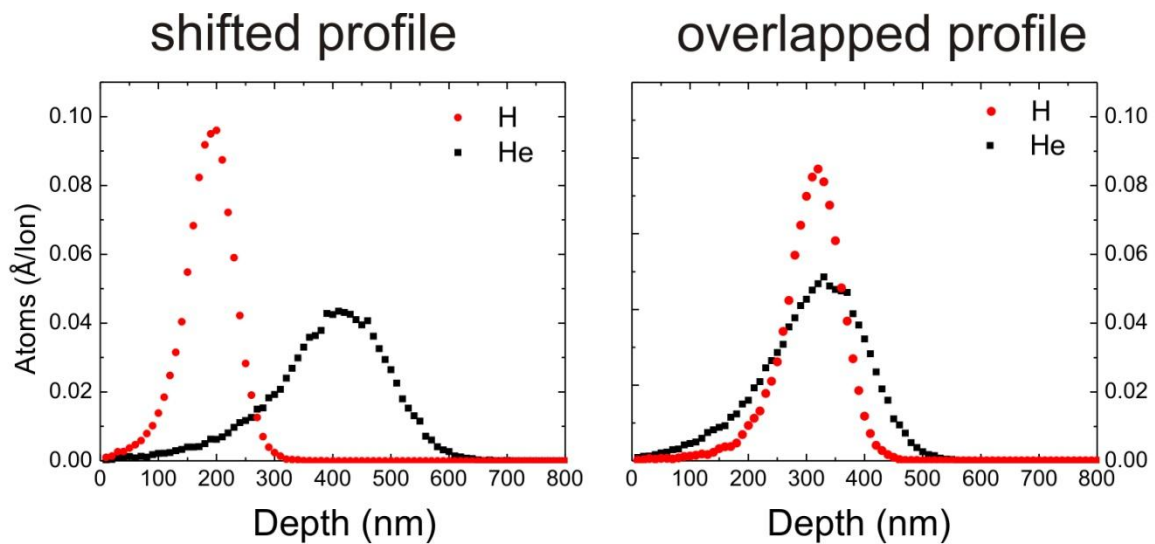


Figure 6.1- SRIM simulated concentration profiles of H and He implanted ions for the (a) **shifted profiles** (45keV for He⁺ and 30keV for H⁺) and (b) **overlapped profiles** (33keV for He⁺ and 60keV for H⁺).

As opposed to the previous procedures, all samples **considered here** were first implanted with He ions. These implantations were conducted at room temperature (RT) to a fluence of $\Phi=1 \times 10^{16} \text{ cm}^{-2}$. Some samples (2, 4, 5 and 6) were then thermally annealed (350°C for 900s) to allow the formation of overpressurized He-plates [Fic 1997, Hue 2006]. After this thermal treatment, H was introduced either by conventional implantation with the target at room temperature or 200°C (sample 5) to a fluence of $\Phi=0.5 \times 10^{16} \text{ cm}^{-2}$, or via plasma hydrogenation (sample 6 only).

After both implantation steps, the samples were annealed at different temperatures in the range of 300-600°C and then characterized by SEM and TEM.

Table 6.1

Sample	He ⁺ implant. (energy, fluence, temperature)	Intermediary annealing	H ₂ ⁺ implant. (energy, fluence, temperature)
overlapped profile			
Sample 1	33 keV, 1.0x10 ¹⁶ cm ⁻² , (amb.) mean depth 300 nm	no	60 keV, 0.5x10 ¹⁶ cm ⁻² , (amb.) mean depth 300 nm
Sample 2	33 keV, 1.0x10 ¹⁶ cm ⁻² , (amb.) mean depth 300 nm	350°C 900s (He-plates)	60 keV, 0.5x10 ¹⁶ cm ⁻² , (amb.) mean depth 300 nm
shifted profiles			
Sample 3	45 keV, 1.0x10 ¹⁶ cm ⁻² , (amb.) mean depth 400 nm	no	30 keV, 0.5x10 ¹⁶ cm ⁻² , (amb.) mean depth 200 nm
Sample 4	45 keV, 1.0x10 ¹⁶ cm ⁻² , (amb.) mean depth 400 nm	350°C 900s (He-plates)	30 keV, 0.5x10 ¹⁶ cm ⁻² , (amb.) mean depth 200 nm
Sample 5	45 keV, 1.0x10 ¹⁶ cm ⁻² , (amb.) mean depth 400 nm	350°C 900s (He-plates)	30 keV, 0.5x10 ¹⁶ cm ⁻² , (200°C) mean depth 200 nm
plasma hydrogenation			
Sample 6	33 keV, 1.0x10 ¹⁶ cm ⁻² , (amb.) mean depth 300 nm	350°C 900s (He-plates)	H ⁺ plasma 300°C (1h)

6.2. Results and comments

6.2.1. He-plates

TEM observations in as-implanted samples (not shown) reveal a continuous buried damaged layer rather centred near the maximum of the vacancy depth profile, as calculated by SRIM code [SRIM 2008]. This layer probably contains mostly He-vacancy or self-interstitial clusters. Figure 6.2 shows cross-sectional TEM micrographs illustrating the most characteristic microstructure features observed in He implanted Si (RT, 1x10¹⁶ cm⁻²) after the annealing at 350°C for 900s: large plate-like structures (i.e. He-plates) located mostly at the center of the damaged layer are observed in both energy cases (45keV Fig. 6.2a and 33keV

Fig. 6.2b). Between the He-plates, there is a high concentration of small defect structures revealed by their diffraction contrast.

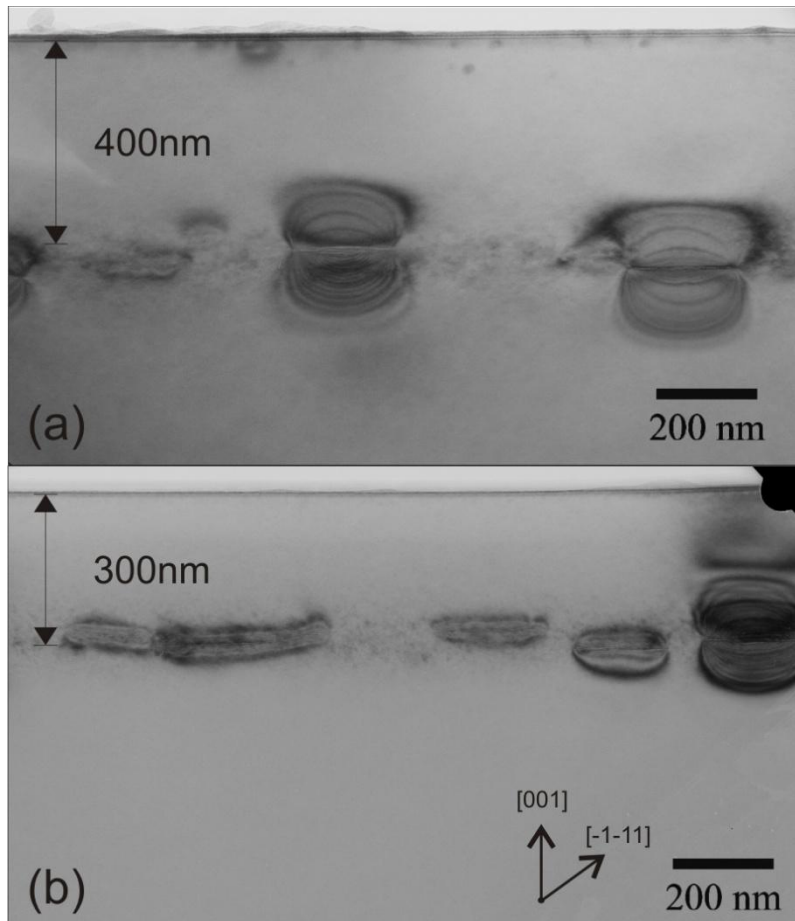


Figure 6.2- Cross-section TEM images of the He implanted ($1 \times 10^{16} \text{cm}^{-2}$)/annealed (350°C for 900s) samples for (a) 45KeV and (b) 33KeV energy cases after annealing. The images were obtained close to the $[-110]$ zone axis orientation in bright-field dynamical two-beam imaging conditions with $g:(004)$. He-plates are seen to be formed at a depth close to the predicted R_p . The cavities tend to be formed at the core of the damage layer.

Figure 6.3 shows a more detailed view of an overpressurized He-plate. The fringes surrounding the plate are ascribed to a strain contrast evidencing its high internal gas pressure [Fic 1997, Hue 2006]. The He-plates are preferentially formed within (001) planes of the Si structure (parallel to the surface), in good agreement with previous studies where it is claimed that $\{100\}$ planes represent the most energetically favorable habit planes for gas-filled plates precipitates [Nas 2005, Hue 2006]. Just to illustrate, the three possible $\{100\}$ plate orientations are identified in the plan-view micrograph in Fig. 6.4a.

We remark that this figure corresponds to a very thin area where the edge-on oriented plates were disrupted (cut) by the sample thinning process and, therefore, are not pressurized anymore. Figure 6.4b shows a top view of two (001) He-plates oriented parallel to the surface, clearly demonstrating the circular shape of the He-plates strain field.

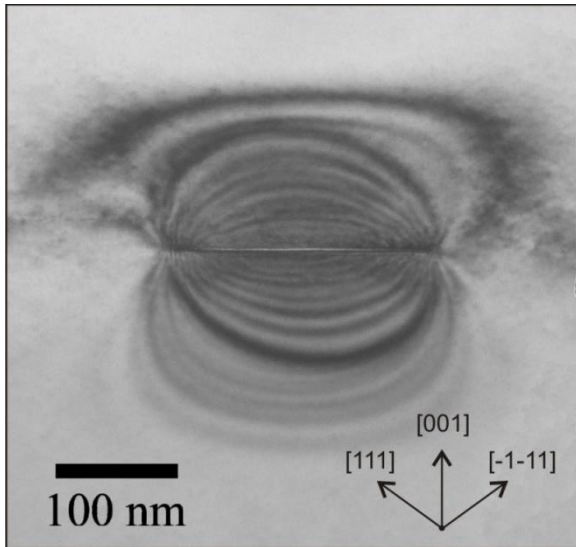


Figure 6.3- TEM image performed close to the $[-110]$ zone axis orientation in bright-field dynamical two-beam conditions with $g:(004)$. The He-plate appears lying on (001) habit planes parallel to the surface. The system of fringes surrounding the cavity is ascribed to a strain contrast resulting from the overpressure of the cavity.

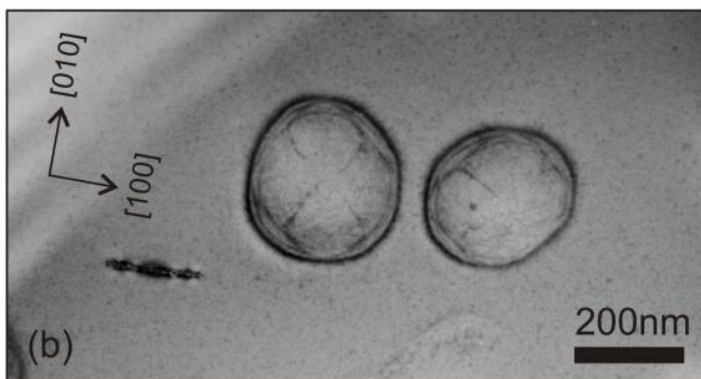
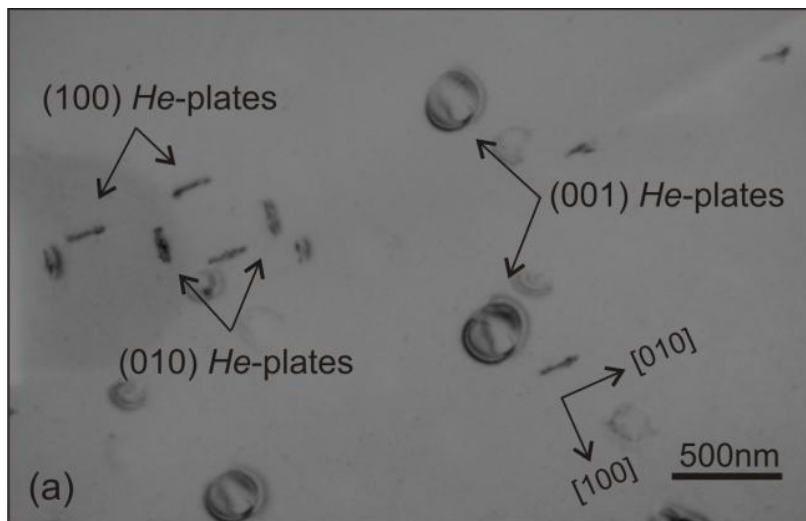


Figure 6.4- Plan-view TEM microscopy of He implanted ($1 \times 10^{16} \text{ cm}^{-2}$ 33keV) Si annealed at 350°C for 900s. (a) The three possible orientations of He-plates are shown and (b) a detailed plan-view of (001) He-plates.

6.2.2. Overlapped H and He profile experiments

Two types of samples presenting *overlapped H and He* profiles were prepared (see Table 6.1). The first one refers to H^+ implantations in **He implanted/non annealed** samples (sample 1), i.e. no He-plates were previously formed. The second one refers to H^+ implantation at room temperature onto **He implanted/annealed** sample (sample 2) containing He-plates. After H^+ implants, the samples were annealed at 400°C for 1800s. The TEM micrographs in Fig. 6.5 show nanocracks in both types of samples. We remark that the depth position of the nanocracks depends on the applied procedure. In sample 1 (Fig. 6.5a and b), the nanocracks are located at the end of the damaged layer, whereas, in sample 2, the nanocracks are located where He-plates are usually found, i.e. at the center of the damaged layer. These observations clearly demonstrate that it is the H implant that induces the formation of the cracks. However, their depth location is influenced by the previous outcome of the He implants.

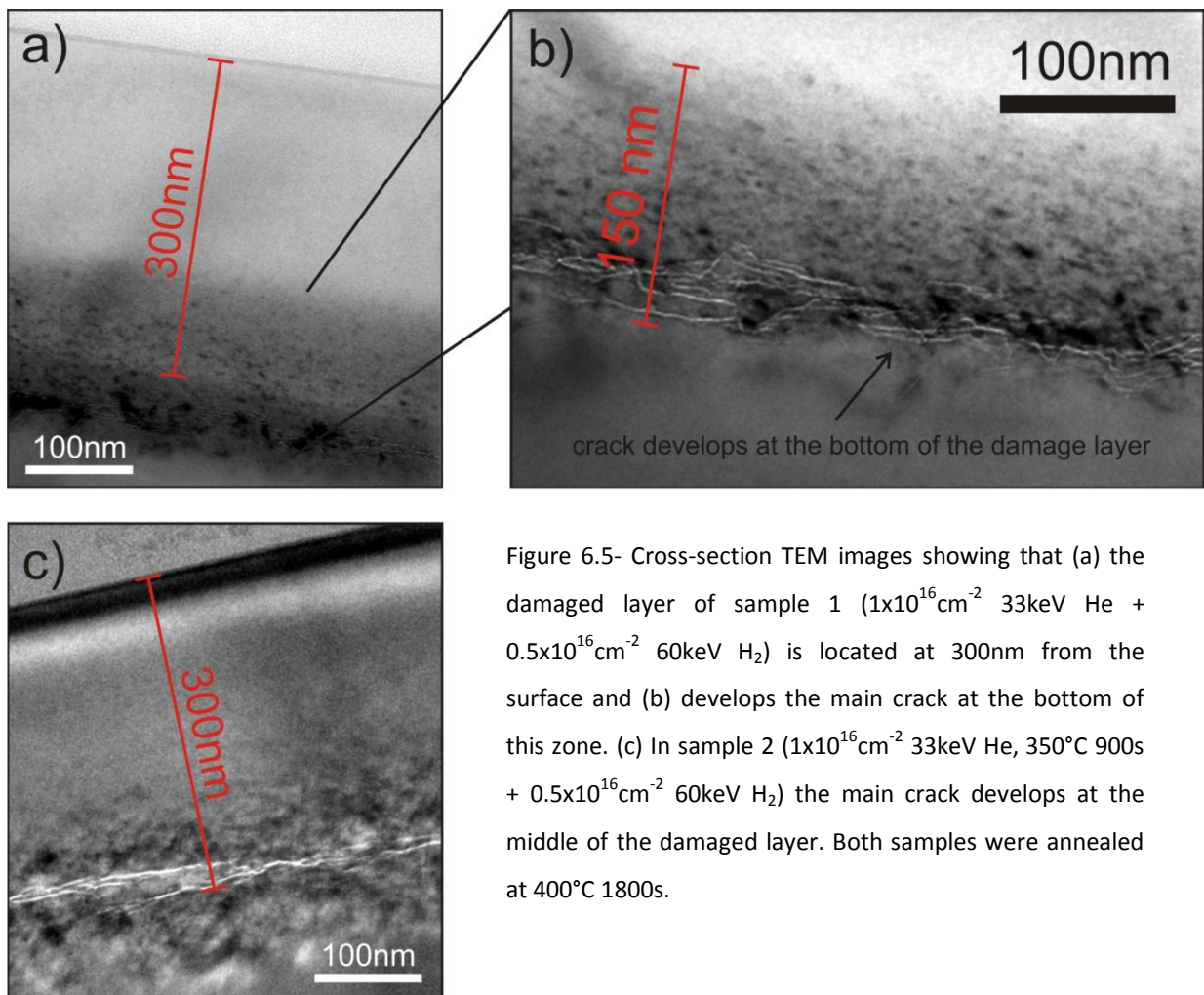


Figure 6.5- Cross-section TEM images showing that (a) the damaged layer of sample 1 ($1 \times 10^{16} \text{cm}^{-2}$ 33keV He + $0.5 \times 10^{16} \text{cm}^{-2}$ 60keV H_2) is located at 300nm from the surface and (b) develops the main crack at the bottom of this zone. (c) In sample 2 ($1 \times 10^{16} \text{cm}^{-2}$ 33keV He, 350°C 900s + $0.5 \times 10^{16} \text{cm}^{-2}$ 60keV H_2) the main crack develops at the middle of the damaged layer. Both samples were annealed at 400°C 1800s.

Hence, we conclude that *He* is trapped into the *He*-plates, and the *H* atoms implanted later migrate and infuse the *He*-plates during the thermal annealing. If the *He*-plates were not previously produced, then the crack develops at a deeper location. In a previous work, using the same energies presented here, the authors shown that the *H* atoms are a little deeper located than the *He* ones [Duo 2001]. Thus, the depth location of the nanocracks may indicate that *He* atoms have migrated to the *H*-rich region.

It is also important to remark that both samples present considerable exfoliation efficiency after a temperature annealing $T > 450^\circ\text{C}$. Figure 6.6 shows a TEM cross-sectional view of an exfoliated region obtained from sample 2 (in this case annealed at 600°C). The “*lateral walls*” of the exfoliated area present cleavage along distinct crystallographic planes. Unexpectedly, on the left side of the image, cleavage occurred along a $\{111\}$ plane. On the right side, however, cleavage took place along a $\{110\}$ plane, the common cleavage plane for Si. The rounded edges observed on both sides show another interesting behavior: *the deviation of the cleavage direction*. It seems to occur due to the complex distribution of stress at the clamped border of the bended Si over-layer. An insert in Fig. 6.6 shows a schema of the deviation process. Figure 6.6 also shows that the remaining sample surface from the exfoliated area presents a roughness consistent with the dispersion of the nanocrack depth distribution shown in Fig. 6.5.

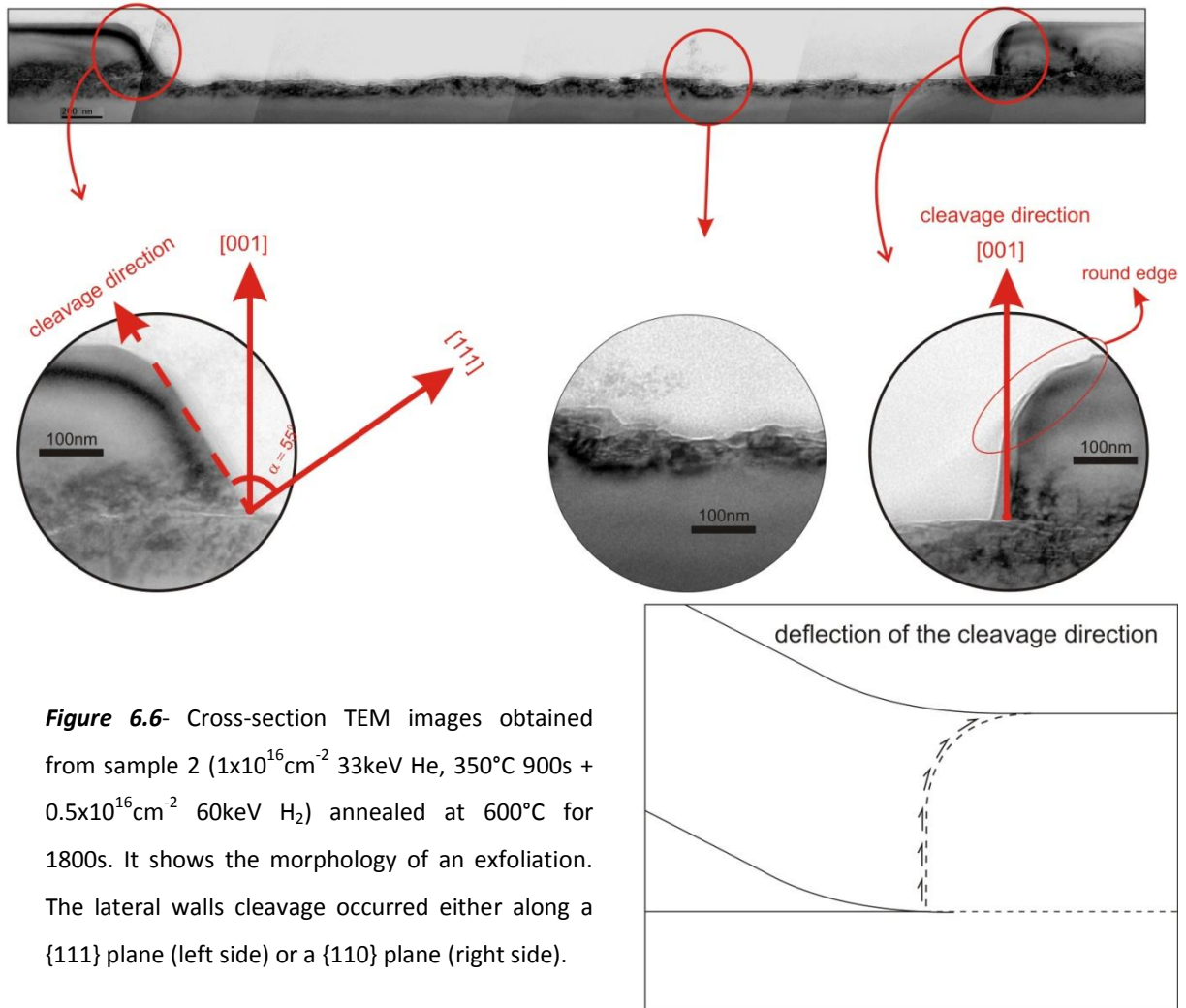


Figure 6.6- Cross-section TEM images obtained from sample 2 ($1 \times 10^{16} \text{ cm}^{-2}$ 33keV He, 350°C 900s + $0.5 \times 10^{16} \text{ cm}^{-2}$ 60keV H₂) annealed at 600°C for 1800s. It shows the morphology of an exfoliation. The lateral walls cleavage occurred either along a {111} plane (left side) or a {110} plane (right side).

6.2.3. Shifted H and He profile experiments

Three types of *shifted profile* cases (samples 3, 4 and 5) were studied (see Table 6.1). After the He implantation, sample 3 was directly room temperature implanted with H. Samples 4 and 5 were first annealed at 350°C for 900s to form the He-plates and then implanted with H at room temperature (sample 4) or at 200°C (sample 5). After the H implantations, all samples were annealed at $T \geq 300^\circ\text{C}$ for 1800s in order to perform the TEM investigation and at $T \geq 450^\circ\text{C}$ to study the exfoliation behaviour. The results obtained from each sample are described below.

Sample 3: He as-implanted + H (RT implantation)

Figure 6.7 shows cross-sectional TEM micrographs obtained from a 400°C annealed sample. Fig. 6.7a presents a general overview where both He and H related layers are

indicated. Figure 6.7b shows a weak beam image revealing that the defect density in the *He* layer is much smaller than in the *H* layer. Figure 6.7c shows in details that crack formation takes place in the *H*-related layer. The observed behaviour is consistent with results described in previous works, where it was showed that *He* atoms migrate towards the *H*-rich region [Wel 1998, Duo 2001]. In Si, because of their inert character, *He* atoms present a high mobility. On the contrary, *H* atoms readily react with Si dangling bonds created by the implantation process and are, therefore, easily trapped. In the case of sample 3, we ascribe the absence of cavities and cracks in the *He* related layer and the formation of cracks **only** in the *H*-related layer to the migration of *He* towards the *H*-rich region.

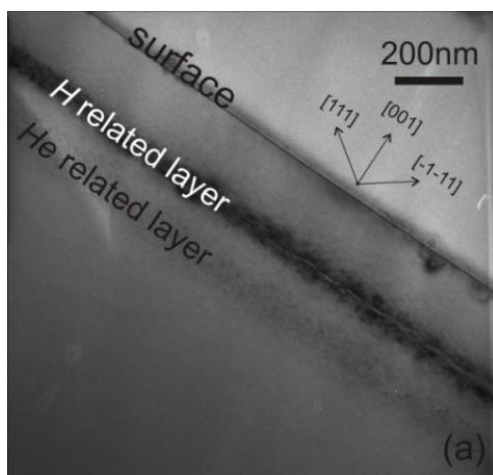
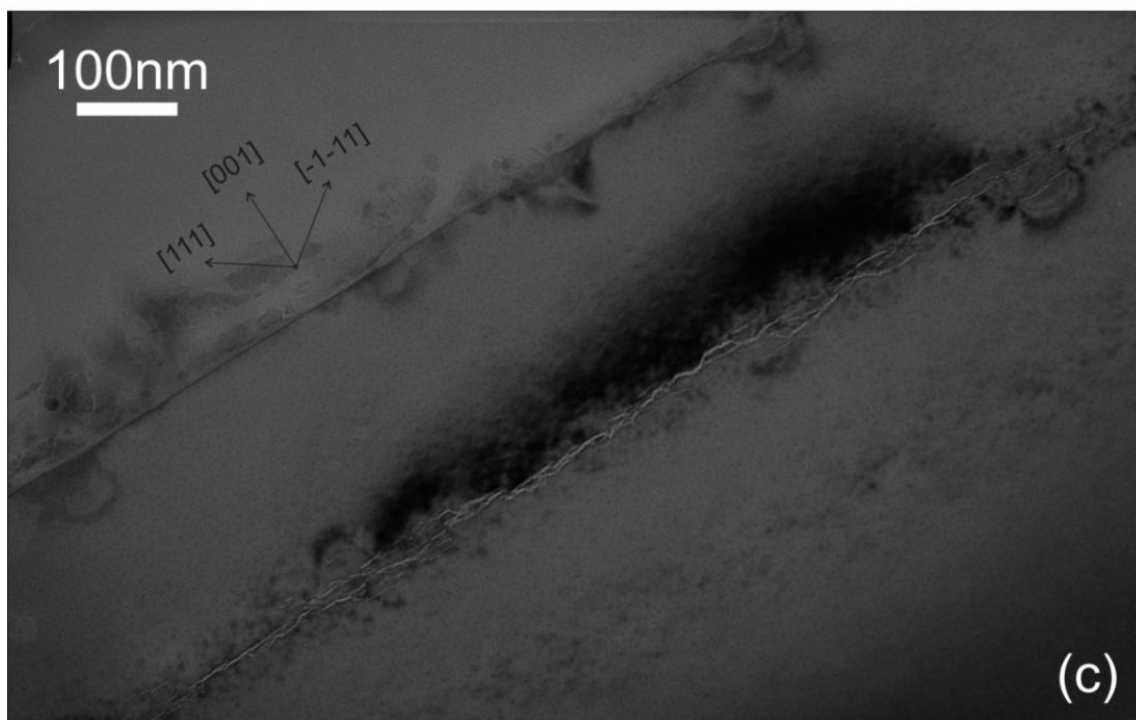
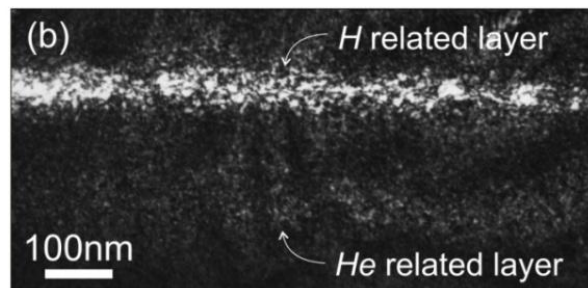


Figure 6.7- (a) TEM image of sample 3 ($1 \times 10^{16} \text{cm}^{-2}$ 45keV He + $0.5 \times 10^{16} \text{cm}^{-2}$ 30keV H₂, 400°C). (b) weak beam contrast revealing the low density of defects found in the *He* related layer and (c) formation of cracks in the *H*-related layer.



Sample 4: He-plates (+350°C 900s) + H (RT implantation)

In this case, He-plates were formed prior to H implantation. Figure 6.8 shows the microstructure features from both layers, resulting from a thermal treatment at 300°C after the H implant. Reminiscent structures of the previously existent He-plates are observed. Instead of a single lamellae plate structure, they now present a kind of “multi-lamellar” plate structure, more detailed illustrated in Fig. 6.9. This is probably induced by the infusion of H atoms into the He-plates. The H layer shows a high concentration of platelets and nanocracks structures.

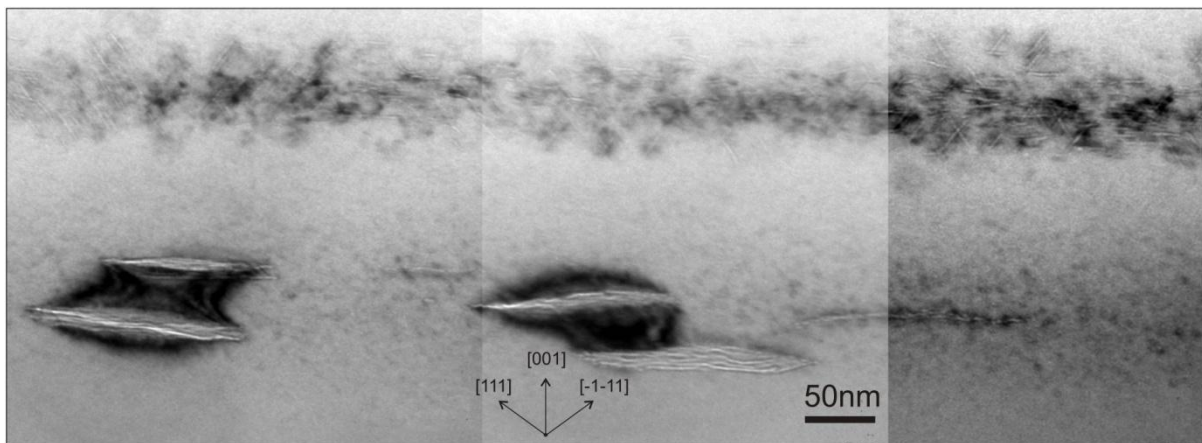


Figure 6.8- TEM image showing the general overview of sample 4 ($1 \times 10^{16} \text{cm}^{-2}$ 45keV He, 350°C 900s + $0.5 \times 10^{16} \text{cm}^{-2}$ 30keV H₂) after 300°C annealing. Both H and He related are clearly distinguished where the previously existent He-plates are still observed and a high density of nanocracks can be seen at the H related Rp.

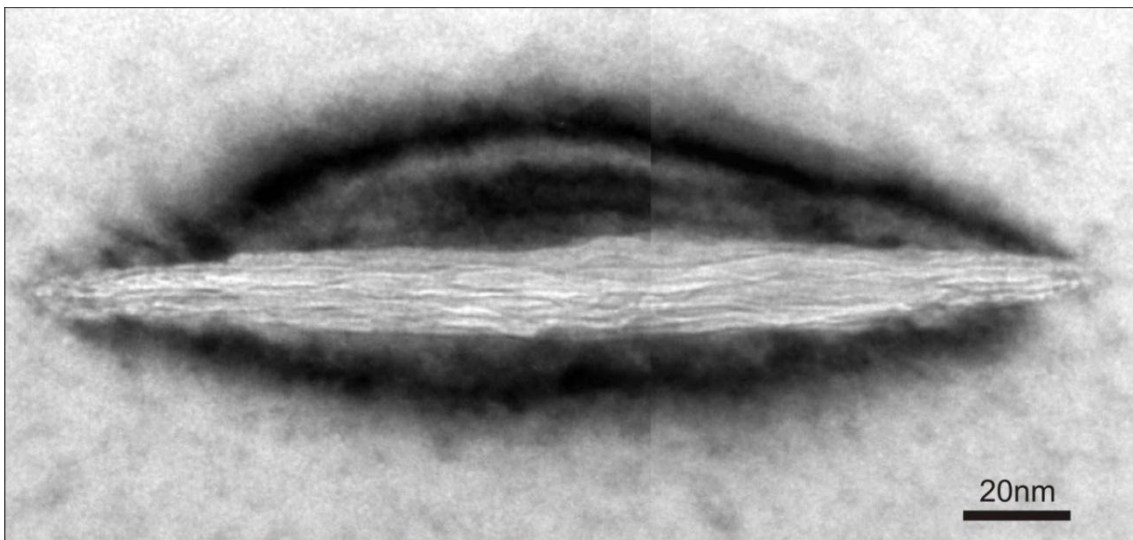


Figure 6.9- TEM image showing the lamellar-like structures resulting from the infusion of H into He-plates.

A careful investigation of the *H*-platelet arrangements reveals interesting features. Figures 6.10a, b and c show details from distinct characteristic regions systematically observed in this sample. In the regions where *He*-plates are not present directly underneath, the *H*-platelets are preferentially aligned along (001) planes, parallel to the surface (Fig. 6.10c). This behavior is in agreement with previous contributions [Bru1995, Wel 1997, Gri 2000, Nas 2005], as well as the results discussed in Chapter 4. On the other hand, in regions directly above a *He*-plate, the *H*-platelets are preferentially aligned to specific {111} lattice variants, with respect to the strain field symmetry axis of the *He*-plate (Fig. 6.10b). It characterizes an arranged system of *oriented satellite cavities* (*H*-platelets) clearly tailored by elastic interaction with the local strain field. This behaviour will be discussed in details in Chapter 7.

In contrast with the previous case (sample 3) *He* atoms do not seem to migrate significantly towards the *H*-rich region. Evidently, the lack of *He* migration towards the *H*-rich region is attributed to the efficient trapping of *He* in the *He*-plates. This restricts the development of large cracks in the *H*-related layer. The TEM investigations suggest that a small amount of *H* have migrated to the *He*-plates.

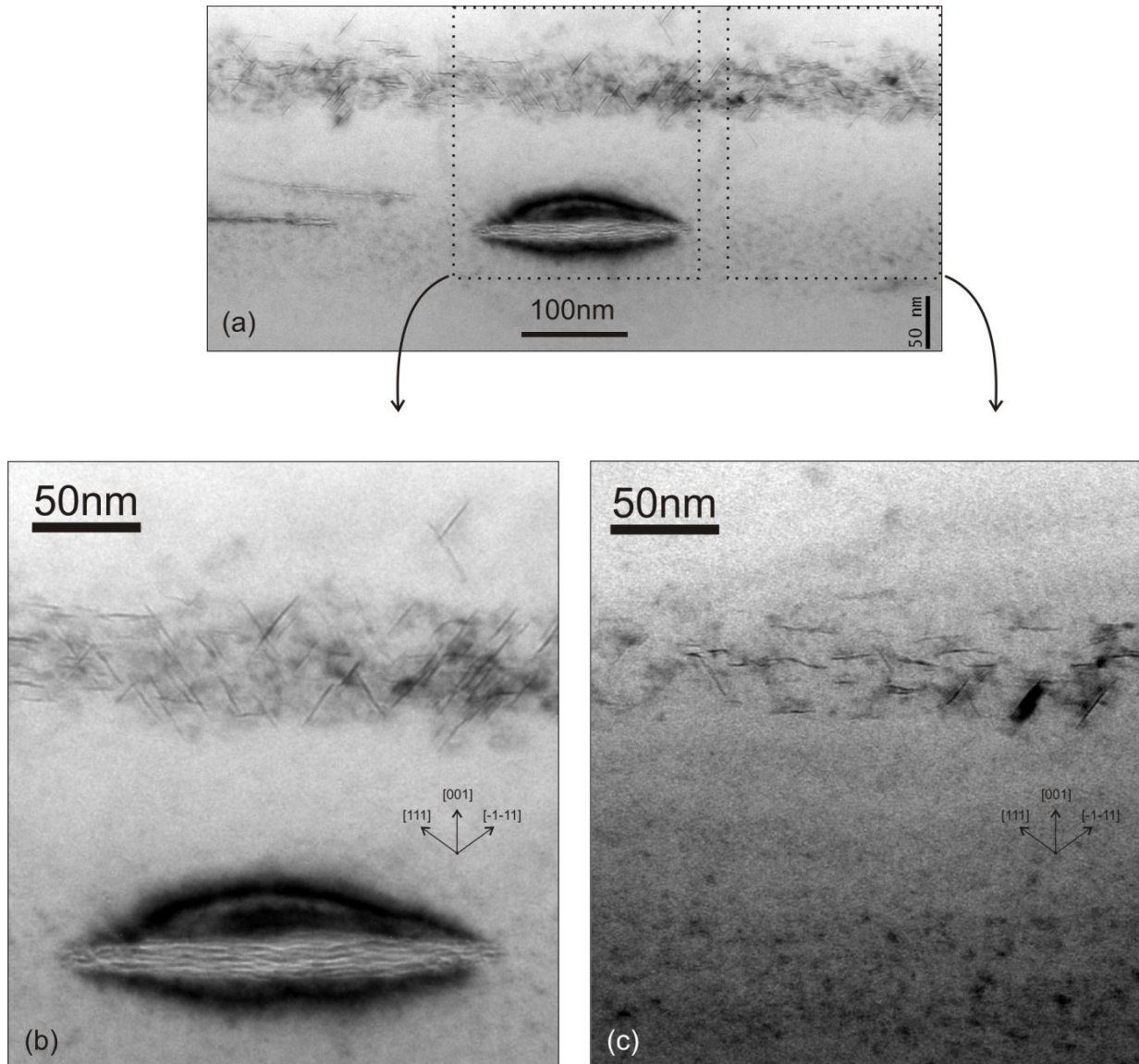


Figure 6.10- Cross-section TEM micrographs (a) characterizing the two typical zones found in sample 4. (b) when nucleated under the influence of the local strain field of an isolated *He*-plate, the *H*-platelets are observed to be aligned to specific {111} lattice variants, with respect to the strain field symmetry axis. (c) in the zones where *He*-plates were not present directly underneath, the *H*-platelets were found to be preferentially aligned along (001) planes.

Sample 5: *He*-plates (+350°C 900s) + *H* (200°C implantation)

Sample 5 was first *He* implanted and then annealed at 350°C for 900s to form the *He*-plates and after implanted with *H* at 200°C. The TEM in Fig. 6.11d (sample annealed at 400°C) shows that the *H* layer contains a low concentration of *H*-platelets (shown in details in the HRTEM images in Fig. 6.11a, b and c). Surprisingly, most of the *H*-platelets are arbitrarily aligned along {111} planes. This indicates that the strain-stress characteristics of

the layer are different from the RT implantation ones, where the in-plane stress causes the preferential alignment of platelets along (001) planes, parallel to the surface. In addition, the *He* related layer presents distinct microstructure features, as compared with the previous cases. It shows a narrow and rather defect-free region containing straight and long cracks.

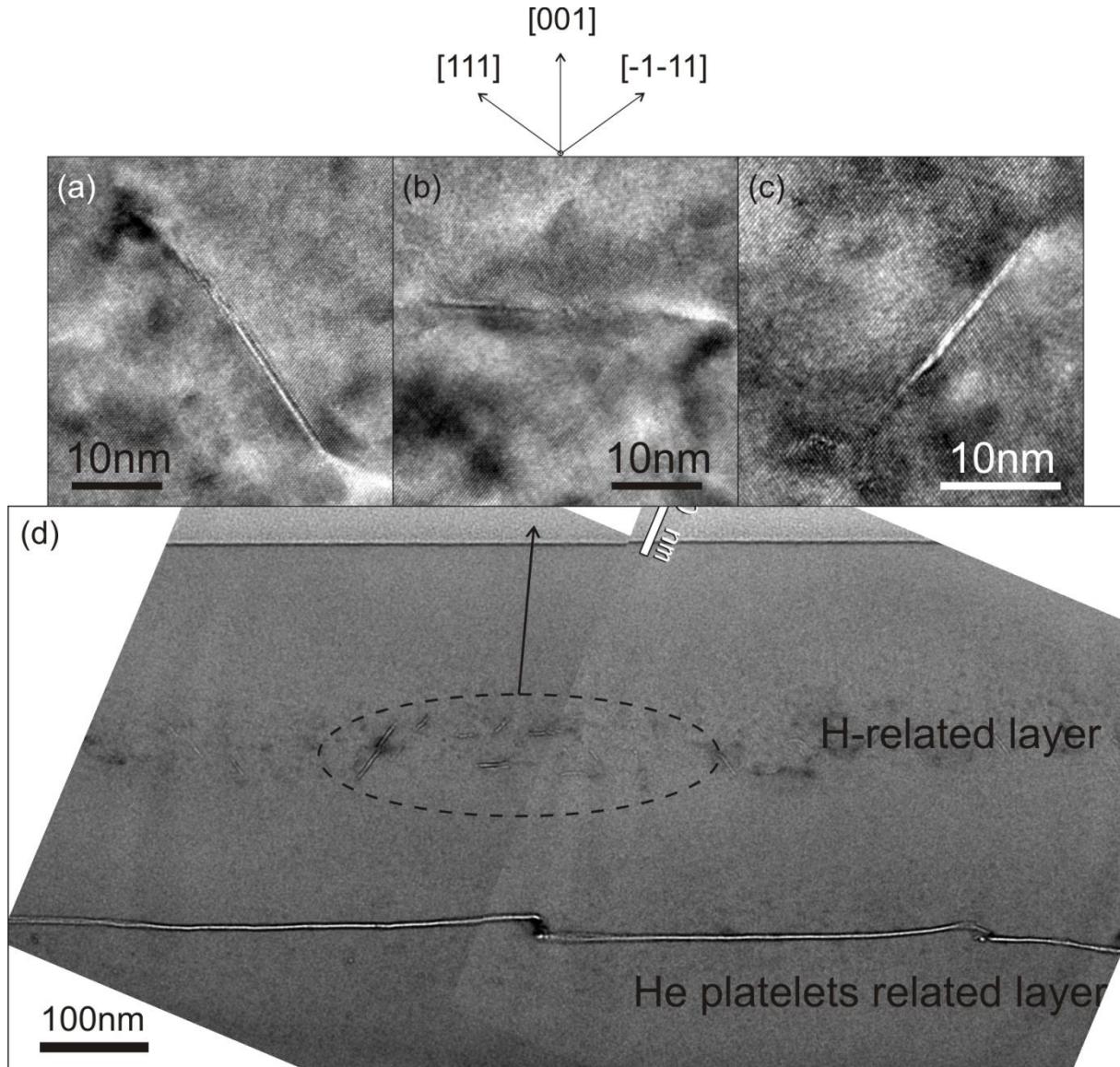


Figure 6.11- Cross-section TEM image of sample 5 ($1 \times 10^{16} \text{ cm}^{-2}$ 45keV He, 350°C 900s + $0.5 \times 10^{16} \text{ cm}^{-2}$ 30keV H₂ at 200°C). A very low density of *H*-platelets cavities were formed in the H related layer and extremely straight and elongated cracks were formed at the *He* related projected range.

H is highly mobile in high temperature implantations [Ter 2007] and the microstructure observed in sample 6 seems to be the result of “hot” *H* interaction (infusion) with the *He*-plates. It demonstrates that it is possible to control, or moreover, may reverse tendencies of *He* or *H* interdiffusion. *He* can be efficiently trapped into *He*-plates and *H* can

be *drifted* to infuse it. An optimization of this cracks system may improve the crystalline quality of ultra-thin layers transfer, where the **usual** roughness of the process is in the order of the transferred film. The roughness reduction of the transferred film is of great interest for the layer transfer technology, since, according to the international technology roadmap for semiconductors, the development of ultrathin SOI substrates with the top silicon layer should achieve 20 nm [ITR 2007].

Furthermore, since a considerable amount of the *H* atoms seem to remain in its own related layer (evidenced by the formation of *H*-platelets), the *H* infusing of *He*-plates demonstrates to be an efficient process of crack growth. The present method follows the opposite sense of species migration described in previous works where the *He* atoms are systematically observed to migrate to *H*-rich regions [Aga 1998, Duo 2001]. The essential differences are:

-In the **usual process**, the *He* atoms have the task of infusing the *H*-platelets in order to dissociate H_2 molecules [Wel 1998] and provide pressure for crack growth [Wel 1998, Aga 1998].

-In the **present process** a high energy (pressure) is already stored in overpressurized *He*-plates, and *H* atoms are required essentially to perform their **main role** [Aga 1998]; i.e. break the strained bonds at the crack tip to relieve the pressure. There is enough energy (pressure) to provide long range crack propagation. More than just providing the pressure, the *He*-plate provides an ideal crack shape to drive the direction of propagation sustained by *H* induced **sub-critical** crack growth. The very straight character of the cracks seems to be related to the high affinity of *H* for strained areas [Höc 2001], resulting in a compulsory placement of *H* to interact with the strained bonds at the crack tip. In this sense, each one of the atomic species essentially plays their main role.

The implantation of *H* at a deeper region (behind *He*-plates) should be more adequate to enhance the trapping efficiency (since no *H* will effuse towards the surface) and to avoid the damage of the layer to be transferred.

Since the observed single cracks have propagated through a relatively damaged-free layer, interesting behaviors of crack interaction phenomena was also observed. Figure 6.12 shows a complex defect that seems to be triggered by a twinning phenomena (and has been

disrupted, producing disordered zones) between two cracks tips. This phenomenon can be related to a mechanical relief and evidences the high stress state typically developed at crack tips.

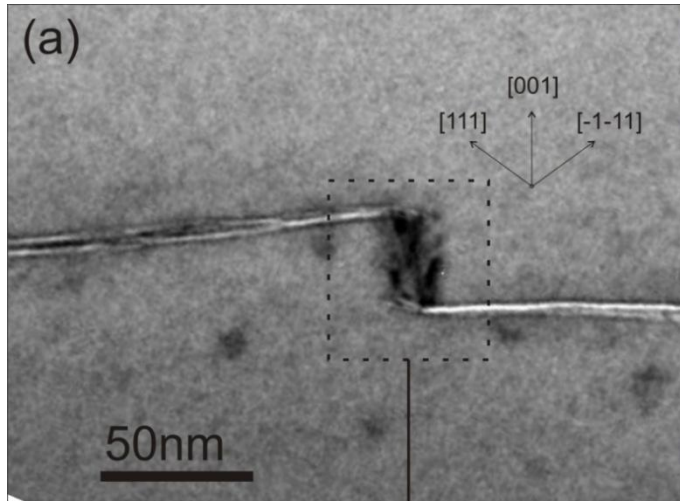
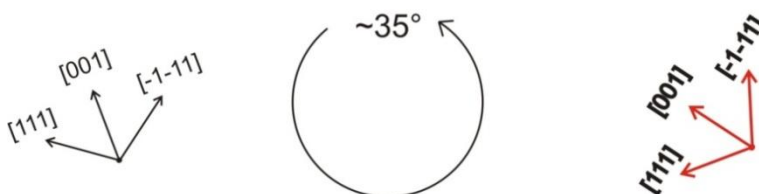
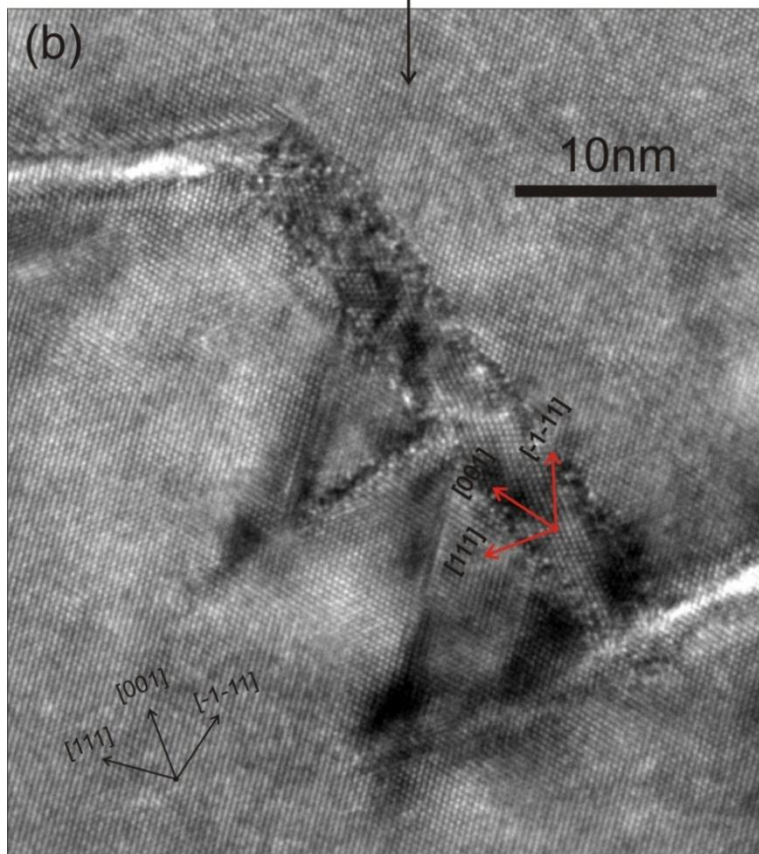


Figure 6.12- TEM images of sample 5 showing (a) the formation of a crystallite between two cracks tips and, (b) a HRTEM image showing that the crystal in the interior of what seems to be a microtwin triggered defect showing a region of the microcrystal presenting $\approx 35^\circ$ in relation to the matrix.



In addition, when two propagating planar cracks are heading towards each other an interaction phenomenon may occur [Gro 2006]. In a first phase, the cracks will tend to approach each other. As their separation distance shortens, each crack tip slightly deviates from their propagation direction and therefore does not merge along the shortest path. Both cracks run around each other up to a certain distance and then turn again to merge with the other. This phenomenon predicted by simulation [Gro 2006] is schematically drawn in Fig. 6.13a. Figure 6.13b-d shows TEM images where this interaction phenomenon is observed.

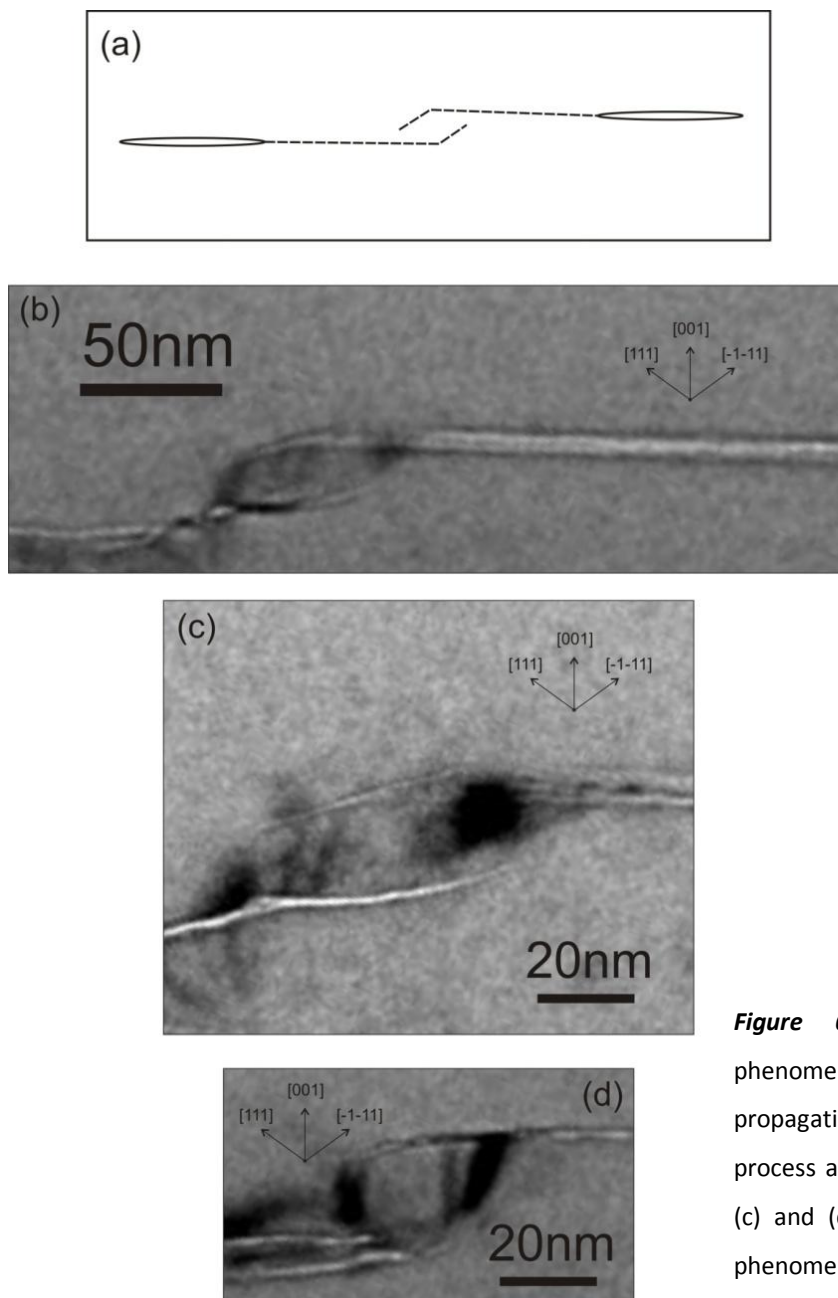


Figure 6.13- Coalescence interaction phenomenon observed in coplanar crack propagation. (a) presents a schema of the process as obtained by simulation and (b), (c) and (d) are TEM observations of the phenomenon.

6.2.4. Plasma hydrogenation experiments

After producing *He*-plates, sample 6 was subjected to plasma hydrogenation at 300°C. One piece of the sample was submitted to the plasma treatment for 3600s (i.e. 1h) and a second piece was treated for 10800s (i.e. 3h). The objective of the experiment was to study the diffusion of *H* into the sample in order to promote the infusion of *H* into the previously existing *He*-plates.

Figures 6.14a and b show the microstructure characteristics for the 1 and 3h of plasma treated samples. The samples surfaces become quite rough due to the plasma etching effects. Cavities and dislocations are observed from the surface up to the layer containing the *He*-plates. This is an inherent characteristic of the plasma hydrogenation process [Che 2005]. The defect concentration in the layer above the *He*-plates seems to increase with the increasing plasma exposition time. However, the *He*-plates apparently behave as excellent trapping structures for hydrogen. No defect or cavity was detected behind the *He*-plates, indicating that the *H* atoms may have not passed through. In both cases, the *He*-plates have developed into long and sharp cracks. Figure 6.15 shows the details of the resulting cracks observed in each sample.

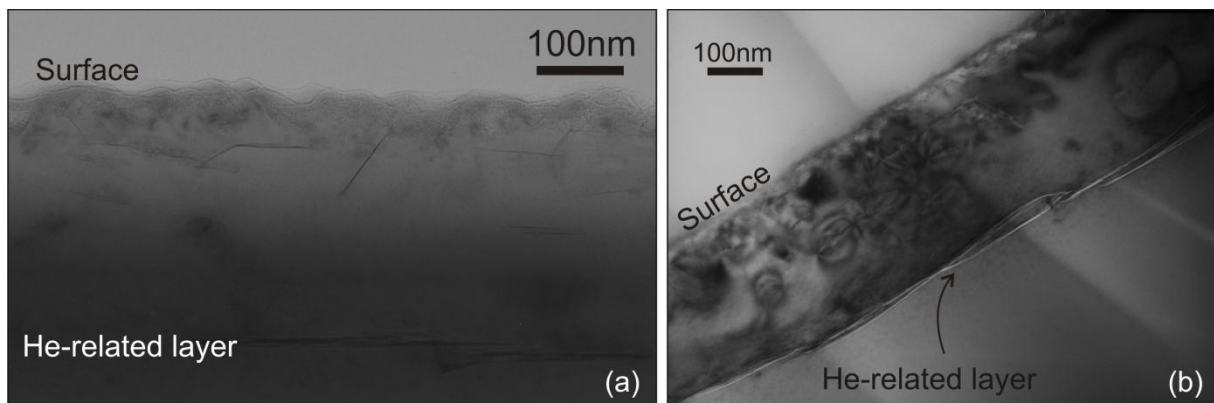


Figure 6.14- Cross-section TEM image of a Si sample previously implanted/annealed with *He* ($1 \times 10^{16} \text{cm}^{-2}$ and 350°C for 900s to produce *He*-plates) exposed to (a) 1h and (b) 3h of plasma hydrogenation.

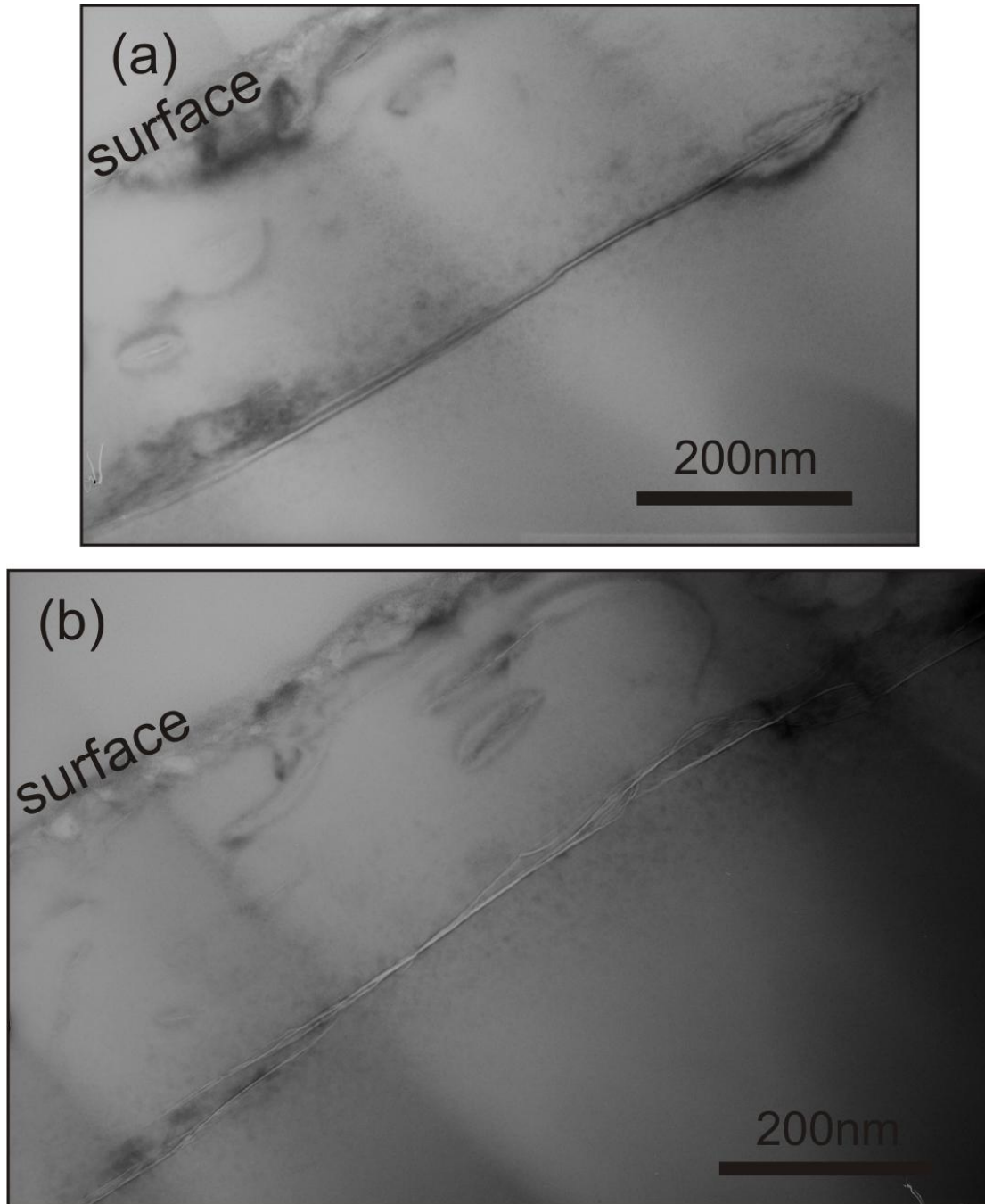


Figure 6.15- Detailed TEM view of the previously *He*-plates transformed into long sharp cracks after (a) 1h and (b) 3h of plasma hydrogenation.

A recent growing interest has been employed on developing plasma hydrogenation based techniques of layer transfer [Che 2004, Che 2005, Sha 2006, Dün 2006]. The results obtained by implantation of *H* at 200°C encourage us to explore the hydrogenation of *He*-plates by plasma hydrogenation technique. The presented preliminary results are optimistic. The *He*-plates were shown to form an excellent trapping layer for the *H* atoms producing

long and sharp cracks. The formation of extended defects and cavities from the surface to the trapping layer is an inherent characteristic of plasma hydrogenation and may be the great remaining challenge to industrialize the technique for layer transfer processes.

6.2.5. Final considerations

This chapter reports some aspects of the interactions between *H* and *He* related defects. Diffusion, nucleation and growth of defects are manipulated to produce distinct cavity and crack-like defects structures, arrangements and geometries. Thus, reveals a wide range of defect engineering possibilities. Evidences of a favorable migration of *He* to *H*-rich regions and vice-versa were obtained by observing the defects formation and evolution. A more accurate measurement of implanted species profiles is necessary to make further statements.

A schematic summary of the implanted species migration tendency for the shifted profiles samples is presented in Fig. 6.26. When both species are implanted at room temperature without intermediary annealing, the *He* atoms have the tendency to migrate to *H*-rich region (Fig. 6.26a). If an annealing is performed after *He* implantation, creating *He*-plates and *H* is implanted at room temperature, very limited exchange of atoms seems to occur (Fig. 6.26b). If *He*-plates are created and *H* is implanted at 200°C, *H* atoms may migrate to the *He*-rich region (Fig. 6.26c).

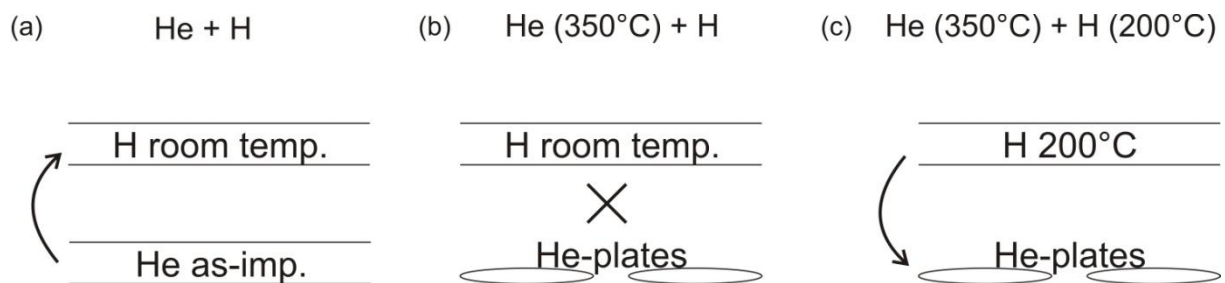


Figure 6.22- Schematic summary of the implanted species tendency of migration for the distinct implantation/annealing conditions of shifted profiles samples.

CHAPTER 7

Ordering of Nanostructures by Stress Engineering

In the study presented in Chapter 6, sub-local organized arrangements of *H*-platelets within nano-size domains were observed to emerge under the influence of localized strain field generated by *He*-plates. The four $\{111\}$ *H*-platelets variants were selectively oriented by the symmetry of the field.

This chapter presents a detailed evaluation of this elastic interaction effect. The outcome of the study is a model based on energy minimization, which quantitatively predicts the formation and distribution of each platelet variant. For completeness, the experimental conditions are summarized in section 7.1, and relevant results are presented in section 7.2. Then the basic assumptions are introduced, and the calculations are described and discussed in details.

7.1. Experimental

The present study emerged from an experiment described in Chapter 6. The samples were submitted to two consecutive implantation and thermal treatment steps. In the first step, the samples were implanted with 45keV He^+ ions at a fluence of $1 \times 10^{16} \text{ cm}^{-2}$ and annealed at 350°C for 900s in high vacuum. This resulted in the formation of overpressurized plate-like cavities [Fic 1997, Hue 2006], named *He*-plates, preferentially oriented parallel to the surface and located at a depth close to the mean projected range of the *He* ions (≈ 400 nm). In the second step, the samples were implanted with 30keV H_2^+ ions at the fluence of $0.5 \times 10^{16} \text{ cm}^{-2}$ and then annealed at 300°C for 1800s, leading to the precipitation of *H*-platelets located ≈ 200 nm above the strain source (*He*-plates). The implantations were performed at room temperature with a current density of $0.5 \mu\text{A} \cdot \text{cm}^{-2}$. The specimens were characterized by transmission electron microscopy (TEM) in cross-section mode.

7.2. Results

Figure 7.1 shows a cross-sectional TEM image taken after the first implantation/annealing step. Two edge-on *He*-plates are observed at a depth $\approx R_p^{He}$, lying on the (001) habit plane, parallel to the surface. The dark fringes surrounding the *He*-plates are obtained under two-beam imaging conditions using reflection $\mathbf{g} = (004)$. They are ascribed to strain induced contrast resulting from the distortion of the crystal lattice, due to the high internal gas pressure of the defects [Fic 1997, Hue 2006]. Figure 7.2a-e shows a series of plan view TEM pictures from *He*-plates produced using particular \mathbf{g} reflections. In each case, a specific zone of the circumferential strain field surrounding the plate is highlighted. The image shown in Fig. 7.2f was obtained using multiple \mathbf{g} vectors, where the strain contrasts is seen surrounding all the plate. Figure 7.3a shows more clearly the fourfold bend contours (flower-like structure) as obtained in the (-100) zone-axis incidence [Ful 2002, Nom 1997]. Figure 7.3b also presents in details the butterfly-like contrast bend contours obtained with two beam conditions using $\mathbf{g} = (-400)$.

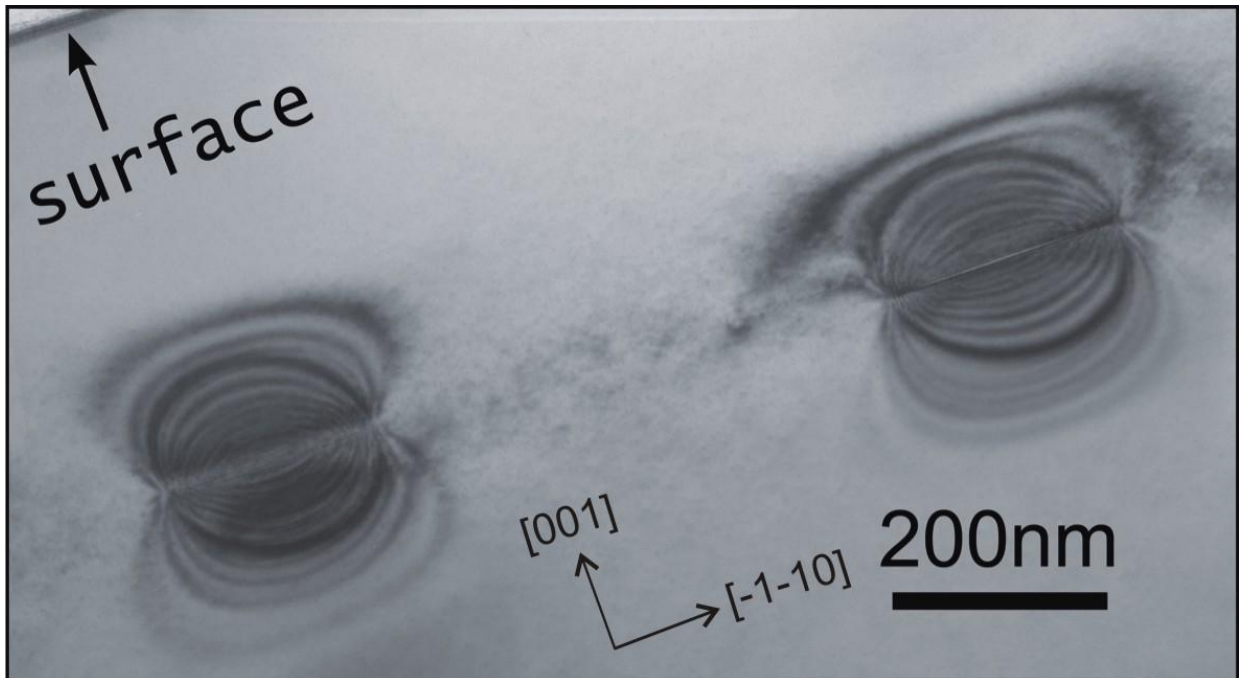


Figure 7.1- Cross-section TEM at dynamical bright-field conditions showing two edge-on *He*-plates formed by the implantation of He^+ (45keV, $1 \times 10^{16} \text{cm}^{-2}$ and annealing at 350°C for 900s).

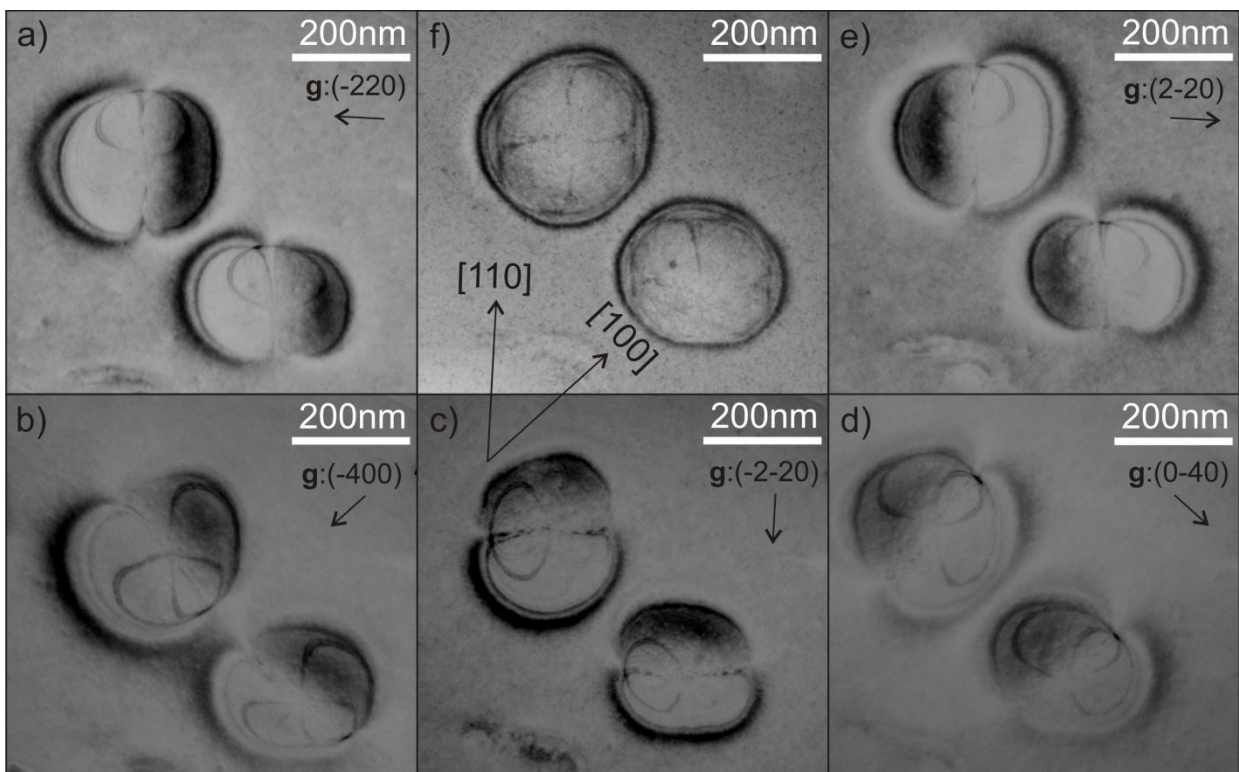


Figure 7.2- Plan-view TEM images showing *He*-plates formed by the implantation of He^+ (45keV, $1 \times 10^{16} \text{cm}^{-2}$ and annealing at 350°C for 900s). The images were obtained using (a) $g: (-110)$, (b) $g: (-400)$, (c) $g: (0-1-1)$, (d) $g: (400)$, (e) $g: (1-10)$, (f) all g vectors. The figure characterizes the cylindrical symmetry of the strain field.

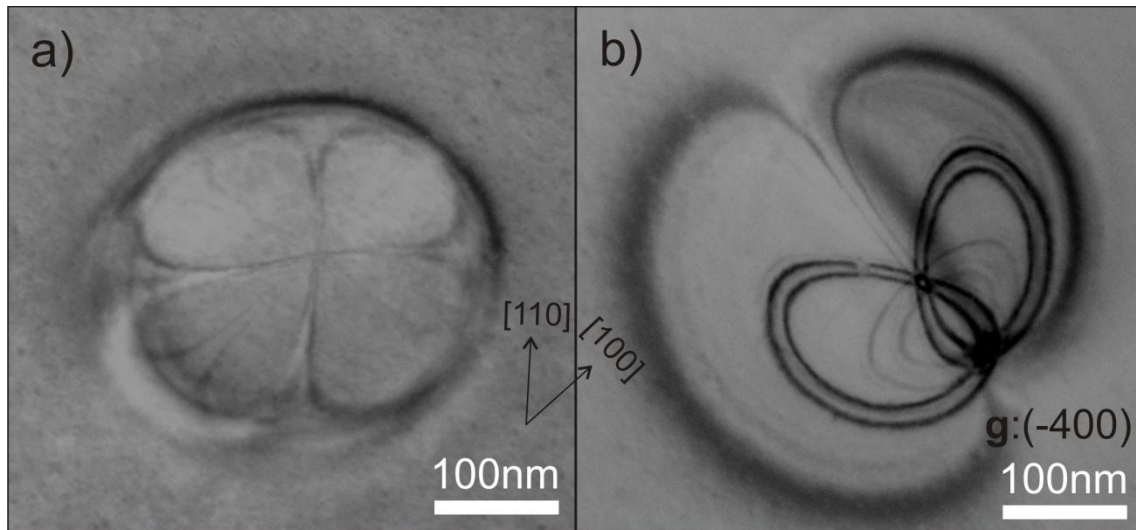


Figure 7.3- Plan-view TEM images of a *He*-plate (45keV, $1 \times 10^{16} \text{cm}^{-2}$ and annealing at 350°C for 900s) showing in detail the contrast obtained by imaging with (a) all the g vectors resulting in a flower-like image and (b) $g: (-400)$, resulting in a butterfly-like image.

Hence, the *He*-plate strain field is characterized in terms of a symmetry axis z oriented perpendicular to the surface and dissecting the *He*-plate. Figure 7.4 shows a 3-D pictographic construction of the structure, indicating the main axis used in the further modeling and calculation.

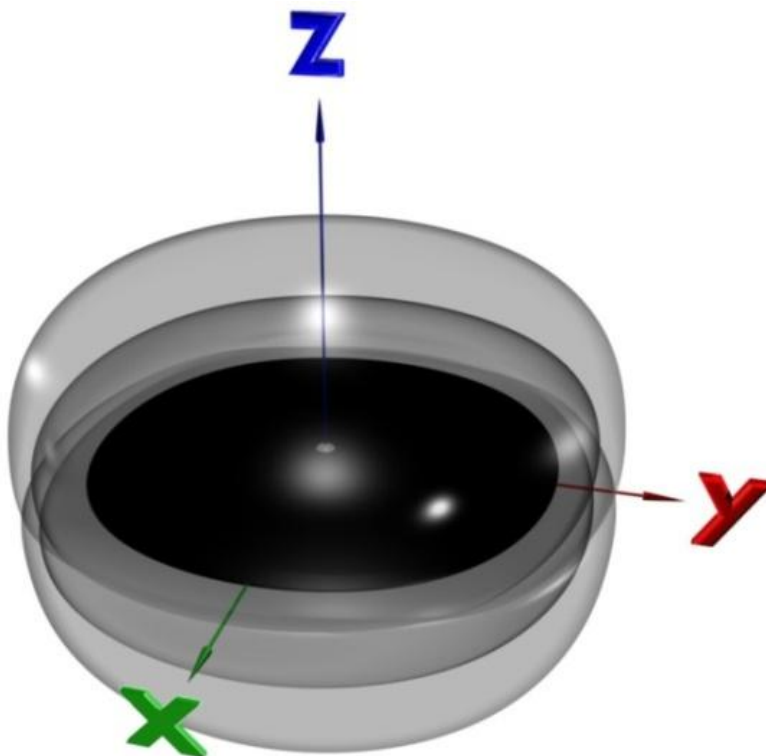


Figure 7.4- Shows a 3-D pictographic representation of the *He*-plate surrounded by its strain field of cylindrical symmetry. The Axes x , y and z as used in the calculation, are also defined.

The TEM shown in the Fig. 7.5 was obtained after *H*-implantation/annealing (300°C for 1800s). It presents the arrangements of *H*-platelets, with respect to the position of the *He*-plate. In the region directly above the *He*-plate, the *H*-platelets are preferentially aligned along specific {111} lattice variants, whilst preferential (001) orientations are observed elsewhere. The (001) preferential orientations are ascribed to elastic interactions between the *H*-platelets and the compressive in-plane stress generated by the implantation induced defects [Höc 2002, Nas 2005].

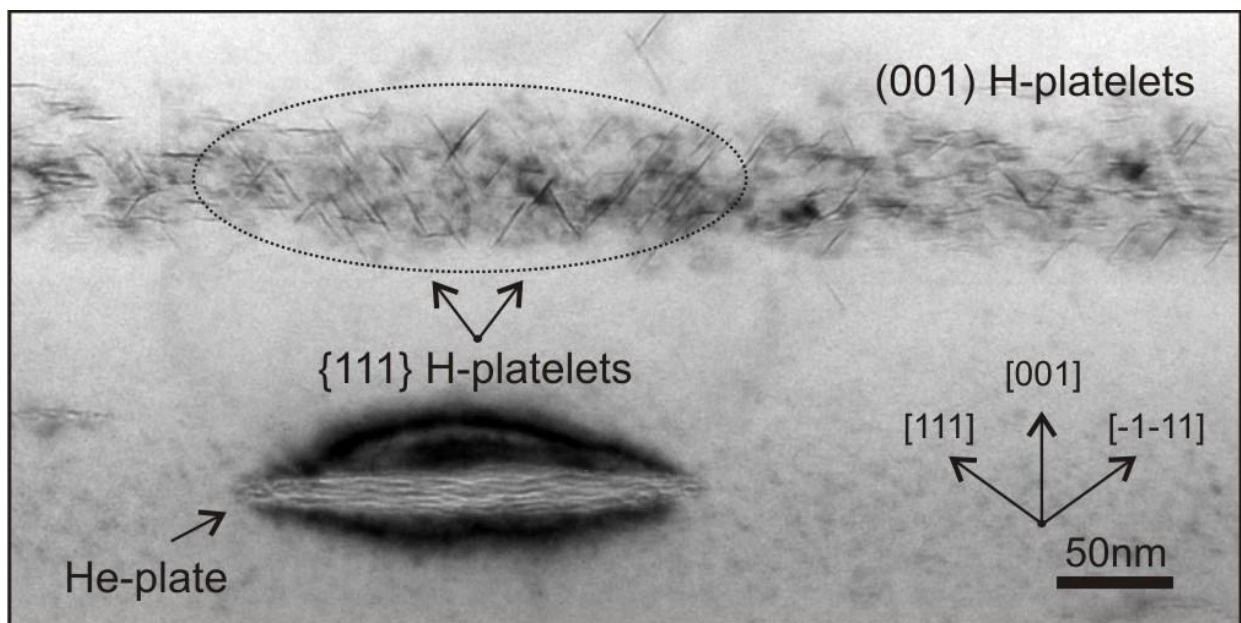


Figure 7.5- Cross-sectional TEM picture obtained after H implantation/annealing (300°C 1800s) showing that, above a *He*-plate, the *H*-platelets are oriented preferentially to specific {111} variants, with respect to the symmetry axis of the strain field. In the regions where no *He*-plate is present, the *H*-platelets are observed to be formed in the (001) planes, parallel to the surface.

Figure 7.6 shows a micrograph obtained from a thinner region of the TEM specimen, where the *He*-plate has been cut through during sample preparation. No strain-contrast is observed since only a pressureless plate cavity remains. In this condition (sample thickness thinner than the diameter of the *He*-plate), the observation shows only *H*-platelets oriented along two edges on {111} variants. The histogram at the top represents the frequency counts of *H*-platelets as a function of the distance from the *z*-axis.

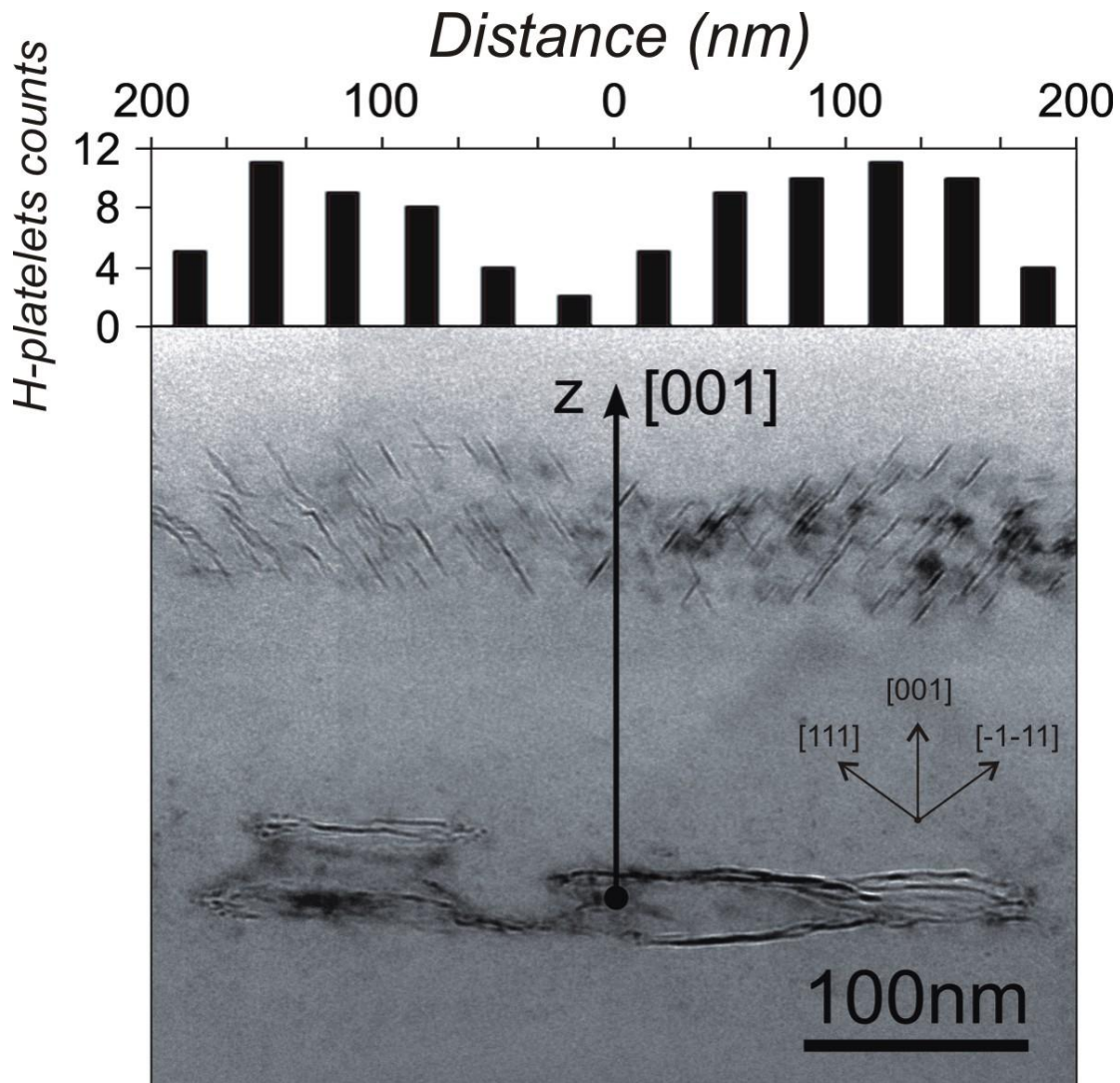


Figure 7.6- Cross-section TEM micrograph obtained from a very thin region of the specimen. The *He*-plate has been cut through during sample preparation leaving a pressureless void (fringes contrast is not observed anymore). In this condition (sample thickness thinner than the diameter of the *He*-plate), the observation is restricted only to cavities nucleated under the influence of its strain field. The formation and distribution of two edges on variants of *H*-platelets is seen in detail. The (-1-11) platelet variant is situated at the left side of the plate, and (111) platelet variant at the right side. The observation is performed along [-110] direction. The histogram at the top represents the frequency counts of *H*-platelets as a function of the distance from the *z* axis.

In general, the in-plane distance between the *He*-plates visibly exceeds their average diameter. The representative pictograph presented in Figure 7.7 summarizes the general scenario: local strain fields from individual *He*-plates induce a specific arrangement of *H*-platelets creating ordered nano-domains embedded into the bulk material.



Figure 7.7- Pictographic representation showing the whole scenario found in the sample. $\{111\}$ particular arrangements of H -platelets are created above the He -plates, and (001) H -platelets are formed in the zones far from He -plates. The distance between each arranged nano-domain exceeds its average diameter.

Due to the cylindrical symmetry of the strain field around the z -axis (see Figs. 7.1 and 7.2), the four possible $\{111\}$ variants of H -platelets are arranged in quadrants. Two $\{111\}$ variants are observed when imaging along the $[-110]$ direction (see Fig. 7.4); the two other variants could be seen performing the observations along the $[-1-10]$ direction. This is an example of unique nanoscale geometrical arrangement of objects with a local fourfold rotation symmetry. The pictograph shown in Fig. 7.6 represents in 3-D the concept of this nanostructured system. This specific arrangement of precipitates own a singular characteristic: the normal direction of each H -platelet variant group converges to the z -axis creating a focal axis.

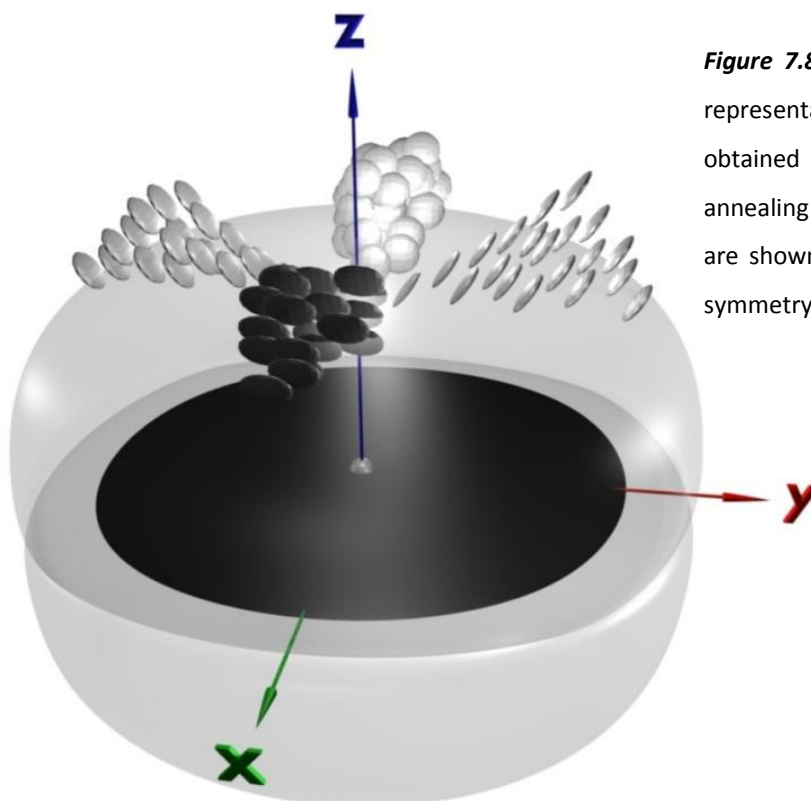


Figure 7.8- Presents a 3-D pictographic representation of the nanostructure, as obtained after both implantations and annealing steps. The H -platelets variants are shown to be arranged in a fourfold symmetry.

Figures 7.9a and b show the frontal and top pictograph views of the nanostructure. The main crystalline directions are represented on the top view defining the four quadrants and their respective $\{111\}$ H -platelets variants.

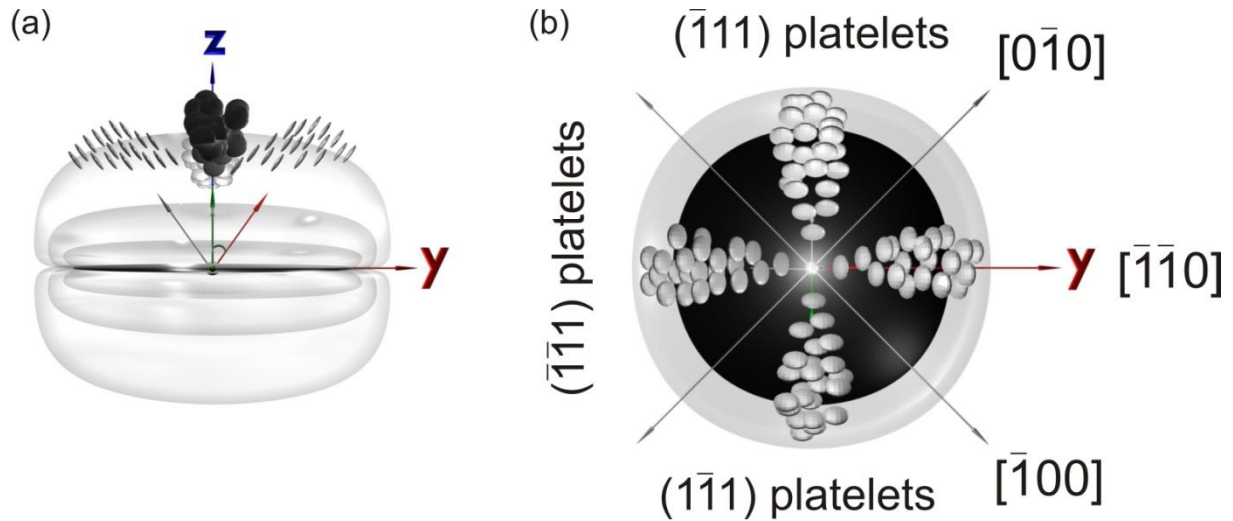


Figure 7.9- Pictographic representation of the nanostructure showing (a) the frontal and (b) the top view. The main crystallographic directions are represented on the top view characterizing the four quadrants, where each one of the $\{111\}$ platelets orientations are formed.

7.3. Model and Discussions

In this section a model for the nucleation of H -platelets under the strain field of a He -plate is developed. First, the basic assumptions are introduced. The second part is dedicated to the calculation of the stress field of a He -plate, as well as the total strain field at any point of the solid with the introduction of the in-plane stress factor. The third part presents the energy minimization criterion for the nucleation of the platelets. In the fourth part the results of the calculations are presented and discussed.

7.3.1. Introduction to the model

In order to understand and explain our experimental observations, a model based on elastic interactions for the nucleation of H -platelets in a semi-infinite solid was developed. The model is grounded on the following hypotheses:

- i) the preferential orientation for the nucleation of H -platelets will be determined by the minimization of their formation energy, with respect to external stress tensor [Nas 2005];
- ii) the H -platelets, as well as the He -plates, are represented as dislocation loops of interstitial nature, with an equivalent burgers vector b_H characterizing their strain-field [Nee 1988, Gri 2000, Nas 2005];
- iii) the H -implantation damage causes an in-plane stress ($\sigma_{yy}^{in-plane}$) and an out-of-plane strain $\left(\frac{\delta d}{d}\right)_z$ in the layer where nucleation of H -platelets takes place. This effect plays an important role in determining the alignment of the precipitates [Höc 2001, Höc 2002, Nas 2005];
- iv) the whole system is placed in a near-surface region, thus its influence on stress and strain distribution has to be accounted for [Hir 1982].

7.3.2. Calculation of the total stress tensor

Calculation of the stress field of a He-plate in a semi-finite solid

In order to simplify the calculation, the strain field of the He -plate (Fig. 7.10b), represented by a dislocation loop, will be modeled in 2-D by a dipole of edge dislocations running along the y -axis (Fig. 7.10c), defined as the $[-1-10]$ direction of the crystal. The z -axis is defined as perpendicular to the surface, i.e. $[001]$ direction. The directions are represented in Fig. 7.10a.

One of the main challenges in solving an elasticity problem is to satisfy all equilibrium requirements (equilibrium and compatibility), and calculate a vector field or a tensor field. This requires at least three and possibly six partial differential equations to be solved. Finding-a solution can be quite difficult. Instead, there is a particular method to construct a general function that satisfies the partial differential equations by definition. The method is known as *Airy's Stress Function*, and it permits to overcome the problem by reducing the coupled partial differential equations to a single partial differential equation, which is then used to deduce the stresses and strains [Hir 1982].

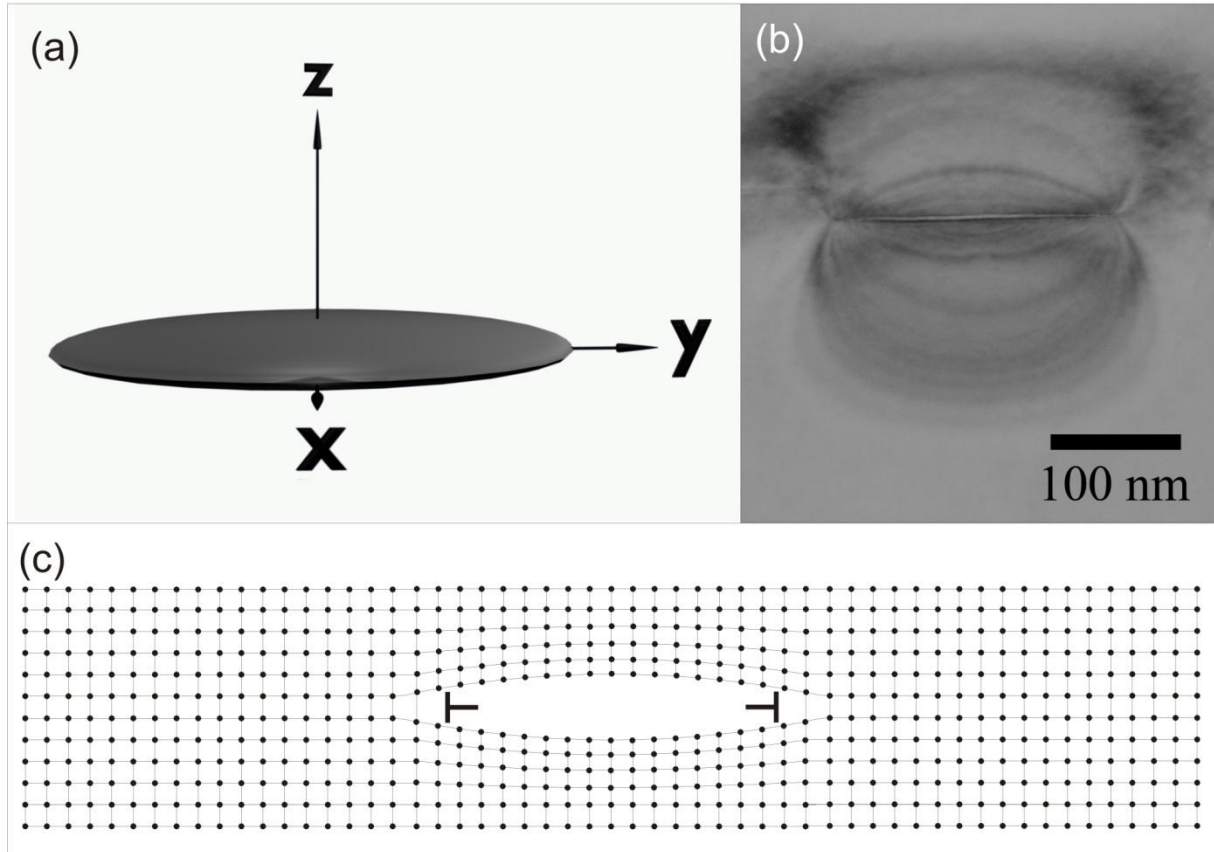


Figure 7.10- (a) pictograph of a He-plate representing the convention of axes used in the model. (b) strain field of a He-plate and (c) the analogy with a dipole of dislocations in 2-D.

The Airy's stress function is defined as a biharmonic function $\phi(z, y)$, where

$$\sigma_{zz} = \frac{\partial^2 \phi}{\partial y^2} \quad (7.1)$$

$$\sigma_{yy} = \frac{\partial^2 \phi}{\partial z^2} \quad (7.2)$$

$$\sigma_{zy} = -\frac{\partial^2 \phi}{\partial z \partial y} \quad (7.3)$$

satisfies the following conditions:

$$\sigma_{xx,x} + \sigma_{xy,y} = 0 \quad (7.4)$$

$$\sigma_{xy,x} + \sigma_{yy,y} = 0 \quad (7.5)$$

$$\Delta \sigma_{xx} + \sigma_{yy} = 0 \quad (7.6)$$

The Airy's function of an edge dislocation of Burger's vector $(0, b)$ in an infinite elastic medium is a classical academic problem, and the solution is given by [Hir 1982],

$$\phi(z, y) = -D \ln r, \quad (7.7)$$

where $r = \sqrt{z^2 + y^2}$ and $D = \frac{\mu b_{eff}}{2\pi(1-\nu)}$, being μ the shear modulus, ν the Poisson's ratio, a

the radius of the *He*-plate and c the distance from the surface. Let us consider a dipole of edge dislocations centered on the z -axis, at a distance $-c$ from the y axis and separated by a distance $2a$, as represented in Fig. 7.10.

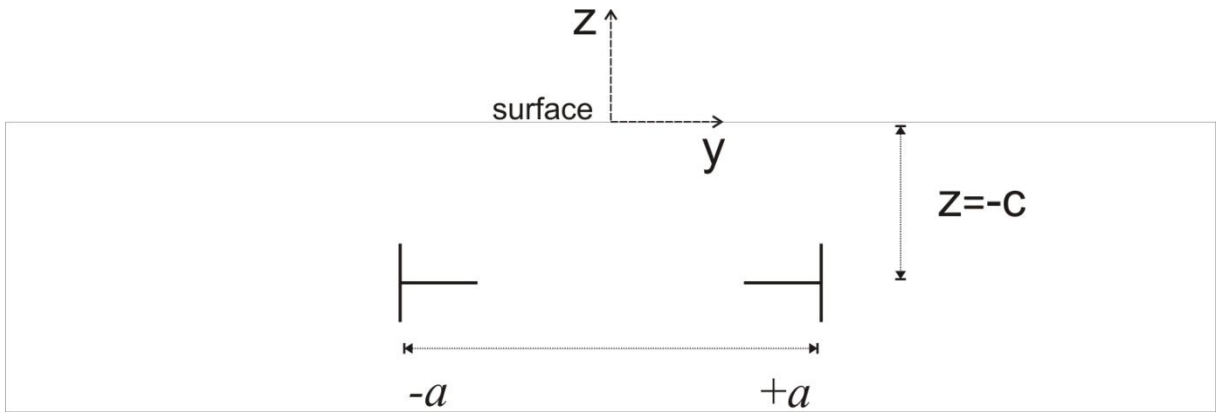


Figure 7.11- Graphic representation of a dipole of edge dislocations centered on the z axis, at a distance $-c$ from the y axis and separated by a distance $2a$.

The stress components of an edge dislocation of burgers vector $(0, b)$ located at $y=-a$ and $z=-c$ are given by:

$$\sigma_{zz}^{edge} = \frac{\partial^2 \phi}{\partial y^2} = -D(y+a) \frac{3z+c + y+a^2}{[z+c^2 + y+a^2]^2} \quad (7.8)$$

$$\sigma_{yy}^{edge} = \frac{\partial^2 \phi}{\partial y^2} = +D(y+a) \frac{z+c - y+a^2}{[z+c^2 + y+a^2]^2} \quad (7.9)$$

$$\sigma_{zy}^{edge} = -\frac{\partial^2 \phi}{\partial z \partial y^2} = D(y+c) \frac{z+c^2 - y+a^2}{[z+c^2 + y+a^2]^2} \quad (7.10)$$

With Eq. 7.8-7.10 we are able to describe the stress components of an edge dislocation at an infinite medium. In order to consider the influence of the proximity of a surface on stress distribution, there is a restrict condition to be satisfied. The total resulting

forces on the surface ($z=0$) needs to be null. To satisfy equilibrium conditions, the normal, as well as the tangential stresses, need to vanish at the surface, hence

$$\sigma_{zz}(y,0) = 0 \quad (7.11)$$

$$\sigma_{xy}(y,0) = 0 \quad (7.12)$$

A method to satisfy the relations 7.11 and 7.12 consist in introducing singularities in the problem [Hir 1982]. Moreover, to satisfy the relation 7.11 a virtual *image dislocation* with opposite Burger's vector ($0, -b$) is introduced at the *image point* $y=-a$ and $z=c$. A second singularity is introduced to equilibrate the tangential forces (relation 7.12) at the surface. There are several methods to overcome this problem as, for example, introducing the *Boussinesq forces* on the surface [Hir 1982]. Finally, in order to obtain the strain and stresses introduced by the edge dislocation in a semi-finite solid, we obtain a total Airy's function as:

$$\phi_{Tot}^{Airy's}(z, y) = \phi^{Edge}(z, y) + \phi^{image}(z, y) + \phi^{Boussinesq}(z, y), \quad (7.13)$$

where $\phi^{Edge}(z, y)$ is the stress function of an edge dislocation, $\phi^{image}(z, y)$ is the stress function of its correspondent image dislocation and $\phi^{Boussinesq}(z, y)$ are the tangential forces introduced by the *Boussinesq forces*. The total Airy's function of an edge dislocation near a free surface is then expressed by:

$$\phi_{Tot}^{Airy's}(z, y) = -Dy \ln \sqrt{z+a^2+y+c^2} + Dy \ln \sqrt{z-a^2+y+c^2} + \frac{2Dazy}{z-a^2+y^2} \quad (7.14)$$

Then, the stress field of a dipole of edge dislocations localized at $y=-a$ and $y=+a$ at $z=-4$ will be given by:

$$\begin{aligned} \phi^{Tot}(z, y) = & -Dy \ln \sqrt{z+a^2+y+c^2} + Dy \ln \sqrt{z-a^2+y+c^2} + \frac{2Dazy}{z-a^2+y^2} \\ & + Dy \ln \sqrt{z+a^2+y-c^2} - Dy \ln \sqrt{z-a^2+y-c^2} - \frac{2Dazy}{z-a^2+y^2} \end{aligned} \quad (7.15)$$

With this, we have completely modeled the strain field of a dislocation dipole at the vicinity of a free surface. The next step is to introduce the in-plane stress factor in the model.

Accounting for the in-plane stress

In order to simplify the calculation, a normalized Airy's function is defined as

$$f^{Airy's}(z, y) = \frac{a \cdot \phi_{Tot}^{Airy's}(z, y)}{D}$$

The in-plane stress ($\sigma_{yy}^{in-plane} = -2\mu \left(\frac{\delta d}{d} \right)_z$, as deduced in Chapter 4) is normalized

in the same manner where a k factor is defined as

$$k = \frac{a}{D} \sigma_{yy}^{in-plane} = a \frac{4\pi(1-\nu)}{b_{eff}^{He-plate}} \left(\frac{\delta d}{d} \right)_z$$

$\left(\frac{\delta d}{d} \right)_z$ usually follows a Gaussian distribution and was taken as constant at its maximum value. The introduction of the factor k as a homogenous in-plane stress in the whole volume of the solid allows to map out a complete cartographic description of the H -platelets variants distribution to any chosen R_p^H . The total stress field at any point (z, y) of the solid can be calculated from the total normalized function $f_{total}^{Airy's}(z, y)$, defined as:

$$f_{total}^{Airy's}(z, y) = \frac{a}{D} \phi_{Tot}^{Airy's} - k \frac{y^2}{2}$$

The total stress components are expressed in terms of the reduced adimensional quantities by:

$$\sigma_{yy}^* = \frac{\partial^2 f_{total}^{Airy's}}{\partial z^2} \quad (7.16)$$

$$\sigma_{zy}^* = -\frac{\partial^2 f_{total}^{Airy's}}{\partial z \partial y} \quad (7.17)$$

$$\sigma_{zz}^* = \frac{\partial^2 f_{total}^{Airy's}}{\partial y^2} \quad (7.18)$$

He-plate effective Burger's vector determination

As the displacement field of a dislocation loop is completely described by its Burger's vector, by analogy, we have to define an effective Burger's vector ($b_{eff}^{He-plate}$). This vector represents the displacement field resulting from the internal gas pressure of the cavity [Gri 2000, Nee 1988].

To predict the effective burgers vector $b_{eff}^{He-plate}$, the pressure of a *He*-plate needs to be estimated. Under equilibrium conditions, the internal gas pressure of the *He*-plate can be calculated by [Har 2002]:

$$p^{Eq} = \sqrt{\frac{\pi\gamma\mu}{a(1-\nu)}} \quad (7.19)$$

where γ is the specific surface free energy and a is the radius of the *He*-plate. Eq. 1.19 is combined with the calculations of $\sigma_{zz}^{*0} = \sigma_{zz}(0, R_p^{He})$ of the dipole as:

$$p^{Airy's} = \sigma_{zz}^{*0} \frac{D}{a} = p^{Eq} = \sqrt{\frac{\pi\gamma\mu}{a(1-\nu)}}.$$

From where the $b_{eff}^{He-plate}$ can be obtained as:

$$b_{eff}^{He-plate} = \sqrt{\frac{\pi\gamma\mu}{a(1-\nu)}} \frac{a2\pi}{\mu\sigma_{zz}^{*0}} \frac{1-\nu}{\mu\sigma_{zz}^{*0}}.$$

The result from the calculation of the σ_{zz} variation from the surface up to $z=-8$ at $y=0$ is shown in the graphic of Fig.7.14. From there, a $\sigma_{zz}^{*0} = 1.8$ is obtained at the center of the dislocation dipole. Taking typical values for silicon ($\gamma=1.38Jm^{-2}$, $\mu=68GPa$ and $\nu=0.22$ [Hue 2006]) and $a=100nm$ (average radius of the *He*-plates) combined with $\sigma_{zz}^{*0} = 1.8$, we obtain a value of $b_{eff}^{He-plate} \approx 7nm$.

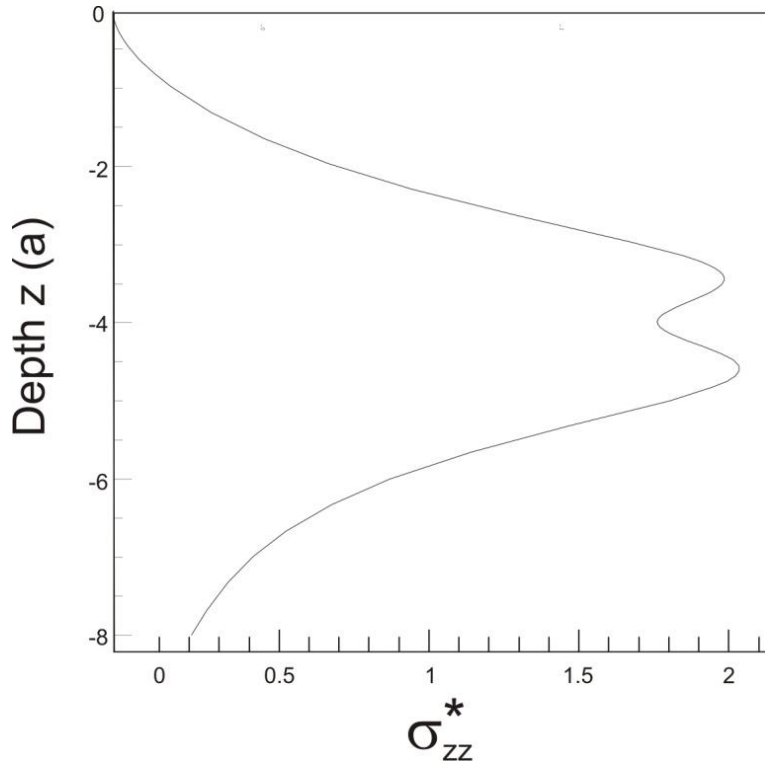


Figure 7.14- The graphic plots the σ_{zz} variation along the z axis at $y=0$. At the center of the dislocation dipole a $\sigma_{zz}^{*0} = 1.8$ is obtained.

7.3.3. Energy minimization criteria

Since the H -platelets were modeled as dislocation loops of interstitial nature $\vec{b}_H = -\vec{b}_H \vec{n}$, the total energy of formation E^T under the influence of a strain field is given by:

$$E^T = E_f + \int \vec{b}_H \cdot \vec{\Sigma} d\vec{S}, \quad (7.20)$$

where E_f is the self-energy, $d\vec{S} = dS \vec{n}$ is a surface element of the dislocation loop and $\vec{\Sigma}$ is the total stress tensor described by the two stress components:

- i) the stress field caused by the overpressurized He -plate at the proximity and;
- ii) the in-plane stress component generated by the implantation damage.

The energy minimization criteria for the nucleation of H -platelets in the presence of external stress fields follows as deduced in Chapter 4, given by the energy density variation expression

$$\frac{\Delta E}{\Delta V} = -n_z^2 \sigma_{zz} + 2\sigma_{zy} n_z n_y + n_y^2 \sigma_{yy} \quad , \quad (7.21)$$

where (n_y, n_z) values are the projections in 2-D of the unitary burgers vectors to each platelet variant. Three possible orientations of H -platelets were considered, (001) and (111) and (100); their (n_y, n_z) values are (0,1) and $(-\sqrt{2}/\sqrt{3}, 1/\sqrt{3})$ and (1,0), respectively.

7.4. Calculation results

In this section, we compare the calculation results with the experimental observations and then use the model to make predictions.

7.4.1. Verification of the experimental observations

The maximum value of $\left(\frac{\delta d}{d}\right)_z$ for $0.5 \times 10^{16} \text{ cm}^{-2} H_2^+$ can be estimated as $\approx 0.3\%$ [Bis 1998]. In combination with the calculated $b_{\text{eff}}^{\text{He-plate}}$ value, we can estimate $k \approx 0.4$. As a first approximation, the formation energy of H -platelets is assumed to be equal, independently of their orientation [Mar 2005]. Under these considerations, the energy minimization criteria can be applied to estimate the orientation of H -platelets as a function of their position with respect to the He-plate. In the following, all the calculations are performed and the results presented in terms of a unit of length $a=100\text{nm}$.

Figure 7.15 shows the results of ΔE calculations considering the two orientations of platelets (001) and (111) experimentally observed. The maps of iso-energetic regions are plotted with ΔE intervals of 0.1 ($\approx 100\text{MPa}$). They predict the energy variation for the formation of platelets at any location from the surface $z=0$ to a depth of $z=-8a$ at the vicinity of a He-plate, which extends from $-a$ to $+a$ and is located at a depth $z=-4a$. The iso-energetic regions for (001)-platelets, Fig. 7.15b, are symmetrically distributed around the stress symmetry axis z . In contrast, (111)-platelets map (Fig. 7.15a) presents asymmetry with respect to the z -axis, where each particular {111} variant is favorable (i.e. has the lowest E^T) in one quadrant of the 3-D structure. Figure 7.15c shows the ΔE level variations at the depth $z = R_p^{\text{He}} / 2 \approx R_p^H$. The formation of (111) platelets is favorable (lower ΔE) from $y=0$ to

$y \approx 1.5a$, from where the (001) platelets become preferential. The frequency count of {111} platelets shown in Fig. 7.6 is clearly related (inversely proportional) to the ΔE level variation given in Fig. 7.15.

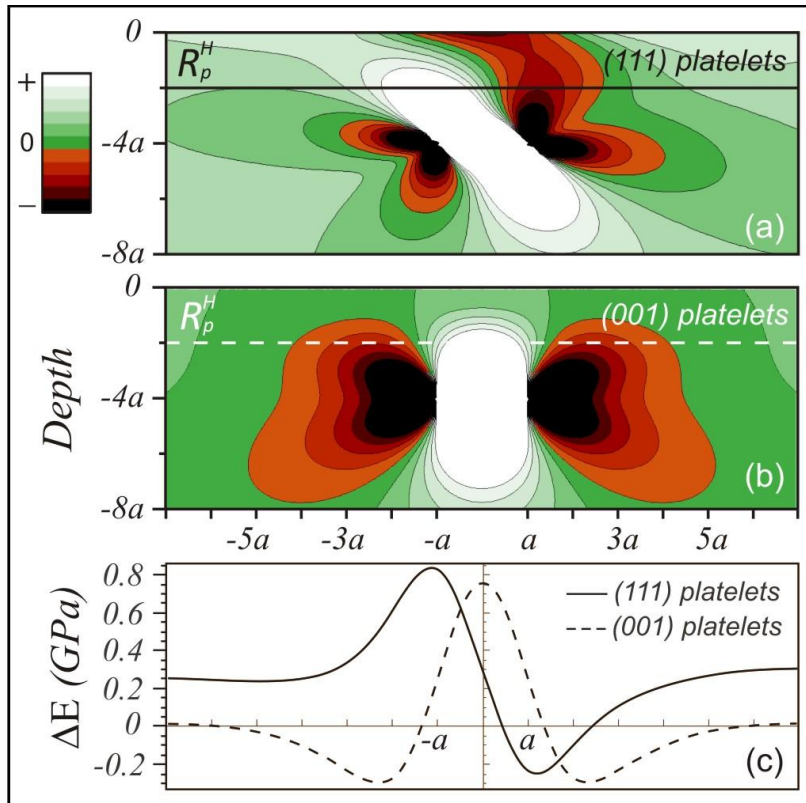


Figure 7.15- Maps of iso-energy regions of (111) platelets (a) and (001) platelets (b). The curves in (c) show the ΔE level variations at $z=-2a$ for (111) platelets (continuous line), and (001) platelets (dashed line).

This result shows that the proposed model presents an excellent agreement with the experimental observations.

7.4.2. Model predictions

The model can be used to predict some interesting results. By changing the H -implantation depth z (i.e. the relative distance between the H -platelets and the strain source), distinct distributions of platelets along y are expected to form. Figure 7.16 shows the ΔE level curves calculated for distinct depths z (intervals of $0.5a$) between the surface and the core of the strain source (He -plate) located at $z=-4a$. The region where the (111) platelets are favorable is approximately centered at $y \approx a$ and it becomes as narrow as it comes closer to the strain source. The (001) platelet variant is always the favorable one after a certain distance from the z -axis. This effect is naturally attributed to the predominance of the in-plane stress far from the He -plate. Moreover, the region for (001) favorable formation

becomes wider (approaches to the z -axis) as it gets closer to the strain source. The formation of (100) platelets (perpendicular to the surface) seems to be favorable exactly along the z -axis. Elsewhere is very unlikely to be formed.

Figure 7.17 shows the ΔE level curves obtained for depths $-50a < z < -4a$ (i.e. underneath the He -plate). Notice that the general feature of the curves is basically the same, but the (111) curve is inversed, as naturally expected, being favorable in the opposite quadrant of the structure. Near the He -plate, the curves are very similar to those obtained for $z > -4a$ (i.e. above the He -plate). However, after a certain distance z from the He -plate ($\pm 1.5a$) the curves at both sides become different (compare the curve obtained for $z < -5.5$ with $z > -2.5$). The surface effect on the stress distribution is very clear at $z = -7.5$, as compared to $z = -0.5$. For a large distance from the He -plate (e.g. $z = -15$) the effect of strain source becomes negligible, and, for $z = -50$, it is completely imperceptible. In this case, the orientation of the H -platelets is determined uniquely by the in-plane stress caused by the implantation.

The second effect that can be easily predicted using the model is related to the variation of the in-plane stress intensity and sign (i.e. factor k). This factor could be tailored, for example, by changing the implantation fluence (since the stress increases with fluence) or using substrates under tensile [Pit 2005] or compressive strain. Figure 7.18 shows, in a series of calculations results, the energy variation maps predicted by changing the k factor from a highly tensile layer ($k = -2$) to a highly compressive layer ($k = 2$). The calculation was performed for a depth $z = -2$. The iso-energetic regions are plotted with ΔE intervals of 0.1 ($\approx 100 \text{ MPa}$). Obviously, (001) platelets are neither affected by the changes of intensity nor the in-plane stress sign. On the other hand, (100) H -platelets, (perpendicular to the surface) becomes strongly favorable in tensile in-plane stress conditions, in accordance with recent observations [Pit 2005], and unfavorable in compressive stress conditions. In general, (111) platelets also become favorable at tensile stress conditions and less favorable in compressive stress.

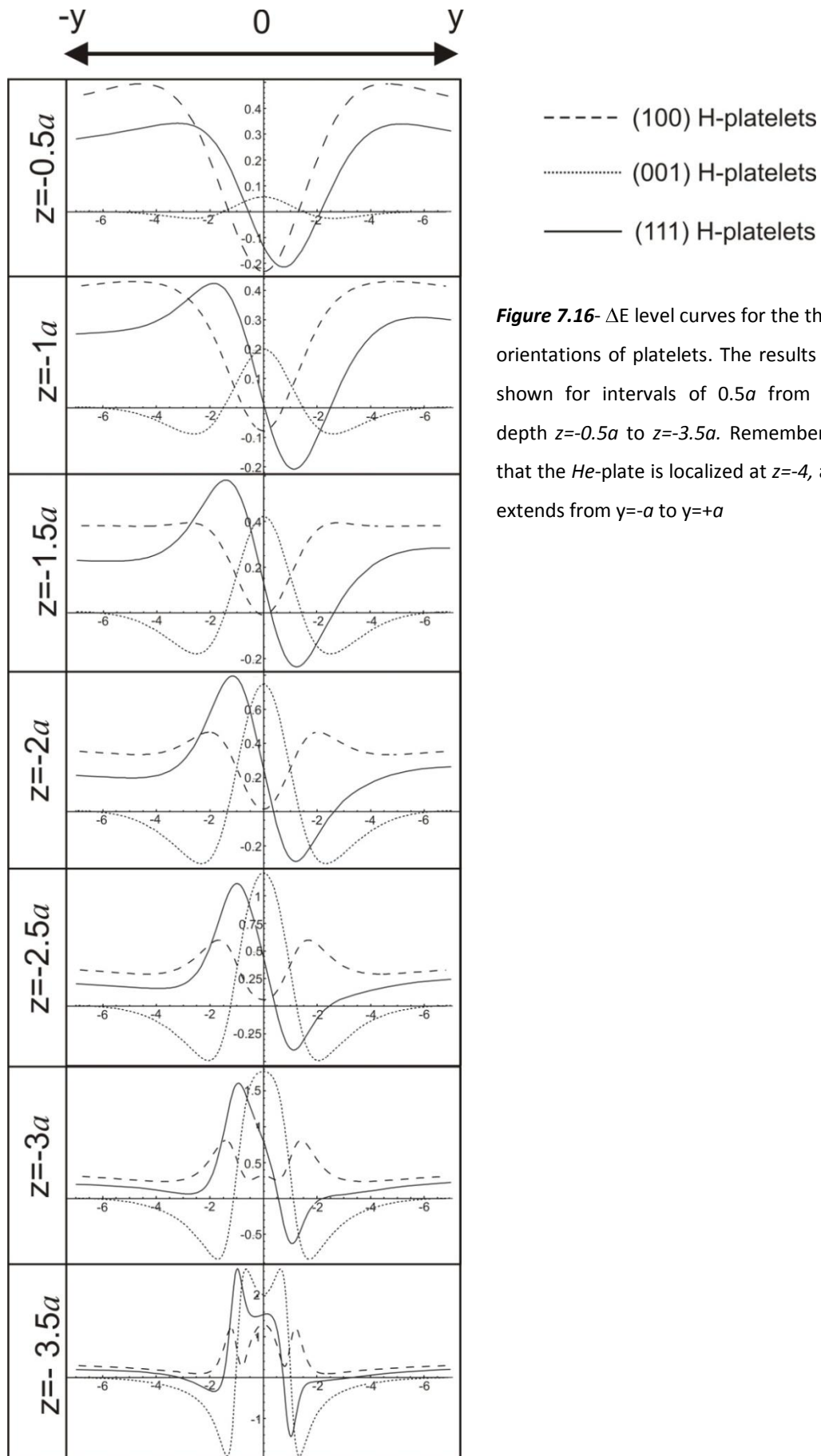


Figure 7.16- ΔE level curves for the three orientations of platelets. The results are shown for intervals of $0.5a$ from the depth $z = -0.5a$ to $z = -3.5a$. Remembering that the *He*-plate is localized at $z = -4$, and extends from $y = -a$ to $y = +a$

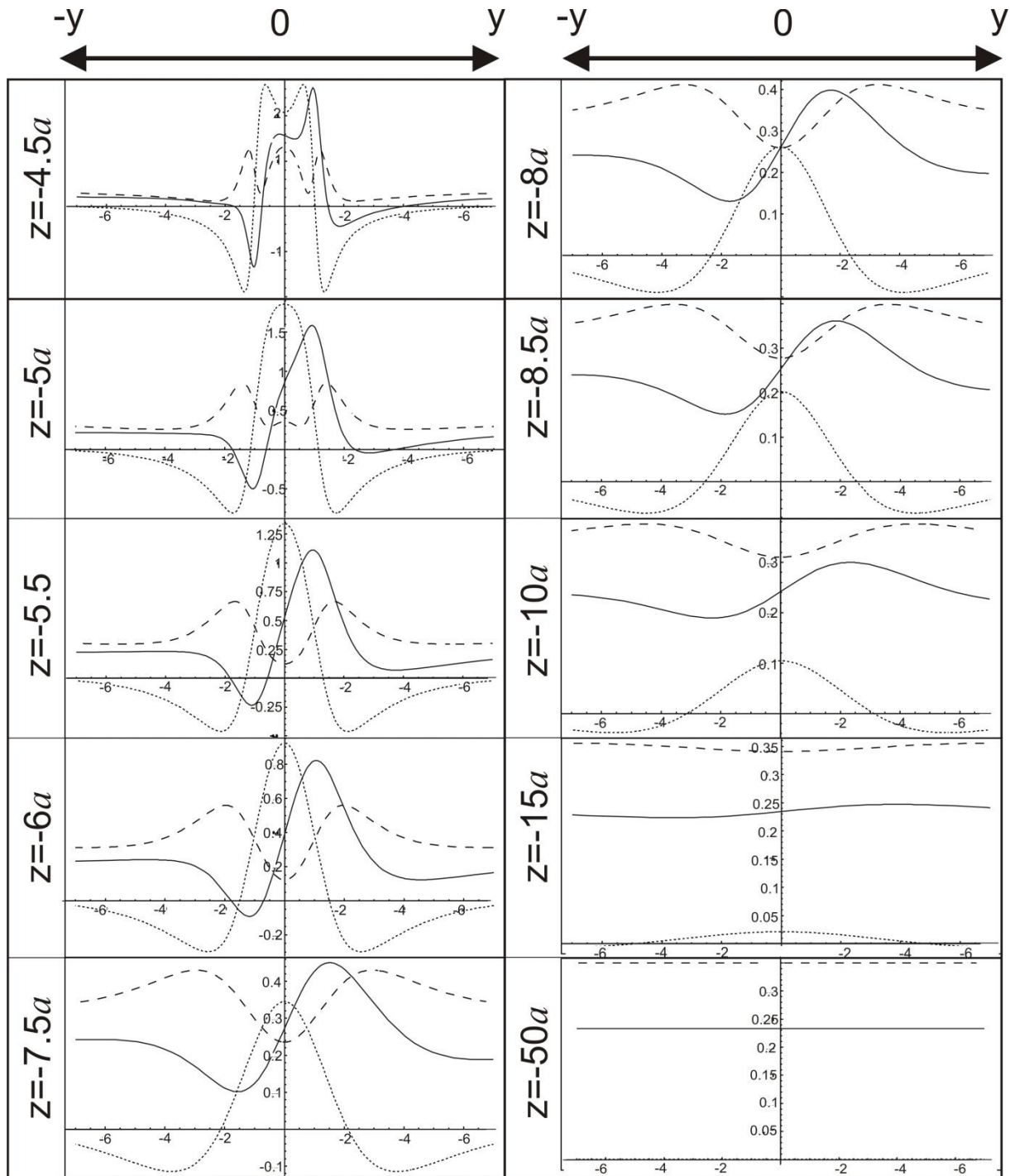


Figure 7.17- Energy level curves for the three distinct orientations of platelets from depth $z=-4.5$ to $z=-50$.

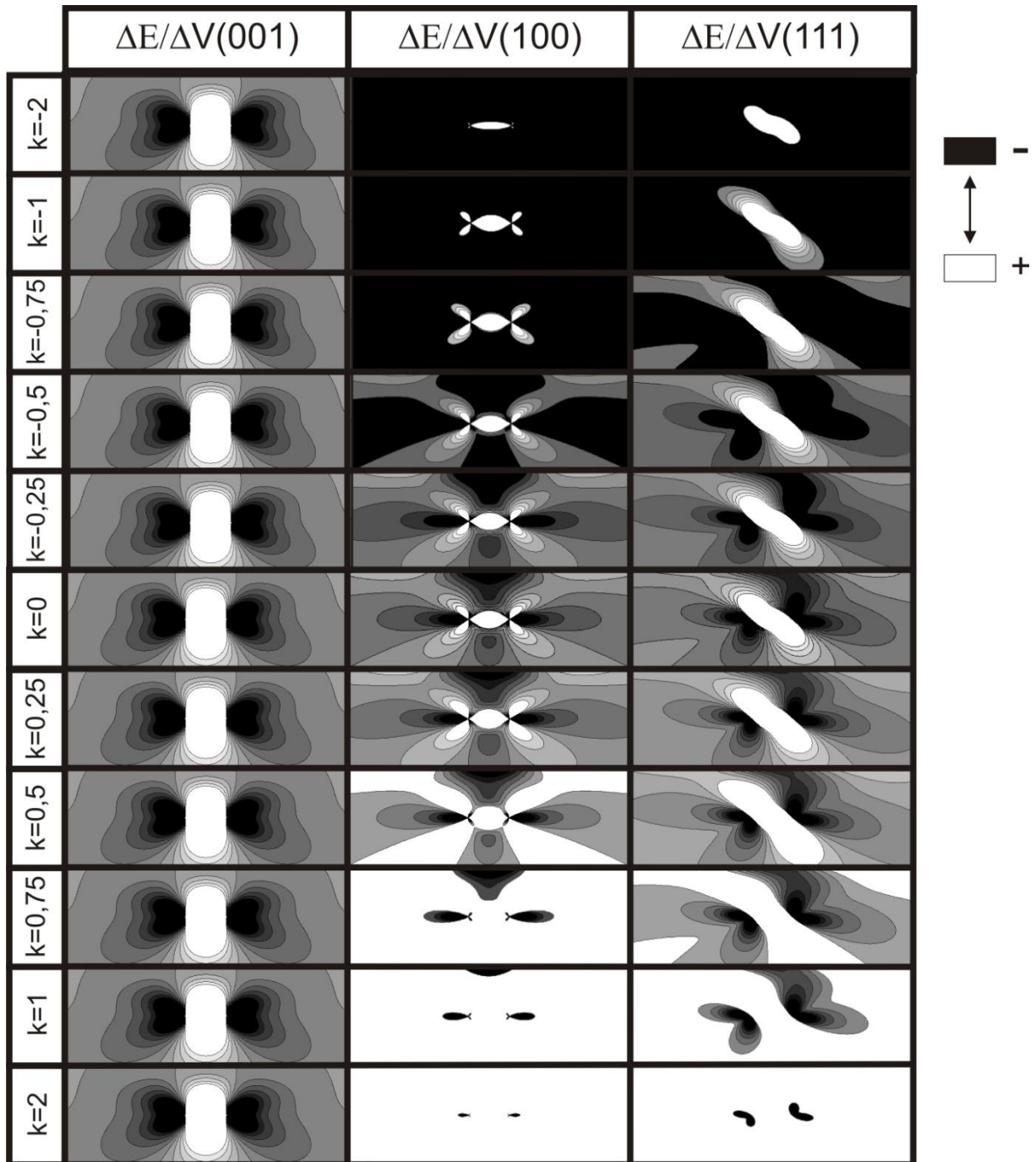


Figure 7.18- Energy level curves for the three distinct orientations of platelets from the depth $y=-4.5$ to $y=-50$.

7.5. Conclusions

The possibility of exploiting local strain sources to tailor a sub-local architecture of platelet-like precipitates, creating arranged nano-domains, was demonstrated in this chapter. We have found that four $\{111\}$ variants of H -platelets in (001) silicon were

organized symmetrically around the symmetry axis of a local strain field. The phenomenon was modeled and the results were in good agreement with the experimental observations.

It seems worth to remark that strain field symmetry (or geometry) can vary depending on the characteristics of the strain source, lattice structure and even on the sample geometry. As a consequence, distinct precipitate arrangements can be imagined. It is also important to point out that equation 7.20 suggests that even a precipitate with higher self-energy ($E_{f1} > E_{f2}$) could become favored by an appropriate stress tensor conditions, resulting in $E_1^T < E_2^T$. Therefore this way, one could imagine that, by adequate stress engineering, it would be possible to induce the formation of new precipitate phases, which so far may have not been observed due to their unfavorable self-energy. This situation found parallel on the discovery of (001) *H*-platelets: *“...the existence of (001) platelets, only seen after ion implantation, was barely acknowledged in 1994 because the {111} surface has in principle lower energy.”* [Ter 2007].

Hence, we propose that nanoscale strain engineering can be further developed and generalized as a tool to tailor specific arrangements of NP's inside discrete nano-domains of a periodic array, as well as to induce the formation of new phases.

SUMMARY AND GENERAL CONCLUSIONS

This work presents a systematic study comprising the microstructure thermal evolution of H_2^+ and He^+ coimplanted (001)-Si substrates. Especial emphasis is given to the blistering and exfoliation phenomena and their relation with the ion induced layer splitting process, usually referred as Smart-Cut[®]. This technology has boosted the development of silicon-on-insulator (SOI) substrates, nowadays a mandatory material for the production of low voltage/low energy ultra-large-scale-integration microelectronic devices. The generic character of the process allows the development of functional heterostructured materials via layer transfer techniques. It provides the possibilities of materials integration even with largely mismatched lattice structures. Therefore, it seems worthwhile to perform systematical studies in order to get more insight into the micromechanisms controlling the ion induced layer splitting process.

In this work, the exfoliation phenomena in H_2^+/H^+ and He^+ (001)-Si coimplanted samples have been investigated as a function of the implantation energy, fluence, fluence rate, annealing protocol and implantation sequence (first H and then He , and vice-versa). The samples were characterized by a combination of microscopy techniques. Scanning Electron Microscopy (SEM) observations of individual exfoliated regions were statistically evaluated in terms of their mean sizes S_{ex} , exfoliation efficiency parameter A_{ex} and exfoliation number densities D_{ex} . Detailed microstructure observation of the exfoliation precursors was performed by Transmission Electron Microscopy (TEM). Surfaces were characterized by Glancing Illumination Optical Microscopy (GIOM) and Atomic Force Microscopy (AFM). In addition, lattice strain measurements were performed by X-Ray Diffraction. The results obtained were discussed in terms of the formation of the exfoliation precursors and their thermal evolution, correlating their elastic and plastic properties, including fracture mechanic concepts and elastic interactions between cavity-like defects.

The range of experimental parameters, including fluences from $\approx 10^{16}$ to 10^{17} cm⁻² and medium (≈ 30 keV) to high (≈ 350 keV) implantation energies, combined with techniques

covering macro and microstructural characterization, as well as the data interpretation methodology and concepts, introduce an unique and original perspective for the study.

In Chapter 3, the effects of implantation (fluence, energy) and thermal protocol (1 or 2 temperature steps) parameters on the exfoliation mean sizes S_{ex} , exfoliation efficiency parameter A_{ex} and density D_{ex} are evaluated. The results obtained show that the exfoliation behavior can be treated as a threshold phenomenon depending on a critical gas concentration in as implanted samples. It was demonstrated that the exfoliation efficiency A_{ex} is rather dependent on the exfoliation mean size S_{ex} . In this work, it is proposed that S_{ex} is governed by two distinct macromechanisms depending on the implantation fluence values. For high fluences, the exfoliation behavior converges to a pressure induced process. For low fluences the exfoliation behavior converges to a cleavage assisted process.

In Chapter 4, the studies were expanded to distinct H:He ratios and fluence rates. It was demonstrated the exfoliation efficiency A_{ex} increases as the H:He ratio changes from 2:1 to 1:1. Detailed microstructure investigation by cross-section TEM observations reveals distinct microstructure features, including the formation and depth distribution of platelets and spherical cavities, depending on the fluence. Strain measurements (by XRD) in combination with elasticity considerations led to the formulation of a model explaining the formation of the microstructure features observed by TEM. Finally, the effect of the current density was investigated. A new phenomenon was uncovered: *the delamination of thin films via crack propagation*. This is a concurrent process to blistering/exfoliation. A phenomenological model based on elasticity and fracture mechanics theory is proposed to explain the results.

Chapter 5 introduces a multilayer exfoliation engineering concept. The process is based on the possibility to control of the exfoliation temperature of distinct implanted layers. It is indeed demonstrated that the exfoliation temperature can be tailored by the implanted fluence. In addition, the results also demonstrate that elastic interactions between distinct layers affect the exfoliation behaviour.

Chapter 6 explores defect engineering concepts of potential interest to manipulate H and He induced structures. The interactions are discussed in terms of trapping and diffusion

concepts. The formation of rather long and straight cracks is obtained by the hydrogenation of He-platelets, either by conventional implantation or plasma immersion treatment. In addition, the formation of arranged nano-domains of *H-platelets* takes place when their nucleation occurs under the influence of local strain fields.

In Chapter 7, the observed sub-local arrangements of the $\{111\}$ *H-platelet* variants are studied in details. The results are described in terms of a model formulated considering the in-plane stress produced by the implantation process and elastic interactions between He-plates (as local strain sources) and the H-platelets. The calculations provide the energy density variation for $\{001\}$ and $\{111\}$ H-platelets at any location with respect to the strain source. The results obtained are in good agreement with the experimental observations. Model predictions are introduced and discussed. The present nanoscale strain engineering concept is proposed as potential method to tailor specific arrangements of precipitates inside discrete nano-domains and to induce the formation of new phases.

Bibliography

- [Aga 1998] A. Agarwal, T. E. Haynes, V. C. Venezia, O. W. Holland, and D. J. Eaglesham, Appl. Phys. Lett. 72,1086 (1998).
- [Ale 2003] P. A. Aleksandrov, E. K. Baranova, I. V. Baranova, V. V. Budaraginy and V. L. Litvinov, Rad. Eff. & Def. in Solids, 158, 771–781 (2003).
- [Ard 1999] W.W. Van Arsdell, S.B. Brown, J. of Microelectromechanical Systems, Vol. 8, 319 - 327 (1999).
- [Asp 1996] Aspar, B., Bruel, M., Zussy, A. M. Cartier, Electron. Lett. 32 (21), 1985–1986 (1996).
- [Asp 1997] B. Aspar, M. Bruel, H. Moriceau, C. Maleville, T. Poumeyrol, A.M. Papon, A. Claverie, G. Benassayag, A.J. Auberton-Hervé and T. Barge, Microelectron. Eng. 36 (1–4), 233–240 (1997).
- [Asp 1998] B. Aspar, C. Lagahé, H. Moriceau, A. Soubié, M. Bruel, A. J. Auberton-Hervé, T. Barge, and C. Maleville, Mater. Res. Soc. Symp. Proc. 510, 381 (1998).
- [Asp 1999] B. Aspar, E. Jalaguier, A. Mas, C. Locatelli, O. Rayssac, H. Moriceau, S. Pocas, A.M. Papon, J.F. Michaud and M. Bruel, Electron. Lett. 35 (12), 1024–1025 (1999).
- [Asp 2000] B.Aspar, C. Lagahe, H. Moriceau, A. Soubie, E. Jalaguier, B. Biasse, A. Papon, A. Chabli, A. Claverie, J. Grisolia, G. Benassayag, T. Barge, F. Letertre and B. Ghyselen, IEEE (2000).
- [Asp 2001] B. Aspar, H. Moriceau, E. Jalaguier, C. Lagahe, A. Soubie, B. Biasse, A.M. Papon, A. Claverie, J. Grisolia, G. Benassayag, F. Letertre, O. Rayssac, T. Barge, C. Maleville, And B. Ghyselen, J. of Electron. Mat., Vol. 30, No. 7, (2001).
- [BCC 2004/8] *Silicon-on-Insulators: Technology and Markets*, BCC Research (2004/08).
- [Bea 1977] K. E. Bean and W. R. Runyan, J. Electrochem. Soc. 124, 5C (1977).
- [Bed 2000] S. W. Bedell, “Blistering and Layer Transfer of Hydrogen Implanted Crystals”, Thesis, University at Albany (2000).
- [Bed 2001] S. W. Bedell and W. A. Lanford, J. Appl. Phys., Vol. 90, No. 3, (2001).
- [Bis 1998] D. Bisero, *et al.*, J. Appl. Phys. 83-8, 4106 (1998).
- [Bru 1995] M. Bruel, *Electron. Lett.*, Vol. 31 No. 14 (1995).
- [Bru 1996] M. Bruel, Nucl. Instrum. Methods B 108 (3), 313–319 (1996).

- [Bru 1998] M. Bruel, B. Aspar, A.J. Auberton-Herve, *Jpn. J. Appl. Phys.* 36 (3B), 1636–1641 (1997).
- [Bru 1999] M. Bruel, *Mater. Res. Innov.*, 3 (1), 9–13 (1999).
- [Caltech] <http://www.design.caltech.edu/Research/MEMS/siliconprop.html>
- [Cel 1983] G. K. Celler, *J. Cryst. Growth* 63, 429 (1983).
- [Cel 1985] G. K. Celler, McD. Robinson, L. E. Trimble, and D. J. Lischner, *J. Cryst. Growth* 132, 211 (1985).
- [Cel 2003] G. K. Celler and S. Cristoloveanu, *J. Appl. Phys.*, Vol. 93, No. 9, 4955-4978 (2003).
- [Cer 1992] G. F. Cerofolini, L. Meda, R. Balboni, F. Corni, S. Frabboni, G. Ottaviani, R. Tonini, M. Anderle, and R. Canteri, *Phys. Rev. B* 46, 2061 (1992).
- [Cer 1995] G. F. Cerofolini et al., *Phys. Stat. Sol. (a)* 150, 539 (1995).
- [Cer 2000] G. F. Cerofolini, F. Corni, S. Frabboni, C. Nobili, G. Ottaviani, and R. Tonini, *Mater. Sci. Eng.* 27, 1 (2000).
- [Cha 1999] Y.J. Chabal, M.K. Weldon, Y. Caudano, B.B. Stefanov and K. Raghavachari, *Physica B* 273-274 (1999)
- [Che 2004] P. Chen and P. K. Chu, T. Höchbauer, M. Nastasi, D. Buca, S. Mantl, N. D. Theodore, T. L. Alford, J. W. Mayer, R. Loo, M. Caymax, M. Cai, S. S. Lau, *Appl. Phys. Lett.*, Vol. 85, No. 21, (2004).
- [Che 2005] P. Chen, P. K. Chu, T. Höchbauer, J.-K. Lee, M. Nastasi, D. Buca, S. Mantl, R. Loo, M. Caymax, T. Alford, J. W. Mayer, N. D. Theodore, M. Cai, B. Schmidt and S. S. Lau, *Appl. Phys. Lett.* 86, 031904 (2005).
- [Chr 2006] D. Christie, *J. of Failure Analysis and Prevention*, 6(3) (2006).
- [Cio 1996] L. Di Cioccio, Y. Le Tiec, F. Letertre, C. Jaussaud and M. Bruel , *Electron. Lett.* **32** (12) p. 1144 (1996).
- [Col 1997] J.-P. Colinge, *Silicon-on-Insulator Technology: Materials to VLSI*, 2nd ed., Kluwer, Boston (1997).
- [Cre 1967] M. Creager, P. C. Paris, *Int. J. of Fracture*, Vol. 3 (1967).
- [Cul 1978] B.D. Cullity, S.R. Stock, *Elements of X-Ray Diffraction*, Addison-Wesley Series in Metallurgy & Materials, (1978).
- [Das 1980] S.K. Das, *Radiation Effects* **53** p. 257 (1980).

- [Dea 1973] G. Dearnaley, J. H. Freeman, R. S. Nelson, J. Stephen, *Ion implantation*. Amsterdam:North Holland (1973).
- [Ded 1973] P.H. Dederichs, *J. Phys. F: Metal Phys.*, Vol. 3 (1973).
- [Del 2003] R. Delamare, « *Etude de la croissance thermique des cavités induites par l'implantation d'hélium dans le silicium* » These, Université d'Orléans (2003).
- [Des 2008] N. Desrosiers, A. Giguère, B. Terreault, M. Chicoine and F. Schiettekatte, *Nucl. Instr. and Meth. in Phys. Res. B* 266 1971–1978 (2008).
- [Don 1991] S.E. Donnelly and J.H. Evans, “Fundamental Aspects of Inert Gases in Solids”, Plenum Press , New York, (1991)
- [Duo 2001] X. Duo, W. Liu, M. Zhang, L. Wang, C. Lin, M. Okuyama, M. Noda, W.-Y. Cheung, P. K. Chu, P. Hu, S. X. Wang, and L. M. Wang, *J. Phys. D, Appl. Phys.* 34, 477 (2001).
- [Dün 2006] W. Düngen, R. Job, T. Mueller, Y. Ma, W. R. Fahrner L. O. Keller, J. T. Horstmann, and H. Fiedler *J. Appl. Phys.* **100**, 124906 (2006).
- [Eer 1977] E. P. EerNisse and S.T. Picraux, *J. Appl. Phys.* **48** (9) (1977).
- [Eri 1988] F. Ericson, S. Johansson, J.-A . Schweitz, *Hardness and fracture toughness of semiconducting materials studied by indentation and erosion techniques*, Mater. Sci. Eng. A , 131–141 (1988).
- [Eva 1977] J. H. Evans, *J. Nucl. Mat.* **68** (1977) 129.
- [Fan 1983] J. C. C. Fan, B.-Y. Tsaur, and M. W. Geis, *J. Cryst. Growth* **63**, 453 (1983).
- [Fen 2004] Xi-Qiao Feng, Y. Huang, *Int. J. of Solids and Structures* 41, 4299–4320 (2004).
- [Fic 1997] P. F. P. Fichtner, J. R. Kaschny, R. A. Yankov, A. Mücklich, U. KreiBig, and W. Skorup, *Appl. Phys. Lett.* 70 (6), (1997).
- [Fra 2002] S. Frabboni, *Phys. Rev. B* 65, 165436 (2002).
- [Fra 2004] S. Frabboni, G. C. Gazzadi, L. Felisari, R. Tonini, F. Corni, and G. Ottaviani *Appl. Phys. Lett.*, Vol. 85, No. 10 (2004).
- [Fre 1997] L.B. Freund, *Appl. Phys. Lett.* 70 (26), 3519–3521 (1997).
- [Ful 2002] B. Fultz, J. Howe, *Transmission electron microscopy and diffractometry of materials*, Springer (2002).
- [Gad 2003] M.A Gad, J.H. Evans-Freeman, N. Cinosi, J. Sarma, *Mater. Sci. Eng. B* 105, 79–82 (2003).

- [Ghi 2007] C Ghica, L C Nistor, H Bender, O Richard, G Van Tendeloo and A Ulyashin J. Phys. D: Appl. Phys. 40, 395–400 (2007).
- [Gib 1984] R. Gibala, R.F. Hehemann, Hydrogen embrittlement and stress corrosion cracking, American Society for Metals, Metals Park, OH (1984).
- [Gig 2005] A. Giguère, N. Desrosiers, and B. Terreault, Appl. Phys. Lett. 87, 211911 (2005).
- [Gig 2007] A. Giguère, B. Terreault, Surf. Coat. Technol. 201, 8205–8209 (2007).
- [Gol 1992] J. I. Goldstein, D. E. Newbury, P. Echlin, D.C. Joy, A.D. Roming, C.E. Lyman, C. Fiori, E. Lifshin, *Scanning Electron Microscopy and X-Ray Microanalysis*, Plenum Press (1992).
- [Gös 1998] U. Gösele and Q.-Y. Tong, Annu. Rev. Mater. Sci. 28, 215 (1998).
- [Gri 1920] A.A. Griffiths, *The theory of rupture and flow in solids*, Phil.Trans.Roy.Soc.Lond. A221, 163 (1920).
- [Gri 2000] J. Grisolia, G. Ben Assayag, and A. Claverie, B. Aspar C. Lagahe and L. Laanab, Appl. Phys. Lett., Vol. 76, No. 7, 14 (2000).
- [Gri 2000] J. Grisolia, These, *Evolution thermique des defaults introduits par implantation ionique d'hydrogène ou helium dans le silicium et le carbure de silicium*, Toulouse (2000).
- [Gro 2006] D. Gross, T. Seelig, *Fracture Mechanics with an Introduction to Micromechanics* Springer-Verlag, Berlin Heidelberg, (2006).
- [Gup 1983] A. Gupta and P. K. Vasudev, Solid State Technol. 26 (2), 104 (1983).
- [Har 2002] M. Hartmann and H. Trinkaus, Phys. Rev. Lett. 88, 055505 (2002).
- [Hen 2007] The Hendrix group, materials and corrosion engineering, <http://www.hghouston.com/Fracture.html> (2007).
- [Hir 1982] J.P. Hirsh and J. Lothe, *Theory of dislocations*, Krieger Publishing Company (1982).
- [Höc 2000] T. Höchbauer, A. Misra, R. Verda, M. Nastasi J.W. Mayer, Y. Zheng and S. S. Lau, PHIL. MAG. B, VOL. 80, N° 11, 1921-1931 (2000).
- [Höc 2001] T. Höchbauer, A. Misra, and M. Nastasi J. W. Mayer, J. Appl. Phys., Vol. 89, No. 11, 1 (2001).
- [Höc 2002] T. Höchbauer, A. Misra, and M. Nastasi and J. W. Mayer, J. Appl. Phys., Vol. 92, No. 5, (2002).
- [Hon 2007] J.-W. Hong, J.-H. Pyeon, J. W. Tedesco and Y.-B. Park, Phys. Rev. B **75**, 214102 (2007).

- [Hua 1998] L.J. Huang, Q. Y. Tong, T.H. Lee, Y.M. Chao, U.M. Gösele, *Electrochemical Society Proceedings* Vol. 98-1 (1998).
- [Hua 1999] L.-J. Huang, Q.-Y. Tong, Y.-L. Chao, and T.-H. Lee T. Martini and U. Gösele *Appl. Phys. Lett.*, Vol. 74, No. 7, (1999).
- [Hua 1999b] L. J. Huang, Q. Y. Tong, and U. Gösele, *Electrochem. Solid State Lett.* 2, 238 (1999).
- [Hue 2006] N. Hueging, M. Luysberg, H. Trinkaus. K. Tillmann, K. Urban, *J. Mater. Sci.* 41, 4454–4465 (2006).
- [Hut 1992] J.W. Hutchinson and Z. Suo, *Advances in applied mechanics*, Vol. 29, *Mixed Mode Cracking in Layered Materials* (1992).
- [Ima 1984] K. Imai and H. Unno, *IEEE Trans. Electron Devices* ED-31, 297 (1984).
- [ITR 2007] International Technology Roadmap for Semiconductors, <http://public.itrs.net>. (2007)
- [Izu 1978] K. Izumi, M. Doken, and H. Ariyoshi, *Electron. Lett.* 14, 593 (1978).
- [Jal 1998] E. Jalaquier, B. Aspar, S. Pocas, J.F. Michaud, M. Zussy, A.M. Papon and M. Bruel, *Electron. Lett.* **34** (4) p.408 (1998).
- [Jas 1983] L. Jastrzebski, *J. Cryst. Growth* **63**, 493 (1983).
- [Job 2005] R. Job, W. Düngen, Y. Ma, Y. L. Huang, and J. T. Horstmann, *Mater. Res. Soc. Symp. Proc.* 864, (2005).
- [Jon 1992] Russell H. Jones, *Stress-Corrosion Cracking*, *ASM international*, (1992)
- [Jur 2000] M. Jurczak, T. Skotnicki, M. Paoli, B. Tormen, J. Martins, J. L. Regolini, D. Dutartre, P. Ribot, D. Lenoble, R. Pantel, and S. Monfray, *IEEE Trans. Electron Devices* 47, 2179 (2000).
- [Kam 1971] M. Kaminsky, *IEEE Trans Nucl Sci NS*, 18:208 (1971).
- [Kan 1985] M. F. Kanninen, C. H. Popelar, *Advanced Fracture Mechanics*, Oxford university press, Oxford (1985).
- [Koz 2000] V.V. Kozlovskii, V.A. Kozlov, V.N. Lomasov, 34 (2), 129–147 (2000).
- [Kub 1999] F. J. Kub, K. D. Hobart, J. M. Pond, and S. W. Kirchoefer, *Electron. Lett.* 35, 477 (1999).
- [Lag 20003] C. Lagahé-Blanchard, N. Sousbie, S. Sartori, H. Moriceau, A. Sousbie, B. Aspar, P. Nguyen, and B. Blondeau, *ECS Proc.* 2003-19, 346 (2003).

- [Las 1986] J. B. Lasky, *Appl. Phys. Lett.* 48, 78(1986).
- [Lea 1982] H. J. Leamy, *Mater. Res. Soc. Symp. Proc.* 4, 459 (1982).
- [Lec 2005] S. Leclerc, A. Declémy, M. F. Beaufort, C. Tromas, and J. F. Barbot, *J. Appl. Phys.* 98, 113506 (2005).
- [Lee 2006] J.-K. Lee, Y. Lin, Q. X. Jia, T. Höchbauer, H. S. Jung, L. Shao, A. Misra, and M. Nastasi, *Appl. Phys. Lett.* 89, 101901 (2006).
- [Lig 1976] E. Ligeon and A. Guivarc'h, *Radiat. Eff.* 27, 129 (1976).
- [Lu 1997] X. Lu, N. W. Cheung, M. D. Strathman, P. K. Chu, Brian Doyle *Appl. Phys. Lett.* 71 (13), (1997).
- [Mar 2005] N. Martsinovich, I. S. Martínez, M. I. Heggie, *Physica Status Solidi C: Conferences* 2-6, 1771-1780 (2005).
- [Mic 2003] C. Miclaus and M. S. Goorsky *J. Phys. D: Appl. Phys.* 36, A177–A180 (2003).
- [Mil 1995] S. Milita and M. Servidori, *J. Appl. Crystallogr.* 28, 666 (1995).
- [Mou 2004] O. Moutanabbir, A. Giguère, and B. Terreault, *Appl. Phys. Lett.* 84, 3286 (2004).
- [Mou 2005] O. Moutanabbir, B. Terreault, M. Chicoine, F. Schiettekatte, *Appl. Phys. A* 80, 1455–1462 (2005).
- [Mou 2005b] O. Moutanabbir and B. Terreault, *Appl. Phys. Lett.* 86, 051906 (2005).
- [Mor 2004] M.J. Morschbacher, D.L. da Silva, P.F.P. Fichtner, E. Oliviero, M. Behar, F.C. Zawislak, B. Hollander, M. Luysberg, S. Mantl, R. Loo, M. Caymax, *Nucl. Instr. and Meth. in Phys. Res. B* 219–220, 703–707 (2004).
- [Nas 2005] Michael Nastasi, Tobias Höchbauer, Jung-Kun Lee, Amit Misra, and John P. Hirth, Mark Ridgway and Tamzin Lafford *Appl. Phys. Lett.* 86, 154102 (2005)
- [Nee 1988] J.H. Neethling, H.C. Snyman and C.A.B. Ball, *J. of Appl. Phys.* 63, 3 (1988).
- [Ngu 2005] P. Nguyen, I. Cayrefourcq, K. K. Bourdelle, A. Boussagol, E. Guiot, N. Ben Mohammed, N. Sousbie, and T. Akatsu, *J. Appl. Phys.* 97, 083527 (2005).
- [Ngu 2007] P. Nguyen, K. K. Bourdelle, T. Maurice, N. Sousbie, A. Boussagol, X. Hebras, L. Portigliatti, and F. Letertre, *J. Appl. Phys.* 101, 033506 (2007).
- [Nic 2000] N. H. Nickel, G. B. Anderson, N. M. Johnson, and J. Walker, *Phys. Rev. B* 62, 8012 (2000).

- [Nom 1997] T. Nomachi, S. Muto, M. Hirata, H. Kohno, Jun Yamasaki, and S. Takeda, *Appl. Phys. Lett.* 71 (2), (1997).
- [Par 2007] Young-Bae Park, Kenneth Diest, and Harry A. Atwater *J. of Appl. Phys.* 102, 074112 (2007)
- [Phi 1985] J. M. Phillips, *Mater. Res. Soc. Symp. Proc.* 37, 143 (1985).
- [Pit 2005] A. J. Pitera, and E. A. Fitzgerald, *J. Appl. Phys.* 97, 104511 (2005).
- [Pri 1985] D. Pribat, L. M. Mercandalli, J. Siejka, and J. Perriere, *J. Appl. Phys.* 58, 313 (1985).
- [Rad 2003] I. Radu, I. Szafraniak, R. Scholz, M. Alexe, and U. Gösele, *J. Appl. Phys.* 94 (12), 7820–7825 (2003).
- [Ros 1990] S.M. Rossnagel, J.J. Cuomo, W.D. Westwood, *Handbook of Plasma Processing Technology - Fundamentals, Etching, Deposition, and Surface Interactions*. William Andrew Publishing/Noyes (1990).
- [Sha 2005] Lin Shao, Yuan Lin, J. G. Swadener, J. K. Lee, Q. X. Jia, Y. Q. Wang, M. Nastasi Phillip E. Thompson N. David Theodore T. L. Alford, J. W. Mayer Peng Chen and S. S. Lau, *Appl. Phys. Lett.* 87, 251907 (2005).
- [Sha 2006] Lin Shao, Yuan Lin, J. G. Swadener, J. K. Lee, Q. X. Jia, Y. Q. Wang, M. Nastasi Phillip E. Thompson N. David Theodore T. L. Alford, J. W. Mayer Peng Chen and S. S. Lau, *Appl. Phys. Lett.* 88, 021901 (2006).
- [Sih 1973] G.C., Sih *Handbook of Stress Intensity Factors*, Lehigh University, Bethlehem, PA (1973).
- [Sil 2004] D. L. Da Silva, *Formação e estabilidade térmica de nanocavidades produzidas pela implantação de He em Si*, Thesis,UFRGS, Porto Alegre (2004).
- [Sne 1946] I. N. Sneddon, *Proc. R. Soc. London A* 187, 229 (1946).
- [SOI 2008] Available from Soitec. Inc., www.soitec.com , (2008)
- [Sou 2006] N. Sousbie, L. Capello, J. Eymery, F. Rieutorda and C. Lagahe, *J. Appl. Phys.* 99, 103509 (2006).
- [SRIM 2008] J.F. Ziegler, J.P. Biersack, SRIM, computer code at the URL <http://www.srim.org> (2008).
- [Ste 2007] S.A. Stepanov, http://sergey.gmca.aps.anl.gov/gid_sl.html (2007).
- [Tad 2000] H. Tada, P.C. Paris, G.C. Irwin, *The Stress Analysis of Cracks Handbook*, third ed. ASME Press, New York (2000).

- [Ter 2007] B. Terreault, *phys. stat. sol. (a)* 204, No. 7 (2007)
- [Ton 1997] Q.-Y. Tong, K. Gutjar, S. Hopfe, U. Gösele and T.H. Lee, *Appl. Phys. Lett.* 70 p. 1390 (1997).
- [Ton 1998] Q.Y Tong, R.W Bower, *MRS Bull.*, 23 (12), 40–44 (1998).
- [Ton 1998b] Q.-Y. Tong, R. Scholz, U. Gösele, T.-H. Lee, L.-J. Huang, Y.-L. Chao, and T. Y. Tan, *Appl. Phys. Lett.*, Vol. 72, No. 1 (1998).
- [Ton 2000] Q.Y. Tong, L.J. Huang, U. Gösele, *J. Electron. Mater.* 29 (7), 928–932 (2000).
- [Ton 2002] R. Tonini, F. Corni, C. Nobili, G. Ottaviani, F. Cazzaniga, and G. Queirolo, *Solid State Phenom.* 82–84, 291 (2002).
- [TSMC 2007] SOI Report (TSMC) Taiwan Semiconductor Manufacturing Company Limited, “19 electronics industry leaders join forces to accelerate SOI (silicon-on-insulator) Innovation into broad markets”, SOI Industry Consortium, 2007.
- [Use 2002] A. Y. Usenko and A. G. Ulyashin, *Jpn. J. Appl. Phys.* 41, 5021 (2002).
- [Use 2003] A. Y. Usenko, W. N. Carr and B. Chen, *J. of Mat. Sci. in Electr.* 14, 305-309 (2003).
- [Var 1997] C. M. Varma, *Appl. Phys. Lett.*, Vol. 71, No. 24, (1997).
- [Wel 1997] M. K. Weldon, V. E. Marsico, Y. J. Chabal, A. Agarwal, D. J. Eaglesham, J. Sapjeta, W. L. Brown, D. C. Jacobson, Y. Caudano, S. B. Christman, and E. E. Chaban, *J. Vac. Sci. Technol. B* 15, 1065 (1997).
- [Wel 1998] M. K. Weldon, M. Collot, and Y. J. Chabal V. C. Venezia, A. Agarwal, T. E. Haynes D. J. Eaglesham, S. B. Christman, and E. E. Chaban *Appl. Phys. Lett.*, Vol. 73, No. 25, 3721 (1998).
- [Wie 1970] S. M. Wiederhorn, H. Bolz, *J. of the American Ceramic Society* 53 (10) , 543–548 (1970).
- [Wil 2002] C. Donald Wilcox, S. Brent Dove, W. Doss McDavid and David B. Greer UTHSCSA ImageTool Version 3.0 , provided at <http://ddsdx.uthscsa.edu/dig/itdesc.html>, (2002).
- [Yam 1985] H. Yamamoto, H. Ishiwara, and S. Furukawa, *Appl. Phys. Lett.* 46, 268 (1985).
- [Yan 2003] F.Q. Yang, *J. Appl. Phys.* 94 (3), 1454–1457 (2003).
- [Yon 1994] T. Yonehara, K. Sakaguchi, and N. Sato, *Appl. Phys. Lett.* 64, 2108 (1994).
- [Yun 1998] C. H. Yun, A. B. Wengrow, and N. W. Cheung, Y. Zheng, R. J. Welty, Z. F. Guan, K. V. Smith, P. M. Asbeck, E. T. Yu, and S. S. Lau, *Appl. Phys. Lett.*, Vol. 73, No. 19, (1998).

[Yun 1999] C.H. Yun , A.B. Wengrow, N.W. Cheung, *Electrochem. Soc. Proc.* 3, 125–130 (1999).

[Yun 2003] C. H. Yun, N. Quitoriano, N. W. Cheung, *Appl. Phys. Lett.*, Vol. 82, No. 10, (2003).

[Zie 1985] J.F. Ziegler, J.P. Biersack, U. Littmark, *The Stopping and Range of Ions in Solids*, Pergamon, New York, (1985).

[Zhe 2001] Y. Zheng, S. S. Lau, T. Höchbauer, A. Misra, R. Verda, X.-M. He, M. Nastasi and J. W. Mayer *J. Appl. Phys.*, Vol. 89, No. 5, (2001).